# Lipid bilayers decorated with photosensitive ruthenium complexes

Bahreman, A.

Cover Page

# Universiteit Leiden

The handle http://hdl.handle.net/1887/22877 holds various files of this Leiden University dissertation

**Author**: Bahreman, Azadeh
**Title**: Lipid bilayers decorated with photosensitive ruthenium complexes
**Issue Date**: 2013-12-17

# Lipid bilayers decorated with photosensitive ruthenium complexes

PROEFSCHRIFT

ter verkrijging van
de graad van Doctor aan de Universiteit Leiden,
op gezag van Rector Magnificus Prof. mr. C.J.J.M Stolker,
volgens besluit van het College voor Promoties
te verdedigen op dinsdag 17 december 2013
klokke 11:15 uur

door

**Azadeh Bahreman**
geboren te Babol, Iran
in 1982

# Samenstelling Promotiecommissie

**Promotor**      Prof. Dr. E. Bouwman
**Co-promotor**   Dr. S. Bonnet

**Overige leden**   Prof. Dr. J.-P. Sauvage (University of Strasbourg, France)
                    Prof. Dr. J.A. Killian (University of Utrecht)
                    Dr. A. Kros (Leiden University)
                    Prof. Dr. J. Brouwer (Leiden University)

*"There may be one fault in a man that conceals a thousand qualities, or one excellence that conceals a thousand faults. The little indicates much."*

Shams Tabrizi

*To my parents*
*and Saeed*

# Table of Contents

# List of abbreviations

| | |
|---|---|
| A2780 | human ovarian carcinoma cell line |
| A2780 R | cisplatin-resistant human ovarian carcinoma cell line |
| A | absorbance |
| $A_{inf}$ | Absorbance at t=infinity |
| ATP | Adenosine triphosphate |
| BCA | bicinchoninic acid |
| biq | 2,2'-biquinoline |
| bpy | 2,2'-bipyridine |
| cisplatin | *cis*-diamminedichloridoplatinum(II) |
| COSY | correlation spectroscopy |
| chol | cholesterol |
| d | doublet (in NMR) |
| dd | doublet of doublet (in NMR) |
| dcbpy | 6,6'-dichloro-2,2'-bipyridine |
| DCC | dicyclohexylcarbodiimine |
| DCM | dichloromethane |
| DLS | dynamic light scattering |
| dmbpy | 6,6'-dimethyl-2,2'-bipyridine |
| DMPA | 4-dimethylaminopyridine |
| DMEM | Dulbecco's Modified Eagle Medium |
| DMPC | 1,2-dimyristoyl-*sn*-glycero-3-phosphocholine |
| DNA | deoxyribonucleic acid |
| DMPG | 1,2-dimyristoyl-*sn*-glycero-3-phosphoglycerol (sodium salt) |
| DOPC | 1,2-dioleoyl-*sn*-glycero-3-phosphocholine |
| DOPG | 1,2-dioleoyl-*sn*-glycero-3-phospho-(1'-rac-glycerol)     (sodium salt) |
| DMSO | Dimethyl sulfoxide |
| DSPE | 1,2-dioctadecanoyl-*sn*-glycero-3-phosphoethanolamine |
| em | emission |
| eq | equivalent |
| ESI-MS | electron spray ionization mass spectrometry |
| Et | ethyl |
| exc | excitation |

| | |
|---|---|
| FCS | fetal calf serum |
| FRET | Förster resonance energy transfer |
| GS | ground state |
| $H_4EDTA$ | ethylenediaminetetraacetic acid |
| HepaRG | human hepatic progenitor |
| HepG2 | liver hepatocellular carcinoma cell line |
| Hmte | 2-(methylthio)ethanol |
| HRMS | high resolution mass spectroscopy |
| I | ionic strength |
| ICP-OES | Inductively Coupled Plasma Optical Emission Spectroscopy |
| irr | irradiation |
| ITC | isothermal titration calorimetry |
| [lipid] | Lipid bulk concentration in a liposome formulation |
| LUVs | Large unilamellar vesicles |
| MC | Metal-centered |
| Me | methyl |
| MLCT | Metal-to-ligand charge transfer |
| NBD-PC | 1-acyl-2-{12-[(7-nitro-2-1,3-benzoxadiazol-4-yl)amino]dodecanoyl}-*sn*-glycero-3-phosphocholine |
| NMR | nuclear magnetic resonance |
| PBS | Phosphate-buffered saline |
| PACT | Photoactivated chemotherapy |
| PDT | photodynamic therapy |
| PEG | polyethylene glycol |
| phen | 1,10-phenanthroline |
| Ph. red | phenolsulfonphthalein |
| ppb | parts per billion |
| ppm | parts per million |
| P/S | penicillin/streptomycin |
| pymi | phenylpiridin-2-ylmethylene-imine |
| rpm | revolutions per minute |
| r.t. | room temperature |
| $[Ru]_{tot}$ | total bulk concentration of ruthenium complex |
| Ru-DMPG | ruthenium complex supported on DMPG liposome |
| RuHmte | ruthenium complex containing an Hmte ligand |
| $RuOH_2$ | ruthenium complex containing an aqua ligand |

| | |
|---|---|
| RuSRR' | ruthenium complex containing a sulfur-containing ligand |
| s | singlet (NMR) |
| T | temperature |
| t | triplet (NMR) or time |
| TEM | transmission electron microscopy |
| terpy | 2,2';6',2"-terpyridine |
| TMS | tetramethylsilane |
| WST-1 | 2-(4-Iodophenyl)-3-(4-nitrophenyl)-5-(2,4-disulfophenyl)-2H-tetrazolium sodium salt |

# 1

## General Introduction

**Abstract**

In this chapter an overview is given concerning photosensitive polypyridyl ruthenium complexes. The photosubstitution reactions of these complexes and their applications as light-controlled molecular machines and light-activatable anticancer compounds are presented. Lipid bilayers are introduced as a link between these two research fields. Lipid bilayers can be used on the one hand as surfaces where the molecular motion of ruthenium complexes can occur, and on the other hand as molecular carriers for drug delivery of anticancer ruthenium compounds.

## 1.1.    Photosensitive polypyridyl ruthenium(II) complexes

### 1.1.1.    Photoreactivity and photophysical properties

Ruthenium(II) complexes with polypyridyl ligands have been extensively studied because they show a variety of interesting properties in the excited-state, such as photosubstitution, photoluminescence, photo-redox chemistry, and photoisomerization processes. The unique photophysical and photochemical properties of these complexes allow them to be used in numerous medicinal and technological applications.[1-3]

$Ru^{II}$ is a $d^6$ octahedral system; the polypyridine ligands usually have σ donor orbitals localized on the nitrogen atoms, and π donor and π* acceptor orbitals delocalized on the aromatic rings. Transition of an electron from a $t_{2g}$ metal-based orbital to a $\pi^*_L$ ligand orbital typically results in a metal-to-ligand charge transfer (MLCT) excited states, whereas promotion of an electron from the $t_{2g}$ to the $e_g$ orbitals gives rise to a metal-centered (MC) excited state (Figure 1.1). The geometry of the metal center in a $^3MC$ excited state is strongly modified with respect to the ground state geometry notably along the metal-ligand bonds. When the lowest excited state has $^3MC$ character, it usually undergoes either fast, radiationless deactivation to the ground state, or ligand dissociation reactions (Figure 1.2a). Thus, the excited state lifetime is very short at room temperature and no radiative decay (luminescence) to the ground state is observed. On the other hand, since the ground state (GS) and MLCT states do not involve a change in $e_g$ orbital occupation, their corresponding potential wells are usually not significantly modified along the Ru–L coordinates. Consequently, when the lowest excited state is $^3MLCT$ it does not undergo fast radiationless decay to the ground state and luminescence is usually observed (Figure 1.2b). In such a case, the lifetime of the $^3MLCT$ excited state is typically temperature dependent, as it can be promoted to the $^3MC$ state thermally, which leads to photosubstitution reaction or rapid non-radiative decays to the ground state.[3-4] Overall, the photochemical behavior of ruthenium(II) complexes, *i.e.,* either their excellent luminescence properties or their ability for photochemical ligand exchange, is strongly influenced by the relative energy levels of the $^3MC$ and $^3MLCT$ excited states.

Many strategies have been considered to modify the energy difference between the $^3MLCT$ and $^3MC$ states of the complex and get the desired behavior under light irradiation. One strategy is the adjustment of the electronic properties of the polypyridyl ligands, which affects the energy of the $^3MLCT$ state and also the ligand

field splitting energy.[4] The second strategy is to vary the steric properties of the ligand to increase or reduce the energy difference between the $^3$MC and $^3$MLCT excited states. Thus, the relative energy levels of the various excited states, and thereby the nature of the lowest excited state, can be controlled by tuning the properties of the polypyridyl ligands in ruthenium(II) complexes.[5-6]
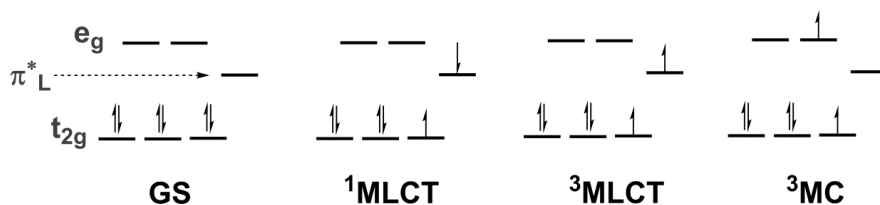


**Figure 1.1.** Schematic orbital diagram for the electronic ground state (GS) and the excited states for [Ru(bpy)$_3$]$^{2+}$ complex. Adapted from reference [4].
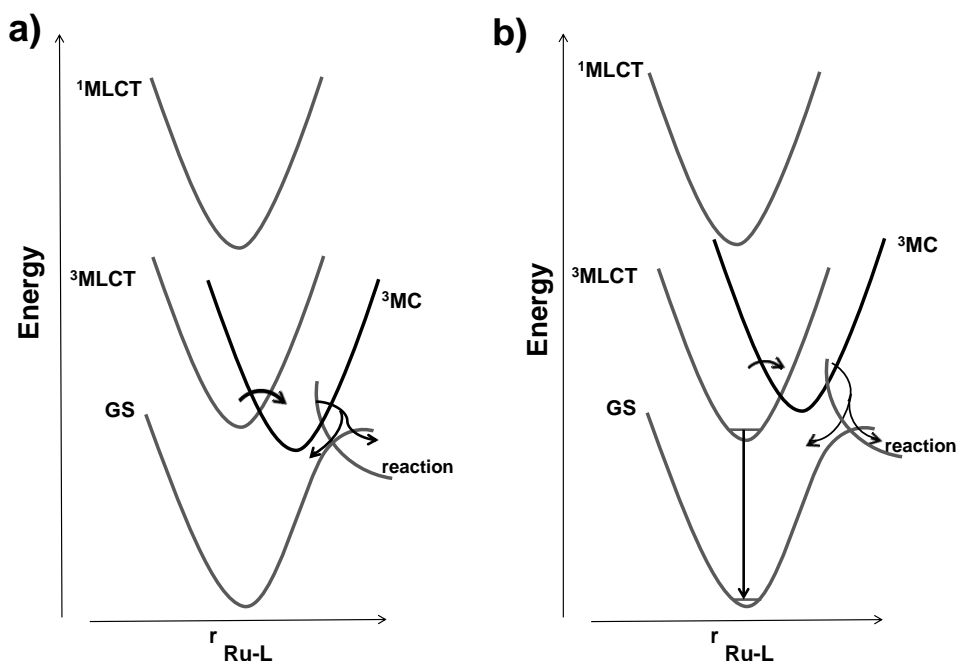


**Figure 1.2.** Potential well diagrams showing the relative energies of the $^3$MC and $^3$MLCT for Ru(II) polypyridyl complexes. (a) The $^3$MC is the lowest excited state, and (b) the $^3$MLCT is the lowest excited state. Ru-L is a coordination bond, where L is a nitrogen- or sulfur-donor ligand. Adapted from reference [3].

$[Ru(bpy)_3]^{2+}$ is one of the most investigated polypyridyl ruthenium(II) complexes (bpy = 2,2'-bipyridine).[3, 7] This complex has $D_3$ symmetry and its lowest excited state is of $^3$MLCT character with a long lifetime at room temperature (~1 µs). It thus undergoes relatively slow radiationless transitions and rather intense emission.[3] By replacing one bpy ligand with a constrained bipyridyl ligand like 1,2-di(pyridin-3-yl)ethane, the ligand field splitting energy decreases due to the modification of the N-Ru-N bite angle. Distortion of the complex and lower ligand field splitting energy reduces the energy of $^3$MC state. A decrease in the energy gap between the $^3$MLCT and $^3$MC is observed and the $^3$MC becomes thermally accessible from the $^3$MLCT state, which facilitates non-radiative decay back to the ground state (GS). As a result at room temperature the emission intensity of the ruthenium complex with 1,2-di(pyridin-3-yl)ethane is much lower (almost no emission in acetonitrile) than the emission of $[Ru(bpy)_3]^{2+}$.[8]

Similarly, using rigid tridentate ligands such as 2,2′;6′,2″-terpyridine (terpy) induces an even greater distortion from the ideal octahedral geometry compared to the Ru(II) complexes containing only bidentate ligands, since the N–Ru–N *trans* angles are significantly smaller than 180° with coordinated terpyridine ligands.[9] As a result, the complex $[Ru(terpy)_2]^{2+}$ for example is only luminescent at 77 K, whereas at room temperature the $^3$MLCT excited state is quenched.[10-11] In the extreme case, Ru[(6,6"-dptpy)]$^{2+}$ (dpterpy = 6,6"-dipheny1-2,2';6',2''-terpyridine) does not show any luminescence even at 77 K. A possible explanation is the presence of inter-ligand steric repulsions, which may further weaken the ligand field splitting, and as a consequence lower the energy of the $^3$MC state below that of the $^3$MLCT state, to fully quench emission.[10] Overall, more distortion in the coordination octahedron results in lower luminescence intensity for Ru(II) complexes.

## 1.1.2. Photosubstitution reactions

Photochemically labile ruthenium(II) complexes are capable of selectively photosubstituting a given ligand upon visible light irradiation.[12-15] Decreasing the energy of the $^3$MC state, for example by introducing distortion in the coordination octahedron, not only renders non-radiative processes more efficient, but also allows for the thermal population of the $^3$MC state from the $^3$MLCT state. Such thermal population of $^3$MC states may lead to photocleavage of one ligand L of the

coordination sphere, followed more or less simultaneously by the coordination of an incoming ligand L', typically a coordinating solvent molecule.[16]

Ruthenium complexes of the $[Ru(terpy)(N-N)(L)]^{2+}$ family, where N–N is a bidentate diimine ligand like 1,10-phenanthroline (phen) or 2,2'-bipyridine (bpy), and L is a neutral monodentate ligand, typically have enough distortion in their coordination sphere to selectively photosubstitute the monodentate ligand L.[17] In a study by Collin *et al.,* the photosubstitution of 2,6- -dimethoxybenzonitrile (MeOBN) by pyridine in a pyridine solution of $[Ru(terpy*)(N-N)(L)]^{2+}$ was investigated, where terpy* is 4'-(3,5-ditertiobutylphenyl)- 2,2';6',2''-terpyridine and N-N is phen or 2,9-dimethyl-1,10-phenanthroline (dmp). The study showed that using a sterically hindered dmp ligand, instead of the non-hindered ligand phen, resulted in an increase of the photosubstitution quantum yield by a factor 20 (Scheme 1.1). More steric interactions between dmp and MeOBN led to more efficient photoexpulsion of MeOBN from the octahedral coordination sphere of the metal.[13]
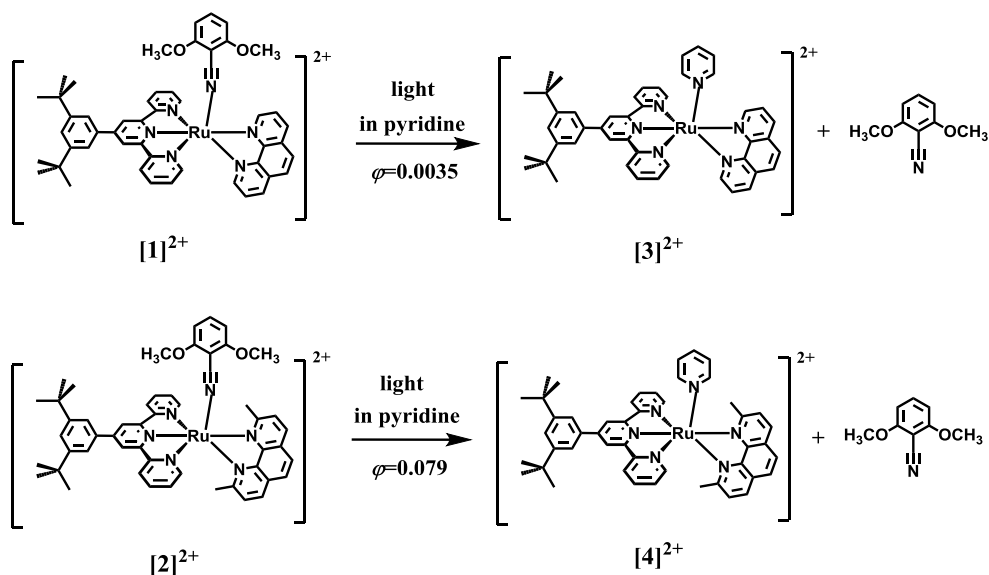


**Scheme 1.1.** Increasing the photosubstitution quantum yield by distorting the coordination sphere of the ruthenium complex. $\varphi$ represents the photosubstitution quantum yield. Adapted from reference [13].

The electronic properties of the ligands can also affect the rate and efficiency of photosubstitution processes. In a recent study by Turro *et al.,*[18] the role of the $^3$MLCT

state in photosubstitution reactions was investigated by changing the electronic properties of the leaving ligands. In this study, the photosubstitution of ligand L in $[Ru(bpy)_2(L)]^{2+}$, where L is a bidentate sulfur-donor ligand like 3,6-dithiaoctane or a bidentate nitrogen-donor ligand like 1,2-diaminoethane, was investigated. Higher photosubstitution quantum yields were reported in the former case. Based on DFT calculation, it was shown that the elongation of the Ru-S bond in the $^3$MLCT triplet state is larger than that of a Ru-N bond, which means that the Ru-S bonds are weaker in the $^3$MLCT excited state than Ru-N bonds, and will lead more efficiently to photosubstitution.

In the ruthenium(II) complexes of the $[Ru(bpy)(X)(Y)]^{2+}$ family, the monodentate ligands X and Y can be efficiently photosubstituted by solvent molecules. Modifying the properties of these monodentate ligands helps promoting the photodissociation of one of them, while allowing the other one to be photochemically stable. Typically, weaker σ donor ligands like phosphites, thioethers, or triazoles, were reported to be photoreleased faster than stronger σ donors such as pyridines, amines, or phosphines. Etchenique and co-workers have investigated the properties of these complexes to apply them as phototriggered caged molecules.[19]  In complex $[5]^{2+}$ (Scheme 1.2), PPh$_3$ is a weaker σ-donor and stronger π-acceptor than the amino group of γ-aminobutyric acid. Thus, upon irradiation with visible light the amine ligand is substituted by a water molecule to give $[6]^{2+}$, but the phosphine ligand in $[6]^{2+}$ remains coordinated even upon further irradiation.[20]
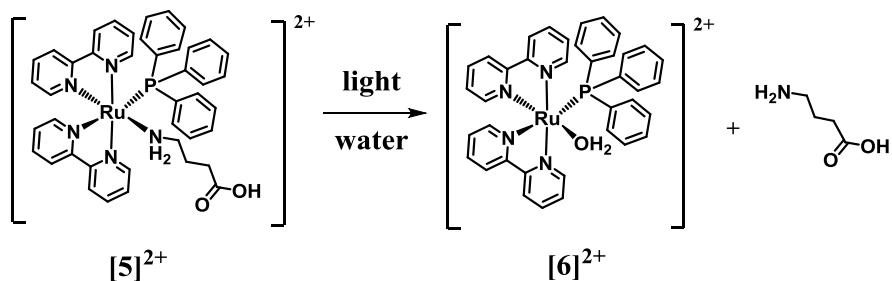


**Scheme 1.2.** Amine *vs.* phosphine reactivity in the photosubstitution of a monodentate ligand in complex $[5]^{2+}$ upon visible light irradiation[20].

### 1.1.3. Ruthenium-based molecular machines

A molecular machine can be defined as an assembly of different molecular components, *i.e.*, a supramolecular structure, designed to perform a specific mechanical function in response to an appropriate external stimulus such as light, electricity, or chemical energy.[21-22] The extension of the concept of machine from the macroscale to the molecular level is believed to be valuable for the development of nano-sized devices. Furthermore, it helps understanding the complex behavior of biological molecular machines such as ATPases or myosin, by mimicking their functions.[23-25] With such a concept in mind, the controlled unidirectional motion of single molecules is an ultimate goal that has been challenged mostly by organic chemists. For example, unidirectional motion in a mechanically interlocked assembly (molecular rotor)[26] and 'walking' of a two-legged molecular unit on a four-foothold molecular track (linear molecular machine),[27] have been reported by Leigh and co-workers.

Light irradiation, in particular, is a powerful tool to induce molecular motion. Several molecular machines have been reported that are powered by photonic stimuli.[28-31] Transition metal-containing catenanes and rotaxanes for example have been considered for building such systems, and among them multicomponent ruthenium(II) complexes, in which one part of the molecule can be set in motion photochemically with respect to the other part.[32-35] These systems take advantage of the dissociative, metal-centered $^3$MC state described in Section 1.1.1 to perform the motion in one direction by photosubstitution of one ligand. The reverse motion usually occurs thermally, to reset the molecule into the initial, photosensitive state. In such systems, sterically hindered chelating ligands are necessary to distort the octahedral geometry of the ruthenium(II) complexes and allow thermal population of the $^3$MC sate from the photochemically generated $^3$MLCT state.[17, 36] Complexes of the $[Ru(diimine)_2(N-N)]^{2+}$ family with hindered N-N ligands have been reported by the group of Sauvage and co-workers.[37-41] Two examples from this family are discussed below.

A rotaxane-based ruthenium complex forms by threading a N-N-containing macrocycle onto a Ru(diimine)$_2$-containing helical axis. Rigidity of the macrocycle is important for obtaining only the *endo*-coordinated isomer, where the helical axis passes through the macrocycle. As shown in Scheme 1.3, a Ru(phen)$_2$-based complex ($[\mathbf{8}]^{2+}$) can act as an axis, and a 6,6'-diphenyl-2,2'-bipyridine-based (dpbpy) macrocycle is threaded through the ruthenium axis to form the pseudo-rotaxane ruthenium complex $[\mathbf{7}]^{2+}$.

Under visible light irradiation, de-coordination of the dpbpy-containing ring was observed, leading to the separate fragments.[40]
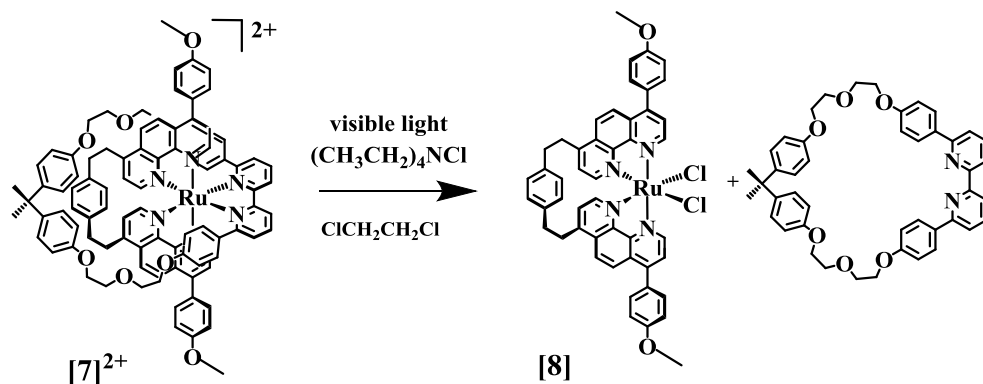


**Scheme 1.3.** Photoinduced dissociation of the macrocycle from a pseudo-rotaxane $[Ru(diimine)_3]^{2+}$ complex. Adapted from reference [40].

The second example consists of the catenane-based ruthenium complex $[9]^{2+}$ containing two interlocked rings. A macrocycle is usually used as a templating element in order to incorporate the $[Ru(diimine)_3]^{2+}$ core in the catenane (see Scheme 1.4).
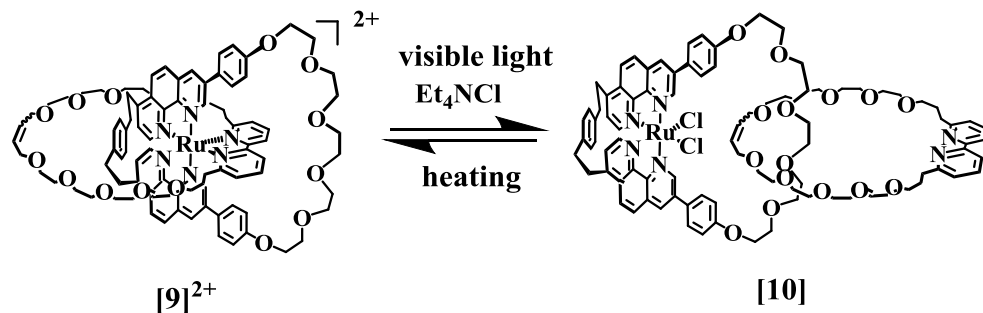


**Scheme 1.4.** The catenane-based ruthenium complex $[9]^{2+}$ undergoes a thermally reversible and complete rearrangement upon visible light irradiation [17].

The $[Ru(diimine)_2]$ -containing fragment is a 63-membered ring incorporating two phen units, whereas the N-N-bidentate fragment is a 42-membered ring containing a 6,6'-disubstituted bipyridine ligand. Light irradiation leads to the dissociation of the bpy ligand from the ruthenium center, to form complex $[10]$. The starting complex

[**9**]$^{2+}$ was recovered by heating the system. The size of the macrocyclic ring has a strong influence on the photoreactivity of the ruthenium complex: a catenane with a smaller ring than in complex [**9**]$^{2+}$ was reported to be less photoreactive.[36] Recently, a biisoquinoline-based 39-membered macrocycle was shown to improve the shuttling kinetics in this kind of mechanically interlocked coordination compounds.[42]

Another strategy reported by the same group[43] is to build a macrocycle using the Ru(terpy)(phen) core instead of Ru(phen)$_2$. In the sixth coordination position a monodentate ligand that can be photosubstituted should be included inside the macrocyclic cavity (Scheme 1.5).[43] In complex [**11**]$^{2+}$ a Ru(terpy)(phen) macrocyclic core was formed by connecting the terpy unit to the phen unit by a (CH$_2$)$_{18}$ linker and the monodentate pyridine ligand is included inside the ring. White light irradiation of this isomer induces the formation of a "photochemical" isomer [**12**]$^{2+}$ where the phen moiety has rotated by an angle of 90° compared to the terpy chelate. Such rotation leads to a major rearrangement of the alkyl linker chain. The reverse rotation of the phen chelate was achieved by heating the photochemical isomer in dimethylsulfoxide to recover, after ligand exchange, the initial "thermal" isomer [**11**]$^{2+}$. This is an example of quantitative, light-induced isomerization of a ruthenium polypyridyl complex.[43]
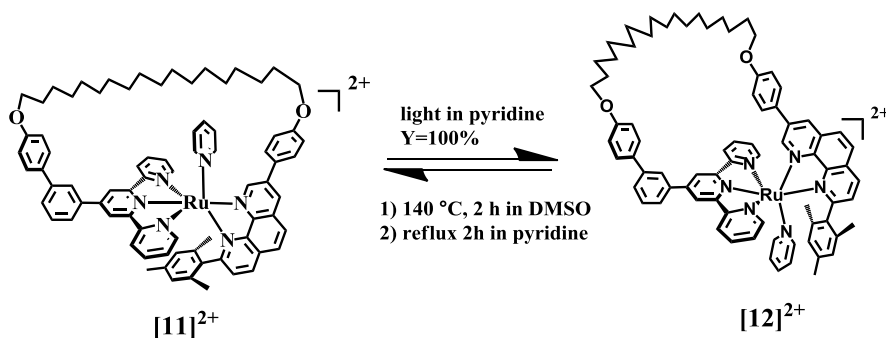


**Scheme 1.5.** Re-organization of a flexible (CH$_2$)$_{18}$ chain by the photoinduced rotation of the phen chelate in [**11**]$^{2+}$. The reverse motion is obtained by heating the complex in DMSO, followed by ligand exchange in pyridine [43].

In all of these examples the light-controlled motion of ruthenium-based molecules was performed in homogeneous solutions. Linear motion in homogeneous solution can be achieved for rotaxane-based transition-metal complexes when the ring moves from a

given position on the rotaxane axle to another position and vice versa.[35] These type of linear motors have been developed in order to mimic natural linear molecular machines such as myosin or kinesin, which move along the linear track of actin filament or microtubules, respectively, using ATP as a fuel (Figure 1.3a).[44] Ideal mimicking of the linear motion of natural molecular machines would be obtained by the development of molecules walking on a surface or on an artificial molecular track.
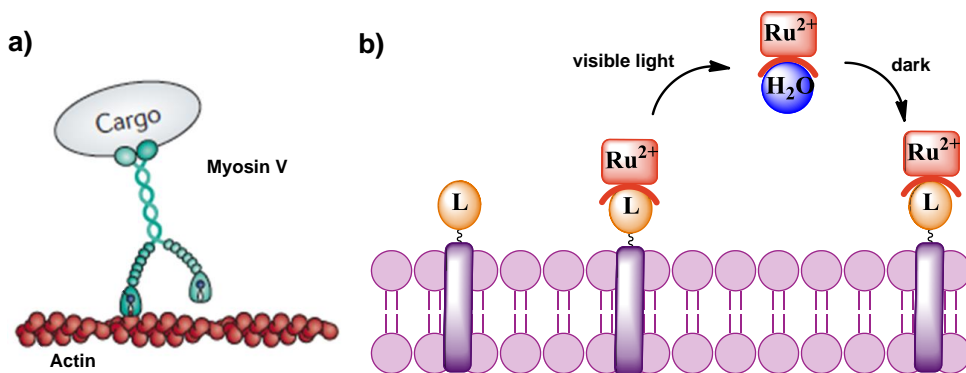


**Figure 1.3.** a) Myosin V works as a dimer that transports intracellular cargos along actin filaments. Adapted from reference [44]. b) Schematic cartoon proposed for the molecular motion of a photosensitive ruthenium complex at the surface of a lipid bilayer. The ruthenium carrier is detached from the lipid bilayer surface upon visible light irradiation (forming an aqua ruthenium complex), while it binds to the membrane embedded ligand L in the dark.

In the research reported in this thesis, such an artificial road was envisioned as being self-assembled at the surface of lipid bilayer membranes. Model membranes do not have the complexity of natural membranes, and their size, geometry, and composition can be optimized.[45] In such a vision, photosensitive ruthenium polypyridyl complexes would be used as molecular carriers to move a load unidirectionally at the surface of an artificial membrane. As shown in Figure 1.3b, the surface of a lipid bilayer can be functionalized with monodentate ligands L that may coordinate to ruthenium complexes. The idea was to use visible light to substitute ligand L by an aqua ligand, thus detaching the ruthenium carrier from the surface of the lipid bilayer. The aqua ruthenium species would diffuse freely near the surface and bind back to the membrane-embedded ligand L under thermal conditions, *i.e.*, in the absence of light.[46] By making the artificial road dissymmetric, the light-controlled motion of the ruthenium carrier from ligand to ligand would occur preferentially in one direction. In

the design of such a supramolecular system, understanding the reactivity of photosensitive ruthenium complexes must be deepened, and the dynamic interaction of the ruthenium complex with a model membrane should be fully understood. Thus, in Section 1.2 the dynamic interaction of metal cations and lipid bilayers will be discussed.

## 1.2. Lipid bilayers

### 1.2.1. Liposomes as model for cellular membranes

The self-assembly of lipid molecules in aqueous solution usually results in the formation of amphiphilic bilayers. In such an assembly the hydrophilic polar heads orient towards the aqueous phase while the hydrophobic part of the lipids form the inner hydrophobic core of the bilayer. Closed, spherical bilayers form structures called vesicles. Artificially synthesized vesicles are usually named liposomes.[47] Liposomes are dynamic systems with flexible surfaces; they have a great variety of topologies and shapes and can be unilamellar, multilamellar or oligovesicular (Figure 1.4).[48]



**Unilamellar**          **Multilamellar**          **Oligovesicular**
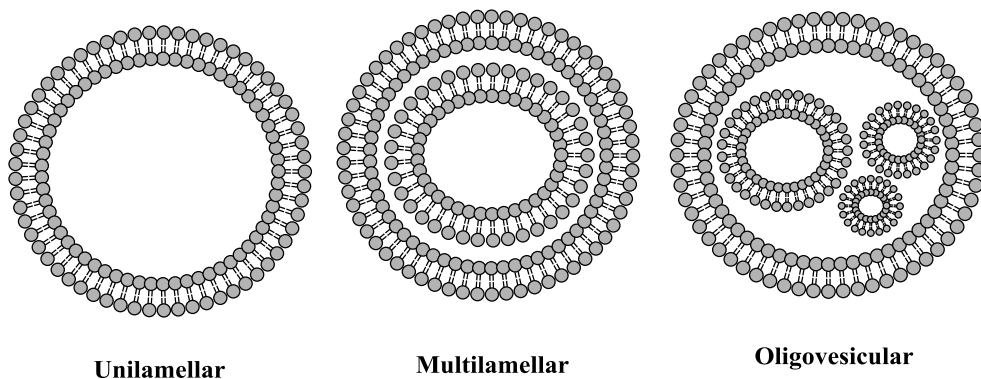
**Figure 1.4.** Schematic presentation of liposome structures of bilayer membranes.

Cell membranes play a crucial role in biological systems and many fundamental molecular processes are controlled by them. Membranes also act as a boundary between the extracellular and intracellular environments of a cell, and represent an essential functional unit for the transportation of materials, energy, and information. Liposomes formed of phospholipids or synthetic lipids have been widely used to mimic the functions and shape of biological membranes,[49-50] and also to develop biomimetic

systems such as nano-scale carrier systems,[51] reaction containers,[52] switchable assemblies,[53] sensors,[54-56] or supramolecular catalysts.[57]

Chemical recognition events on cellular membranes are the initial steps toward cellular signaling, and mimicking these functions is an important goal in the development of nano-scale molecular systems.[58] Usually, synthetic receptors are incorporated into liposomes that can interact with guest molecules or metal ions, which mostly leads to vesicular aggregation or fusion.[59] Interactions between liposomes can be controlled using electrostatic interactions,[60] hydrogen bonding,[61] but also metal ion coordination.[58-59] Metal ion coordination reactions in liposomal systems are more specifically discussed in the next section.

### 1.2.2. Dynamic systems involving liposomes and metals

In nature, important biological functions depend on metal ions interactions with cellular membranes. For example, it is known for a long time that calcium ions can bind to biological cell membranes containing phospholipids to induce liposome aggregation, and ultimately liposomal fusion.[62] Artificial membranes (liposomes) can be equipped with membrane-embedded ligands to control interaction with metal ions or complexes, in particular those involving transition metals.[63] Metal ion coordination to several membrane-embedded ligands can occur either on the same vesicle (intravesicular binding) or between two different vesicles (intervesicular binding). Only intervesicular binding induces aggregation, adhesion, or fusion of vesicles.[64]

The interaction between metal ions and lipid vesicles depends on several factors such as the charge of the lipid bilayer, the nature of the metal ions, or the nature and number of coordination sites of the membrane-embedded ligand (monodentate, bidentate, *etc.*). In addition, the ligand conformation and orientation in the lipid bilayer, and the strength of the metal-ligand coordination, can have an effect on the metal-bilayer interaction. It is noteworthy to briefly discuss these factors as an introduction to Chapters 2, 4, and 5 of this thesis.

Negatively charged phospholipids are known to aggregate or fuse in presence of metal cations such as $Ca^{2+}$, $Mg^{2+}$, or lanthanoid ions.[65] The nature of these interactions is believed to be mostly electrostatic and involves coordination of the phosphate head groups of the lipids to the metal ion. However, better selectivity and stronger metal-lipid interactions can be obtained with membrane-embedded ligands. For example,

intervesicular interaction has been reported for vesicles functionalized with terpyridine ligands (terpy), which aggregated in the presence of $Fe^{2+}$ ions. The aggregation process proved to be reversible, as the addition of the strongly chelating ligand $Na_2H_2edta$ (disodium salt of ethylendiaminetetraacetic acid) recovered the initial situation of non-aggregated vesicles (Figure1.5).[66] Lehn and co-workers[58] have reported similar aggregation phenomena for vesicles equipped with bipyridine (bpy) ligands in presence of $Ni^{2+}$ or $Co^{2+}$ cations. The coordination reaction first induced vesicle aggregation, which was followed by vesicle fusion.
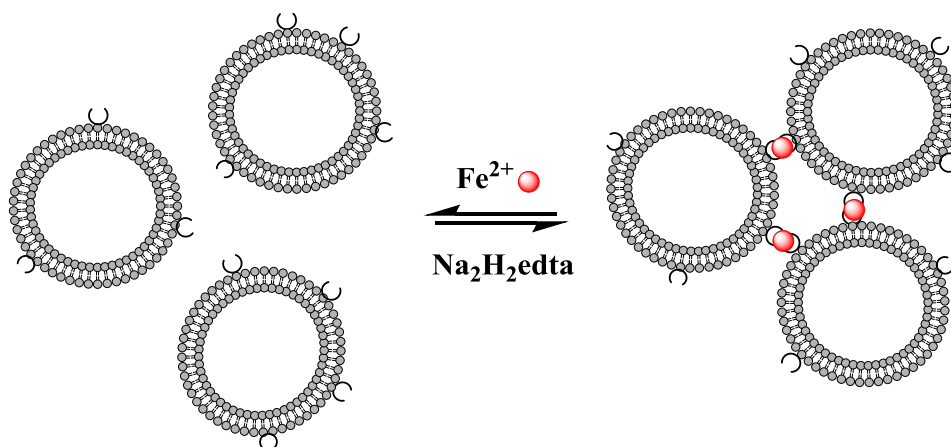


**Figure 1.5.** Aggregation of terpyridine-modified liposomes upon addition of iron(II) cations. Adapted from reference [66].

Besides the nature and number of coordination sites of the embedded ligands, the strength of the coordination bond plays a role in driving metal-lipid interactions. In other words, different metal ions may interact differently with one given ligand receptor incorporated in liposomes. In a study reported in 2007,[67] liposomes composed of amphiphilic cyclodextrins containing adamantyl-functionalized ethylenediamine ligands (L) were prepared. When $Cu^{2+}$ was added to the liposome sample, intravesicular interactions resulted in the formation of $[CuL_2]^{2+}$ complexes at the membrane, and no sign of aggregation was observed (Figure 1.6a). In contrast, after addition of $Ni^{2+}$ a mixture was formed comprising L, NiL and $[NiL_2]^{2+}$, and intervesicular interactions resulted in vesicle aggregation (Figure 1.6b). In fact, the stronger metal-ligand coordination bond in $[CuL_2]^{2+}$ resulted in exclusively

intravesicular interaction, while the weaker metal-ligand coordination bond in $[NiL_2]^{2+}$ resulted in predominantly intervesicular interaction.
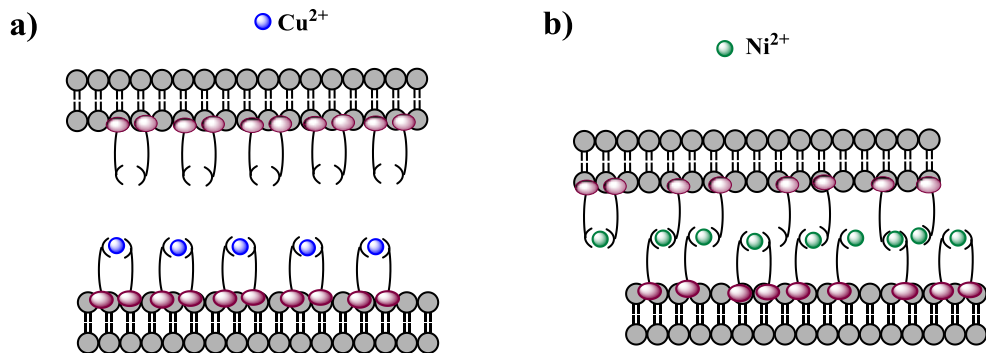


**Figure 1.6.** Orthogonal multivalent interactions within one bilayer and between two different bilayers of amphiphilic cyclodextrin-based liposomes. (a) Vesicle surface saturated with $[CuL_2]^{2+}$ (intravesicular interaction). (b) Two vesicles interacting *via* multiple coordination sites on $Ni^{2+}$ and L (intervesicular interaction). Adapted from reference [67].

Conformational changes of ligands inserted in a membrane, in response to metal coordination and/or external stimuli, can be used to control the reactivity of liposomes towards metal ions. For example, light irradiation can induce photoisomerization of membrane-embedded ligands, which might influence ligand coordination to metal ions. Kikuchi and co-workers reported supramolecular systems that mimic information processing in biological signal transduction systems.[49, 68] Molecular communication occurs between a molecular emitter and a molecular receiver (see Figure 1.7). A molecular switch based on an azobenzene-containing peptide lipid was embedded in a lipid bilayer. This molecular switch exhibited photoresponsive recognition behavior towards $Zn^{2+}$, which allowed for controlling the binding of a small liposome to a giant liposomal receiver. Upon UV light irradiation, the azobenzene ligand embedded in the small and giant liposomes significantly changed their configuration through photoisomerization of the N=N double bond, from the *trans* form to the *cis* form. As the metal-binding affinity of the *cis* isomer is much higher than that of the *trans* isomer; after addition of $Zn^{2+}$ the metal ion was stabilized by forming a complex with two ligands in the *cis* conformation only. Thus, the small liposome equipped with *cis* ligands bound to a receiver liposome that had the same molecular conformation. In contrast, visible light irradiation converted the *cis* isomer to the *trans* isomer, which has a lower metal-binding affinity. Thus, light-induced *cis-trans* isomerization of the

ligand modified the adhesion of the small liposomes to the receiver liposomes, *i.e.*, the metal-ligand interaction at the lipid membrane was modulated using light as external stimulus.[68]
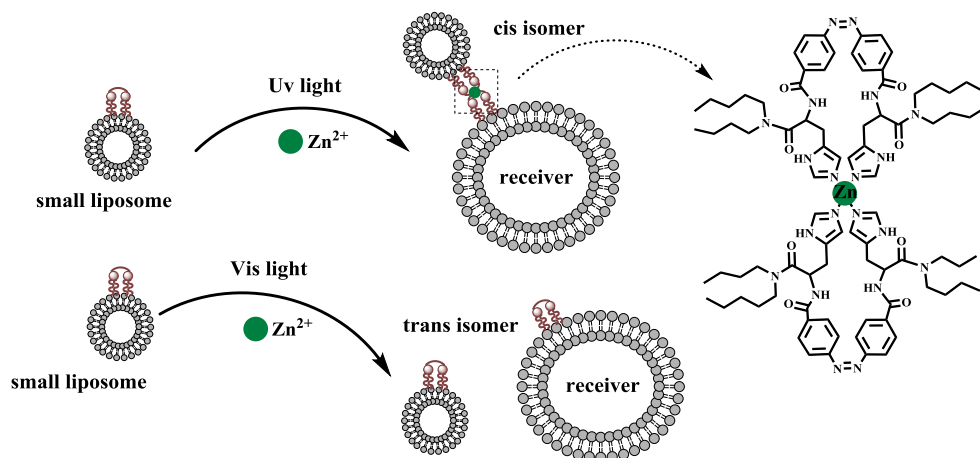


**Figure 1.7.** Photonic control of the binding of a molecular capsule (small liposome) to a molecular receiver (large liposome) by using a molecular switch. Adapted from reference [68].

Metal coordination can also influence ligand conformation, which can be used to regulate the association and dissociation of adhering liposomes. In a study by Ravoo *et al.*[64] a p-tert-butylbenzyl dimer with a flexible N,N'-bis(3-aminopropyl)ethylenediamine spacer was used as a non-covalent linker between cyclodextrin-functionalized liposomes (Figure 1.8). This linker induces adhesion of the liposomes by the formation of hydrophobic cyclodextrin/$^t$Bu-phenyl inclusion complexes in absence of metal ions. In the presence of $Cu^{2+}$, the tetraamine linker molecule formed a stable coordination complex and switched its conformation from linear to bent, which led to the dissociation of the intervesicular complexes and to the dispersion of the vesicle clusters. This process was reversible, as in presence of a strong chelating ligand such as $Na_2H_2edta$ the $Cu^{2+}$ ions were removed from the system and liposomal adhesion was re-established (Figure 1.8). Overall, ligand shape changes, lipid bilayers, and metal coordination influence each other, and such interactions would need to be understood and controlled when building a molecular machine at a bilayer surface based on metal coordination.
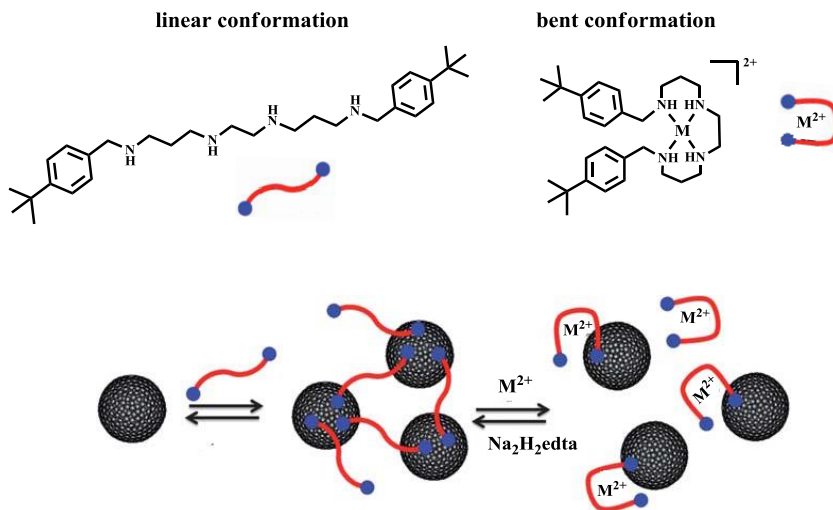
**Figure 1.8.** Coordination of $Cu^{2+}$ to a tetraamine ligand and a schematic representation of the metal ion responsive supramolecular system, in which vesicle adhesion or dispersion is controlled by the reversible conformational change of the spacer induced by metal ion coordination. Adapted from reference [64].

Metal binding to ligands embedded in neutral membranes can induce ligand dispersion and prevent ligand aggregation in the lipid bilayer membranes due to electrostatic repulsion between the cationic metals at the membrane surface. Arnold and co-workers in 1995 reported a liposomal sensor system that was able to detect $Cu^{2+}$ ions based on this principle.[69] The system relies on the excimer–monomer equilibrium of a pyrene dye. Neutral liposomes were functionalized with a lipid conjugate containing a pyrene moiety that was inserted into the lipophilic part of the membrane, and that was attached to a ligand facing the aqueous phase (Figure 1.9). The lipid conjugates with neutral head groups formed clusters in the liposomal bilayer in absence of $Cu^{2+}$, which showed the typical pyrene excimers emission. After addition of $Cu^{2+}$ ions and subsequent metal-ligand coordination the positively charged coordination complexes at the membrane repelled each other, which induced the dispersion of the membrane-embedded ligands and disrupted the pyrene eximers. The pyrene monomer and its excimer show very distinguishable emission spectra, which was used to detect coordination of the copper ions.
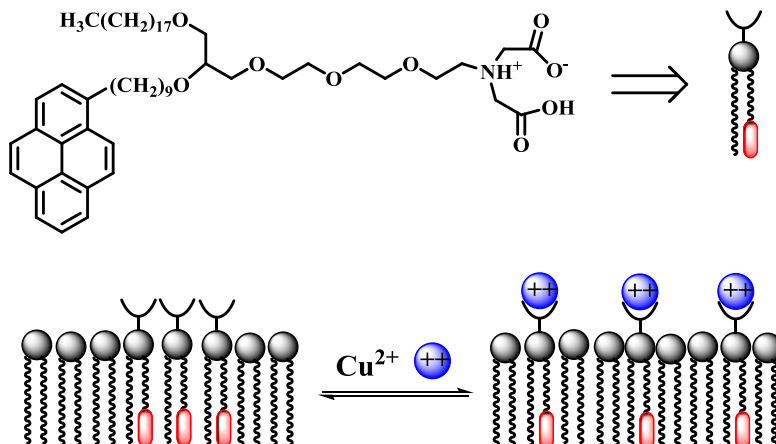
**Figure 1.9.** Metal ion sensor based on the switching of the monomer–excimer equilibrium of a pyrene moiety in a neutral liposome. The equilibrium is modified by the electrostatic repulsion between positive charges upon binding of $Cu^{2+}$ at the membrane surface. Adapted from reference [63].

Coordination of metal cations to membrane-embedded ligands can also modify the membrane permeability for metal cations. For example a 2004 study[65] showed that coordination of $Eu^{3+}$ ions to membrane-embedded diketonate ligands promotes the transportation of the $Eu^{3+}$ ions across the lipid bilayer surface. It was an artificial functional system mimicking the selective transport of metal ions by ionophores in biology.

The last factor to take into account in the design of a metal-based molecular transporter at the surface of a lipid bilayer is the site of metal-ligand coordination, which may be either the bilayer-water interface of the lipid membrane, or its lipophilic region. The latter type of coordination has been used to create liposomal ion sensors that mimic ion transportation through biological membranes *via* ion channels.[70] Webb and co-workers[71] have reported such kind of ion channels that can be gated "open" or "closed" by the addition or removal of palladium(II) ions. In the example shown in Figure 1.10 a pyridyl-cholate moiety was incorporated in unilamellar liposomes composed of neutral phospholipids. These liposomes also encapsulated a pH-sensitive dye (Figure 1-10a). Addition of $PdCl_2$ led to the linkage of two pyridyl-cholate moieties *via* coordination of the pyridine subunits to $Pd^{2+}$. The palladium(II) bis(pyridyl) motives created a channel through the membrane, which facilitated alkali metal ion transport. After addition of NaOH the transportation of the $Na^+$ ion resulted in an increase in pH, which was detected by a fluorescence increase of the encapsulated

dye. Subsequent addition of a palladium(II)-chelating agent (hexathia-18-crown-6 (18S6)) disconnected the channels, which stopped the flow of sodium ions and the evolution of fluorescence.
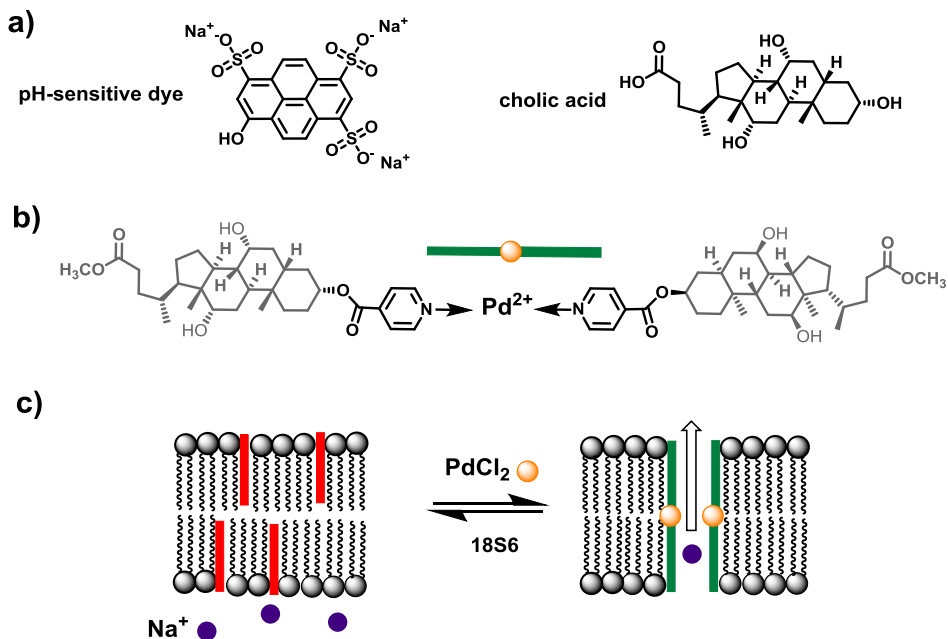


**Figure 1.10.** a) Chemical structure of a pH-sensitive encapsulated dye and cholic acid, b) pyridyl-cholate conjugate and coordination to a $Pd^{2+}$ ion , c) a schematic representation showing the gating of an artificial ion channels; either opened by the addition of $PdCl_2$, or closed by the addition of the hexathia-18-crown-6 ligand (18S6, bottom). Adapted from reference [71].

Overall, the examples detailed above illustrate the many options available when designing dynamic systems involving liposomes and metals. The dynamics of systems involving ligands, metal, and lipid bilayers, depend on a variety of factors that should be controlled in order to control molecular motion of the metal center at the membrane surface. In particular, intervesicular interactions like aggregation or fusion, ligand conformational changes, coordination in the lipophilic region of the membrane, or deep insertion of the ruthenium complex into the lipid bilayers, may reduce or impair the motion of ruthenium compounds at the membrane. In addition, neutral ligands may aggregate in the membrane and be dispersed upon coordination of the positively charged ruthenium complex, which would add another level in the complexity of the motion of the complexes. Finally, the ruthenium-ligand coordination bond should be

light-sensitive and stable in the dark if one wants to control the motion using light. For this PhD project, neutral monodentate thioether-cholesterol conjugates with flexible polyethyleneglycol linker were chosen, as there are flexible enough not to have one preferred conformation or configuration, do not significantly interact with protons in water, and may disperse homogeneously in the two dimensions of the membrane.

Next to their potential as metal sensors or as surfaces where molecular motion could occur, liposomes are mostly known for their application in drug delivery, as they can notably improve drug targeting towards cancer cells. In the next section the advantages of liposomal drug carrier systems in medicinal chemistry are introduced, before discussing the potential of ruthenium complexes as anticancer drugs.

## 1.3.  Ruthenium-decorated liposomes as light-activatable prodrugs

### 1.3.1.  Liposomes as drug carriers in cancer therapy

The major goal in drug delivery is to effectively deliver molecular drugs to their biological target in order to avoid toxic side effects for the patient. Three basic requirements for a successful drug delivery system in anticancer research are: (I) prolonged blood circulation of the drug, (II) sufficient accumulation of the drug in the tumor, and (III) controlled drug release and uptake by tumor cells.[72] Nano-sized drug delivery systems like micelles, liposomes, and nanoparticles, can be modified to incorporate targeting moieties that allow for specific delivery of the drug to cancer cells expressing specific receptors at their surface. Gregoriadis *et al.* [73] in 1974 proposed the first liposomal-based drug carrier in cancer chemotherapy, and since then the interest in liposomal drug carriers has increased significantly.[72] One of the most acknowledged advantage of liposomes is their ability to deliver both hydrophobic and hydrophilic drugs, as well as mixtures of these. Water-soluble drugs can be encapsulated in the internal aqueous compartment of the liposome, whereas lipophilic drugs can be included within the hydrophobic part of the phospholipid bilayer.[74] Moreover, liposomes tend to accumulate at cancer tumor sites rather than at normal tissues. The structure of the microvasculature in tumors has large openings (up to 500 nm), which allows liposomes diffusion inside the tumors.[75] Beside their size, the surface charge of liposomes and their lipid composition play critical roles in their circulation lifetimes in the blood.[76] It has been proven that "stealth" liposomes, *i.e.*, liposomes coated with synthetic polyethyleneglycol polymers (PEG), have

significantly increased half-life in the blood compared to liposomes of the same composition but deprived of PEG chains. Such long circulation half-life times allow efficient delivery of this kind of liposomes to cancer cells via the so-called "Enhanced Permeability and Retention" (EPR) effect.[77-78]

There are two main strategies for efficient targeting of liposomes to tumors and drug-release: (I) site-specific delivery, which can be achieved by coating the liposomes with ligands or antibodies that target overexpressed receptors in the tumor tissue; (II) site-specific triggering by external stimuli like pH,[79-80] temperature,[81] or light,[82-83] to release the encapsulated drug.[72] Using light as a triggering signal, for example, is possible with photosensitive liposomes made of lipids that can either isomerize, fragment, or polymerize upon light irradiation.[84]

Light-triggered drug activation is a basic concept used primarily in a treatment modality called "photodynamic therapy" (PDT). In PDT a photosensitizer is applied to the diseased tissue. This photosensitizer absorbs photons and transfers its energy to the triplet ground state of the dioxygen molecule, to form the excited state of $O_2$ called singlet oxygen ($^1O_2$). The high oxidizing properties of $^1O_2$ can then induce cell death by fast reactions with proteins, lipids, or nucleic acids.[85-87] Most photosensitizers applied in clinical treatments are rather hydrophobic and tend to form aggregates in aqueous media, which reduces their photosensitizing efficacy as only monomeric species are usually photoactive. Liposomes have been used in PDT since they can significantly decrease photosensitizer aggregation. A variety of photosensitizer drugs, such as tetramethyl hematoporphyrin (TMHP), fullerene (C60/C70), and zinc phthalocyanine (ZnPc), have been used in combination with liposomes.[87-89] In a recent study by Lissi *et al.*[90] the photophysical and photochemical properties of ZnPc photosensitizers in THF was compared with those of ZnPc incorporated in phosphatidylcholine liposomes. The results showed that dye incorporation into liposomes decreases ZnPc aggregation and provide a better photodynamic activity on HeLa cancer cell line (cervical cancer cells).

Despite the variety of liposomal drug delivery systems reported in the scientific literature, there are only few examples of liposomes used for encapsulating metal-based drugs. Hence, some of the few systems described so far will be briefly discussed here. Anticancer platinum compounds, in particular cisplatin (*cis*-diamminedichloridoplatinum), are one of the few metal-based anticancer agents that

have been considered for liposomal drug delivery. The antitumor property of cisplatin is largely due to its binding to nuclear DNA. However, cisplatin tends to bind to blood plasma proteins as well, particularly those with thiol groups such as human serum albumin and other proteins with high cysteine content. Such binding mostly leads to deactivation of cisplatin, and it induces side effects during cisplatin chemotherapy. [91-92] Liposomal drug delivery is believed to be able to solve or at least reduce these problems. In the literature, mostly poorly water-soluble platinum compounds such as cisplatin have been incorporated into the hydrophilic core of liposomes (Figure 1.11a).[93-94] However, in a recent study by Kaluderovic *et al.*[95] a water-insoluble platinum drug was incorporated into the lipophilic part of lecithin liposomes (Figure 1.11b) and the cytotoxicity of this formulation was tested on several tumor cell lines as well as normal cells. The results showed that a liposome-incorporated cisplatin drug had higher cytotoxicity and selectivity for some cancer cell lines such as human thyroid carcinoma cells SW1736, compared to non-encapsulated complex [**14**] or cisplatin [**13**].
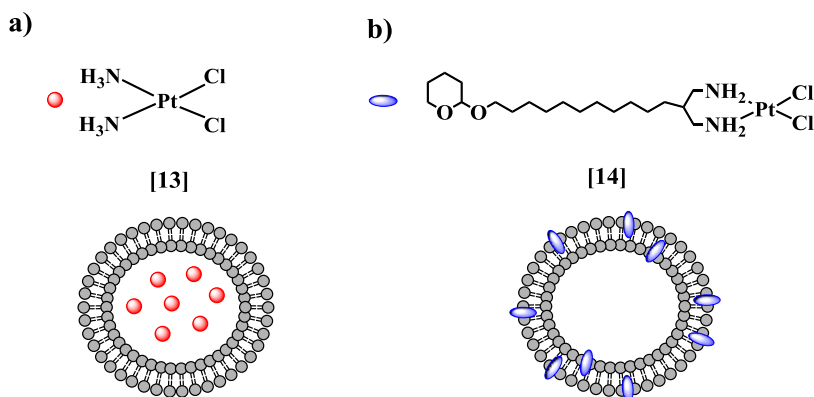


**Figure 1.11.** a) Cisplatin loaded in the hydrophilic core of a liposome. b) Lipophilic cisplatin analog loaded in the lipid bilayer of a liposome. Adapted from reference [95].

Most drugs are toxic in high dosage, which restricts their clinical application in cancer therapy. In order to overcome the high dosage toxicity, the drug activity needs to be controlled, for example by encapsulation in liposomes. In 2006 Halloran *et al.* [96] developed a liposomal system for encapsulating arsenic-based drugs. Arsenic trioxide ($As_2O_3$) is a promising agent for the treatment of blood and bone marrow cancers. However, clinical application of this drug to other cancers has been limited due to its

toxicity at higher doses. This problem was solved by encapsulation of high doses of $As_2O_3$ in phospholipid liposomes that were able to release the drug in a controlled fashion, *i.e.*, upon pH variation. While the therapeutic agent remained in the liposome at physiological pH (7.4), it was released at lower pH (4.0), typical of the endocytic compartments involved in the cellular uptake of liposomes.

The cellular uptake pathway can also be changed by encapsulation of metallodrugs in liposomes, which sometimes leads to better cellular uptake of a liposome formulation compared to the non-encapsulated drug. For example, gallium nitrilotriacetate is a therapeutic agent that has been proven to be effective for the treatment of several cancer types. $Ga^{3+}$ ions are mostly taken up by cancer cells via a transferrin (TF) receptor pathway, and it competes with iron cellular uptake. The transferrin-independent uptake mechanism is also possible, but this accounts for only 10% of the total $Ga^{3+}$ uptake. In a study from 1993[97] it was reported that encapsulation of gallium nitrilotriacetate in negatively charged liposomes provided a transferrin-independent route for the delivery of $Ga^{3+}$ ions to cancer cells.
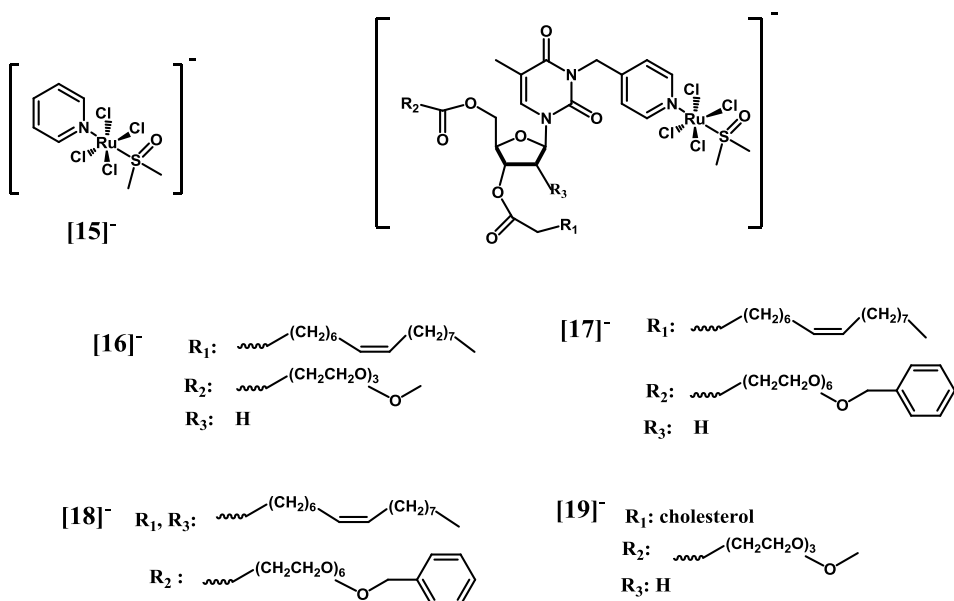


**Figure 1.12.** Structural formula of complex AziRu [**15**]$^-$ and AziRu functional nucleolipids [**16**]$^-$, [**17**]$^-$, [**18**]$^-$, and [**19**]$^-$. Adapted from references [98-99].

Until recently no study has been reported for the liposomal drug delivery of ruthenium-based anticancer compounds. In 2012 Paduana and co-workers[98-99] reported the first systems of this kind. Ruthenium(III) complexes functionalized with different amphiphilic nucleosides (Figure 1.12) were incorporated in the lipophilic phase of neutral liposomes. The ruthenium complex [**15**]¯ (named AziRu) was chemically linked to the nucleolipid (a hybrid molecule containing a nucleic acid unit and amphiphilic moieties) via an Ru-N coordination bond. The anticancer activity of these ruthenium-functionalized liposomes was investigated on several cancer cell lines and compared with free AziRu. [98-99] The results showed higher *in vitro* anti-proliferative activities for the ruthenium-containing liposomes than for free AziRu. It was reported that the liposomal formulation facilitated the internalization of the ruthenium complex and postponed its hydrolysis in physiological conditions. This work showed for the first time the capacity of ruthenium-decorated liposomes to be used in drug delivery.

## 1.3.2.  Ruthenium complexes as anticancer drugs

### 1.3.2.1.  Cytotoxicity of ruthenium complexes and mechanism of action

Since the discovery of cisplatin, many transition metal complexes have been synthesized and tested for their anticancer activity. In recent years, ruthenium-based molecules have attracted much attention as promising antitumor agents. Ruthenium complexes have three properties that make them potentially suitable for medicinal use: I) slow ligand-exchange kinetics similar to those of Pt(II) complexes, II) multiple accessible oxidation states allowing prodrug activation strategies, and III) the ability to mimic iron binding to certain biologic molecules such as albumin and transferrin.[100] Since rapidly dividing cells, such as cancer cells, have a greater demand for iron compared to normal cells, transferrin receptors are over-expressed in tumors, which may allow for more effective delivery of ruthenium-based drugs to cancer cells.[101-102] Moreover, Ru(II) complexes have octahedral coordination spheres, in contrast to the square-planar geometry of Pt(II) compounds, which may allow for obtaining different toxicity profiles for ruthenium compounds and addressing cisplatin-resistant cancer cells.[103-104]

Among the many ruthenium complexes that have been investigated only two compounds, namely NAMI-A[105] and KP1019,[106] have entered human clinical trials

(Figure 1.13). Despite their structural and chemical similarities, these two Ru(III) complexes show different antitumor behavior. In pre-clinical studies, NAMI-A has shown inhibitory effects against the formation of metastases in a variety of animal tumor models, although it appeared to lack direct cytotoxicity towards human tumors.[107] In contrast, KP1019 has proven to be cytotoxic against a wide range of primary human tumors by inducing apoptosis.[106]
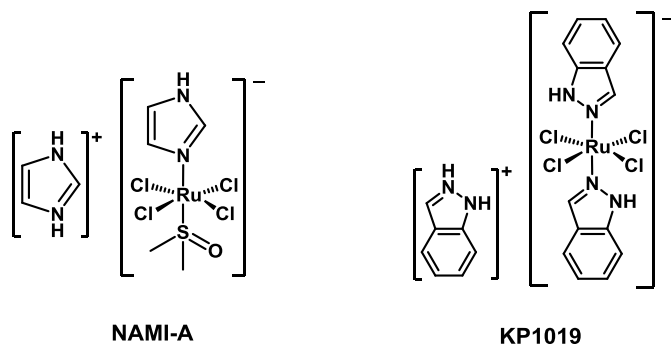


**NAMI-A**

**KP1019**

**Figure 1.13.** Chemical structures of anticancer ruthenium complexes NAMI-A and KP1019.

Most ruthenium complexes investigated for medicinal purposes, including NAMI-A and KP1019, undergo ligand exchange in biological media. Usually the metal complex is first hydrolyzed to give an aqua complex, which is often believed to interact with DNA through the formation of coordination bonds between the metal center and nitrogen ligands or DNA phosphate groups on the DNA bases,[108] leading to metal-DNA adduct formation and cell death (Scheme 1.6). This mechanism is quite often called "irreversible binding" because it involves the formation of a coordination bond.[109] Binding of the ruthenium(II) center to DNA has been hypothesized for a wide range of ruthenium-based analogues of cisplatin, such as for example $[RuCl_2(DMSO)_4]$,[107] $[Ru(bpy)_2Cl_2]$, $[Ru(terpy)Cl_3]$,[110-111] or complexes of the type $[Ru(terpy)(N-N)(L)]^{2+}$, where N-N is a bidentate diimine ligand like bpy or phen.[112] However, in the case of substitutionally inert polypyridyl Ru(II) complexes of $[Ru(diimine)_3]^{2+}$ family , cytotoxic effects were also obtained *via* van der Waals interactions with DNA.[113-115] All interactions with DNA not involving coordination to the metal center are usually called "reversible" binding, and are divided into four categories: I) electrostatic interaction, II) intercalation, III) groove binding (molecules

occupy the minor or major groove of DNA), and IV) binding to non-canonical DNA such as mismatch, G-quadruplex, or triplex DNA structures, which involves a combination of electrostatic and van der Waals interactions.[109]
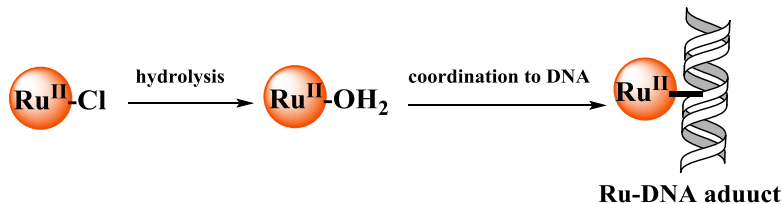


**Figure 1.14.** Hydrolysis and coordination of a Ru(II) complex to the nucleophilic DNA binding sites.

In recent years innovative studies have shown that other mechanisms such as topoisomerase enzymes inhibition,[116] or mitochondria-mediated apoptosis,[117-118] may be responsible for the cytotoxicity of metallodrugs, in particular for saturated complexes unable to coordinate to DNA. In a study by Gazzer *et al.*, the cytotoxicity mechanism of the coordinatively saturated Ru(II) complex $[Ru(dppz)_2(CppH)]^{2+}$ (CppH =2-(2′-pyridyl)pyrimidine-4-carboxylic acid; dppz = dipyrido[3,2-a:2′,3′-c]phenazine) was investigated in detail.[119] It was proposed that this compound exerted its toxicity through a mitochondria-related pathway rather than *via* binding to nuclear DNA. Although the complex was shown to bind to calf thymus DNA by intercalation, this interaction is not involved in the toxicity mechanism *in vitro*.

### 1.3.2.2. Photoactivated chemotherapy

Photoactivated chemotherapy (PACT) consists in the light-controlled activation of a drug at the tumor site, which results in greater specificity for the action of a drug. The concept of an inactive precursor, or "prodrug", is important in this field.[120] The challenge is to develop compounds that are thermally stable, but can be triggered by low energy light irradiation to generate toxic species with anticancer properties similar to that of other chemotherapeutics.[121] The activity of light-produced cytotoxic agents ideally depends on their ability to interact with biopolymers or bio-aggregates such as cell membranes, proteins, or DNA. Damage to DNA can occur by photoinduced electron transfer between the excited state of the photoactivated molecule and DNA.[122] Another method is photodynamic therapy (PDT).[85-86] Since in PDT the toxicity is oxygen-dependent and tumor cells are generally hypoxic, new approaches

based on photoinduced ligand substitution in transition metal complexes are interesting alternatives, where a coordinatively saturated metal complex would either bind to nucleic acids or proteins after photochemically losing a biologically inactive ligand (Figure 1.15-I), and/or releasing photochemically a biologically active organic ligand (Figure 1.15-II).[108, 123]
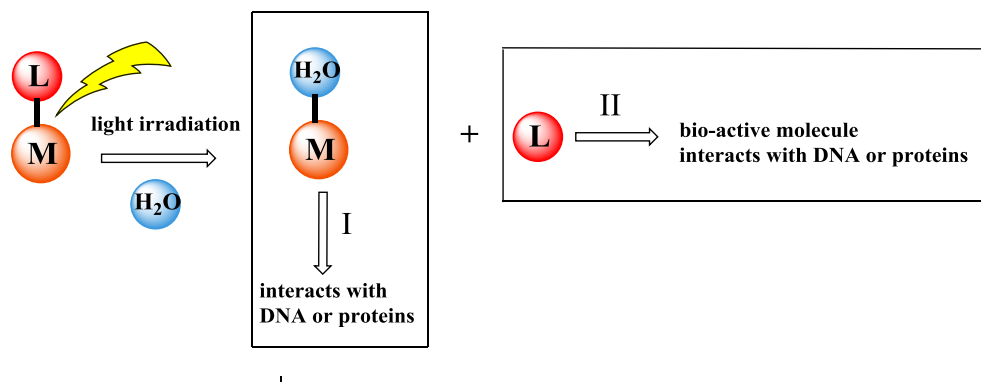


**Figure 1.15.** Photochemotherapy using a photosensitive metal-based prodrug and two possible cytotoxicity mechanisms involving photosubstitution. M: metal complex, L: photosubstituted ligand, M-$H_2O$: hydrolyzed metal complex.

Ruthenium complexes are particularly attractive for photoactivated chemotherapy (PACT), as their photophysical properties can be tuned, they strongly absorb in the visible region (400-600 nm), and are kinetically inert.[123] As mentioned in Section 1.1.2. complexes with distorted octahedral geometry are prone to ligand dissociation under visible light irradiation. Thus, steric and electronic properties of the ligands can be tuned to obtain Ru(II) complexes suitable for PACT.[124] For example, in a recent publication by Glazer and co-workers[121] the light-induced cytotoxicity of three [Ru(bpy)$_2$(N-N)]$^{2+}$ complexes, where N-N is a sterically hindered bidentate diimine ligand, was investigated and compared with that of cisplatin. A high cytotoxicity was reported for the more strained Ru(II) compounds [**21**]$^{2+}$ and [**22**]$^{2+}$ (Figure 1.16), compared to the less strained complex [**20**]$^{2+}$ and cisplatin. As both hindered complexes were inert in the dark and only became cytotoxic by visible light irradiation, the phototoxicity is believed to result from the photosubstitution of the hindered N-N ligand, followed by covalent binding of ruthenium to DNA.
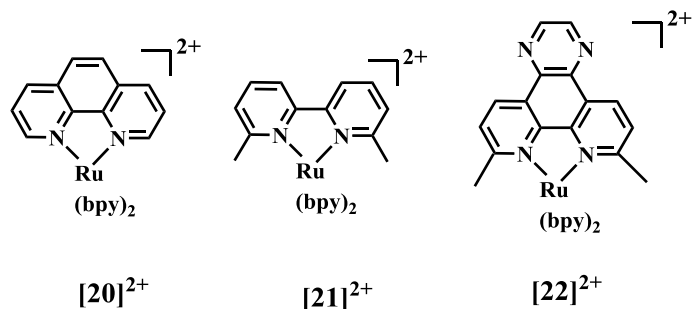
**Figure 1.16.** Structures $[Ru(bpy)_2(N-N)]^{2+}$ complexes with reported anticancer activity. [121]

The photoinduced cytotoxicity of polypyridyl Ru(II) complexes also depends on the electronic properties of the spectator ligands. Nair and co-workers[125] have recently investigated the cytotoxicity of a series of Ru(II) complexes of the type [Ru(Rterpy)(N-N)Cl]$^+$ (Figure 1.17). The Ru-Cl bond can be cleaved by light and Cl$^-$ be photosubstituted by the nucleobase of a DNA fragment. It was shown that the electronic properties of the substituent X on the Xterpy ligand influence the ground state properties of its ruthenium complex, and thus the photolability of the Ru-Cl bond. As benzimidazole is more electron withdrawing than imidazole, compounds [**23**]$^+$ and [**24**]$^+$ with an imidazole substituent on the Xterpy ligand were found to be more phototoxic towards cancer cells under irradiation at 440 nm than [**25**]$^+$ and [**26**]$^+$.
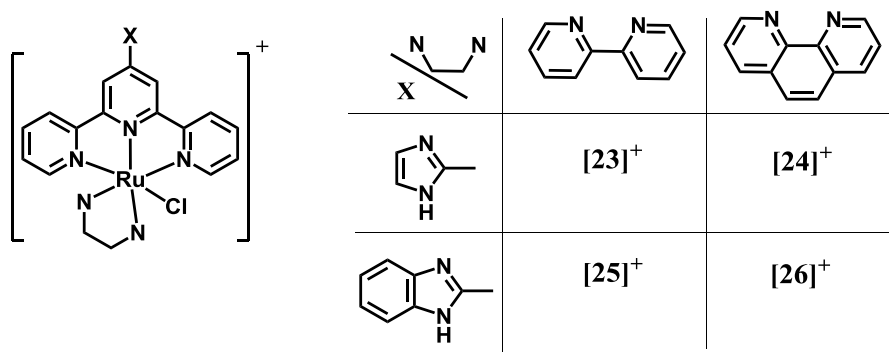


**Figure 1.17.** [Ru (Rterpy)(N-N)Cl]$^+$ complexes with different light-induced cytotoxic properties. Adapted from reference [125].

Effective light absorption by the photoactive drug inside human tissues is another significant challenge in PACT. The penetration depth of light in human tissue is highly

wavelength dependent, and significant penetration only takes place in the range of 600–850 nm, which is referred to as the "photodynamic window".[126-127] Many efforts have been dedicated to achieve photochemical activation of ruthenium complexes with low-energy photons. Changing the electronic properties of the polypyridyl ligands can extend the light activation of the ruthenium complexes towards longer wavelengths, as discussed in a recent review by Turro *et al.* [128] It was shown that in ruthenium complexes [Ru(N-N)₂(L)₂]⁺ (L=NH₃, pyridine, or CH₃CN, N-N=bpy or phen), if one of the N-N ligands is replaced by a cyclometallating ligand such as phpy⁻ (see Figure 1.18) the negative charge of the carbon-based ligand induces an increase in the energy of the HOMO orbital of the complex, and thus reduces the energy needed to promote an electron to the $\pi^*$ orbital of the diimine ligand. As a result the MLCT absorption band is red-shifted to 690 nm. Compound [**27**]⁺ (Figure 1.18) showed very good phototoxicity on advanced ovarian epithelial cancer cells upon irradiation at 690 nm.[128] The cytotoxicity of this compound upon low-energy light irradiation enhanced the potential of this compound as a phototherapeutic agent.[129]
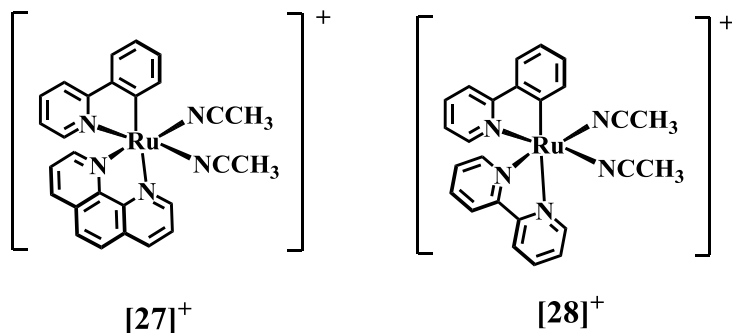


**Figure 1.18.** Chemical formulae of [Ru(phen)(phpy)(CH₃CN)₂]⁺ ([**27**]⁺) and [Ru(bpy)(phpy)(CH₃CN)₂]⁺ ([**28**]⁺).

In the development of light-activated ruthenium-based cytotoxic compounds, efficient targeting is also a great challenge. Mesoporous silica nanoparticles (MSNPs) have recently been reported by Sauvage and coworkers to be efficient nano-carriers for ruthenium dipyridophenazine (dppz) complexes.[130] As shown in Figure 1.19. the ruthenium complexes were grafted on the surface of the nanoparticles *via* nitrile ligand **29**. The resulting supramolecular assembly showed fast cellular uptake, and while the ruthenium-modified nanoparticle was unreactive in the dark, upon visible light

irradiation the Ru-nitrile coordination bond was cleaved to release the ruthenium complex from the surface of the nanoparticles. The resulting cytotoxic aqua complex $[30]^{2+}$ was able to form mono-adducts with DNA and induce cytotoxicity. As discussed in session 1.3.1. liposomes also have great potential to be used as metallodrug carriers that improve drug targeting to tumors. Liposomes functionalized with photosensitive ruthenium complexes have been proposed by our group as a support for the molecular motion of ruthenium-based molecular machines.[46] However, they have not been used until now for the delivery of phototoxic ruthenium complexes to cancer cells, and no toxicity or phototoxicity data have been reported yet. Ideally, ruthenium-functionalized liposomes might be taken up by cancer cell, where light irradiation would release the ruthenium aqua complex (Figure 1.20). In Chapter 5 of this thesis the initial efforts in this direction are described.
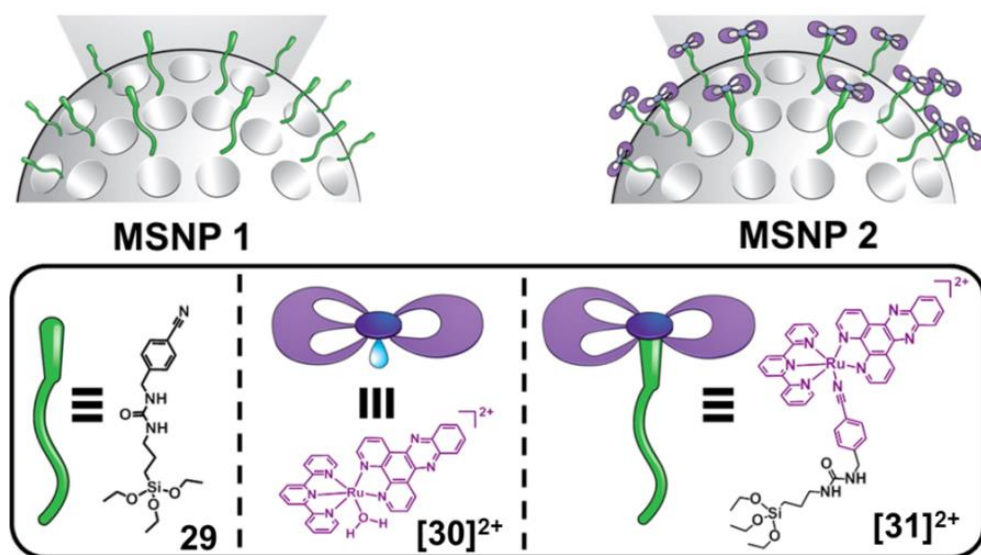


**Figure 1.19.** Structural formula of the nitrile ligand **29**, ruthenium-aqua complex $[30]^{2+}$, and ruthenium−dppz complex $[31]^{2+}$. Ligand **29** is grafted onto the surface of nanoparticles (MSNP 1), followed by coordination of $[30]^{2+}$ in the dark to form ruthenium-functionalized nanoparticle (MSNP 2). Image taken from reference [130].
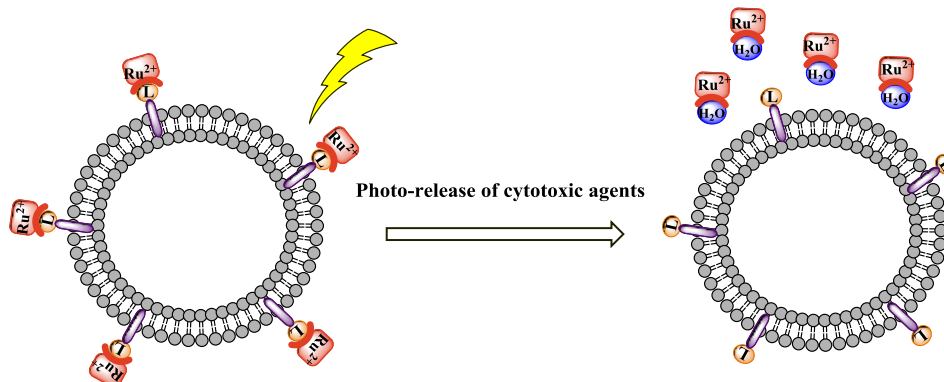
**Figure 1.20.** Liposomes decorated with photosensitive ruthenium-based anticancer prodrugs. Cleavage of the Ru-L coordination bonds upon light irradiation leads to release of the potentially cytotoxic ruthenium-aqua complexes.

## 1.4.    Aim and scope of this thesis

Polypyridyl ruthenium(II) complexes of the $[Ru(terpy)(N-N)(L)]^{2+}$ family, where N-N is a diimine ligand and L is a monodentate ligand, have been known for a long time. However, there are very few studies on liposomes functionalized with these complexes, and on the interaction of ruthenium complexes with lipid bilayers. The research described in this thesis focuses on the photoreactivity and coordination chemistry of $[Ru(terpy)(N-N)(L)]^{2+}$ complexes both in homogenous aqueous solutions and at the surface of lipid bilayers. Their potential application either for the building of light-controlled molecular machines (chapters 2, 3, and 4), or as light-activatable anticancer prodrugs (chapters 5 and 6), is described.

In Chapter 2 the coordination chemistry of $[Ru(terpy)(dcbpy)(SRR')]^{2+}$ complexes (dcbpy=6,6'-dichloro-2,2'-bipyridine and SRR'=thioether ligand), is reported in homogeneous aqueous media. The Ru-S coordination bond was found to form spontaneously in the dark and to be efficiently broken by light irradiation. The potential of this system in supramolecular chemistry is presented by describing the repeatable formation and breakage of the Ru-S bond at the surface of anionic lipid bilayers.

In Chapter 3 an attempt to optimize the dynamics of the light-sensitive interconversion between $[Ru(terpy)(N-N)(SRR')]^{2+}$ (RuSRR') and $[Ru(terpy)(N-N)(H_2O)]^{2+}$ (RuOH$_2$) species in homogeneous aqueous media is reported. The effect of the steric hindrance

of the spectator diimine N-N ligand on the kinetics and thermodynamic of the Ru-S bond formation and hydrolysis is discussed, both in the dark and under light irradiation.

In Chapter 4 the mechanism of the coordination of ruthenium polyryridyl complexes to sulfur ligands embedded in lipid bilayers is described. The kinetics of the coordination reaction at the membrane interface was found to be highly dependent on the charge of the lipid bilayer. This study highlights the differences between coordination chemistry at membranes and coordination chemistry in homogeneous conditions.

In Chapter 5 the application of ruthenium-decorated liposomes in photochemotherapy is described. The photoreactivity of a series of photosensitive ruthenium complexes incorporated in liposomes with different surface charge (neutral or negative) is reported. The dark stability of the liposomes, their cellular uptake, and their cytotoxicity in the dark and under visible light irradiation are discussed.

In Chapter 6 the functionalization of a $[Ru(terpy)(N-N)(SRR')]^{2+}$ complex with a fluorescent rhodamine dye is reported. The dye-functionalized ruthenium complex was initially considered for monitoring the molecular motion of ruthenium complexes at the surface of a lipid bilayer. However, the emission of the dye appeared to be quenched by the nearby ruthenium complex, leading to the sensitization of ligand photosubstitution reactions with low-energy photons. This study demonstrates that efficient cleavage of the Ru-S bond can be obtained with yellow photons that, in theory, do not have enough energy. Our results provide thorough understanding of the effect of irradiation wavelength on ruthenium-based photosubstitution reactions.

Parts of this thesis have been published,[131-132] have been submitted,[133-134] or are in preparation for publication. [135]

## 1.5. References

[1]     K. Kalyanasundaram, *Coord. Chem. Rev.* **1982**, *46*, 159-244.
[2]     V. Balzani, A. Juris, *Coord. Chem. Rev.* **2001**, *211*, 97-115.
[3]     A. Juris, V. Balzani, F. Barigelletti, S. Campagna, P. Belser, A. Vonzelewsky, *Coord. Chem. Rev.* **1988**, *84*, 85-277.
[4]     P. S. Wagenknecht, P. C. Ford, *Coord. Chem. Rev.* **2011**, *255*, 591-616.
[5]     G. A. Crosby, R. J. Watts, D. H. Carstens, *Science* **1970**, *170*, 1195-&.
[6]     G. A. Crosby, *Acc. Chem. Res.* **1975**, *8*, 231-238.

[7]     S. Campagna, F. Puntoriero, F. Nastasi, G. Bergamini, V. Balzani, in *Photochemistry and Photophysics of Coordination Compounds I, Vol. 280* (Eds.: V. Balzani, S. Campagna), **2007**, pp. 117-214.

[8]     T. C. Strekas, H. D. Gafney, S. A. Tysoe, R. P. Thummel, F. Lefoulon, *Inorg. Chem.* **1989**, *28*, 2964-2967.

[9]     S. Pyo, E. Pérez-Cordero, S. G. Bott, L. Echegoyen, *Inorg. Chem.* **1999**, *38*, 3337-3343.

[10]    J. R. Kirchhoff, D. R. McMillin, P. A. Marnot, J. P. Sauvage, *J. Am. Chem. Soc.* **1985**, *107*, 1138-1141.

[11]    J. R. Winkler, T. L. Netzel, C. Creutz, N. Sutin, *J. Am. Chem. Soc.* **1987**, *109*, 2381-2392.

[12]    A. C. Laemmel, J. P. Collin, J. P. Sauvage, *Eur. J. Inorg. Chem.* **1999**, 383-386.

[13]    S. Bonnet, J. P. Collin, J. P. Sauvage, E. Schofield, *Inorg. Chem.* **2004**, *43*, 8346-8354.

[14]    S. Bonnet, J. P. Collin, P. Sauvage, *Inorg. Chem.* **2006**, *45*, 4024-4034.

[15]    T. Kojima, T. Morimoto, T. Sakamoto, S. Miyazaki, S. Fukuzumi, *Chem. Eur. J.* **2008**, *14*, 8904-8915.

[16]    X. Y. Wang, A. Del Guerzo, R. H. Schmehl, *J. Photochem. Photobiol. C Photochem. Rev.* **2004**, *5*, 55-77.

[17]    S. Bonnet, J.-P. Collin, *Chem. Soc. Rev.* **2008**, *37*, 1207-1217.

[18]    R. N. Garner, L. E. Joyce, C. Turro, *Inorg. Chem.* **2011**, *50*, 4384-4391.

[19]    L. Zayat, O. Filevich, L. M. Baraldo, R. Etchenique, *Phil. Trans. R. Soc. A* **2013**, *371*.

[20]    L. Zayat, M. G. Noval, J. Campi, C. I. Calero, D. J. Calvo, R. Etchenique, *ChemBioChem* **2007**, *8*, 2035-2038.

[21]    J. P. Collin, V. Heitz, J. P. Sauvage, in *Molecular Machines, Vol. 262* (Ed.: T. R. Kelly), **2005**, pp. 29-62.

[22]    V. Balzani, A. Credi, B. Ferrer, S. Silvi, M. Venturi, in *Molecular Machines, Vol. 262* (Ed.: T. R. Kelly), **2005**, pp. 1-27.

[23]    W. Yang, Y. Li, H. Liu, L. Chi, Y. Li, *Small* **2012**, *8*, 504-516.

[24]    S. Silvi, M. Venturi, A. Credi, *Chem. Commun.* **2011**, *47*, 2483-2489.

[25]    R. Ballardini, V. Balzani, A. Credi, M. T. Gandolfi, M. Venturi, *Acc. Chem. Res.* **2001**, *34*, 445-455.

[26]    D. A. Leigh, J. K. Y. Wong, F. Dehez, F. Zerbetto, *Nature* **2003**, *424*, 174-179.

[27]    M. von Delius, E. M. Geertsema, D. A. Leigh, *Nature Chem.* **2010**, *2*, 96-101.

[28]    N. Ruangsupapichat, M. M. Pollard, S. R. Harutyunyan, B. L. Feringa, *Nature Chem.* **2011**, *3*, 53-60.

[29]    A. M. Brouwer, C. Frochot, F. G. Gatti, D. A. Leigh, L. Mottier, F. Paolucci, S. Roffia, G. W. H. Wurpel, *Science* **2001**, *291*, 2124-2128.

[30]    N. Armaroli, V. Balzani, J.-P. Collin, P. Gaviña, J.-P. Sauvage, B. Ventura, *J. Am. Chem. Soc.* **1999**, *121*, 4397-4408.

[31]    N. Koumura, R. W. J. Zijlstra, R. A. van Delden, N. Harada, B. L. Feringa, *Nature* **1999**, *401*, 152-155.

[32]    S. Bonnet, J. P. Collin, M. Koizumi, P. Mobian, J. P. Sauvage, *Adv. Mater.* **2006**, *18*, 1239-1250.

[33]    J. P. Collin, V. Heitz, S. Bonnet, J. P. Sauvage, *Inorg. Chem. Commun.* **2005**, *8*, 1063-1074.

[34]    P. R. Ashton, R. Ballardini, V. Balzani, E. C. Constable, A. Credi, O. Kocian, S. J. Langford, J. A. Preece, L. Prodi, E. R. Schofield, N. Spencer, J. F. Stoddart, S. Wenger, *Chem. Eur. J.* **1998**, *4*, 2413-2422.

[35]    J. P. Collin, C. Dietrich-Buchecker, P. Gavina, M. C. Jimenez-Molero, J. P. Sauvage, *Acc. Chem. Res.* **2001**, *34*, 477-487.

[36]    P. Mobian, J.-M. Kern, J.-P. Sauvage, *Angew. Chem. Int. Ed.* **2004**, *43*, 2392-2395.
[37]    J. P. Sauvage, M. Ward, *Inorg. Chem.* **1991**, *30*, 3869-3874.
[38]    J. P. Sauvage, J. P. Collin, J. C. Chambron, S. Guillerez, C. Coudret, V. Balzani, F. Barigelletti, L. Decola, L. Flamigni, *Chem. Rev.* **1994**, *94*, 993-1019.
[39]    J. P. Sauvage, *Chem. Commun.* **2005**, 1507-1510.
[40]    J. P. Collin, D. Jouvenot, M. Koizumi, J. P. Sauvage, *Eur. J. Inorg. Chem.* **2005**, 1850-1855.
[41]    J. P. Collin, A. C. Laemmel, J. P. Sauvage, *New J. Chem.* **2001**, *25*, 22-24.
[42]    F. Durola, J. Lux, J.-P. Sauvage, O. S. Wenger, *Supramol. Chem.* **2011**, *23*, 42-52.
[43]    S. Bonnet, J. P. Collin, J. P. Sauvage, *Chem. Commun.* **2005**, 3195-3197.
[44]    C. Veigel, C. F. Schmidt, *Nat. Rev. Mol. Cell Biol.* **2011**, *12*, 163-176.
[45]    Y.-H. M. Chan, S. G. Boxer, *Curr. Opin. Chem. Biol.* **2007**, *11*, 581-587.
[46]    S. Bonnet, B. Limburg, J. D. Meeldijk, R. J. M. K. Gebbink, J. A. Killian, *J. Am. Chem. Soc.* **2011**, *133*, 252-261.
[47]    M. L. Immordino, F. Dosio, L. Cattel, *Int. J. Nanomedicine* **2006**, *1*, 297-315.
[48]    S. Šegota, D. u. i. Težak, *Adv. Colloid Interface Sci.* **2006**, *121*, 51-75.
[49]    M. Mukai, K. Maruo, Y. Sasaki, J. Kikuchi, *Chem. Eur. J.* **2012**, *18*, 3258-3263.
[50]    B. Gruber, B. Koenig, *Chem. Eur. J.* **2013**, *19*, 438-448.
[51]    O. Onaca, R. Enea, D. W. Hughes, W. Meier, *Macromol. Biosci.* **2009**, *9*, 129-139.
[52]    P. Walde, K. Cosentino, H. Engel, P. Stano, *ChemBioChem* **2010**, *11*, 848-865.
[53]    T. Fenske, H.-G. Korth, A. Mohr, C. Schmuck, *Chem. Eur. J.* **2012**, *18*, 738-755.
[54]    D. L. Giokas, A. G. Vlessidis, *Anal. Chim. Acta* **2011**, *683*, 156-169.
[55]    Q. Yan, R. Zhou, C. Fu, H. Zhang, Y. Yin, J. Yuan, *Angew. Chem.* **2011**, *123*, 5025-5029.
[56]    X. Zhang, S. Rehm, M. M. Safont-Sempere, F. Würthner, *Nat Chem* **2009**, *1*, 623-629.
[57]    C. B. Minkenberg, F. Li, P. van Rijn, L. Florusse, J. Boekhoven, M. C. A. Stuart, G. J. M. Koper, R. Eelkema, J. H. van Esch, *Angew. Chem. Int. Ed.* **2011**, *50*, 3421-3424.
[58]    A. Richard, V. Marchi-Artzner, M. N. Lalloz, M. J. Brienne, F. Artzner, T. Gulik-Krzywicki, M. A. Guedeau-Boudeville, J. M. Lehn, *Proc. Natl. Acad. Sci. U. S. A.* **2004**, *101*, 15279-15284.
[59]    D. A. Jose, B. Konig, *Org. Biomol. Chem.* **2010**, *8*, 655-662.
[60]    I. Tsogas, D. Tsiourvas, G. Nounesis, C. M. Paleos, *Langmuir* **2005**, *21*, 5997-6001.
[61]    M. Ma, A. Paredes, D. Bong, *J. Am. Chem. Soc.* **2008**, *130*, 14456-14458.
[62]    J. Voskuhl, B. J. Ravoo, *Chem. Soc. Rev.* **2009**, *38*, 495-505.
[63]    F. Mancin, P. Scrimin, P. Tecilla, U. Tonellato, *Coord. Chem. Rev.* **2009**, *253*, 2150-2165.
[64]    S. K. M. Nalluri, J. B. Bultema, E. J. Boekema, B. J. Ravoo, *Chemical Science* **2011**, *2*, 2383-2391.
[65]    V. Marchi-Artzner, M. J. Brienne, T. Gulik-Krzywicki, J. C. Dedieu, J. M. Lehn, *Chem. Eur. J.* **2004**, *10*, 2342-2350.
[66]    E. C. Constable, W. Meier, C. Nardin, S. Mundwiler, *Chem. Commun.* **1999**, 1483-1484.
[67]    C. W. Lim, O. Crespo-Biel, M. C. A. Stuart, D. N. Reinhoudt, J. Huskens, B. J. Ravoo, *Proc. Natl. Acad. Sci. U. S. A.* **2007**, *104*, 6986-6991.
[68]    M. Mukai, K. Maruo, J. I. Kikuchi, Y. Sasaki, S. Hiyama, Y. Moritani, T. Suda, *Supramol. Chem.* **2009**, *21*, 284-291.
[69]    D. R. Shnek, D. W. Pack, F. H. Arnold, D. Y. Sasaki, *Angew. Chem. Int. Ed.* **1995**, *34*, 905-907.
[70]    U. Devi, J. R. D. Brown, A. Almond, S. J. Webb, *Langmuir* **2011**, *27*, 1448-1456.
[71]    C. P. Wilson, S. J. Webb, *Chem. Commun.* **2008**, 4007-4009.

[72]    T. L. Andresen, S. S. Jensen, K. Jorgensen, *Prog. Lipid Res.* **2005**, *44*, 68-97.
[73]    Gregoria.G, E. J. Wills, C. P. Swain, A. S. Tavill, *Lancet* **1974**, *1*, 1313-1316.
[74]    W. T. Al-Jamal, K. Kostarelos, *Acc. Chem. Res.* **2011**, *44*, 1094-1104.
[75]    F. Yuan, M. Dellian, D. Fukumura, M. Leunig, D. A. Berk, V. P. Torchilin, R. K. Jain, *Cancer Res.* **1995**, *55*, 3752-3756.
[76]    N. Maurer, D. B. Fenske, P. R. Cullis, *Expert Opin. Biol. Ther.* **2001**, *1*, 923-947.
[77]    A. L. Klibanov, K. Maruyama, V. P. Torchilin, L. Huang, *FEBS Lett.* **1990**, *268*, 235-237.
[78]    K. Djanashvili, T. L. M. ten Hagen, R. Blange, D. Schipper, J. A. Peters, G. A. Koning, *Bioorg. Med. Chem.* **2011**, *19*, 1123-1130.
[79]    J. Connor, L. Huang, *J. Cell Biol.* **1985**, *101*, 582-589.
[80]    M. B. Yatvin, W. Kreutz, B. A. Horwitz, M. Shinitzky, *Science* **1980**, *210*, 1253-1254.
[81]    D. Needham, M. W. Dewhirst, *Adv. Drug Delivery Rev.* **2001**, *53*, 285-305.
[82]    N. Fomina, J. Sankaranarayanan, A. Almutairi, *Adv. Drug Delivery Rev.* **2012**, *64*, 1005-1020.
[83]    C. Alvarez-Lorenzo, L. Bromberg, A. Concheiro, *Photochem. Photobiol.* **2009**, *85*, 848-860.
[84]    S. J. Leung, M. Romanowski, *Theranostics* **2012**, *2*, 1020-1036.
[85]    D. Dolmans, D. Fukumura, R. K. Jain, *Nat. Rev. Cancer* **2003**, *3*, 380-387.
[86]    B. W. Henderson, T. J. Dougherty, *Photochem. Photobiol.* **1992**, *55*, 145-157.
[87]    C. Decker, F. Steiniger, A. Fahr, *J. Liposome Res.* **2013**, *23*, 154-165.
[88]    A. S. L. Derycke, P. A. M. de Witte, *Adv. Drug Delivery Rev.* **2004**, *56*, 17-30.
[89]    A. Yavlovich, B. Smith, K. Gupta, R. Blumenthal, A. Puri, *Mol. Membr. Biol.* **2010**, *27*, 364-381.
[90]    A. M. Garcia, E. Alarcon, M. Munoz, J. C. Scaiano, A. M. Edwards, E. Lissi, *Photochem. Photobiol. Sci.* **2011**, *10*, 507-514.
[91]    R. C. Dolman, G. B. Deacon, T. W. Hambley, *J. Inorg. Biochem.* **2002**, *88*, 260-267.
[92]    K. J. Barnham, M. I. Djuran, P. delSocorroMurdoch, J. D. Ranford, P. J. Sadler, *Inorg. Chem.* **1996**, *35*, 1065-1072.
[93]    B. Baruah, A. Surin, *J. Biol. Inorg. Chem.* **2012**, *17*, 899-910.
[94]    M. L. Krieger, N. Eckstein, V. Schneider, M. Koch, H.-D. Royer, U. Jaehde, G. Bendas, *Int. J. Pharm.* **2010**, *389*, 10-17.
[95]    G. N. Kaluderovic, A. Dietrich, H. Kommera, J. Kuntsche, K. Maeder, T. Mueller, R. Paschke, *Eur. J. Med. Chem.* **2012**, *54*, 567-572.
[96]    H. Chen, R. C. MacDonald, S. Li, N. L. Krett, S. T. Rosen, T. V. O'Halloran, *J. Am. Chem. Soc.* **2006**, *128*, 13348-13349.
[97]    J. Monkkonen, C. S. Brown, T. T. Thompson, T. D. Heath, *Pharm. Res.* **1993**, *10*, 1130-1135.
[98]    G. Mangiapia, G. D'Errico, L. Simeone, C. Irace, A. Radulescu, A. Di Pascale, A. Colonna, D. Montesarchio, L. Paduano, *Biomaterials* **2012**, *33*, 3770-3782.
[99]    L. Simeone, G. Mangiapia, G. Vitiello, C. Irace, A. Colonna, O. Ortona, D. Montesarchio, L. Paduano, *Bioconjug. Chem.* **2012**, *23*, 758-770.
[100]   J. Reedijk, *Proc. Natl. Acad. Sci. U. S. A.* **2003**, *100*, 3611-3616.
[101]   Z. M. Qian, H. Y. Li, H. Z. Sun, K. Ho, *Pharmacol. Rev.* **2002**, *54*, 561-587.
[102]   M. J. Clarke, F. C. Zhu, D. R. Frasca, *Chem. Rev.* **1999**, *99*, 2511-2533.
[103]   W. Han Ang, P. J. Dyson, *Eur. J. Inorg. Chem.* **2006**, *2006*, 4003-4018.
[104]   E. S. Antonarakis, A. Emadi, *Cancer Chemother. Pharmacol.* **2010**, *66*, 1-9.
[105]   J. M. Rademaker-Lakhai, D. van den Bongard, D. Pluim, J. H. Beijnen, J. H. M. Schellens, *Clin. Cancer Res.* **2004**, *10*, 3717-3727.

[106] C. G. Hartinger, M. A. Jakupec, S. Zorbas-Seifried, M. Groessl, A. Egger, W. Berger, H. Zorbas, P. J. Dyson, B. K. Keppler, *Chem. Biodiversity* **2008**, *5*, 2140-2155.

[107] G. Sava, S. Pacor, A. Bergamo, M. Cocchietto, G. Mestroni, E. Alessio, *Chem-Biol. Interact.* **1995**, *95*, 109-126.

[108] M. J. Clarke, *Coord. Chem. Rev.* **2003**, *236*, 207.

[109] M. R. Gill, J. A. Thomas, *Chem. Soc. Rev.* **2012**, *41*, 3179-3192.

[110] O. Novakova, J. Kasparkova, O. Vrana, P. M. van Vliet, J. Reedijk, V. Brabec, *Biochemistry* **1995**, *34*, 12369-12378.

[111] P. M. van Vliet, S. M. S. Toekimin, J. G. Haasnoot, J. Reedijk, O. Nováková, O. Vrána, V. Brabec, *Inorg. Chim. Acta* **1995**, *231*, 57-64.

[112] D. Ossipov, S. Gohil, J. Chattopadhyaya, *J. Am. Chem. Soc.* **2002**, *124*, 13416-13433.

[113] S. Schäfer, I. Ott, R. Gust, W. S. Sheldrick, *Eur. J. Inorg. Chem.* **2007**, *2007*, 3034-3046.

[114] J. Liu, W. Zheng, S. Shi, C. Tan, J. Chen, K. Zheng, L. Ji, *J. Inorg. Biochem.* **2008**, *102*, 193-202.

[115] E. Corral, A. C. G. Hotze, H. den Dulk, A. Leczkowska, A. Rodger, M. J. Hannon, J. Reedijk, *J. Biol. Inorg. Chem.* **2009**, *14*, 439-448.

[116] J.-F. Kou, C. Qian, J.-Q. Wang, X. Chen, L.-L. Wang, H. Chao, L.-N. Ji, *J. Biol. Inorg. Chem.* **2012**, *17*, 81-96.

[117] C. Tan, S. Wu, S. Lai, M. Wang, Y. Chen, L. Zhou, Y. Zhu, W. Lian, W. Peng, L. Ji, A. Xu, *Dalton Trans.* **2011**, *40*, 8611-8621.

[118] M. J. Pisani, P. D. Fromm, Y. Mulyana, R. J. Clarke, H. Körner, K. Heimann, J. G. Collins, F. R. Keene, *ChemMedChem* **2011**, *6*, 848-858.

[119] V. Pierroz, T. Joshi, A. Leonidova, C. Mari, J. Schur, I. Ott, L. Spiccia, S. Ferrari, G. Gasser, *J. Am. Chem. Soc.* **2012**, *134*, 20376-20387.

[120] N. J. Farrer, L. Salassa, P. J. Sadler, *Dalton Trans.* **2009**, 10690-10701.

[121] B. S. Howerton, D. K. Heidary, E. C. Glazer, *J. Am. Chem. Soc.* **2012**, *134*, 8324-8327.

[122] L. Marcelis, C. Moucheron, A. K.-D. Mesmaeker, *Philos. Trans. Roy. Soc. London Ser. A* **2013**, *371*.

[123] G. Stochel, A. Wanat, E. Kuliś, Z. Stasicka, *Coord. Chem. Rev.* **1998**, *171*, 203-220.

[124] G. Ragazzon, I. Bratsos, E. Alessio, L. Salassa, A. Habtemariam, R. J. McQuitty, G. J. Clarkson, P. J. Sadler, *Inorg. Chim. Acta* **2012**, *393*, 230-238.

[125] G. Sathyaraj, M. Kiruthika, T. Weyhermueller, B. U. Nair, *Dalton Trans.* **2012**, *41*, 8460-8471.

[126] R. Weissleder, V. Ntziachristos, *Nat. Med.* **2003**, *9*, 123-128.

[127] P. Zhang, W. Steelant, M. Kumar, M. Scholfield, *J. Am. Chem. Soc.* **2007**, *129*, 4526-+.

[128] A. M. Palmer, B. Pena, R. B. Sears, O. Chen, M. El Ojaimi, R. P. Thummel, K. R. Dunbar, C. Turro, *Phil. Trans. R. Soc. A* **2013**, *371*.

[129] R. B. Sears, L. E. Joyce, M. Ojaimi, J. C. Gallucci, R. P. Thummel, C. Turro, *J. Inorg. Biochem.* **2013**, *121*, 77-87.

[130] M. Frasconi, Z. C. Liu, J. Y. Lei, Y. L. Wu, E. Strekalova, D. Malin, M. W. Ambrogio, X. Q. Chen, Y. Y. Botros, V. L. Cryns, J. P. Sauvage, J. F. Stoddart, *J. Am. Chem. Soc.* **2013**, *135*, 11603-11613.

[131] A. Bahreman, B. Limburg, M. A. Siegler, R. Koning, A. J. Koster, S. Bonnet, *Chem. Eur. J.* **2012**, *18*, 10271-10280.

[132] A. Bahreman, B. Limburg, M. A. Siegler, E. Bouwman, S. Bonnet, *Inorg. Chem.* **2013**, *52*, 9456-9469.

[133] A. Bahreman A, J. A Cuello-Garibo, Bonnet S., *Dalton Trans.*, submitted 2013.

[134] A. Bahreman, M. Rabe, A. Kros, G. Bruylants, S. Bonnet., submitted 2013.

[135]    A. Bahreman, E.Van Geest, C. Balemans,  L. Lupica Spangnolo, M. Heger, S. Bonnet., in preparation.

# 2

# Ruthenium polypyridyl complexes hopping at anionic lipid bilayers *via* a supramolecular bond sensitive to visible light
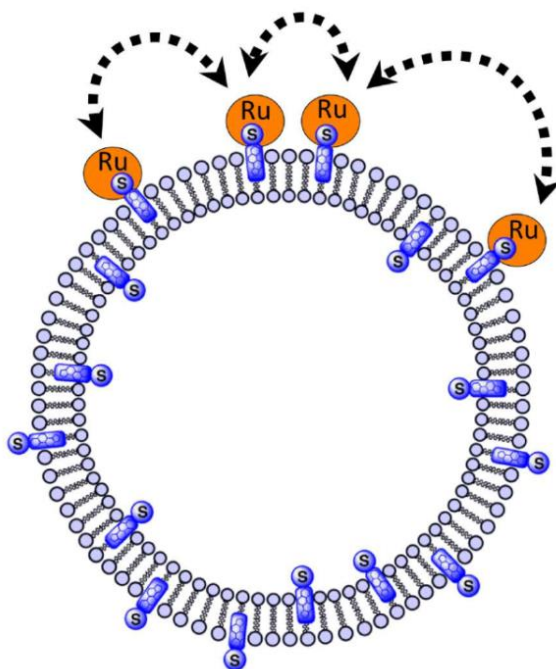
**Abstract**

The new ruthenium complex [Ru(terpy)(dcbpy)(Hmte)](PF$_6$)$_2$ ([**2**](PF$_6$)$_2$) was synthesized, where dcbpy is 6,6'-dichloro-2,2'-bipyridine, terpy is 2,2';6',2''-terpyridine, and Hmte is 2-(methylthio)ethanol. The X-ray structure shows that the Ru$^{2+}$ ion is in a distorted octahedral geometry, revealing steric congestion between dcbpy and Hmte. In water, [**2**]$^{2+}$ forms spontaneously by reacting Hmte and the aqua complex [Ru(terpy)(dcbpy)(H$_2$O)]$^{2+}$ ([**1**]$^{2+}$), with a second-order rate constant of 0.025 s$^{-1}\cdot$M$^{-1}$ at 297 K. In the dark, the Ru-S bond of [**2**]$^{2+}$ is thermally unstable and partially hydrolyzes; in fact, both complexes [**1**]$^{2+}$ and [**2**]$^{2+}$ are in equilibrium characterized by an equilibrium constant $K$ of 151 M$^{-1}$. By shining visible light at an aqueous solution containing [**2**]$^{2+}$ the Ru-S bond is selectively broken to release [**1**]$^{2+}$, *i.e.*, the equilibrium is shifted by visible light irradiation. Such light-induced equilibrium shifts were repeated four times without signs of major degradation; the Ru-S coordination bond in [**2**]$^{2+}$ can be described as a robust light-sensitive supramolecular bond in water. In order to demonstrate the potential of this system in supramolecular chemistry a new thioether-cholesterol conjugate (**4**) was synthesized that inserts into lipid bilayers via its cholesterol moiety, and coordinates to ruthenium via its sulfur atom. Anionic DMPG lipid vesicles (DMPG=dimyristoylphosphatidylglycerol sodium salt) functionalized with this thioether-conjugate were prepared, to which the aqua complex [**1**]$^{2+}$ efficiently coordinates. Upon visible light irradiation on the Ru-decorated vesicles the Ru-S bond is selectively broken, thus releasing [**1**]$^{2+}$ that stays at the water-bilayer interface. When light is switched off the metal complex spontaneously coordinates back to the membrane-embedded thioether ligands without a need to heat the system. This process was repeated four times at 308 K, thus achieving the light-triggered hopping of the metal complex at the water-bilayer interface.

## 2.1. Introduction

Shining light onto a chemical system is an attractive way to trigger molecular motion[1-5] or influence self-assembly,[6-8] because it does not modify concentrations. In addition, some chromophores have a very specific absorption band, which makes their photoexcitation very selective and allows for precisely controlling the system. Several light-responsive processes have been used to trigger molecular or supramolecular events, such as the *cis-trans* isomerization of azobenzene,[9-17] alkene,[18-20] or overcrowded alkenes,[21-23] the closing/opening of diarylethenes,[24-28] the cleavage of coordination bonds,[29-34] or the linkage isomerization of transition metal complexes.[35-37] Over the years, light-responsive supramolecular interactions such as that between *trans* azobenzene and cyclodextrin, have led to a particularly large number of applications in nanotechnology, chemical biology, and drug delivery.[38-58]

In this work, a new form of light-responsive supramolecular interaction based on coordination compounds is described. "Supramolecular" specifically means here that the two interacting molecular fragments are involved in a true thermodynamic equilibrium at room temperature, with kinetics occurring at the timescale of minutes to tens of minutes. This equilibrium involves a Ru-S coordination bond that spontaneously forms in aqueous solution and in the dark, but is selectively broken under visible light irradiation.
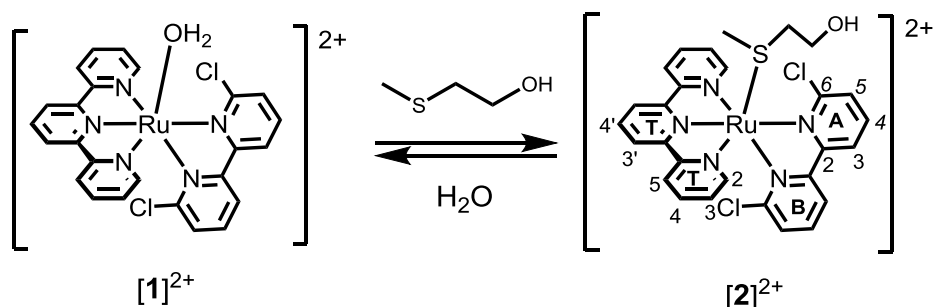


**Scheme 2.1.** Equilibrium between [**1**]$^{2+}$, Hmte, and [**2**]$^{2+}$ in water.

## 2.2. Results

### 2.2.1. Synthesis and X-ray crystal structure

The orange Hmte complex [**2**](PF$_6$)$_2$ was prepared by heating [Ru(terpy)(dcbpy)Cl]Cl ([**3**]Cl)[59] and two equivalents of AgPF$_6$ in Hmte. According to $^1$H NMR spectroscopy in acetone-d$_6$ the protons of the Hmte ligand are high-field shifted in [**2**](PF$_6$)$_2$ compared to the free ligand, which shows coordination of the ligand to the polypyridyl ruthenium complex. Single crystals suitable for X-ray structure determination were obtained by slow diffusion of diisopropyl ether in an Hmte solution of [**2**](PF$_6$)$_2$. As expected the Hmte ligand coordinates *via* its soft sulfur atom to ruthenium(II) (see Figure 2.1). The ruthenium center is in a distorted octahedral environment, typical for terpy-bound complexes. Noteworthy the dcbpy ligand is positioned out of the plane perpendicular to the terpyridine ligand, with Ru1-N4-C20-C21, Ru1-N5-C21-C20, Ru1-N4-C16-Cl1 and Ru1-N5-C25-Cl2 torsion angles larger than 20°. Such strong distortions, combined with a rather long Ru1-S1 bond distance (2.3819(6) Å), altogether suggest significant steric hindrance between the chloro substituents of dcbpy and the thioether Hmte ligand.[60]
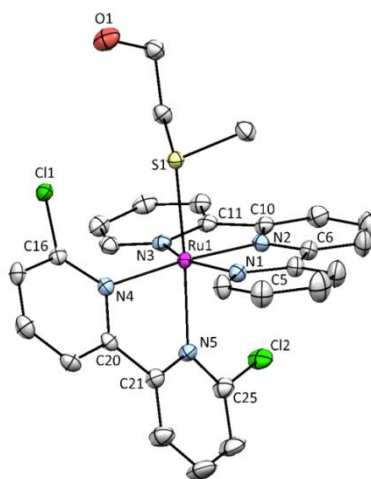


**Figure 2.1.** Displacement ellipsoid plot (given at 50% probability level) of complex [**2**](PF$_6$)$_2$. Hexafluoridophosphate counter ions and hydrogen atoms have been omitted for clarity. Selected bond length (Å): Ru-S1: 2.3819(6), Ru1-N1: 2.084(2), Ru1-N2: 1.962(1), Ru1-N3: 2.074(2), Ru1-N4: 2.126(2), Ru1-N5: 2.115(2). Selected angles (°): Ru1-N4-C20-C21: 21.5(3), Ru1-N5-C21-C20: 22.0(3), Ru1-N4-C16-Cl1: 23.9(3), Ru1-N5-C25-Cl2: −21.3(3), Ru1-N1-C5-C6: 2.4(3), Ru1-N3-C11-C10: 7.6(3), Ru1-N2-C6-C5: 4.9(3), Ru1-N2-C10-C11: 0.7(3).

## 2.2.2.  Thermodynamics and kinetics in homogeneous aqueous solution

According to ^{1}H NMR the Ru-S bond of $[2]^{2+}$ is not stable in water and in the dark. Upon dissolution of $[2](PF_6)_2$ in $D_2O$ two A5 doublets (see Scheme 2.1 for proton notation) at 7.19 and 7.12 ppm reveal the presence of two different ruthenium species in solution (Figure 2.2a). The doublet at 7.19 ppm corresponds to the thioether-bound complex $[2]^{2+}$, as it is the most intense signal in the initial spectrum, and as its intensity increases upon addition of free Hmte. The doublet at 7.12 ppm corresponds to the aqua complex $[1]^{2+}$, which can be synthesized independently in the form of $[1](PF_6)_2$ (see Appendix II, section AII.1). Thus, at 297 K the Ru-S bond of $[2]^{2+}$ slowly and partially hydrolyses to reach an equilibrium with $[1]^{2+}$ and free Hmte. The equiliberium constant $K$ was determined by dissolving the chloride complex $[3]Cl$ and different amounts of Hmte in $D_2O$ (see section 2.4.3 and Figure 2.2a). The Ru-Cl bond of $[3]^+$ is indeed quantitatively and rapidly hydrolyzed in $D_2O$ to give $[1]^{2+}$, as shown by the unique A5 doublet observed at 7.12 ppm upon dissolution of $[3]Cl$ in $D_2O$. In presence of different relative amounts of free Hmte and $[3]Cl$, and after equilibration in the dark at 297 K the two expected A5 doublets at 7.19 and 7.12 ppm can be integrated to obtain the relative concentrations in species $[2]^{2+}$ and $[1]^{2+}$, respectively. A plot of the ratio *[RuHmte]/[RuOH₂]* *vs*. *[Hmte]* was drawn, where *[RuHmte]*, *[RuOH₂]*, and *[Hmte]*, are the concentrations in $[2]^{2+}$, $[1]^{2+}$, and Hmte, respectively (see Figure 2.2b). A straight line was found, which shows that indeed the reaction shown is Scheme 2.1 is a thermodynamic equilibrium. The slope of this line numerically corresponds to the equilibrium constant $K$; a value of 151(8) $M^{-1}$ was found at 297 K and in the dark.

The kinetics for the coordination of Hmte to $[1]^{2+}$ were investigated by UV-vis spectroscopy. Upon adding a large excess of Hmte to an aqueous solution of $[1]^{2+}$, the UV-vis spectrum of the solution gradually evolves within minutes in the dark to give a new absorption maximum at 467 nm (Figure AII.1). The clear isosbestic point at 465 nm shows that the coordination of Hmte to ruthenium is selective. In such pseudo first-order conditions the first-order rate constants $k'_1$ were determined for different concentrations in Hmte (Figure AII.2a). It was found that the order of Hmte in the coordination reaction was one at 297 K (Figure AII.2b), and a value of 0.025(1) $M^{-1}·s^{-1}$ was found for the second-order rate constant $k_1$. Typically, half-reaction times at room temperature are ~3 min with Hmte concentrations of ~0.2 M. Such reaction rate is several orders of magnitude faster than for comparable systems with the unhindered bpy ligand, which typically react within several hours above 60 °C (see

also Chapter 3).[59, 61] Knowing the equilibrium constant $K$ and the rate constant $k_1$ for the substitution of $H_2O$ by Hmte, the first-order rate constant $k_{-1}$ for the *thermal* substitution of Hmte by water in the dark was calculated to be $1.6(9) \times 10^{-4}$ s$^{-1}$ at 297 K (see section 2.4.5). This corresponds to a half-time of 75 min for the spontaneous cleavage of the Ru-S bond of [2]$^{2+}$ in pure water. Thus, the steric hindrance exerted by the dcbpy chelate on the coordination sphere of the complex not only has an effect on the structure of the Hmte complex [2]$^{2+}$, as revealed by X-ray crystallography, but also on the rate of formation and cleavage of the Ru-S coordination bond in the dark.
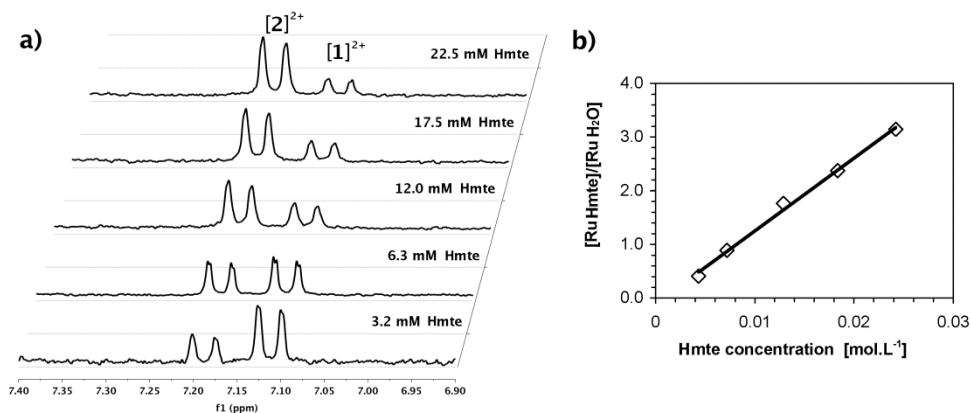


**Figure 2.2.** a) $^1$H NMR spectra (A5 region, 7.40-6.90 ppm in D$_2$O) of equilibrated samples containing [2]$^{2+}$, [1]$^{2+}$ and free Hmte; Hmte concentrations are given at t=0 (before equilibration). b) Plot of the *[RuHmte]/[RuOH$_2$]* ratio *vs. [Hmte]*, at the equilibrium and in the dark. Conditions: *T* = 297 K, *[Ru]$_{tot}$*=2.8 mM.

## 2.2.3. Photochemistry in homogeneous aqueous solution

Ruthenium polypyridyl complexes like [Ru(terpy)(bpy)(L)]$^{2+}$ are known to selectively photosubstitute the monodentate ligand by a solvent molecule upon visible light irradiation.[29, 62-64] The photoreactivity of this type of complexes is based on the thermal conversion of the photochemically generated $^3$MLCT state into a dissociative, metal-centered $^3$MC state. This process is more efficient when the ligand field strength is low, which can be achieved with sterically hindering ligands (see also Chapter 3).[29, 31, 60, 64] The Ru-S bond in [2]$^{2+}$ was indeed found to be photochemically cleaved by visible light irradiation in water, to form [1]$^{2+}$. When an aqueous solution of [2](PF$_6$)$_2$ was irradiated at 465 nm a faster increase of the absorbance at 500 nm was observed compared to the dark reaction, with a clear isosbestic point at 452 nm (Figure AII-3).

$$r_{photo} = \frac{dn_{RuHmte}}{dt} = k_\varphi \cdot n_{RuHmte} \qquad \textbf{(Equation 2.1)}$$

$$k_\varphi = \frac{\Phi \cdot \varphi \cdot (1 - 10^{-A_e})}{n_{Ru_{(tot)}}} \qquad \textbf{(Equation 2.2)}$$

The expression of the rate and of the pseudo first-order rate constant $k_\varphi$ of the purely photochemical substitution of Hmte by water is given in Equations 2.1 and 2.2 where $n_{RuHmte}$ is the number of moles of $[2]^{2+}$ in the cuvette, $\Phi$ is the photon flux, $\varphi$ the photochemical quantum yield of the reaction, $A_e$ the absorbance of the solution at the irradiation wavelength $\lambda_e$, and $n_{Ru(tot)}$ the total number of moles of ruthenium in the sample. In this system measuring $\varphi$ was challenging because of the *a priori* comparable values of $k'_1$, $k_{-1}$, and $k_\varphi$ at room temperature (see Chapter 3 for more details). To do so, the solution was irradiated from the top of the UV-Vis cuvette, while absorption spectra were taken from the side, *i.e.*, along the optical axis of the UV-Vis spectrometer (see Figure AI.1). In our experimental conditions a value of 0.097(9) was obtained for the photosubstitution quantum yield $\varphi$ at 297 K, which is one order of magnitude higher than for comparable unhindered bpy complexes.[61] Such a high efficiency is consistent with previous studies in pyridine,[60] which had shown that steric hindrance on the spectator diimine chelates increased the photosubstitution quantum yield of Ru(II) polypyridyl complexes. Although the Ru-S bond of $[2]^{2+}$ is thermally not stable in water the photochemical cleavage of the Ru-S bond is typically one order of magnitude faster than the thermal reaction (see Chapter 3, Table 3.4).

The fast kinetics of the equilibrium shown in Scheme 2.1, coupled to the high photosubstitution quantum yield $\varphi$, made us envision that the bimolecular equilibrium between $[1]^{2+}$ and $[2]^{2+}$ may be shifted by visible light irradiation in an aqueous solution containing an excess of free Hmte. White light irradiation was thus realized inside a $^1$H MAS NMR spectrometer on a sample containing $[1]^{2+}$, $[2]^{2+}$, and Hmte in D$_2$O, initially equilibrated at 297 K. Before irradiation, the $^1$H MAS NMR spectrum of the solution showed two A5 doublets at 7.16 and 7.08 ppm, characteristic for the species $[2]^{2+}$ and $[1]^{2+}$, respectively. The slightly different values compared to standard solution NMR spectroscopy is due to different setup of the MAS NMR equipment. The *[RuOH$_2$]/[RuHmte]* ratio at the equilibrium in the dark was ~0.24, *i.e.*, the major ruthenium species was for $[2]^{2+}$. Upon irradiation, the relative intensity of the doublet

at 7.08 ppm increased (Figure 2.3), showing the gradual enrichment of the system in $[\mathbf{1}]^{2+}$ due to the photochemical cleavage of the Ru-S bond. After 30 minutes of irradiation a steady state was obtained, characterized by a *[RuOH₂]/[RuHmte]* ratio of 3.4, *i.e.*, a majority of $[\mathbf{1}]^{2+}$. In a second step the lamp was turned off, upon which the sample spontaneously returned to its original state (*[RuOH₂]/[RuHmte]* ~ 0.24) within ~30 min. This experiment unequivocally showed that the thermal equilibrium between $[\mathbf{1}]^{2+}$ and $[\mathbf{2}]^{2+}$ can be perturbed by visible light, and that only these two species (as well as free Hmte, visible in the aliphatic region) are present during and after irradiation at room temperature.
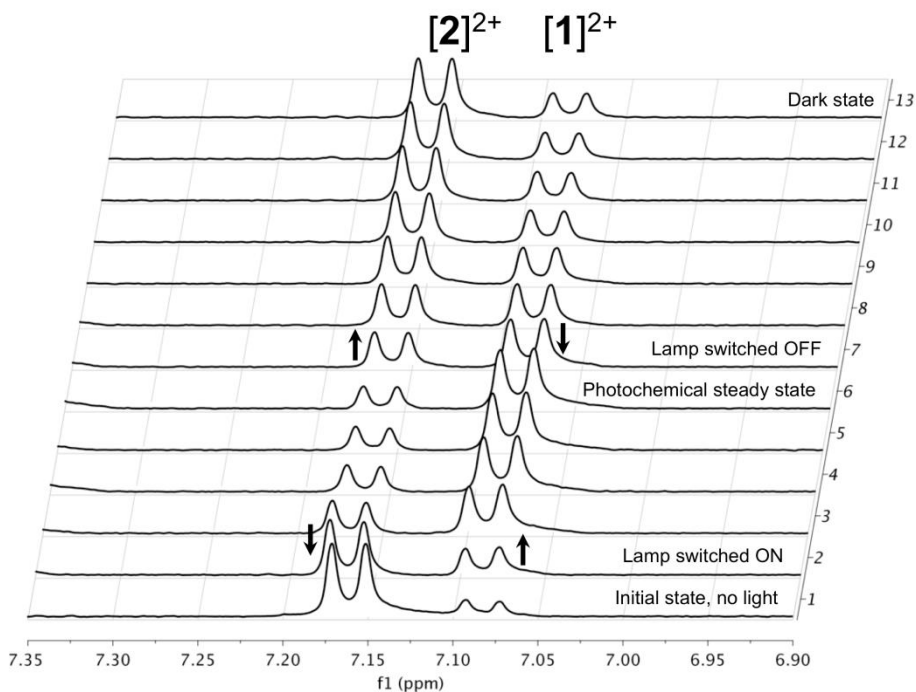


**Figure 2.3.** Light-induced changes of the equilibrium between $[\mathbf{2}]^{2+}$, $[\mathbf{1}]^{2+}$ , and Hmte in water at 298 K, as shown by $^1$H MAS NMR during white-light irradiation *in situ* (lines 2 to 6) and after switching off the lamp (lines 7 to 13). Spectra taken every 5 minutes.

## 2.2.4. Repeated shift of a bimolecular equilibrium using light

In order to check whether shifting the equilibrium by light could be repeated several times, further experiments were performed using UV-Vis spectroscopy and

monochromatic (blue) light. An aqueous solution of $[1]^{2+}$, $[2]^{2+}$, and Hmte, was prepared and equilibrated at 297 K. In the experimental conditions chosen the composition of the solution was measured to comprise 33% of $[1]^{2+}$ and 67% of $[2]^{2+}$ by deconvolution of the UV-vis spectrum. Irradiation at 465 nm was performed 4 times during ~1 h, each time followed by ~2 h of equilibration in the dark. The UV-vis spectra were recorded both under irradiation and in the dark, at 5 minute intervals during 15 h at 297 K. Figure 2.4 shows the evolution of the percentage of the aqua complex $[1]^{2+}$ *vs.* time. Similar photochemical steady states were obtained all four times, characterized by 75-80% of the aqua complex $[1]^{2+}$. During each period in the dark an increase of the concentration of the thioether complex $[2]^{2+}$ was observed, thus showing that the system spontaneously tries to recover its equilibrium state at a $[2]^{2+}/[1]^{2+}$ ratio of 2:1. Thus, the combination of $^1$H NMR and UV-vis analysis shows that this system is rather robust, involving only the four species $[1]^{2+}$, $[2]^{2+}$, free Hmte, and water, which interconvert in a repeatable way upon switching on or off a source of visible light. To our knowledge, this is the first demonstration that light-induced ligand substitution reactions on ruthenium(II) can be controlled by light at one and the same temperature, and in a repetitive fashion. In homogeneous solution, the Ru-S bond of complex $[2]^{2+}$ appears as a light-sensitive supramolecular bond that spontaneously forms in the dark, but is broken by visible light irradiation.
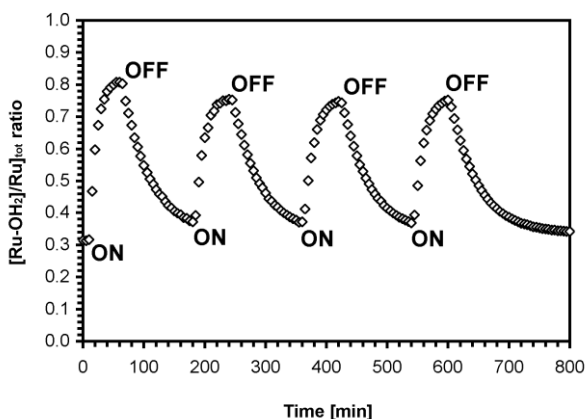


**Figure 2.4.** Plot of the time evolution of the percentage of $[1]^{2+}$ in an initially equilibrated homogeneous solution containing $[2]^{2+}$ and Hmte upon switching ON or OFF several times a source of blue light. Conditions: $\lambda_e$ = 465 nm, photon flux :$3.9 \times 10^{-9}$ Einstein·s$^{-1}$, sample temperature 297 K, concentration $[Ru]_{tot}$ = $1.4 \times 10^{-4}$ M, $[Hmte]$= $9.8 \times 10^{-3}$ M, spectra measured at 5 minutes interval.
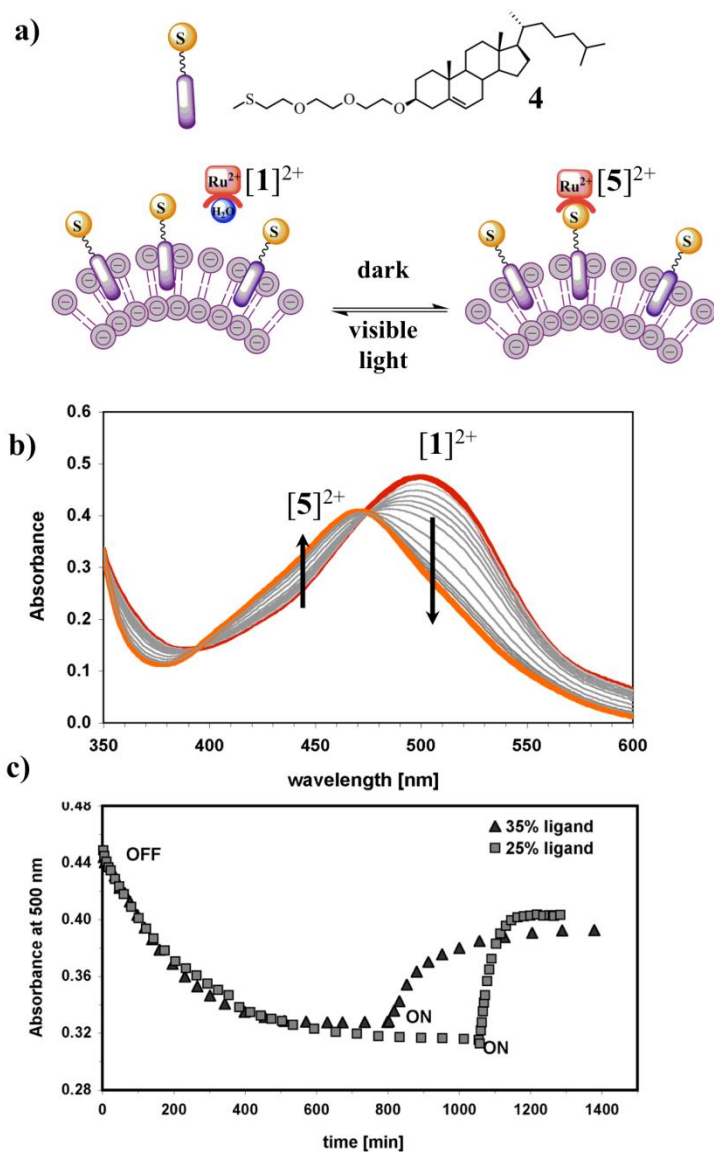
**Figure 2.5.** a) Scheme showing the chemical structure of **4**, the thermal binding of aqua complex [**1**]$^{2+}$ to a lipid bilayer incorporating **4** to give [**5**]$^{2+}$, and light-induced unbinding. b) Time evolution of the UV-vis spectrum of a solution containing DMPG vesicles decorated with 25 mol% of ligand **4** after addition of [**1**](PF$_6$)$_2$ at $t$=0, in the dark and at room temperature. c) Time evolution of the absorbance at 500 nm of a solution containing DMPG vesicles functionalized with 25 or 35 mol% of ligand **4** after addition of [**1**](PF$_6$)$_2$ at t=0, in the dark (OFF) and under blue light irradiation ($\lambda_e$=465 nm, ON). Condition: $T$ = 297 K, $[Ru]_{tot}$= 6.7 ×10$^{-2}$ mM, [**4**]=0.30 mM (25 mol%) or 0.42 (35 mol%), $[lipid]_{tot}$ = 1.3 mM (as liposomes), photon flux 3.9×10$^{-9}$ Einstein·s$^{-1}$.

In our quest towards the light-controlled unidirectional motion of individual molecules we considered using this photosensitive Ru-S bond to achieve the light-induced hopping of Ru-based complexes at the surface of (large) unilamellar lipid bilayers. Liposomes represent an appealing system to define an interface where molecular motion can take place: they are easy to synthesize, transparent, and can be further deposited on glass surfaces. In addition, the water-bilayer interface can easily be functionalized using molecular building blocks covalently bound to cholesterol derivatives. Thus, we considered functionalizing liposomes with thioether ligands, and hopping ruthenium complexes at their surface by the repeated dark formation and light-induced cleavage of the Ru-S bond (Figure 2.5a).[61] The thioether-cholesterol conjugate **4** shown in Figure 2.5a was synthesized as described in Appendix II, section AII.1. Large unilamellar anionic DMPG vesicles including 25 mol% or 35 mol% of ligand **4** were prepared by standard extrusion methods; dynamic light scattering measured an average size distribution centered around 140 nm diameter, and cryo-TEM pictures showed the corresponding well-defined, spherical assemblies typical of large unilamellar vesicles (Figure 2.6a).
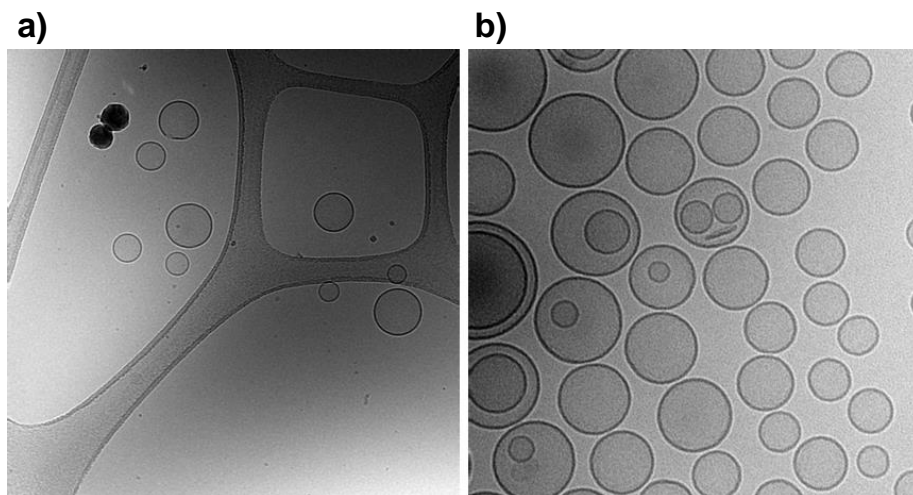


**Figure 2.6.** Cryo-TEM images of DMPG vesicles decorated with 25 mol% of ligand **4** (a) before and (b) after adding 5 mol% of complex [**1**](PF$_6$)$_2$. Images taken at 17000 (a) and 34000 (b) magnification; the size of the whole image is 1.51 μm for (a) and 0.724 μm for (b). Conditions: *[lipid]$_{tot}$* = 1.3 mM (as liposomes), vesicle average diameter= 140 nm. Total concentration *[Ru]$_{tot}$* = $6.7 \times 10^{-2}$ mM.

It is shown previously that positively charged aqua ruthenium complexes similar to $[\mathbf{1}]^{2+}$ but containing an unhindered bpy chelate, strongly interact with negatively charged lipid bilayer membranes, and that coordination reaction at membrane-embedded ligands can take place at high temperatures.[61] Knowing that with hindered Ru complexes such as $[\mathbf{1}]^{2+}$ the coordination chemistry is much faster and occurs at room temperature, a solution of $[\mathbf{1}]^{2+}$ was directly added to the thioether-decorated vesicles to observe whether coordination would take place at 297 K. In the dark, the initial absorption maximum of the solution, situated at 496 nm and characteristic of $[\mathbf{1}]^{2+}$ in presence of DMPG liposomes, gradually disappeared to give rise to a new band at 473 nm (Figure 2.5b). The clear isosbestic point at 480 nm shows that a single reaction is taking place. These evolutions are attributed to the formation of the Ru-S complex $[Ru(terpy)(dcbpy)(\mathbf{4})]^{2+}$ (noted $[\mathbf{5}]^{2+}$) at the lipid-water interface (see Figure 2.5a and 2.5b). As $[\mathbf{5}]^{2+}$ is not thermodynamically stable it was not possible to measure its extinction coefficient in the environment of the bilayer as was done for $[\mathbf{2}]^{2+}$ in homogeneous solution. Thus, it was not possible to calculate the final conversion of the coordination reaction. However, from the absence of a shoulder around 500 nm in the last UV-Vis spectrum shown on Figure 2.5b it can be assumed that the conversion is almost complete. Half-reaction times of 165 and 87 min were found for bilayers containing 25 mol% and 35 mol% of ligand $\mathbf{4}$, respectively (Figure 2.5c). Thus, like for homogeneous solutions a higher concentration of thioether ligands at the DMPG membrane leads to shorter reaction times. Cryo-TEM images of the samples after adding $[\mathbf{1}]^{2+}$ and equilibration in the dark resembles that taken before addition of ruthenium (Figure 2.6b), showing that the morphology of the vesicles is not modified by the presence and coordination of the ruthenium complex.

After reaching the thermal equilibrium at room temperature the sample was irradiated from the top with blue light ($\lambda_e = 465$ nm), and the evolution of the system was followed by UV-vis spectroscopy (Figure 2.5c). For both vesicle samples the absorbance at 500 nm gradually increased, indicating de-coordination of the sulfur ligand from the ruthenium complex and back-formation of the aqua complex $[\mathbf{1}]^{2+}$. Unlike in homogeneous conditions the photosubstitution of the thioether ligand by water was not complete for the sample containing 35 mol% of ligand $\mathbf{4}$, and the absorbance at 500 nm when the photochemical steady state was reached was lower than for the sample containing 25 mol% of ligand $\mathbf{4}$(see Figure 2.5c). In other words, although $[\mathbf{1}]^{2+}$ predominates in both cases at the photochemical steady state, thermal

binding of [**1**]$^{2+}$ to the membrane-embedded ligand may occur also during irradiation. Considering the kinetic results in homogeneous solution (see above), at higher concentration of **4** in the bilayer the rate of the thermal coordination should be higher, hence the *[RuOH$_2$]/[Ru]$_{tot}$* ratio and the absorbance of the solution at 500 nm at the photochemical steady state are expected to be lower. Finally, the photosubstitution quantum yield at the membrane was measured for the sample containing 25 mol% ligand **4** (see Figure AII.4), and a value of 0.065(6) was found, which is consistent with the value found in homogeneous solution.

### 2.2.5. The coordination reactions occur at the surface of the bilayer

As recently shown for unhindered ruthenium complexes,[61] the positively charged ruthenium complexes [**5**]$^{2+}$ and [**1**]$^{2+}$ were expected to stay in proximity of the DMPG membrane, whether bound or not to the membrane-embedded thioether ligand. In order to prove this, complex [**1**]$^{2+}$ was added to DMPG vesicles including 25 mol% of ligand **4**, and the sample was equilibrated at room temperature. In a second step, the large unilamellar vesicles (LUVs) were filtered using an Amicon centrifugal filter device, to yield an almost colorless filtrate and orange vesicles on the filter. This orange color indicates the presence of complex [**5**]$^{2+}$ at the lipid vesicles, whereas according to ICP-OES  (Inductively Coupled Plasma Optical Emission Spectroscopy) only 3% of the initially added ruthenium was found in the colorless filtrate. These 3% may correspond to the amount of non-coordinated aqua ruthenium complexes [**1**]$^{2+}$ remaining when the equilibrium with [**5**]$^{2+}$ is obtained, although it cannot be fully excluded that filtration slightly perturbs the chemical equilibrium at the vesicle surface. To check whether the Ru-DMPG interaction required the presence of the thioether ligand at the bilayer surface the same experiment was performed with DMPG vesicles functionalized with 25 mol% of simple cholesterol, *i.e.*, anionic membranes deprived of thioether ligand. After equilibration at room temperature and filtration with the Amicon device the filtrate showed 12% of the ruthenium initially present in the sample according to ICP-OES, whereas the filter was stained with red-colored lipid vesicles. Thus, even in absence of coordinating thioether ligands a large fraction (88%) of the aqua complex interacts with the bilayer, *i.e.*, the "free" aqua complex [**1**]$^{2+}$ stays close to the bilayer surface. In a control experiment, zwitterionic 1,2-dimyristoyl-*sn*-glycero-3-phosphocholine (DMPC) vesicles were prepared containing 25 mol% of ligand **4** or cholesterol. After adding [**1**]$^{2+}$ and equilibration overnight both samples were filtered on the Amicon device, to leave a colorless residue in the filter and an intense red color

in the filtrate indicating the presence of $[\mathbf{1}]^{2+}$. According to ICP-OES the Ru concentration in the filtrate was found to be 96 and 90% of the initial Ru concentration in presence and in absence of coordinating thioether ligands, respectively. Thus, with neutral DMPC vesicles there is a negligible interaction between $[\mathbf{1}]^{2+}$ and the lipid bilayer, whether thioether ligands are embedded in the membrane or not. Overall, these results confirm that the interaction between polypyridyl Ru(II) complexes and DMPG membranes is based on electrostatic forces, and that the coordination chemistry between the aqua complex $[\mathbf{1}]^{2+}$ and the thioether ligands takes place at the negatively charged surface of the lipid bilayer (see Chapter 4).

### 2.2.6. Hopping of a ruthenium complex at the surface of a lipid bilayer

In order to check whether the results observed in homogeneous solution would stay valid for a supramolecular system the thermal binding and light-induced unbinding of $Ru^{2+}$ at the surface of anionic DMPG lipid bilayers were repeated at 35 °C using a sample containing 35 mol% of ligand **4** and 5 mol% of complex $[\mathbf{1}]^{2+}$. The sample, initially equilibrated in the dark, was irradiated for 1 h at 465 nm and left in the dark for 2 h four consecutive times, while UV-vis spectra were recorded at 3-minute intervals. The time evolution of the absorbance at 500 nm is shown in Figure 2.7. Isosbestic points were obtained for each irradiation and each dark period, showing the selectivity of all reactions. A slow increase of the baseline was observed, which is attributed to water evaporation over long reaction times at 308 K. In the experimental setup indeed the UV-vis cell was left open to allow for irradiation from the top of the cuvette. A high absorbance at 500 nm was observed at the end of each irradiation period, showing the presence of a majority of $[\mathbf{1}]^{2+}$; reversely, a low absorbance at 500 nm was found in the end of each dark period, showing the presence of a majority of $[\mathbf{5}]^{2+}$. According to all results above, the ruthenium complex $[\mathbf{1}]^{2+}$ hops from coordination site to coordination site at the water-bilayer interface. This motion is triggered by visible light.
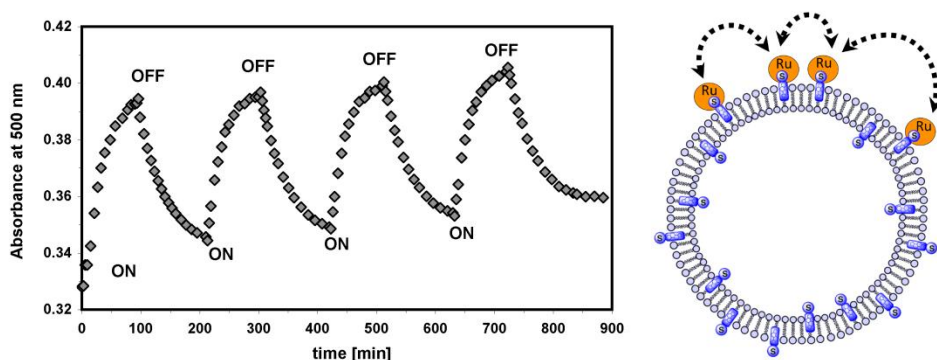
**Figure 2.7.** Left: Time evolution of the absorbance at 500 nm of an equilibrated solution initially containing DMPG vesicles functionalized with 35 mol% of ligand **4** and 5 mol% of [**1**](PF$_6$)$_2$. At t=0 the sample is alternatively irradiated with blue light ($\lambda_e$=465 nm, ON) or left in the dark (OFF). Right: representation of the light-induced hopping of a Ru complex on DMPG lipid bilayer. Conditions: $T$ = 308 K, *[lipid]$_{tot}$* = 1.3 mM (as liposomes), vesicle average size= 140 nm, total concentration *[Ru]$_{tot}$* = $6.7 \times 10^{-2}$ mM , spectra measured every 3 minutes, photon flux ~$3.9 \times 10^{-9}$ Einstein·s$^{-1}$. Absorbance baseline due to light scattering at the vesicles was removed.

## 2.3. Discussion and conclusion

The effects of steric hindrance on the photo- and thermal reactivity of polypyridyl ruthenium complexes has been studied by Sauvage[29, 60] and Takeuchi,[59, 65] respectively. The photoreactivity of this type of complexes, based on the generation of a $^3$MC state with strong dissociative character,[62-63] is efficient only if the ligand field strength is low enough, which can be achieved by using sterically hindered ligands. Very often however, steric hindrance also hinders thermal coordination of the photocleaved ligand back to the metal, and the system must be heated to recover its initial photoreactive state.[1, 31, 61, 66] In this work, we show that in contrast to previous photoresponsive systems the steric hindrance of the dcbpy chelate destabilizes both the aqua- and the thioether-bound ruthenium complexes. Such destabilization leads to these two complexes being in thermal equilibrium at room temperature and in the dark. In these conditions the destabilization of the aqua complex [**1**]$^{2+}$ is strong enough to lead to the spontaneous formation of thioether complexes such as [**2**]$^{2+}$ or [**5**]$^{2+}$ in water. Meanwhile, the photoreactivity of the thioether complexes is high enough to allow for the selective cleavage of the Ru-S bond upon visible light irradiation, thus

shifting the equilibrium towards a steady state where the ruthenium complex is in majority bound to water.[67] Upon switching off the light, the equilibrium in favor of the thioether-bound complexes is re-established, typically within 30 to 120 minutes at room temperature, and whether the metal complex is in homogeneous solution or adsorbed at lipid bilayers.

In the latter case, the unique combination of the cationic complex [**1**]$^{2+}$, a negatively charged lipid bilayer, and a thioether-cholesterol ligand such as **4**, results in the repeated hopping of the photosensitive metal complex at the water-membrane interface without a need to heating the system. Due to the excellent selectivity of both photochemical and thermal ligand substitution reactions, such hopping was repeated four times without alteration of the dark equilibrium state, or of the photochemical steady state. Thus, sterically hindered metal complexes such as [**1**]$^{2+}$ might allow for controlling with light the motion of individual molecules.

To conclude, this work shows that the Ru-S coordination bond between [**1**]$^{2+}$ and thioether ligands in water is truly supramolecular, *i.e.*, it involves a thermodynamical equilibrium that is established within minutes to hours at room temperature and in the dark. In addition, the sensitivity of this equilibrium to visible light irradiation is not accompanied by secondary degradation processes. To our knowledge only a small number of robust supramolecular interactions is sensitive to visible light and compatible with water; they are all based on the isomerization of covalent double bonds.[6-7, 25] The present work adds a new member in the toolbox of self-assembly in water, which consists in a bimolecular equilibrium that can be shifted by visible light.

## 2.4.    Experimental section

### 2.4.1.   General

$^{1}$H and $^{13}$C NMR spectra were recorded using a Bruker DPX-300 spectrometer; chemical shifts are indicated in ppm relative to TMS. Electrospray mass spectra were recorded on a Finnigan TSQ-quantum instrument using an electrospray ionization technique (ESI-MS). UV-vis spectra were obtained on a Perkin-Elmer Lambda 900 spectrophotometer, or on a Cary Varian UV-visible spectrometer. Liposomes size distributions were determined by dynamic light scattering (DLS) in a Zetasizer (Malvern Instruments Ltd.,U.K.) operated at 633 nm. 2-Dimyristoyl-*sn*-glycero-3-phosphoglycerol sodium salt (DMPG), 1,2-dimyristoyl-*sn*-glycero-3-phosphocholine (DMPC) were obtained from Avanti Polar Lipids

and stored at −18 °C. 6,6'-dibromo-2,2'-bipyridine[68] and [Ru(terpy)Cl₃][69] were synthesized using literature procedures. [**3**]Cl and [**1**](PF₆)₂ were synthesized by modified literature procedures (see Appendix II, Section AII.1).[70] 2-(Methylthio)-ethanol, PCl₅, POCl₃ and AgPF₆ were purchased from Sigma-Aldrich and used as such.

### 2.4.2. Synthesis

[**2**](PF₆)₂: [**3**]Cl (50 mg, 79 µmol) and AgPF₆ (75 mg, 300 µmol) were dissolved in Hmte (1 mL). The purple solution was quickly heated to 100 °C. After 5 minutes, the orange solution was filtered to remove insoluble AgCl, after which Et₂O was added to precipitate the compound. The orange/red solid was filtered and recrystalized from hot EtOH to yield [**2**](PF₆)₂ (60 mg, 78%). *$^1$H NMR (300 MHz, Acetone-d6, 298 K,* see Scheme 2.1 for proton notation*) δ* 8.94 (d, *J* = 8.1 Hz, 1H, B3), 8.87 (d, *J* = 8.1 Hz, 2H, T3'5'), 8.77 (d, *J* = 8.1 Hz, 2H, T33''), 8.67 (d, *J* = 8.1 Hz, 1H, A3), 8.59 − 8.47 (m, 4H, T66''+T4'+B4), 8.34 − 8.23 (m, 3H, B5+T44''), 8.03 (t, *J* = 8.0 Hz, 1H, A4), 7.77 − 7.70 (m, 2H, T55''), 7.42 (d, J = 8.0 Hz, 1H, A5), 3.52 (t, *J* = 5.7 Hz, 2H, S-CH₂-C<u>H</u>₂), 1.76 (t, *J* = 5.8 Hz, 2H, S-C<u>H</u>₂), 1.18 (s, 3H, S-<u>Me</u>). $^{13}$C NMR was impossible due to slow decomposition of the product in acetone. *UV-vis: λ$_{max}$* (*ε* in L·mol$^{−1}$·cm$^{−1}$) in pure H₂O: 467 nm (6640). *ES MS m/z (calc):* 650.0 (650.6 [M − 2 PF₆− H]⁺), 590.0 (590.4 [M − 2 PF₆ − Hmte + MeO]⁺), 578.0 (577.43 [M − 2 PF₆ − Hmte + H₂O]⁺]), 558.1 (558.4 [M − 2 PF₆ − Hmte −H]⁺), 296.4 (295.7 [M − 2 PF₆ + MeOH]²⁺). Anal. Calcd for C₂₈H₂₅Cl₂F₁₂N₅OP₂RuS: C, 35.72; H, 2.68; N, 7.44; S, 3.41. Found: C, 34.57; H, 2.51; N, 7.21; S, 3.12. *Crystal growing:* Large single crystals of complex [**2**](PF₆)₂ suitable for X-ray structure determination were grown by vapor diffusion of diisopropylether into a solution of the compound in Hmte (~20 mg in 0.5 mL Hmte).

*C*rystal structure data for [**2**](PF₆)₂: Fw = 941.50, dark orange lath, 0.45 × 0.20 × 0.05 mm³, triclinic, *P*$\overline{1}$ (no. 2), *a* = 8.28578(11), *b* = 10.46214(12), *c* = 19.7560(2) Å, α = 87.3323(10), *β* = 88.7860(10), *γ* = 84.6069(10)°, *V* = 1702.92(3) Å³, *Z* = 2, *D*$_x$ = 1.836 g cm$^{−3}$, *µ* = 0.873 mm$^{−1}$, abs. corr. range: 0.764–0.959. 29119 Reflections were measured up to a resolution of (sin *θ/λ*)$_{max}$ = 0.59 Å$^{−1}$. 5991 Reflections were unique (*R*$_{int}$ = 0.0559), of which 5377 were observed [*I* > 2σ(*I*)]. 531 Parameters were refined with 208 restraints. *R*1/*wR*2 [*I* > 2σ(*I*)]: 0.0293/0.0698. *R*1/*wR*2 [all refl.]: 0.0349/0.0716. S = 1.055. Residual electron density found between −0.43 and 0.57 eÅ$^{−3}$.

### 2.4.3. Determination of the equilibrium constant K

The equilibrium constant (unit: M$^{−1}$) for the equilibrium shown in Scheme 2.1 is defined by:

$$K = \frac{[RuHmte]}{[Hmte] \cdot [RuOH_2]}$$

A stock solution of $[\mathbf{1}]^{2+}$ was prepared by dissolving complex $[\mathbf{3}]Cl$ in $D_2O$ (solution **A**, 10 mg in 5 mL, 2.85 mM); a second stock solution of Hmte in $D_2O$ was prepared (solution **B**, 15 μL Hmte in 1 mL, 163 mM). Five NMR tubes were prepared containing 0.5 mL of solution **A** (1.4 μmol $[\mathbf{3}]Cl$). To each NMR tube was added 10 μL, 20 μL, 40 μL, 60 μL, or 80 μL of solution **B** corresponding to initial Hmte concentrations of 3.2, 6.3, 12.0, 17.5 and 22.5 mM, respectively. Each NMR tube was put in a water bath for 30 minutes at 50 °C and left to equilibrate overnight at room temperature. After this NMR spectra were measured at room temperature to determine the relative integral of the two species, and checked by another NMR spectrum to ensure the sample was at equilibrium. A plot of *[RuOH₂]/[RuHmte]* as a function of the concentration in Hmte was made to determine the equilibrium constant *K*, where *[RuHmte]* represents the concentration in $[\mathbf{2}]^{2+}$ and *[RuOH₂]* the concentration in $[\mathbf{1}]^{2+}$.

## 2.4.4. Order in Hmte and determination of the second-order rate constant $k_1$ for the thermal substitution of water by Hmte on complex $[\mathbf{1}]^{2+}$

Stock solutions of complex $[\mathbf{3}]Cl$ (solution **C**, 7.53 mg in 50 mL $H_2O$, $2.14 \times 10^{-4}$ M) and Hmte (solution **D**, 438.10 mg in 10 mL $H_2O$, $4.75 \times 10^{-1}$ M) were prepared. For a typical experiment, 2 mL of solution **C** was added to a UV-vis cell, which was placed in a UV-vis spectrometer equipped with temperature control set to 297 K and stirring. To this solution was added *x* mL of $H_2O$, and $1-x$ mL of solution **D**, where *x* was 0.2 mL, 0.4 mL, 0.6 mL or 0.8 mL. After the addition a UV-vis spectrum was taken every 30 seconds for a total of 6 minutes. For each spectrum *[RuHmte]* and *[RuOH₂]*, *i.e.*, the concentrations in $[\mathbf{2}]^{2+}$ and $[\mathbf{1}]^{2+}$, respectively, were determined by deconvolution knowing the extinction coefficients of both species at 440 and 500 nm ($\varepsilon$ = 5430 and 3609 L·mol⁻¹·cm⁻¹ for $[\mathbf{2}]^{2+}$, respectively, and 4680 and 7130 L·mol⁻¹·cm⁻¹ for $[\mathbf{1}]^{2+}$, respectively). The rate constants *k'₁* were determined by plotting *ln([RuOH₂]/[Ru]ₜₒₜ) vs.* time. Values of 0.000861, 0.00168, 0.00241, and 0.00313 s⁻¹ were found for *k'₁* for Hmte concentrations of 0.0317, 0.0634, 0.0951, and 0.126 M, respectively. Plotting *k'₁ vs. [Hmte]* afforded a straight line corresponding to a first order for Hmte (Figure AII.2). The slope of this line gives for the second-order rate constant *k₁* a value of 0.025 s⁻¹·M⁻¹ ($R^2$ = 0.995).

### 2.4.5. Rate constant for the thermal substitution of Hmte by water on complex [2]$^{2+}$

At the thermodynamic equilibrium between [1]$^{2+}$, free Hmte, [2]$^{2+}$, and water, the rates for the formation and hydrolysis of complex [2]$^{2+}$ are equal:

$$k_{-1} \cdot [RuHmte]_{eq} = k_1 \cdot [RuOH_2]_{eq} \cdot [Hmte]_{eq}$$

Thus the second order rate constant $k_{-1}$ for the thermal substitution of Hmte by water is numerically given by $k_{-1} = \frac{k_1}{K}$

### 2.4.6. $^1$H MAS NMR under irradiation

To determine the effect of light on the chemical equilibria, $^1$H NMR was performed on a Bruker 400 DMX equipped with a MAS probe (Bruker). A sample was prepared by adding to complex [3]Cl (3.2 mg, 4.56 μmol) 0.5 mL of a D$_2$O solution of Hmte (6.7 mg, 72.7 μmol in 2.5 mL). The sample was put in a water bath at 50 °C for 30 minutes and cooled down to room temperature overnight for equilibration. The solution was loaded into a 4 mm clear sapphire rotor and inserted into the MAS probe. $^1$H NMR spectra (64 scans) were taken every 5 minutes at 298 K with a spinning frequency of 2 kHz in the dark, or under white light irradiation. The light produced by a 1000 W xenon arc lamp equipped with a water filter and an infrared filter was brought perpendicularly to the rotation axis of the rotor through a fiber optic wire. The sample was irradiated during 30 minutes in total, and left in the dark during 60 minutes. *[RuHmte]* and *[RuOH$_2$]*, *i.e.*, the relative concentration in [2]$^{2+}$ and [1]$^{2+}$, respectively, were determined by integration of the peaks at 7.16 ppm and 7.08 ppm, respectively. We attribute the slight difference in chemical shift compared to 7.19 and 7.12 ppm, respectively, to the MAS NMR experimental setup that is different from the standard setup used for solution NMR.

### 2.4.7. Repeatedly shifting the equilibrium by blue light irradiation

To a UV-vis cell containing 2 mL of a water solution of [3]Cl (0.214 mM) was added 1 mL of a water solution of Hmte (prepared with 27.15 mg Hmte in 10 mL H$_2$O, thus *[Hmte]* = 9.82 mM). The cell was mixed and kept closed in the dark overnight for equilibration at 297 K. The cell was put in a UV-vis spectrophotometer equipped with stirring, and a LED light source was adapted that can irradiate the solution from the top ($\lambda_e$ = 465 nm, $\Delta\lambda_{1/2}$ = 25 nm, photon flux ~3.9×10$^{-9}$ Einstein·s$^{-1}$, optical path length 3 cm). The lamp was turned on for 1 hour at *t* = 0, 3, 6, and 9 hours, the rest of the time it stayed switched off. UV-vis spectra were taken at 5 min intervals, either under irradiation or in the dark, for a total of 15 hours. For each spectrum *[RuHmte]* and *[RuOH$_2$]*, *i.e.*, the concentrations in [2]$^{2+}$ and [1]$^{2+}$,

respectively, were determined by deconvolution knowing the extinction coefficients of both species at 440 and 500 nm ($\varepsilon$ = 5430 and 3609 L.mol$^{-1}$·cm$^{-1}$ for [**2**]$^{2+}$, respectively, and 4680 and 7130 L·mol$^{-1}$·cm$^{-1}$ for [**1**]$^{2+}$, respectively). The ratio *[RuOH$_2$]/[RuHmte]* was finally plotted as a function of time.

### 2.4.8. Vesicle preparation

DMPG or DMPC lipid and ligand **4** (25 or 35 mol%) were mixed from a chloroform: methanol (4:1) stock solution and dried under a flow of argon for a few hours. They were subsequently placed under vacuum to remove traces of organic solvents. Afterwards the lipid films were hydrated in a chloride-free buffer containing 10 mM of phosphates, and 40 mM of K$_2$SO$_4$ (total ionic concentration 50 mM), at pH=7. The final concentration of the lipids was 2.5 mM. The lipid suspensions were freeze-thawed 10 times (from liquid N$_2$ temperature to +323 °C) and then extruded 11 times (at 323 °C) by using an Avanti mini-extruder through polycarbonate membranes with 200 nm pore diameter. The size of the vesicles before and after adding [**1**]$^{2+}$ were distributed between 130 and 150 nm as measured by DLS. The morphology of the vesicles before and after adding [**1**]$^{2+}$ were determined by Cryo-transmission Electron microscopy. The samples were stored at 277 °C and used within 6 days.

### 2.4.9. Vesicle filtration experiments

1.6 mL samples containing either DMPG or DMPC vesicles functionalized with 25 mol% of either cholesterol or ligand **4**, were prepared as above. Each sample was diluted with the buffer (1.0 mL) before complex [**1**]$^{2+}$ was added (0.40 mL of a 5.0×10$^{-4}$ M stock solution of [**1**](PF$_6$)$_2$, to reach a total volume of 3 mL, and final concentrations of 1.3 mM for the lipids and 6.7×10$^{-5}$ M for Ru. The samples were stirred overnight at room temperature and in the dark. Absorbance maxima were measured at 500 nm for both DMPC samples and for the DMPG sample containing cholesterol, which corresponded to the presence of [**1**]$^{2+}$. By contrast the absorbance maxima at 473 nm for the sample containing **4** corresponded to the formation of complex [**5**]$^{2+}$. In a second step, each sample was centrifuged using a Milipore Ultra-4 centrifugal filter units, at 297 K and 4300 rpm during 90 minutes. The ruthenium concentration of each filtrate was determined by inductively coupled plasma atomic emission spectroscopy (ICP-OES) on a Varian VISTA-MPX spectrometer. The concentrations were found to be 275 ppb and 62 ppb for DMPG samples containing cholesterol and ligand **4**, respectively, and 2.05 and 2.19 ppm for DMPC samples containing cholesterol and ligand **4**, respectively. These values correspond to 12% and 3%

of the initially added Ru for DMPG, and 90% and 96% for DMPC, as the value found for the reference sample was 2.28 ppm (100%).

## 2.4.10. Irradiation and quantum yield measurement in vesicle samples

1.6 mL of a vesicle sample containing DMPG and 25 mol% of ligand **4** (2.5 mM) was taken in a UV-vis cell. 1 mL of a buffer solution at pH=7 was added and the volume of the cell was completed by adding 0.4 mL of a $5 \times 10^{-4}$ M stock solution of $[1]^{2+}$ (ratio $[1]^{2+}$ to ligand **4** was 1 to 5) . Final lipid concentration in the cell was 1.3 mM.  The absorbance of the sample at 500 nm was 0.46. In a second step the sample was stirred in the dark overnight while UV-vis spectra were measured every 3 minutes (Figure AII.4 left). At the thermal equilibrium the absorption maximum was 473 nm, which characterized the formation of complex $[5]^{2+}$ at the water-bilayer interface, and the absorbance at 473 nm was 0.40. In a third step the sample was irradiated for 90 minutes with a custom-made LED lamp ($\lambda_e$ = 465 nm, $\Delta\lambda_{1/2}$ = 25 nm) fitted to the top of the UV-vis cell. The absorbance of the solution was measured every 3 minutes during irradiation. Knowing the extinction coefficient and absorbance of $[1]^{2+}$ at 500 nm (see Appendix I, section AI.1) the extinction coefficient of $[5]^{2+}$ at 500 nm was calculated to determine the concentration of $[5]^{2+}$ by deconvolution of each UV-vis spectrum during irradiation. By determining the slope of the plot *ln([RuSRR']/[Ru]$_{tot}$)* as a function of irradiation time ($4.5(4)\times10^{-3}$ s$^{-1}$ for t<72 min, see Figure AII.4 right) and knowing  photon flux at the irradiation wavelength, a quantum yield of 0.065(5) was obtained for the photosubstitution of **4** by water at the bilayer-water interface (see Appendix I, section A.I.3  for quantum yield measurements).

## 2.4.11. Cryo-electron transmission microscopy

A few microliters of vesicle preparation were applied to glow-discharged lacey carbon EM grids. Excess medium was automatically blotted onto Whatman no. 4 filter paper for 1 to 2 sec. in a controlled environment operated at room temperature and 100% humidity. Subsequently, the specimen was vitrified by plunging into liquid propane/ethane. Samples were stored in liquid nitrogen until use. Grids were mounted in a Gatan 626 cryo holder (Gatan, Pleasanton, U.S.A.) and images were recorded on a Tecnai 20 FEG (FEI Company) operated at 200 keV. Images were recorded at −8 micron under focus on a 2k × 2k camera mounted behind an energy filter (Gatan) operated at a slit width of 20 eV.

## 2.4.12. Supporting Information

Appendix I: General procedure for the determination of extinction coefficients; calculation the concentrations of reacting species from the UV-vis spectra, and quantum yield.

Appendix II: synthetic procedures for dcbpy, [**3**]Cl, [**1**](PF$_6$)$_2$, and for compound **4**; X-ray crystal structure determination procedure; Plots for rate constant and quantum yield measurements.

## 2.5.    References

[1]     S. Bonnet, J.-P. Collin, *Chem. Soc. Rev.* **2008**, *37*, 1207-1217.
[2]     S. Saha, J. F. Stoddart, *Chem. Soc. Rev.* **2007**, *36*, 77-92.
[3]     N. Katsonis, M. Lubomska, M. M. Pollard, B. L. Feringa, P. Rudolf, *Prog. Surf. Sci.* **2007**, *82*, 407-434.
[4]     S. Silvi, M. Venturi, A. Credi, *Chem. Commun.* **2011**, *47*, 2483-2489.
[5]     P. Ceroni, A. Credi, M. Venturi, V. Balzani, *Photochem. Photobiol. Sci.* **2010**, *9*, 1561-1573.
[6]     S. K. M. Nalluri, B. J. Ravoo, *Angew. Chem. Int. Ed.* **2010**, *49*, 5371-5374.
[7]     S. K. M. Nalluri, J. B. Bultema, E. J. Boekema, B. J. Ravoo, *Chem. Eur. J.* **2011**, *17*, 10297-10303.
[8]     J. W. Li, J. M. A. Carnall, M. C. A. Stuart, S. Otto, *Angew. Chem. Int. Ed.* **2011**, *50*, 8384-8386.
[9]     A. Ueno, H. Yoshimura, R. Saka, T. Osa, *J. Am. Chem. Soc.* **1979**, *101*, 2779-2780.
[10]    T. Muraoka, K. Kinbara, T. Aida, *Nature* **2006**, *440*, 512-515.
[11]    K. Kinbara, T. Aida, *Chem. Rev.* **2005**, *105*, 1377-1400.
[12]    T. Hugel, N. B. Holland, A. Cattani, L. Moroder, M. Seitz, H. E. Gaub, *Science* **2002**, *296*, 1103-1106.
[13]    S. Shinkai, T. Ogawa, T. Nakaji, Y. Kusano, O. Nanabe, *Tetrahedron Lett.* **1979**, *20*, 4569-4572.
[14]    S. Shinkai, T. Minami, Y. Kusano, O. Manabe, *J. Am. Chem. Soc.* **1983**, *105*, 1851-1856.
[15]    B. Jousselme, P. Blanchard, N. Gallego-Planas, J. Delaunay, M. Allain, P. Richomme, E. Levillain, J. Roncali, *J. Am. Chem. Soc.* **2003**, *125*, 2888-2889.
[16]    H. Y. Jiang, S. Kelch, A. Lendlein, *Adv. Mater.* **2006**, *18*, 1471-1475.
[17]    K. Ichimura, S. Oh, M. Nakagawa, *Science* **2000**, *288*, 1624-1626.
[18]    T. Muraoka, K. Kinbara, T. Aida, *J. Am. Chem. Soc.* **2006**, *128*, 11600-11605.
[19]    E. M. Perez, D. T. F. Dryden, D. A. Leigh, G. Teobaldi, F. Zerbetto, *J. Am. Chem. Soc.* **2004**, *126*, 12210-12211.
[20]    D. A. Leigh, J. K. Wong, F. Dehez, F. Zerbetto, *Nature* **2003**, *424*, 174-179.
[21]    N. Koumura, R. W. J. Zijlstra, R. A. v. Delden, N. Harada, B. L. Feringa, *Nature* **1999**, *401*, 152-155.
[22]    A. C. Coleman, J. M. Beierle, M. C. A. Stuart, B. Macia, G. Caroli, J. T. Mika, D. J. van Dijken, J. W. Chen, W. R. Browne, B. L. Feringa, *Nat. Nanotechnol.* **2011**, *6*, 547-552.
[23]    W. R. Browne, B. L. Feringa, *Nat. Nanotechnol.* **2006**, *1*, 25-35.
[24]    A. Mulder, A. Jukovic, F. W. B. van Leeuwen, H. Kooijman, A. L. Spek, J. Huskens, D. N. Reinhoudt, *Chem. Eur. J.* **2004**, *10*, 1114-1123.
[25]    M. Akazawa, K. Uchida, J. J. D. de Jong, J. Areephong, M. Stuart, G. Caroli, W. R. Browneb, B. L. Feringa, *Org. Biomol. Chem.* **2008**, *6*, 1544-1547.
[26]    M. Takeshita, M. Irie, *Tetrahedron Lett.* **1998**, *39*, 613-616.
[27]    J. Gan, J. L. Pozzo, F. Vogtle, *Mol. Cryst. Liq. Cryst.* **2005**, *430*, 99-106.

[28]    A. Mulder, A. Jukovic, L. N. Lucas, J. van Esch, B. L. Feringa, J. Huskens, D. N. Reinhoudt, *Chem. Commun.* **2002**, 2734-2735.
[29]    A.-C. Laemmel, J.-P. Collin, J.-P. Sauvage, *Eur. J. Inorg. Chem.* **1999**, 383-386.
[30]    E.-R. Schofield, J.-P. Collin, N. Gruber, J.-P. Sauvage, *Chem. Commun.* **2003**, 188-189.
[31]    P. Mobian, J.-M. Kern, J.-P. Sauvage, *Angew. Chem. Int. Ed.* **2004**, *43*, 2392-2395.
[32]    J.-P. Sauvage, *Chem. Commun.* **2005**, 1507-1510.
[33]    J.-P. Collin, A.-C. Laemmel, J.-P. Sauvage, *New J. Chem.* **2001**, *25*, 22-24.
[34]    J.-P. Collin, D. Jouvenot, M. Koizumi, J.-P. Sauvage, *Inorg. Chem.* **2005**, *44*, 4693-4698.
[35]    S. Bonnet, J.-P. Collin, J.-P. Sauvage, *Inorg. Chem.* **2006**, *45*, 4024-4034.
[36]    P. Coppens, I. Novozhilova, A. Kovalevsky, *Chem. Rev.* **2002**, *102*, 1803-1803.
[37]    J. J. Rack, *Coord. Chem. Rev.* **2009**, *253*, 78-85.
[38]    Y. Wang, M. Zhang, C. Moers, S. Chen, H. Xu, Z. Wang, X. Zhang, Z. Li, *Polymer* **2009**, *50*, 4821-4828.
[39]    G. Wenz, B. Han, A. Muller, *Chem. Rev.* **2006**, *106*, 782-817.
[40]    Y. Wang, N. Ma, Z. Wang, X. Zhang, *Angew. Chem. Int. Ed.* **2007**, *46*, 2823-2826.
[41]    P. Wan, Y. Jiang, Y. Wang, Z. Wang, X. Zhang, *Chem. Commun.* **2008**, 5710-5712.
[42]    H. Murakami, A. Kawabuchi, K. Kotoo, M. Kunitake, N. Nakashima, *J. Am. Chem. Soc.* **1997**, *119*, 7605-7606.
[43]    J. Zou, B. Guan, X. Liao, M. Jiang, F. Tao, *Macromolecules* **2009**, *42*, 7465-7473.
[44]    Y.-L. Zhao, J. F. Stoddart, *Langmuir* **2009**, *25*, 8442-8446.
[45]    G. Pouliquen, C. Amiel, C. Tribet, *J. Phys. Chem. B* **2007**, *111*, 5587-5595.
[46]    S. Tamesue, Y. Takashima, H. Yamaguchi, S. Shinkai, A. Harada, *Angew. Chem. Int. Ed.* **2010**, *49*, 7461-7464.
[47]    K. Peng, I. Tomatsu, A. Kros, *Chem. Commun.* **2010**, *46*, 4094-4096.
[48]    X. Chen, L. Hong, X. You, Y. Wang, G. Zou, W. Su, Q. Zhang, *Chem. Commun.* **2009**, 1356-1358.
[49]    H. Niino, A. Yabe, A. Ouchi, M. Tanaka, Y. Kawabata, S. Tamura, T. Miyasaka, W. Tagaki, H. Nakahara, K. Fukuda, *Chem. Lett.* **1988**, 1227-1230.
[50]    S. K. M. Nalluri, B. J. Ravoo, *Angew. Chem. Int. Ed. Engl* **2010**, *49*, 5371-5374.
[51]    I. Tomatsu, A. Hashidzume, A. Harada, *J. Am. Chem. Soc.* **2006**, *128*, 2226-2227.
[52]    J. Liu, G. Chen, M. Guo, M. Jiang, *Macromolecules* **2010**, *43*, 8086-8093.
[53]    X. Liao, G. Chen, X. Liu, W. Chen, F. Chen, M. Jiang, *Angew. Chem. Int. Ed.* **2010**, *49*, 4409-4413.
[54]    I. Tomatsu, A. Hashidzume, A. Harada, *Macromolecules* **2005**, *38*, 5223-5227.
[55]    A. Ueno, Y. Tomita, T. Osa, *Tetrahedron Lett.* **1983**, *24*, 5245-5248.
[56]    P. V. Jog, M. S. Gin, *Org. Lett.* **2008**, *10*, 3693-3696.
[57]    D. P. Ferris, Y.-L. Zhao, N. M. Khashab, H. A. Khatib, J. F. Stoddart, J. I. Zink, *J. Am. Chem. Soc.* **2009**, *131*, 1686-1688.
[58]    G. Chen, M. Jiang, *Chem. Soc. Rev.* **2011**, *40*, 2254-2266.
[59]    C. A. Bessel, J. A. Margarucci, J. H. Acquaye, R. S. Rubino, J. Crandall, A. J. Jircitano, K. J. Takeuchi, *Inorg. Chem.* **1993**, *32*, 5779-5784.
[60]    S. Bonnet, J.-P. Collin, J.-P. Sauvage, E. R. Schofield, *Inorg. Chem.* **2004**, *43*, 8346-8354.
[61]    S. Bonnet, B. Limburg, J. D. Meeldijk, R. J. M. Klein Gebbink, J. A. Killian, *J. Am. Chem. Soc.* **2011**, *133*, 252-261.
[62]    J. Van Houten, R. J. Watts, *Inorg. Chem.* **1978**, *17*, 3381-3385.
[63]    C. R. Hecker, P. E. Fanwick, D. R. McMillin, *Inorg. Chem.* **1991**, *30*, 659-666.
[64]    A.-C. Laemmel, J.-P. Collin, J.-P. Sauvage, *Cr. Acad. Sci. Paris IIc* **2000**, *3*, 43-49.

[65]    R. A. Leising, J. S. Ohman, K. J. Takeuchi, *Inorg. Chem.* **1988**, *27*, 3804-3809.

[66]    J.-P. Collin, D. Jouvenot, M. Koizumi, J.-P. Sauvage, *Eur. J. Inorg. Chem.* **2005**, 1850-1855.

[67]    dummy6-Rudcbpy, **2012**.

[68]    X. L. Bai, X. D. Liu, M. Wang, C. Q. Kang, L. X. Gao, *Synthesis* **2005**, 458-464.

[69]    R. A. Leising, S. A. Kubow, M. R. Churchill, L. A. Buttrey, J. W. Ziller, K. J. Takeuchi, *Inorg. Chem.* **1990**, *29*, 1306-1312.

[70]    C. Che, C. Ho, T. Lau, *J. Chem. Soc. Dalton Trans.* **1991**, 1901-1907.

# 3

Spontaneous formation in the dark, and visible light-induced cleavage, of a Ru-S bond in water: a thermodynamic and kinetic study
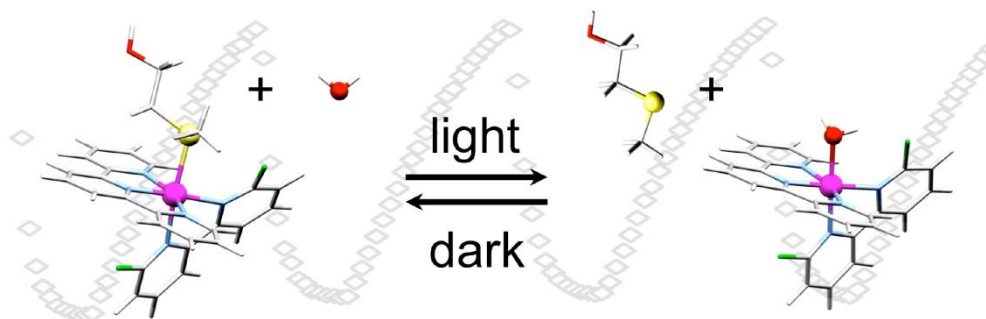
**Abstract**

In this work the thermal and photochemical reactivity of a series of ruthenium complexes [Ru(terpy)(N-N)(L)](X)$_2$ (terpy = 2,2';6',2"-terpyridine, L=2-(methylthio)ethanol (Hmte) or water, and X$^-$ is Cl$^-$ or PF$_6^-$) with four different bidentate chelates N-N=bpy (2,2'-bipyridine), biq (2,2'-biquinoline), dcbpy (6,6'-dichloro-2,2'-bipyridine), or dmbpy (6,6'-dimethyl-2,2'-bipyridine), is described. For each chelate N-N the thermodynamic constant of the dark equilibrium between the aqua and Hmte complexes, the Hmte photosubstitution quantum yield, and the rate constants of the thermal interconversion between the aqua and Hmte complexes, were measured at room temperature. By changing the steric hindrance and electronic properties of the spectator N-N ligand along the series bpy, biq, dcbpy, dmbpy the dark reactivity clearly shifts from a non-labile equilibrium with N-N=bpy, to a very labile thermal equilibrium with N-N=dmbpy. According to variable-temperature rate constant measurements in the dark near pH =7 the activation enthalpies for the thermal substitution of H$_2$O by Hmte are comparable for all ruthenium complexes, whereas the activation entropies are negative for bpy and biq, and positive for dcbpy and dmbpy complexes. These data are indicative of a change in the substitution mechanism, being interchange associative with non-hindered or poorly hindered chelates (bpy, biq), and interchange dissociative for more bulky ligands (dcbpy, dmbpy). For the most labile dmbpy system, the thermal equilibrium is too fast to allow significant modification of the composition of the mixture using light, and for the non-hindered bpy complex the photosubstitution of Hmte by H$_2$O is possible but thermal binding of Hmte to the aqua complex does not occur at room temperature. By contrast, with N-N = biq or dcbpy the thermodynamic and kinetic parameters describing the formation and breakage of the Ru-S bond lie in a range where the bond forms spontaneously in the dark, but is efficiently cleaved under light irradiation. Thus, the concentration between the aqua and Hmte complex in solution can be efficiently controlled at room temperature using visible light irradiation.

## 3.1.   Introduction

Visible light is an efficient tool to control molecular and supramolecular metal-based systems[1-10] for applications in material science,[11-14] nanotechnologies,[15-24] or medicine.[25-44] Among the vast family of photosensitive compounds ruthenium(II) polypyridyl complexes certainly play a prominent role.[18, 45] Whereas $[Ru(bpy)_3]^{2+}$-type complexes are notorious for their luminescence,[46-49] complexes bearing terpyridyl-like ligands, or sterically hindered chelating ligands, have emerged for their ability to selectively photosubstitute one of the ligands of the coordination sphere by solvent molecule(s).[24, 48, 50-53] Such reactivity is based on low-lying, metal-centered ($^3$MC) excited states with dissociative character that are thermally populated from the photochemically generated metal-to-ligand charge-transfer ($^3$MLCT) excited states. In such systems, the photosubstitution reaction can be used to power a molecular machine [20, 22-23, 54-59] or trigger molecular switches.[12-14, 60] More recently, visible light-induced photosubstitution reactions have been proposed as a new way to activate "caged" bioactive ruthenium complexes or ligands.[28, 32, 35, 37, 42, 61]

It has been clearly demonstrated, notably by Sauvage *et al*, that in solution the steric properties of the spectator ligands influence dramatically the quantum efficiency of photosubstitution reactions.[23, 62] This phenomenon is interpreted as a cause of the distortion of the coordination octahedron induced by steric bulkiness, which in turn lowers the ligand field splitting energy of the complex and brings the $^3$MC states closer in energy to the photogenerated $^3$MLCT states. However, the electronic and steric properties of the ligand set also influence the thermal reactivity of the metal complex. In principle, the thermal coordination of sterically hindered ligands requires more energy than that of unhindered ligands.[23] Two decades ago however, Takeuchi *et al*. reported the reverse phenomenon in a family of complexes $[Ru(terpy)(N-N)(L)]^{2+}$ (terpy = 2,2';6',2"-terpyridine, L = $H_2O$ or $CH_3CN$), where the rate of the thermal substitution of the aqua ligand by acetonitrile at room temperature increased with more sterically hindered spectator diimine ligands N-N.[63] This work introduced a quantitative measure of the steric bulkiness of diimine chelates, but it remained elusive on the reasons for the higher lability of the aqua ligand observed with hindered spectator chelates. The reaction was studied at a single temperature, and based on earlier work[64] a dissociative-interchange substitution mechanism was proposed without variable-temperature kinetic measurements.

Inspired by these results the substitution reaction of $[Ru(terpy)(dcbpy)(H_2O)]^{2+}$ (dcbpy = 6,6'-dichloro-2,2'-bipyridine) with 2-methylthioethanol (hereafter, Hmte) in pure water has been studied in Chapter 2. At room temperature, binding of the thioether ligand to afford $[Ru(terpy)(dcbpy)(Hmte)]^{2+}$ is a fast reaction. We realized that considering the high photosubstitution quantum yield of the Hmte complex (0.13 at 465 nm) to afford the starting aqua complex $[Ru(terpy)(dcbpy)(H_2O)]^{2+}$, this system represents a very interesting tool in supramolecular chemistry, as the chemical equilibrium between the aqua and the Hmte ruthenium complexes can be shifted by visible light, while re-establishing itself in the dark. This work is expanded in this Chapter by studying in water the thermal coordination of Hmte to $[Ru(terpy)(N-N)(H_2O)]^{2+}$ (hereafter, RuOH_2) with a series of three other bidentate ligands having different steric demands, namely N-N = bpy (2,2'-bipyridine), biq (2,2'- biquinoline), and dmbpy (6,6'-dimethyl-2,2'-bipyridine, see Scheme 3.1).
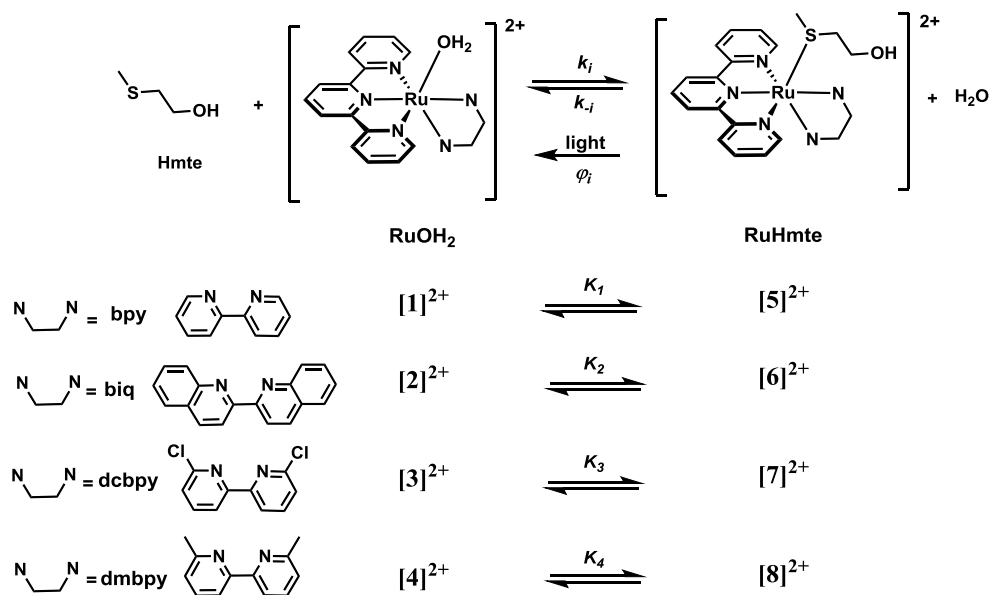


**Scheme 3.1.** The thermal equilibrium between $[Ru(terpy)(N-N)(H_2O)]^{2+}$ and $[Ru(terpy)(N-N)(Hmte)]^{2+}$, and the photosubstitution of Hmte by an aqua ligand. $k_i$ are second-order rate constants for the thermal substitution of $H_2O$ by Hmte (unit: $M^{-1} \cdot s^{-1}$), $k_{-i}$ are first-order rate constants for the thermal substitution of Hmte by $H_2O$ (unit: $s^{-1}$), $K_i$ the thermodynamic equilibrium constants (unit: $M^{-1}$), and $\varphi_i$ are the quantum yields for the photosubstitution of Hmte by $H_2O$ (dimensionless). Indexes $i$ refer to the complexes with N-N=bpy ($i$=1), N-N=biq ($i$=2), N-N=dcbpy ($i$=3), and N-N=dmbpy ($i$=4).

The aim of the present work was double: first, achieving a thorough understanding of the effect of sterically hindering substituents on the bidentate ligand on the thermal *and* photochemical reactivity of Ru(II) complexes in water (Scheme 3.1). Secondly, unraveling the mechanism of the thermal coordination of Hmte to the aqua complex, and gain understanding of the counter-intuitive observation that ligand binding to more hindered complexes is faster.

## 3.2.    Results

### 3.2.1.    Synthesis and crystal structure

The new complex [Ru(terpy)(bpy)(Hmte)](PF$_6$)$_2$ ([**5**](PF$_6$)$_2$) was synthesized by silver-induced removal of the chloride ligand of [Ru(terpy)(bpy)Cl]Cl ([**9**]Cl) in presence of Hmte at elevated temperatures (see Scheme 3.2). [**5**](PF$_6$)$_2$ was characterized by ^{1}H NMR and ^{13}C NMR spectroscopy, electrospray mass spectrometry (ES-MS), elemental analysis, and electron absorption spectroscopy (UV-vis). ^{1}H NMR spectroscopy in acetone-d$_6$ showed that the protons of the Hmte ligand (3.55 ppm, 2.00 ppm, 1.53 ppm) are shielded in [**5**](PF$_6$)$_2$ compared to free Hmte (3.89 ppm, 2.58 ppm, 2.07 ppm) due to coordination to the ruthenium polypyridyl complex. Single crystals of [**5**](PF$_6$)$_2$ were obtained by slow vapor  diffusion of toluene into a solution of [**5**](PF$_6$)$_2$ in Hmte. The crystal structure of the complex was determined by single-crystal X-ray diffraction (see Figure 3.1). As expected, the Hmte ligand is coordinated to ruthenium(II) *via* its soft sulfur atom. The bpy ligand in [**5**](PF$_6$)$_2$  is positioned almost perpendicular to the terpy. The comparison of the crystal structure of [**5**](PF$_6$)$_2$ to that of the complex [Ru(terpy)(dcbpy)(Hmte)](PF$_6$)$_2$ ([**7**](PF$_6$)$_2$ see Chapter 2) shows that the torsion angles Ru1-N4-C20-C21 and Ru1-N5-C21-C20 for the bpy derivative are much smaller than those of the dcbpy derivative (see Table 3.1), which suggests that the coordination sphere is less distorted in [**5**](PF$_6$)$_2$. Moreover, the Ru1-S1 bond in [**5**](PF$_6$)$_2$ is slightly shorter (2.3690(5) Å) than that in [**7**](PF$_6$)$_2$ (2.3819(6) Å, see Table 3.1), also indicating less steric hindrance in [**5**](PF$_6$)$_2$. These results are similar to those reported for [Ru(terpy*)(phen)(dms)](PF$_6$)$_2$ and [Ru(terpy*)(dmp)(dms)](PF$_6$)$_2$ (terpy*=4′-(3,5-di-t-butylphenyl)-2,2′;6′;2″-terpyridine, phen=1,10-phenanthroline, dmp=2,9-dimethyl-1,10-phenanthroline, dms= dimethyl sulfide).[62]
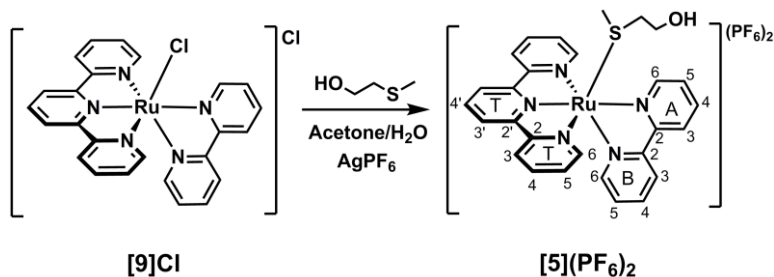
**Scheme 3.2.** Synthesis and numbering scheme of [Ru(terpy)(bpy)(Hmte)](PF$_6$)$_2$ ([**5**](PF$_6$)$_2$).
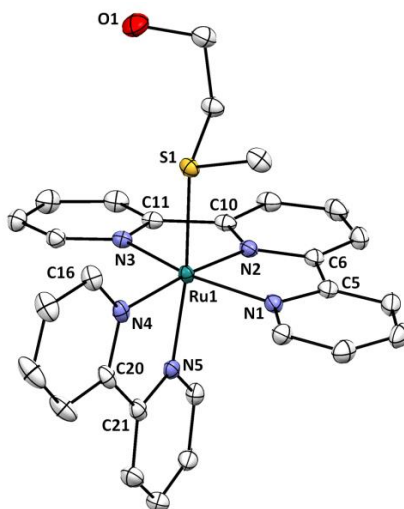


**Figure 3.1.** Displacement ellipsoid plot (at 50% probability level) of complex [**5**](PF$_6$)$_2$. Hexafluoridophosphate counter ions and H atoms were omitted for clarity.

Unlike [**5**](PF$_6$)$_2$ and [**7**](PF$_6$)$_2$, the RuHmte complexes [Ru(terpy)(biq)(Hmte)](PF$_6$)$_2$ ([**6**](PF$_6$)$_2$) and [Ru(terpy)(dmbpy)(Hmte)](PF$_6$)$_2$ ([**8**](PF$_6$)$_2$) could not be isolated in the solid state. Mixing [Ru(terpy)(biq)(Cl)]Cl ([**10**]Cl) or [Ru(terpy)(dmbpy)(Cl)]Cl ([**12**]Cl), respectively, with AgPF$_6$ and Hmte in water, was followed by precipitation, but the resulting salts [**6**](PF$_6$)$_2$ and [**8**](PF$_6$)$_2$ were always impure, even after chromatography. Preparation of [**6**]$^{2+}$ and [**8**]$^{2+}$ in aqueous solution is straightforward, however, as they spontaneously and quantitatively form upon mixing [**10**]Cl or [**12**]Cl and an excess of Hmte in pure water – thus without addition of AgPF$_6$. According to $^1$H-NMR in such conditions [**6**]$^{2+}$ or [**8**]$^{2+}$ are the only ruthenium species present in

solution (see Figures 3.2, and AIII.2). Both complexes were fully characterized in solution by ^{1}H and ^{13}C NMR, ES-MS, and UV-vis spectroscopy (see section 3.5.1).

**Table 3.1.** Selected bond lengths (Å) and torsion angles (°) for [**5**]$(PF_6)_2$ and [**7**]$(PF_6)_2$.

|  | [**5**]$(PF_6)_2$ | [**7**]$(PF_6)_2$[a] |
|---|---|---|
| Ru1-S1 | 2.3690(5) | 2.3819(6) |
| Ru1-N1 | 2.061(1) | 2.084(2) |
| Ru1-N2 | 1.961(1) | 1.962(2) |
| Ru1-N3 | 2.066(1) | 2.074(2) |
| Ru1-N4 | 2.092(1) | 2.126(2) |
| Ru1-N5 | 2.064(1) | 2.115(2) |
| Ru1-N4-C20-C21 | 2.3(2) | 21.5(3) |
| Ru1-N5-C21-C20 | 10.5(2) | 22.0(3) |
| Ru1-N1-C5-C6 | 1.8(2) | 2.4(3) |
| Ru1-N3-C11-C10 | 5.0(2) | 7.6(3) |
| Ru1-N2-C6-C5 | 2.7(2) | 4.9(3) |
| Ru1-N2-C10-C11 | 2.8(2) | 0.7(3) |

[a] Taken from Chapter 2.

Dissolution of the non-hindered bpy complex [**9**]Cl in water leads to a slow equilibrium between the chlorido complex [**9**]$^+$ and the aqua complex [Ru(terpy)(bpy)(H$_2$O)]$^{2+}$ ([**1**]$^{2+}$).[32, 65] This equilibrium establishes only after hours at room temperature. By contrast, the chlorido complexes [**10**]Cl or [**12**]Cl are, within minutes at room temperature, fully hydrolyzed into the aqua species [**2**]$^{2+}$ or [**4**]$^{2+}$, respectively. Indeed, according to ^{1}H NMR adding increasing amounts of D$_2$O to CD$_3$OD solutions of [**10**]Cl or [**12**]Cl leads, within the time necessary for recording a ^{1}H NMR spectrum, to the formation of a second species (see Figure AIII.3). In pure D$_2$O, the ^{1}H NMR spectrum of [**10**]Cl or [**12**]Cl shows a unique A8 or A5 doublet at 6.75 ppm or 6.78 ppm (see Figures 3.2 and AIII.1), respectively. Aqua Ru(II) complexes are very weak acids in water, with typical pKa values above 9.5. The pKa of [**2**]$^{2+}$ and [**4**]$^{2+}$ were unknown; UV-vis titration led to values of 9.5 and 10.5, respectively (see Figure AIII.4), which is comparable to that of [**1**]$^{2+}$ (9.7) and [**3**]$^{2+}$ (10.9).[66-67] As a consequence, complexes [**1**]$^{2+}$-[**4**]$^{2+}$ are not deprotonated in pure

water near pH 7, and dissolving in MilliQ water [**10**]Cl or [**12**]Cl produces only the aqua complex [**2**]$^{2+}$ or [**4**]$^{2+}$, respectively. A similar observation is reported in Chapter 2 for the dcbpy system. Thus, the hydrolysis of the Ru-Cl bond in water is fast at room temperature with hindered N-N ligands (biq, dmbpy, or dcbpy), and the hindered chlorido compounds are good precursors for the corresponding aqua complexes in non-basic solutions.
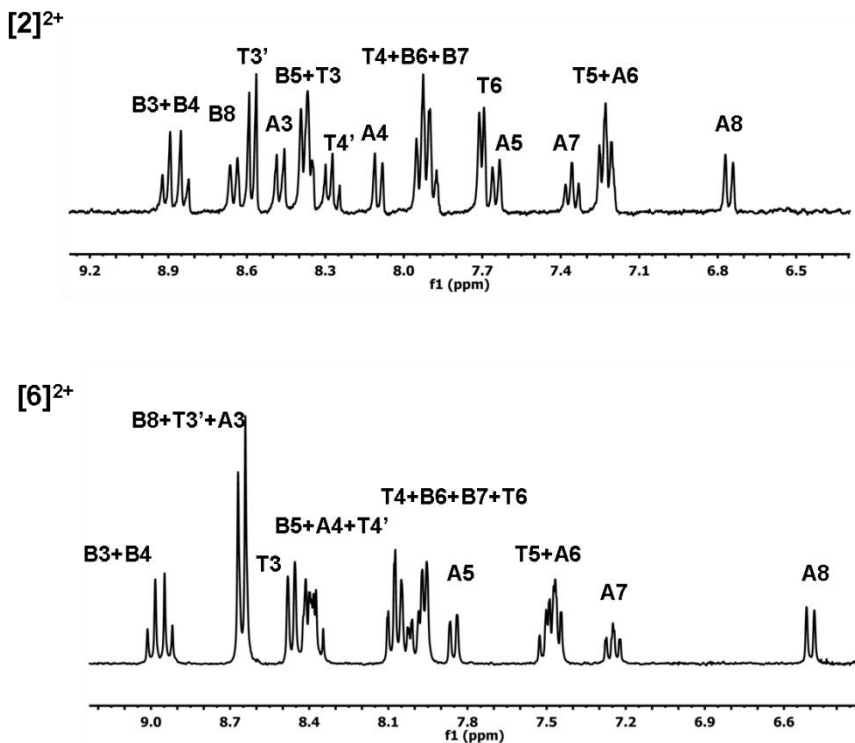


**Figure 3.2.** $^1$H NMR of a solution of [**2**]Cl$_2$ (top) and [**6**]Cl$_2$ (down) in pure D$_2$O near pH 7 (aromatic region 6.4-9.2 ppm), N-N=biq. See Figure AIII.1 for proton attributions. Conditions: *[Ru]$_{tot}$*=12 mM, *[Hmte]*=0 (top) or 0.93 M (bottom), MilliQ water (pH ~ 7), 298 K. See Appendix III, Figure AIII.1 for proton notation.

As noted above, with hindered complexes (N-N=biq, dmbpy, or dcbpy) addition of an excess of Hmte to a solution of the chlorido precursor complex [Ru(terpy)(N-N)Cl]Cl (hereafter noted RuCl) in pure water leads, in the dark and at room temperature, to an equilibrium between the corresponding aqua species [Ru(terpy)(N-N)(H$_2$O)]$^{2+}$ ([**2**]$^{2+}$-[**4**]$^{2+}$, noted RuOH$_2$) and the S-bonded Hmte ruthenium complexes [Ru(terpy)(N-

N)(Hmte)]$^{2+}$ ([**6**]$^{2+}$-[**8**]$^{2+}$, noted RuHmte). Thioether ligands are not basic and, unlike for amine or pyridine ligands where a buffer is required, here the addition of even large excesses of Hmte to solutions of the aqua complex [**2**]$^{2+}$-[**4**]$^{2+}$ does not lead to significant deviations of the pH from 7. This was also observed upon adding Hmte to [**1**]$^{2+}$, which can be introduced in solution in the form of [**1**](PF$_6$)$_2$. Typically, in presence of 0.1 M Hmte a 10$^{-4}$ M solution of [**1**](PF$_6$)$_2$, [**10**]Cl, [**11**]Cl, or [**12**]Cl in MilliQ water has a pH of 7.2-7.4, *i.e.*, the aqua complex [**1**]$^{2+}$, [**2**]$^{2+}$, [**3**]$^{2+}$, or [**4**]$^{2+}$ is not deprotonated. The substitution of the aqua ligand in [**1**]$^{2+}$ by Hmte can be studied above 50 °C, whereas for the hindered biq, dcbpy, and dmbpy system it was studied at room temperature and above (see below). The overall equilibria for the four systems are summarized in Scheme 3.1.

### 3.2.2.  Thermodynamic Study

^{1}H NMR experiments were performed in D$_2$O to measure the equilibrium constants $K_2$ and $K_4$ for the equilibria between [**2**]$^{2+}$ and [**6**]$^{2+}$ (N-N=biq), and between [**4**]$^{2+}$ and [**8**]$^{2+}$ (N-N=dmbpy), respectively (see Scheme 1).  For each reaction, NMR samples containing the RuCl precursor [**10**]Cl or [**12**]Cl and different initial amounts of free Hmte were prepared. After equilibration at 297 K in the dark, the ^{1}H NMR spectrum of each sample was measured.  Integration of the two A8 doublets at 6.35 ([**6**]$^{2+}$) and 6.75 ([**2**]$^{2+}$) ppm for N-N=biq, or of the two A5 doublets at 6.86 ([**8**]$^{2+}$) and 6.78 ([**4**]$^{2+}$) ppm for N-N=dmbpy, allowed for calculating the relative amounts of RuHmte and RuOH$_2$ present in solution (see Figures 3.3 and AIII.1).  A plot of the ratio *[RuHmte]/[RuOH$_2$] vs. [Hmte]* is shown in Figure 3.4, where *[RuHmte]*, *[RuOH$_2$]*, and *[Hmte]* represent the concentrations of the thioether complex, of the aqua complex, and of the free thioether ligand, respectively. For both reactions straight lines were obtained. According to Equation 3.1 the slope of each line corresponds to the thermodynamic equilibrium constant $K_2$ (N-N=biq) and $K_4$ (N-N=dmbpy); the values were found to be 143(10) M$^{-1}$ and 37(2) M$^{-1}$, respectively, at 297 K, in pure water and in the dark. These values are both slightly lower than that of the dcbpy system ($K_3$= 151(8) M$^{-1}$ in the same conditions, see Chapter 2 and Table 3.2).

$$\frac{[RuHmte]_{eq}}{[RuOH_2]_{eq}} = K_i \cdot [Hmte]_{eq} \qquad \textbf{(Equation 3.1)}$$
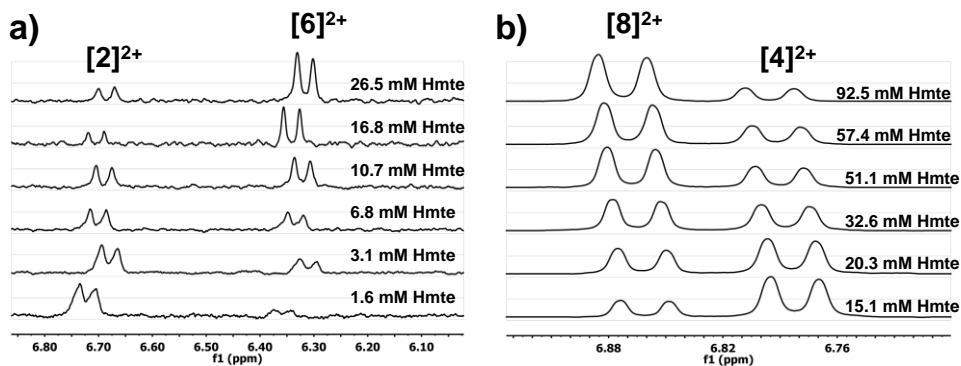
**Figure 3.3.** Evolution of the $^1$H NMR spectra, at the equilibrium between RuOH$_2$ and RuHmte, with different initial concentrations of Hmte for a) the equilibrium between $[2]^{2+}$ and $[6]^{2+}$ (N-N=biq); b) the equilibrium between $[4]^{2+}$ and $[8]^{2+}$ (N-N=dmbpy). Condition: a) $[Ru]_{tot}=$ 5.13 mM, b) $[Ru]_{tot}=$ 12.7 mM, in D$_2$O, pH ~ 7 (pure water), $T$=297 K, in the dark. The initial amounts of Hmte are indicated on each spectrum.
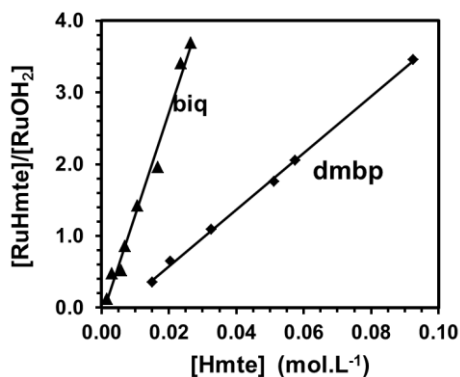


**Figure 3.4.** Plots of the ratio *[RuHmte]/[RuOH$_2$]* at the equilibrium at 297 K, as a function of the equilibrium concentration in free Hmte. *[RuHmte]* and *[RuOH$_2$]* represents the concentrations (in mol·L$^{-1}$) in $[6]^{2+}$ and $[2]^{2+}$, respectively (N-N=biq), or in $[8]^{2+}$ and $[4]^{2+}$, respectively (N-N=dmbpy).

Knowing the equilibrium constant for each reaction and using $\Delta G^{\circ}_i = -R \cdot T \cdot \ln(K_i)$, the free Gibbs energies $\Delta G^{\circ}_2$, $\Delta G^{\circ}_3$, and $\Delta G^{\circ}_4$ were calculated at 297 K to be $-12(2)$ kJ·mol$^{-1}$, $-13(2)$ kJ·mol$^{-1}$, and $-9(1)$ kJ·mol$^{-1}$, respectively, showing a lower thermodynamic driving force towards the formation of RuHmte for the most hindered dmbpy system, in water and at room temperature (see Table 3.3). The establishment of the thermodynamic equilibrium for the unhindered N-N=bpy system is too slow at room temperature to be measured, and the corresponding equilibrium constant $K_1$ could not be obtained directly (see below).

### 3.2.3.   Kinetic Study

Kinetic measurements were performed using UV-vis spectroscopy to compare the rate of the thermal substitution of the aqua ligand in $[\mathbf{1}]^{2+}$, $[\mathbf{2}]^{2+}$, and $[\mathbf{4}]^{2+}$ by Hmte in pure water. After adding a large excess of Hmte to an aqueous solution of $[\mathbf{10}]^{+}$ or $[\mathbf{12}]^{+}$, the UV-vis spectrum of each solution with absorption maximum at 549 or 486 nm, respectively, gradually evolved within minutes in the dark to give rise to a new absorption maximum at 519 or 463 nm, corresponding to the Hmte complex $[\mathbf{6}]^{2+}$ or $[\mathbf{8}]^{2+}$, respectively. Clear isosbestic points (see Figures 3.5b and 3.5c) indicated a selective reaction involving only RuOH$_2$ and RuHmte. Remarkably, a solution of $[\mathbf{1}]^{2+}$ containing large excess of the Hmte ligand is kinetically stable at room temperature, and coordination of the thioether ligand only takes place at temperatures above 323 K. At such high temperatures, the Hmte complex $[\mathbf{5}]^{2+}$ forms selectively, as shown by the clear isosbestic point at 455 nm and the final $\lambda_{max}$ at 450 nm, which is identical to that of the isolated complex (see Figure 3.5a). For the two systems N-N=bpy and biq the plots of ln$([RuOH_2]/[Ru]_{tot})$ vs. time were found linear at 323 and 297 K, respectively (Figure AIII.6), where $[RuOH_2]$ is the concentration in $[\mathbf{1}]^{2+}$ or $[\mathbf{2}]^{2+}$, and [Ru]$_{tot}$ is the total ruthenium concentration. The pseudo first-order rate constants $k'_i$ ($i$=1 or 2) were extracted from the slopes of these lines (see Figure 3.6), and a plot of $k'_i$ vs. [Hmte] was found linear (Figure AIII.7), thus showing that the coordination of Hmte to $[\mathbf{1}]^{2+}$ and $[\mathbf{2}]^{2+}$ is first order in the ligand Hmte.

For N-N=dmbpy the plot of ln$([RuOH_2]/[Ru]_{tot})$ vs. time at 297 K was not linear (see Figures 3.6d and AIII.6) because with such a sterically hindered chelate the thermal back-substitution of Hmte by water cannot be neglected, i.e., $k_{-4}$ becomes comparable to $k'_4$. Equation 3.2 and 3.3 give the general expression of the rate of the thermal formation of the RuHmte complex in pseudo first-order conditions. By integration Equation 3.4 was obtained, which was used to fit the plot ln$([RuOH_2]/[Ru]_{tot})$ vs. time and extract the values of $k_{obs}=k_{-4}+k'_4$ (see Appendix III, section AIII.6). Finally, a plot of $k_{obs}$ vs. [Hmte] afforded a straight line, showing that also for N-N=dmbpy the coordination of Hmte to $[\mathbf{4}]^{2+}$ is first order in Hmte (see Figure AIII.7 and *section AIII.7*) for the full treatment). Overall, like for N-N=dcbpy (see Chapter 2) the rate laws for N-N=bpy, biq, and dmbpy were found to be first order in the Hmte ligand (see Figure AIII.7). The second-order rate constants $k_i$ and the half-reaction time $t_{1/2(i)}$ (calculated with [Hmte]= 0.2 M) are given in Table 3.2. At room temperature the N-N=biq and N-N=dmbpy systems are slower and faster, respectively, compared to the

N-N=dcbpy system. With N-N=bpy Hmte does not coordinate to $[1]^{2+}$ at 297 K, but $k_1$ and $t_{1/2(1)}$ can be measured at 323 K (8.2(5) $\times 10^{-4}$ M$^{-1}$. s$^{-1}$ and 71 min, respectively, at *[Hmte]* = 0.2 M). Even at such high temperatures the rate of the coordination reaction was found to be 8 times slower than the rate of the N-N=biq system at 297 K (all other conditions being identical), which highlights the low lability of the non-hindered bpy system, compared to the sterically hindered ones.

$$\frac{d[RuHmte]}{dt} = -\frac{d[RuOH_2]}{dt} = k'_4[RuOH_2] - k_{-4}[RuHmte] \quad \textbf{(Equation 3.2)}$$

$$\frac{d[RuHmte]}{dt} = k'_4[Ru]_{tot} - (k'_4 + k_{-4})[RuHmte] \quad \textbf{(Equation 3.3)}$$

$$[RuHmte] = \frac{k'_4[Ru]_{tot}}{(k'_4 + k_{-4})} - \frac{c.e^{-(k'_4+k_{-4})t}}{(k'_4 + k_{-4})} \quad \textbf{(Equation 3.4)}$$

The pseudo first-order rate constants $k_{-i}$, and half-reaction times $t_{1/2(-i)}$ for the *thermal* hydrolysis of the RuHmte complexes with N-N=biq, dcbpy, and dmbpy, in the dark and at 297 K, were determined from the knowledge of the thermodynamic equilibrium constants $K_i$, and the second-order rate constants $k_i$ (see Table 3.2). Equation 3.5, written at the equilibrium, indeed rearranges into Equation 3.6.

$$k_{-i}[RuHmte]_{eq} = k_i[Hmte]_{eq}[RuOH_2]_{eq} \quad \textbf{(Equation 3.5)}$$

$$k_{-i} = \frac{k_i}{K_i} \quad \textbf{(Equation 3.6)}$$

For the N-N=bpy system measuring $K_1$ was not possible at room temperature and $k_{-1}$ could not be calculated. However, $k_{-1}$ could be obtained experimentally by heating an aqueous solution of [**5**](PF$_6$)$_2$ at high temperatures (>343 K), and monitoring by UV-vis spectroscopy the thermal substitution of Hmte by water at different temperatures. Subsequently, the activation parameters for the thermal hydrolysis of $[5]^{2+}$ were extracted *via* an Eyring plot (see Figure AIII.8 and Table III.3): values of 110(6) kJ·mol$^{-1}$ and –22(15) J·mol$^{-1}$·K$^{-1}$ were found for $\Delta H^{\ddagger}_{-1}$ and $\Delta S^{\ddagger}_{-1}$, respectively. By extrapolation of the values of $k_{-1}$ at T>323 K, the value of $\Delta G^{\ddagger}_{-1}$ and $k_{-1}$ at 297 K were calculated to be 117(10) kJ·mol$^{-1}$ and 1.5(9) $\times 10^{-8}$ s$^{-1}$, respectively. The equilibrium constant $K_1$ at room temperature (6.8(8) $\times 10^{+3}$ M$^{-1}$) was obtained using Equation 3.6

and the extrapolated value of $k_1$ at 297 K (see below and Table 3.2). These extrapolated values for N-N=bpy are less precise than the direct measurements done for N-N=biq, dcbpy, and dmbpy considering the significant error on $\Delta S^{\ddagger}_{-1}$. However, they give qualitative information about how *stable* and *inert* the non-hindered complex [**5**]$^{2+}$ is. Finally, comparing the kinetic data in Table 3.2 shows that the thermal lability of both species RuOH$_2$ and RuHmte increases along the series bpy, biq, dcbpy, dmbpy, *i.e.*, upon increasing the steric hindrance of the spectator N-N ligands. Such higher lability results in faster thermal coordination, but also faster hydrolysis of the Hmte ligand, while the thermodynamic driving force for Hmte binding to ruthenium is lowered.
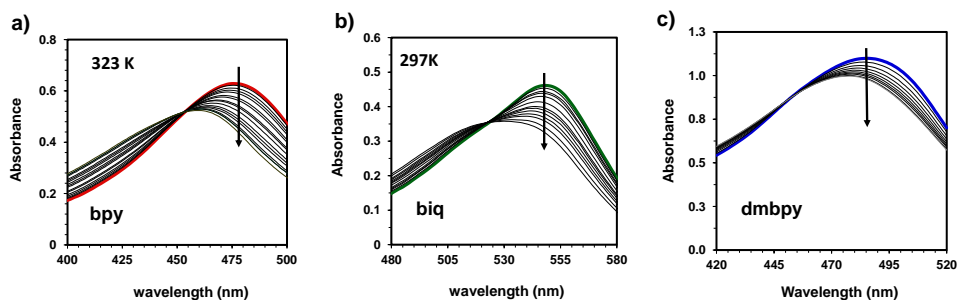


**Figure 3.5.** Time evolution of the UV-vis spectra of aqueous solutions initially containing (a) [**1**]$^{2+}$, (b) [**2**]$^{2+}$, and (c) [**4**]$^{2+}$, and a large excess of Hmte in MilliQ water (pseudo-first order conditions). Conditions: (a) T=323 K, [Ru]$_{tot}$=6.6 ×10$^{-5}$ M, *[Hmte]*=0.07 M, (b) T=297 K, *[Ru]$_{tot}$*=6.6×10$^{-5}$ M, *[Hmte]*= 0.067 M, and (c) T=297 K, *[Ru]$_{tot}$* = 2.1×10$^{-4}$ M, *[Hmte]* = 0.032 M.

**Table 3.2.** Thermodynamic and kinetic data at 297 K for the interconversion between [Ru(terpy)(N-N)(H$_2$O)]$^{2+}$ and [Ru(terpy)(N-N)(Hmte)]$^{2+}$ complexes, where N-N is bpy, biq, dcbpy, and dmbpy. Conditions: in the dark, pure water, pH ~ 7.

| $i$ | N-N | $K_i$ (M$^{-1}$) | $k_i$ (M$^{-1}$·s$^{-1}$) | $t_{1/2(i)}$ (min) [a] | $k_{-i}$ (s$^{-1}$) | $t_{1/2(-i)}$ (min) |
|---|---|---|---|---|---|---|
| 1* | bpy | 6800(100) | 1.0(9) ×10$^{-4}$ | 590(60) | 1.5(9)×10$^{-8}$ | 77(7)×10$^{+5}$ |
| 2 | biq | 143(10) | 6.4(1)×10$^{-3}$ | 9.0(9) | 4.5(9)×10$^{-5}$ | 257(80) |
| 3† | dcbpy | 151(8) | 2.5(1)×10$^{-2}$ | 2.3(1) | 1.6(9)×10$^{-4}$ | 74(9) |
| 4 | dmbpy | 37(2) | 1.2(5)×10$^{-1}$ | 0.43(5) | 3.3(9)×10$^{-3}$ | 6.5(5) |

* Data extrapolated at 297 K from the temperature-dependent kinetic measurements above 323 K (see text and Table 3.3). Uncertainties are high but the low rate constant obtained confirms the absence of measurable binding of Hmte to the unhindered aqua complex [**1**]$^{2+}$ at room temperature. † data taken from Chapter 2 for comparison. [a] Calculated for *[Hmte]*=0.2 M ($t_{1/2(i)}$)

### 3.2.4.   Activation parameters for the coordination of Hmte

In order to obtain mechanistic information the rate of the thermal substitution of the aqua ligand by Hmte in [**1**]$^{2+}$, [**2**]$^{2+}$, [**3**]$^{2+}$, or [**4**]$^{2+}$, was studied at different temperatures using UV-vis spectroscopy. In pseudo first-order conditions the plot of ln*([RuOH$_2$]/[Ru]$_{tot}$) vs.* time at different temperatures afforded straight lines for N-N=bpy, biq, and dcbpy complexes (Figure 3.6a-c), which allowed determining the second-order rate constants $k_i$ at different temperatures for all three reactions (Table AIII.2). For N-N=dmbpy the ln*([RuOH$_2$]/[Ru]$_{tot}$) vs.* time dataset was found non-linear as explained above (Figure 3.6d). It was modeled using Equation 3.4 and the values $k_4$ and $k_{-4}$ could also be determined at five different temperatures (see Table AIII.1). The activation enthalpy $\Delta H^{\ddagger}_i$, activation entropy $\Delta S^{\ddagger}_i$, and activation Gibbs energy at 297 K, $\Delta G^{\ddagger}_i$, are defined, for each reaction, by the Eyring equation (Equation 3.7). In this equation $k_i$ represents the second-order rate constant, $k_B$ is the Boltzmann constant $(1.38 \times 10^{-23}$ J·K$^{-1})$, $h$ is Plank's constant $(6.63 \times 10^{-34}$ J·s), and $R$ is the gas constant $(8.314$ J·mol$^{-1}$·K$^{-1})$. An Eyring plot of ln$(k_i/T)$ *vs. 1/T* for the four systems afforded straight lines (see Figure 3.7), from which the values of $\Delta H^{\ddagger}_i$ and $\Delta S^{\ddagger}_i$ could be extracted. The activation Gibbs energies, $\Delta G^{\ddagger}_i$, were calculated at 297 K using the equation $\Delta G^{\ddagger}_i = \Delta H^{\ddagger}_i - T \cdot \Delta S^{\ddagger}_i$ (see Table 3.3).

$$ln\frac{k_i}{T} = \frac{-\Delta H^{\ddagger}_i}{R} \cdot \frac{1}{T} + ln\frac{k_B}{h} + \frac{\Delta S^{\ddagger}_i}{R} \quad \textbf{(Equation 3.7)}$$

Quite surprisingly the four activation *enthalpies* were found too similar to account for the clear differences in reactivity between the four N-N ligands. By contrast, unexpected differences in activation entropies were observed: the values for the less hindered N-N=bpy and N-N=biq bidentate ligands were found to be negative, whereas for the more hindering chelates N-N=dcbpy and N-N=dmbpy the values were found to be positive. When both contributions of enthalpy and entropy are taken into account, a clear trend was observed: the activation Gibbs energies $\Delta G^{\ddagger}_i$ decreases along the series bpy, biq, dcbpy, dmbpy. Such acceleration of the coordination of Hmte to the aqua complex appears to be a consequence of a drastic increase of the activation entropy $\Delta S^{\ddagger}_i$, *i.e.*, a change in the substitution mechanism, rather than a simple destabilization of RuOH$_2$, which would lead to a decrease of the activation enthalpy $\Delta H^{\ddagger}_i$ (see discussion).
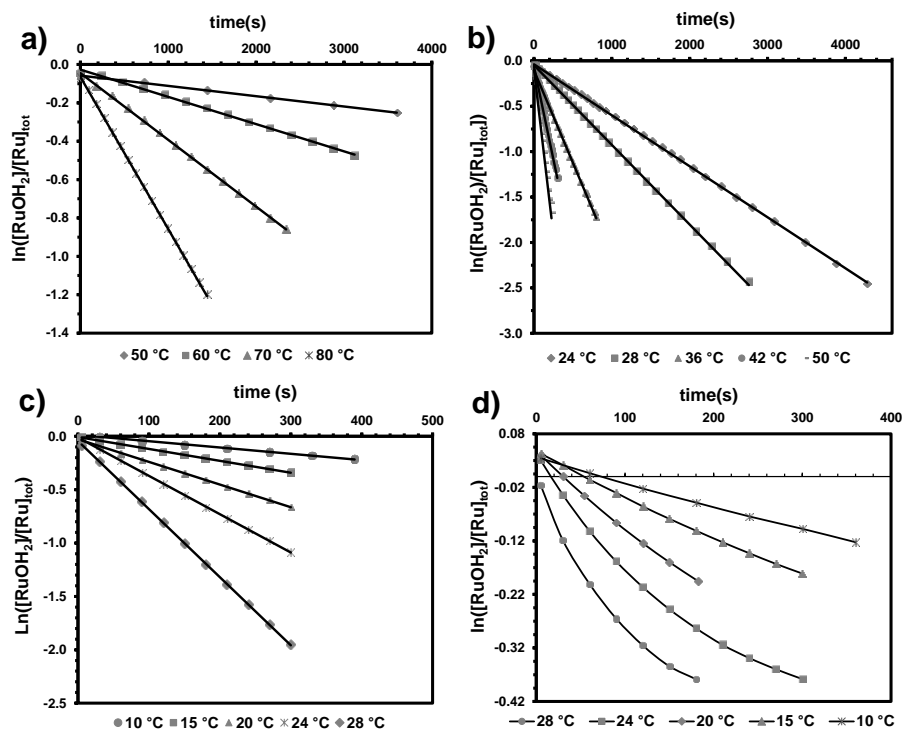
**Figure 3.6.** Plots of ln$([RuOH_2]/[Ru]_{tot})$ vs. time at different temperatures for the thermal coordination, in the dark and in pure water (pH ~ 7), of Hmte to a) $[\mathbf{1}]^{2+}$, b) $[\mathbf{2}]^{2+}$, c) $[\mathbf{3}]^{2+}$ (see Chapter 2) and d) $[\mathbf{4}]^{2+}$. All the numerical values of $k'_i$ and $k_i$ are given in Tables AIII.1 and AIII.2. Conditions: (a) $[Ru]_{tot}$=6.6 ×10$^{-5}$ M, $[Hmte]$=0.067 M, (b) $[Ru]_{tot}$=6.6×10$^{-5}$ M, $[Hmte]$= 0.067 M, (c) $[Ru]_{tot}$=1.4 ×10$^{-4}$ M, $[Hmte]$=0.16 M, and (d) $[Ru]_{tot}$ = 2.1×10$^{-4}$ M, $[Hmte]$ = 0.032 M.
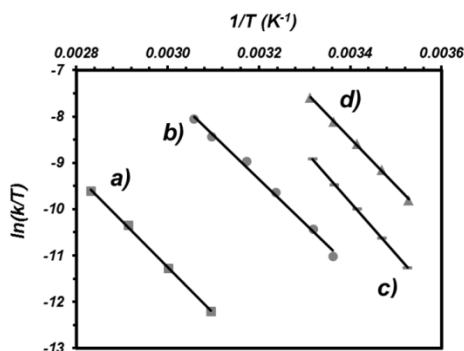


**Figure 3.7.** Eyring plots for the thermal substitution of $H_2O$ by Hmte for $[Ru(terpy)(N-N)(H_2O)]^{2+}$ in pure water, where N-N is a) bpy, b) biq, c) dcbpy, and d) dmbpy. The slope of the line is $-\Delta H^{\ddagger}_i/R$, and the y-intercept is ln$(k_B/h)+\Delta S^{\ddagger}_i/R$. See Table 3.3 for numerical values.

**Table 3.3.** Activation parameters for the thermal coordination of Hmte to RuOH$_2$ ($i$) and thermal hydrolysis of RuHmte ($-i$), where N-N is bpy ($i$=1), biq ($i$=2), dcbpy ($i$=3), or dmbpy ($i$=4). Condition: $T$= 297 K, in the dark, MilliQ water, pH ~ 7.

| N-N | $\Delta H^{\ddagger}_i$ (kJ·mol$^{-1}$) | $\Delta S^{\ddagger}_i$ (J·mol$^{-1}$·K$^{-1}$) | $\Delta G^{\ddagger}_i$ (297 K) (kJ·mol$^{-1}$) | $\Delta G^{\ddagger}_{-i}$ (297 K) (kJ·mol$^{-1}$) | $\Delta G^{\bullet}_i$ (297) (kJ·mol$^{-1}$·K$^{-1}$) |
|---|---|---|---|---|---|
| **bpy** | 83(1) | −48(9) | 97(5) | 117(20) | −20(2) |
| **biq** | 79(3) | −20(8) | 85(4) | 97(6) | −12(2) |
| **dcbpy** | 93(1) | +38(4) | 82(3) | 94(4) | −13(2) |
| **dmbpy** | 85(1) | +20(2) | 79(3) | 88(4) | −9(1) |

These variable-temperature measurements also allowed us obtaining the values of $\Delta G^{\ddagger}_{-i}$ for the thermal substitution of Hmte by water in [**6**]$^{2+}$, [**7**]$^{2+}$, or [**8**]$^{2+}$, from the values of $\Delta G^{\ddagger}_i$ and $\Delta G^{\circ}_i$, and using the equation $\Delta G^{\ddagger}_{-i} = \Delta G^{\ddagger}_i - \Delta G^{\circ}_i$. Upon increasing the steric hindrance of the bidentate chelate, $\Delta G^{\ddagger}_{-i}$ was found to decrease as well (see Table 3.3), *i.e.*, the coordinated Hmte ligand becomes more and more labile in water. Overall, our data clearly indicate that increasing the bulkiness of the substituent on the bidentate chelate N-N increases the lability of both monodentate ligands (H$_2$O and Hmte), whereas it decreases the thermodynamic driving force for the formation of the RuHmte species.

### 3.2.5. Photochemistry

#### 3.2.5.1. Quantum yield determination

Ruthenium polypyridyl complexes are known for their ability to photosubstitute a ligand of the coordination sphere by a solvent molecule upon visible light irradiation. [20-21, 24, 45, 50] The Ru-S bond of [**5**]$^{2+}$, [**6**]$^{2+}$, [**7**]$^{2+}$, or [**8**]$^{2+}$ can indeed be cleaved by visible light irradiation in water, to afford the ruthenium aqua complexes [**1**]$^{2+}$, [**2**]$^{2+}$, [**3**]$^{2+}$, or [**4**]$^{2+}$, respectively (see Scheme 3.1). This photochemical process comes in addition to the thermal hydrolysis of the Hmte complex, the kinetics of which significantly varies depending on the steric hindrance of the bidentate chelate N-N (see above and Table 3.2). Different methods were used for measuring the photosubstitution quantum yields $\varphi_i$ of the four ruthenium compounds [**5**]$^{2+}$-[**8**]$^{2+}$ (see Appendix I, section AI.3 and Appendix III, section AIII.9). For [**5**]$^{2+}$ full conversion to [**1**]$^{2+}$ is obtained after 30 minutes irradiation at 452 nm using a 1000 W Xe lamp fitted with a bandpath filter. The photochemical reaction can be followed by UV-vis spectroscopy

(Figure AIII.9), and a value of 0.022(6) was found for $\varphi_1$ at room temperature and at 452 nm, which is consistent with previous work.[32]

On the other hand, measuring the photosubstitution quantum yields $\varphi_2$, $\varphi_3$, and $\varphi_4$ for $[\mathbf{6}]^{2+}$, $[\mathbf{7}]^{2+}$ and $[\mathbf{8}]^{2+}$, respectively, was challenging because of the rapid equilibrium between RuHmte and RuOH$_2$ (see also Chapter 2). For these compounds standard measurements cannot be realized, so that another method was used consisting in the perturbation with light of the thermal equilibrium between RuOH$_2$ and RuHmte (see Appendix III, section AIII.9). In short, the ratio $[RuHmte]_{eq}/[RuOH_2]_{eq}$ is measured by UV-vis spectroscopy at the equilibrium in the dark (eq), and compared to the ratio $[RuHmte]_{ss}/[RuOH_2]_{ss}$ at the steady state under visible light irradiation (ss). Both ratios can be expressed as a function of $k'_i$, $k_{-i}$, and $k_{\varphi i}$ (Equation 3.8a and 3.8b), where $k_{\varphi i}$ is a first-order rate constant for the photochemical substitution of Hmte by H$_2$O (unit: s$^{-1}$, see Equation 3.9 and Appendix III, section AIII.9).

a) $\dfrac{[RuHmte]_{eq}}{[RuOH2]_{eq}} = \dfrac{k_i \, [Hmte]}{k_{-i}}$　　b) $\dfrac{[RuHmte]_{ss}}{[RuOH2]_{ss}} = \dfrac{k_i \, [Hmte]}{k_{-i} + k_{\varphi i}}$　　**(Equation 3.8)**

$$k_{\varphi i} = \frac{\Phi \cdot \varphi_i \cdot (1 - 10^{-A_e})}{n_{Ru_{(tot)}}}$$　　**(Equation 3.9)**

First the value of $k_{-i}$ was obtained in the dark from Equation 3.8a knowing the value of $k_i$; Then the value of $k_{\varphi i}$ can be obtained under irradiation using Equation 3.8b, and from the values of $k_{\varphi i}$ the photosubstitution quantum yields $\varphi_i$ were calculated using Equation 3.9. Numerical values $\varphi_2 = 0.12(4)$ (at 520 nm), $\varphi_3 = 0.13(4)$ (at 465 nm), and $\varphi_4 = 0.30(10)$ (at 465 nm) were found for the biq, dcbpy, and dmbpy systems, respectively, at 297 K. These values are significantly higher than $\varphi_1$, as expected for sterically hindered complexes. The value of $\varphi_3$ found by this method was close to that obtained using a more direct method (0.097(9)) (see Chapter 2).

Interestingly, comparing (Table 3.4) the pseudo first-order rate constant for the thermal substitution of H$_2$O by Hmte, $k'_i$, and the first-order rate constants $k_{-i}$ and $k_{\varphi i}$ for the thermal and photochemical substitution of Hmte by H$_2$O, respectively, highlights that with N-N=biq or N-N=dcbpy the values of $k_{\varphi i}$ are one order of magnitude *higher* than that of $k'_i$ and $k_{-i}$. By contrast, for N-N=dmbpy $k_{\varphi 4}$ is one order of magnitude *lower*

than $k_{-4}$ and $k'_4$. Thus, by increasing too much the steric hindrance of the spectator diimine bidentate ligand (N-N=dmbpy), the thermal lability of Hmte increases to a point where the light-induced shifting of the thermal equilibrium between $RuOH_2$ and RuHmte becomes difficult to realize. For such compounds shifting appreciably the equilibrium in favor of the aqua complex would require much higher light intensities. For N-N=biq and N-N=dcbpy low light intensities efficiently perturb the thermal equilibrium between $RuOH_2$ and RuHmte. As shown in Figure AIII.10b and AIII.10c, during light irradiation the ratio *[RuHmte]/[RuOH$_2$]* varies significantly: a steady state can be reached where Ru is mostly bound to $H_2O$, whereas in the dark it is mostly bound to Hmte. Thus, moderately hindered compounds such as those with biq and dcbpy represent a better compromise between thermal and photochemical lability, and afford a light-sensitive Ru-S coordination bond in water. In contrast, the thermal reactivity of non-hindered (N-N=bpy) or too hindered (N-N=dmbpy) complexes is either too low, or too high, respectively.

**Table 3.4**. Photochemical and thermal first-order rate constant values for a typical visible light irradiation experiment with interconversion between $[Ru(terpy)(N-N)(H_2O)]^{2+}$ and $[Ru(terpy)(N-N)(Hmte)]^{2+}$ (N-N=biq, dcbpy, or dmbpy). Conditions: $T$= 297 K, solvent = MilliQ water (pH ~ 7). The photon flux $\Phi$ is indicated.

| N-N | *[Hmte]* | $k'_i$ | $k_{-i}$ | $k_{\varphi i}$ | $\Phi$ | $\varphi_i$ |
|---|---|---|---|---|---|---|
| | (M) | (s$^{-1}$) | (s$^{-1}$) | (s$^{-1}$) | (Einstein·s$^{-1}$) | |
| **biq** | 0.011 | $7.3\times10^{-5}$ | $4.4\times10^{-5}$ | $4.2\times10^{-4}$ | $9.8\times10^{-10}$ | 0.12(4) |
| **dcbpy** | 0.010 | $2.2\times10^{-4}$ | $1.1\times10^{-4}$ | $1.1\times10^{-3}$ | $3.9\times10^{-9}$ | 0.13(4) |
| **dmbpy** | 0.20 | $1.8\times10^{-2}$ | $4.5\times10^{-2}$ | $2.0\times10^{-3}$ | $3.9\times10^{-9}$ | 0.30(10) |

### 3.2.5.2. Reversibility of the light-induced equilibrium shift

In Chapter 2 it was shown that the blue light-induced shifting of the equilibrium between $RuOH_2$ and RuHmte in water for the N-N=dcbpy system could be repeated at least up to four cycles at room temperature. Considering the similar kinetic properties of the N-N=biq system, these studies was repeated for $[\mathbf{6}]^{2+}$ using green light. The thermal equilibrium between $[\mathbf{6}]^{2+}$ and $[\mathbf{2}]^{2+}$ in water was perturbed by light irradiation ($\lambda_e$=520 nm) for a period of 45 minutes, followed by a dark period of 90 minutes. This cycle was repeated four times, and the state of the system was monitored by UV-vis spectroscopy. The time evolution of the ratio *[RuOH$_2$]/[Ru]$_{tot}$* is shown in Figure 3.8.

Like for N-N=dcbpy, the N-N=biq system shows reversible light-induced shift of the equilibrium between $[6]^{2+}$ and $[2]^{2+}$, and no sign of degradation was observed after four cycles. The composition of the solution varies between 45% of $[2]^{2+}$ in the dark and up to 85% of $[2]^{2+}$ after irradiation in the steady state. These results show that the biq system is robust and only contains the two ruthenium compexes $[2]^{2+}$ and $[6]^{2+}$ that interconvert upon switching on and off a source of green light. Like for N-N=dcbpy, the Ru-S coordination bond forms spontaneously in the dark and is cleaved by visible light irradiation.
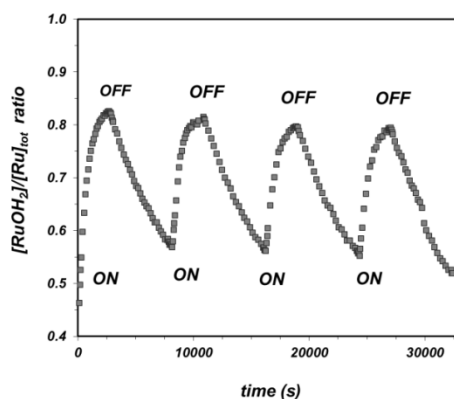


**Figure 3.8.** Plot of the ratio $[RuOH_2]/[Ru]_{tot}$ *vs.* time upon switching ON and OFF several times a source of green light ($\lambda_e$=520 nm) in presence of $[6]^{2+}$ and $[2]^{2+}$, and Hmte. Conditions: $T$= 297 K, MilliQ water (pH ~ 7); photon flux $\Phi$=9.8(5)×10$^{-9}$ Einstein.s$^{-1}$; $[Ru]_{tot}$ = 8.6×10$^{-5}$ M , $[Hmte]$ = 0.011 M, spectra measured every 1 minute.

## 3.3.    Discussion

Following previous work of Takeuchi,[63-64] Rack,[12-14] or Sauvage[24, 62] on the influence of steric hindrance on the photoreactivity of polypyridyl ruthenium(II) compounds it was realized in Chapter 2 that in the dark the Ru-S coordination bond of hindered complexes such as [Ru(terpy)(dcbpy)(Hmte)]$^{2+}$ spontaneously forms at room temperature and in neutral aqueous solutions, while still keeping a very high sensitivity to visible light irradiation. As dark formation and photochemical breakage can both occur such systems open new possibilities for building supramolecular systems driven by visible light irradiation. However, the higher lability observed with the dcbpy complex seemed counter-intuitive: for other light-sensitive complexes such as

$[Ru(phen)_2(dmbpy)]^{2+}$, steric hindrance leads to efficient photosubstitution[24] indeed, but also to a difficult thermal binding of the hindered chelate to the Ru center. The present study was undertaken to understand the relationship between thermal lability and steric hindrance for ruthenium complexes of the $[Ru(terpy)(N-N)(Hmte)]^{2+}$ family, and to gather temperature-dependent kinetic data that had been overlooked in the past.

First, it might be noticed that the substitutents in *ortho* position to the coordinated nitrogen atoms of N-N=biq, dcbpy, and dmbpy do not only increase the steric bulk of the coordination sphere around the metal, but they also exert on electronic effect on the metal center, which may in turn influence the rates of ligand substitutions. These effects can be seen for example on the absorption maxima of the RuHmte complexes $[5]^{2+}$-$[8]^{2+}$, which lies at significant higher wavelength for N-N=biq ($\lambda_{max}$=519 nm) than for N-N=bpy, dcbpy, or dmbpy ($\lambda_{max}$=450, 467, and 463 nm, respectively). These electronic effects might play a role in fine-tuning the activation enthalpies and entropies of the thermal substitution reactions. However, one substituent of the bidentate chelate and the monodentate ligand coordinated to the metal center lie in very close spatial proximity, thus leading to significant distortion of the geometry in the ground state (compare for example the X-ray structures of $[5]^{2+}$ and $[7]^{2+}$ in Chapter 2 and 3, respectively). Thus, in the following discussion the change in mechanism along the series bpy, biq, dcbpy, dmbpy is mostly interpreted as a consequence of the increasing steric demands of the spectator diimine chelate.

Usually, the higher thermal lability for sterically hindered complexes is explained in terms of destabilization of the ground-state hexacoordinated species, compared to the transition state of the thermal substitution reaction. In such interpretation, the reaction always follows a dissociative interchange mechanism.[63, 68-71] Applied to our system, this explanation should lead to enthalpy ($\Delta H^{\ddagger}_i$) being the main reason for the decreased activation Gibbs energies ($\Delta G^{\ddagger}_i$) when going from N-N=bpy to N-N=dmbpy. However, our data show that the increased lability of the hindered complexes in water is due to variations of the entropic term ($\Delta S^{\ddagger}_i$) in Eyring's equation. Although $\Delta S^{\ddagger}_i$ values are known to contain significant experimental errors and may be less accurate than, for example, activation volumes $\Delta V^{\ddagger}_i$, the similarities in $\Delta H^{\ddagger}_i$ for the four systems and the clear differences in $\Delta S^{\ddagger}_i$, as seen in Figure 3.7, allow for drawing mechanistic conclusions. Considering that for all four systems the rate law is first order in Hmte, it is concluded that there is a shift in the mechanism of the thermal substitution of $H_2O$ by Hmte, from interchange associative with N-N=bpy and biq, marked by $\Delta S^{\ddagger}_i$<0, to

interchange dissociative with N-N=dcbpy and dmbpy, marked by $\Delta S_i^{\ddagger} > 0$.[72-81] As shown in Scheme 3.3, $H_2O$ is still present in the coordination sphere when the Ru-S bond-making occurs, and in an interchange mechanism bond making occurs before the second coordination sphere has had time to relax. For less bulkier chelates (N-N=bpy, biq) the Ru-S bond-making is essentially synchronous with the Ru-O bond-breaking ($I_a$ mechanism). Hydrogen bonding between Hmte and the aqua ligand may also contribute to stabilizing the hepta-coordinated transition state. Thus, a more compact transition state and more constraints for the unhindered chelates N-N=bpy and biq lead to negative values for the activation entropy, and thus to significantly (bpy) or slightly (biq) lower substitution rate constants. In contrast, for bulkier systems the Ru-S bond making only occurs when $RuOH_2$ is already partially broken, but before $H_2O$ exits from the second coordination sphere ($I_d$ mechanism). Thus, there is no formation of a coordinatively unsaturated and potentially highly reactive pentacoordinated state, which would cancel the dependence of the substitution rate law in *[Hmte]*. The less compact transition state for N-N=dcbpy and dmbpy increases the degrees of freedom of both incoming and leaving monodentate ligands, thus resulting in positive activation entropies for the substitution process, which significantly enhances its rate constants.[64, 68, 76, 81-86]
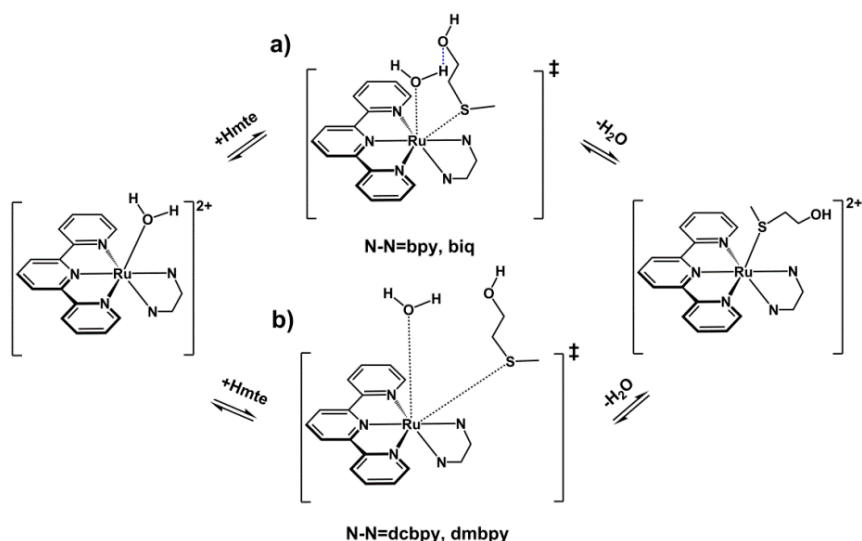


**Scheme 3.3.** The proposed transition states for the substitution of the aqua ligand in [Ru(terpy)(N-N)(H$_2$O)]$^{2+}$ by Hmte, where a) N-N=bpy, biq (more compact transition state with hydrogen-binding contributing to a loose hepta-coordinated transition state) and b) N-N=dcbpy,dmbpy (less compact transition state).

## 3.4.  Conclusion

The thermodynamic, kinetic, and photochemical properties of a series of polypyridyl ruthenium complexes [Ru(terpy)(N-N)(L)]$^{2+}$ with N-N is bpy, biq, dcbpy, or dmbpy, and L is H$_2$O or Hmte, have been determined in water near neutral pH. Our data provide a global understanding of the influence of the N-N chelate on the reactivity of these systems. Qualitatively, a global acceleration of all thermal and photochemical ligand exchange processes is observed when the steric hindrance of the spectator diimine chelate is increased. Variable-temperature kinetic data show that the increased lability of the monodentate ligand with hindered N-N chelates is due to entropy, and that the mechanism of the thermal ligand substitution reaction changes from interchange associative to interchange dissociative following the series N-N=bpy, biq, dcbpy, dmbpy. Analysis of the relative values of the rate constants for the thermal and photochemical ligand substitution reactions also shows that by increasing the steric hindrance too much (N-N = dmbpy) the lability in the dark becomes so high that no appreciable change of the composition of the solution can be obtained by light irradiation, unless exceptionally intense light would be used. With intermediate steric hindrance (N-N=biq or dcbpy) the Ru-S bond forms spontaneously in the dark at room temperature but it is efficiently cleaved under mild irradiation, which will allow using these systems in supramolecular chemistry. With the non-hindered ligand N-N=bpy, the photosensitivity of the Hmte complex is lower and the monodentate ligands (Hmte and H$_2$O) are non-labile at room temperature. Overall, changing the N-N bidentate ligand appears as an efficient means to tune the thermal and photochemical reactivities of [Ru(terpy)(N-N)L]$^{2+}$ complexes.

## 3.5.  Experimental section

### 3.5.1.  Synthesis

$^1$H and $^{13}$C NMR spectra were recorded using a Bruker DPX-300 spectrometer; chemical shifts are indicated in ppm relative to TMS. Electrospray mass spectra were recorded on a Finnigan TSQ-quantum instrument using an electrospray ionization technique (ESI-MS). UV-vis spectra were obtained on a Perkin-Elmer Lambda 900 spectrophotometer or on a Varian Cary 50 UV-visible spectrometer. The classical routes for synthesizing [Ru(terpy)(biq)(Cl)]Cl ([**10**]Cl),[63] [Ru(terpy)(dmbpy)(Cl)]Cl ([**12**]Cl),[66] and [Ru(terpy)(dcbpy)(Cl)]Cl ([**11**]Cl),[66] were modified (see *Appendix III, section AIII.1*). [Ru(terpy)Cl$_3$],[87] 6,6'-dichloro-2,2'-bipyridine,[88] [Ru(terpy)(bpy)(Cl)]Cl ([**9**]Cl),

[Ru(terpy)(bpy)(H$_2$O)](PF$_6$)$_2$ ([1](PF$_6$)$_2$), [32, 67] were synthesized following literature procedures. [Ru(terpy)(dcbpy)(Hmte)](PF$_6$)$_2$([7](PF$_6$)$_2$) was synthesized as explained in Chapter 2. 2,2';6',2"-terpyridine was purchased from ABCR GmbH & Co.KG. 2,2'-bipyridine, 6,6'-dimethyl-2,2'-bipyridine, 2,2'-biquinoline, 2-(methylthio)-ethanol (Hmte), and AgPF$_6$ were purchased from Sigma-Aldrich and used as such.

**[Ru(terpy)(bpy)(Hmte)](PF$_6$)$_2$** ([5](PF$_6$)$_2$): [9]Cl (56 mg, 0.10 mmol) and AgPF$_6$ (57 mg, 0.22 mmol) were dissolved in 3:5 acetone/H$_2$O mixture (16 mL). To this solution was added Hmte (90 μL, 1.0 mmol). The mixture was refluxed under argon for 8 hours in the absence of light, after which it was filtered hot over celite. Evaporation of the filtrate gave an orange solid, which was taken up in acetone and reprecipitated with Et$_2$O. Filtration of the suspension yielded [5](PF$_6$)$_2$ as an orange powder (69 mg, 79%). ^{1}H NMR (300 MHz, Acetone, 298 K) δ 9.95 (d, J = 5.6 Hz, 1H, A6), 9.03 – 8.87 (m, 3H, A3+T3'), 8.78 (d, J = 8.1 Hz, 2H, T3), 8.72 (d, J = 8.2 Hz, 1H, B3), 8.59 – 8.42 (m, 2H, A4+T4'), 8.26 – 8.09 (m, 3H, A5+T4), 8.09 – 7.94 (m, 3H, B4+T6), 7.63 – 7.47 (m, 3H, B6+T5), 7.31 (t, J = 6.6 Hz, B6, B5), 3.55 (t, J = 5.5 Hz, 2H, S-CH$_2$-C<u>H</u>$_2$), 2.03 – 1.97 (m, 2H, S-C<u>H</u>$_2$), 1.53 (s, 3H, S-<u>Me</u>). ^{13}C NMR (75 MHz, Acetone, 297 K) δ 158.48+157.94+157.23+157.18 (B2+A2+T2+T2'), 153.89 (T6), 152.61 (A6), 150.56 (B6), 139.34 (T4), 138.67+138.58 (B4+A4), 137.42 (T4'), 129.03 (T5), 128.37 (A5), 127.71 (B5), 125.45 (T3), 125.16 (A3), 124.76 (T3'), 124.30 (B4), 58.37 (S-CH$_2$-<u>C</u>H$_2$), 37.17 (S-<u>C</u>H$_2$), 14.38 (S-<u>Me</u>). *UV-vis:* λ$_{max}$ (ε in L·mol$^{-1}$·cm$^{-1}$) in pure H$_2$O: 450 nm (6600). *ES MS m/z (calc):* 728.0 (727.7 [M − PF$_6$]$^+$), 582.1 (581.7 [M − 2 PF$_6$ − H]$^+$), 261.5 (261.3 [M − 2PF$_6$ − Hmte + MeOH]$^{2+}$). Anal. Calcd for C$_{28}$H$_{27}$F$_{12}$N$_5$O$_2$P$_2$RuS: C, 38.54; H, 3.12; N, 8.03; S, 3.67. Found: C, 38.25; H, 3.41; N, 7.94; S, 3.78. *Crystal growing:* Large single crystals of compound [5](PF$_6$)$_2$ were grown by vapor diffusion of toluene into a solution of [1](PF$_6$)$_2$ in Hmte (~10 mg in 0.5 mL mte). *Crystal structure data:* [C$_{28}$H$_{27}$N$_5$ORuS](PF$_6$)$_2$; Fw = 872.62, red block, 0.45 × 0.25 × 0.24 mm$^3$, monoclinic, C2/c (no. 15), a = 24.06815(17), b = 10.86063(8), c = 24.69614(19) Å, β = 93.6407(7)°, V = 6442.43(8) Å$^3$, Z = 8, D$_x$ = 1.799 g cm$^{-3}$, μ = 0.755 mm$^{-1}$, abs. corr. range: 0.769–0.867. 31610 Reflections were measured up to a resolution of (sin θ/λ)$_{max}$ = 0.65 Å$^{-1}$. 5673 Reflections were unique (R$_{int}$ = 0.0367), of which 5375 were observed [I > 2σ(I)]. 511 Parameters were refined with 195 restraints. R1/wR2 [I > 2σ(I)]: 0.0207/0.0517. R1/wR2 [all refl.]: 0.0226/0.0525. S = 1.051. Residual electron density found between −0.55 and 0.37 eÅ$^{-3}$.

**[Ru(terpy)(biq)(Hmte)]Cl$_2$** ([6]Cl$_2$): [10]Cl (4.0 mg, 6.0 μmol) was dissolved in D$_2$O (0.50 mL). To this solution a large excess of Hmte (50 μL, 0.51 mmol) was added and stirred for 5 minutes. The mixture was kept for 3 h at 80 °C in a water bath. According to ^{1}H NMR

and ES MS, [**6**]$^{2+}$ is the only ruthenium species in solution. (*For atom numbering see Figure AIII.1*) $^1$H NMR (300 MHz, D$_2$O, 298 K) δ 8.97 (dd, *J* = 19.4, 8.8 Hz, 2H, B3+B4), 8.66 (d, *J* = 8.2 Hz, 4H, B8+T3'+A3), 8.47 (d, *J* = 8.0 Hz, 2H, T3), 8.43 − 8.33 (m, 3H, B5+A4+T4'), 8.14 − 7.92 (m, 6H, T4+B6+B7+T6), 7.85 (d, *J* = 7.4 Hz, 1H,A5), 7.55 − 7.40 (m, 3H, T5+A6), 7.25 (t, *J* = 7.9 Hz, 1H,A7), 6.50 (d, *J* = 8.8 Hz, 1H,A8), 3.30 (t, *J* = 7.1, 4.4 Hz, 2H,S-CH$_2$-C̲H̲$_2$), 1.54 (t, *J* = 5.8 Hz, 2H, S-C̲H̲$_2$-CH$_2$), 1.03 (s, 3H, C̲H̲$_3$-S). $^{13}$C NMR (75 MHz, D$_2$O, 297 K) δ 159.83+159.80 (T2+T2'), 158.17+158.00 (A2+B2), 153.46 (T6), 150.19+149.91 (A8a+B8a), 140.32+139.36 (B8+A8), 139.46 (T4), 137.94 (T4'), 133.09 (B6+A6), 130.60+130.05 (A7+B7), 129.75+128.80 (B4a+ A4a), 129.64+129.04 (A4+B4), 128.76 (T5), 126.92+123.06 (B5+A5), 125.03+124.34 (T3+T3'), 121.24+120.87 (A3+B3), 57.32 (S-CH$_2$-C̲H̲$_2$), 46.78 (S-C̲H̲$_2$-CH$_2$), 8.48 (C̲H̲$_3$-S). *UV-vis:* $λ_{max}$ (ε in L·mol$^{-1}$·cm$^{-1}$) in pure H$_2$O: 519 nm (5600). *ES MS* m/z *(calc):* 682.0 (682.1 [M–2Cl–H]$^+$), 295.5 (295.3 [M–2Cl–Hmte]$^{2+}$).

**[Ru(terpy)(dmbpy)(Hmte)]Cl$_2$** ([**8**]Cl$_2$): [**12**]Cl (4.0 mg, 6.8 μmol) was dissolved in D$_2$O (0.50 mL). To this solution a large excess of Hmte (24 μL, 0.28 mmol) was added. The mixture was stirred for 5 minutes. The compound was not isolated as it would react back to [**12**]Cl upon evaporation of water. According to $^1$H-NMR and MS [**8**]$^{2+}$ is the the only ruthenium species present in solution. (*For atom notations see Figure AIII.1*) $^1$H NMR (300 MHz, D$_2$O, 298 K) δ 8.57 (d, *J* = 8.2 Hz, 2H, T3'), 8.45 (d, *J* = 8.0 Hz, 3H, B3+T3), 8.26 (t, *J* = 8.1 Hz, 1H, T4'), 8.21 − 8.01 (m, 6H, B4+A3+T4+T6), 7.81 (d, *J* = 7.6 Hz, 1H, B5), 7.61 (t, *J* = 7.9 Hz, 1H, A4), 7.55 − 7.46 (m, 2H, T5), 6.88 (d, *J* = 7.6 Hz, 1H, A5), 3.26 (t, *J* = 5.7 Hz, 2H, S-CH$_2$-C̲H̲$_2$), 3.09 (s, 3H, H7), 1.39 (t, *J* = 5.6 Hz, 2H, S-C̲H̲$_2$), 1.27 (s, 3H, H7'), 0.87 (s, 3H, S-M̲e̲). $^{13}$C NMR (300 MHz, D$_2$O) δ 165.61+164.45 (B6+A6), 158.94+158.38 (T2+T2'), 158.12+158.06 (B2+A2), 153.82 (T6), 138.99 (T4), 138.33 (A4), 138.15 (B4), 136.95 (T4'), 128.58 (T5), 127.76 (A5), 127.32 (B5), 124.61 (T3), 123.77 (T3'), 121.80 (A3), 121.38 (B3), 56.46 (HO-C̲H̲$_2$-), 34.71 (Me-S-C̲H̲$_2$-), 26.86 (A7), 22.00 (B7), 11.70 (M̲e̲-S). *UV-vis:* $λ_{max}$ (ε in L·mol$^{-1}$·cm$^{-1}$) in pure H$_2$O: 463 nm (5700). *ES MS m/z (calc):* 610.1 (609.8 [M – 2Cl – H]$^+$), 305.6 (305.3 [M – 2 Cl]$^{2+}$).

**General procedure for the hydrolysis in CD$_3$OD of [Ru(terpy)(N-N)(Cl)]Cl ([10]Cl, [11]Cl, or [12]Cl, N-N=biq, dcbpy, or dmbpy) :** Three NMR samples of compound [**10**]Cl (2.2 mg, 3.3×10$^{-3}$ mmol), [**11**]Cl (2.8 mg, 4.8×10$^{-3}$ mmol), or [**12**]Cl (2.9 mg, 4.6×10$^{-3}$ mmol) were dissolved in MeOD (500 μL). An $^1$H NMR spectrum was recorded for each sample. Then, 20 μL, 40 μL, 80 μL, and 160 μL of D$_2$O were added successively to each NMR tube, and $^1$H NMR spectra were recorded after each addition (see Figure AIII.3).

### 3.5.2. Equilibrium constant determination

**(a)** For N-N=biq (Hmte+[**2**]Cl$_2$ $\leftrightarrows$ H$_2$O+[**6**]Cl$_2$): A stock solution **A** of [**10**]Cl (17 mg in 5.0 mL D$_2$O, 5.1 mM) and a stock solution **B** of Hmte (92 mg Hmte in 2.0 mL D$_2$O, 0.50 M) were prepared. Eight NMR tubes containing 0.50 mL of solution **A** (2.5 μmol [**10**]Cl) were prepared, and to each tube was added 2.5 μL, 5.0 μL, 8.0 μL, 10 μL, 15 μL, 26 μL, 34 μL, or 35 μL solution **B**, resulting in 0.50, 1.0, 1.6, 2.0, 3.0, 5.2, 6.8 or 7.0 equivalents of Hmte, respectively. The NMR tubes were put in a water bath for 30 minutes at 50 °C and left standing overnight at room temperature. After equilibration, $^1$H NMR spectra of all samples were measured at room temperature, to determine the relative integral of [**6**]$^{2+}$ and [**2**]$^{2+}$. Then the ratio *[RuHmte]/[RuOH$_2$]* were determined by integration of the peaks at 6.35 and 6.75 ppm corresponding to [**6**]$^{2+}$ and [**2**]$^{2+}$, respectively, where *[RuHmte]* represents the concentration in [**6**]$^{2+}$ and *[RuOH$_2$]* the concentration in [**2**]$^{2+}$. A plot of *[RuHmte]/[RuOH$_2$]* as a function of equilibrium concentration in Hmte was made. The slope of the plot numerically corresponds to $K_2$ (see Figure 3.4 and Equation 3.1).

**(b)** For N-N=dmbpy (Hmte+[**4**]Cl$_2$ $\leftrightarrows$ H$_2$O+[**8**]Cl$_2$): A stock solution **C** of [**12**]Cl (40 mg in 5.0 mL D$_2$O, 13 mM) was prepared. NMR samples, each containing 0.50 mL of stock solution **C** (6.4 μmol [**12**]Cl) were prepared. To each NMR tube was added a known amount of pure Hmte (0.60 μL, 1.2 μL, 1.8 μL, 2.4 μL, 3.0 μL, 4.5 μL or 6.0 μL) to give 1.0, 2.0, 3.0, 4.0, 5.0, 7.5, 10 or 20 equivalents, respectively. Each NMR tube was stirred for 5 minutes and then left to stand for more than 10 minutes at room temperature. After equilibration, $^1$H NMR spectra of all samples were measured at room temperature. The ratio *[RuHmte]/[RuOH$_2$]* were determined by integration of the peaks at 6.86 and 6.78 ppm, where *[RuHmte]* represents the concentration in [**8**]$^{2+}$ (δ= 6.86 ppm) and *[RuOH$_2$]* the concentration in [**4**]$^{2+}$ (δ=6.78 ppm). A plot of *[RuHmte]/[RuOH$_2$]* as a function of equilibrium concentration in Hmte was made. The slope of the plot numerically corresponds to K$_4$ (see Figure 3.4 and Equation 3.1).

The values for Gibbs free energy $\Delta G^{\circ}_i$ at 297 were calculated for both reactions using the equation $\Delta G_i^{\circ} = -R \cdot T \cdot \ln(K_i)$

### 3.5.3. Kinetics

A Perkin-Elmer Lambda 900 UV-vis spectrometer equipped with stirring and temperature control was used for kinetic experiments. The measurement procedure of the extinction coefficients of all aqua and Hmte complexes used in the kinetic study is described in the Appendix I, section AI.1. The experimental procedure for calculation of the rate constants at 297 K from the slope of a plot of $k'_i$ vs. *[Hmte]* is explained in the section AIII.7.

**Thermal substitution of H$_2$O by Hmte on RuOH$_2$ complexes ($k_i$, $\Delta H^{\ddagger}_i$, $\Delta S^{\ddagger}_i$, $\Delta G^{\ddagger}_i$).** Stock solutions **D** of complex [**1**](PF$_6$)$_2$ (2.0 mg in 25 mL H$_2$O, 1.0×10$^{-4}$ M), **E** of [**10**]Cl (1.6 mg in 25 mL H$_2$O, 1.0×10$^{-4}$ M), **F** of [**11**]Cl (3.7 mg in 25 mL H$_2$O, 2.1×10$^{-4}$ M), **G** of [**12**]Cl (3.5 mg in 25 mL H$_2$O, 2.2×10$^{-4}$ M), and **H** and **I** of Hmte (460 mg in 25.0 mL H$_2$O, 2.00×10$^{-1}$ M (**H**), and 438 mg in 10.0 mL H$_2$O, 4.70×10$^{-1}$ M (**I**)) were prepared. 2.0 mL of **D**, **E**, **F,** or **G** was added to a UV-vis cuvette, which was placed in the UV-vis spectrometer. The temperature was set at 50, 60, 70 or 80 °C for **D**, 24, 28, 35, 42, or 50 °C for **E**, and 10, 15, 20, 24 or 28 °C for **F** and **G**. After obtaining a constant temperature in each cuvette, 1.0 mL of **H** was added to **D** and **E**, or 1 mL of **I** to **F**, or 0.8 mL H$_2$O plus 0.2 mL of **I** to **G**, for each experiment at each temperature (final Hmte and Ru concentrations for each experiments are given in Tables AIII.1 and AIII.2) In such conditions, Hmte is in large excess (pseudo first-order condition). After addition of Hmte, a UV-vis spectrum was taken every 60 seconds for **D** and every 30 seconds for **E**, **F**, or **G**. For each spectrum, the concentrations in RuHmte and RuOH$_2$ were determined by deconvolution of the UV-vis spectra knowing the extinction coefficients of both RuHmte and RuOH$_2$ species (see Appendix I). The pseudo first order rate constants $k'_i$ at each temperature for each sample **D**, **E**, **F**, or **G** were determined from the slope of the plot of ln*([RuOH$_2$]/[Ru]$_{tot}$) vs.* time, and $k_i$ were then calculated knowing the concentration of Hmte in the solution (see Tables AIII.1 and AIII.2). By plotting ln($k_i$/T) as a function of 1/T for each sample, the activation enthalpy and entropy were calculated from the slope and y-intercept of the Eyring plot, respectively. $\Delta G^{\ddagger}_i$ at 297 K was calculated for each reaction using the Equation $\Delta G^{\ddagger}_i = \Delta H^{\ddagger}_i - T \cdot \Delta S^{\ddagger}_i$ (see Table 3.3).

**Thermal substitution of Hmte by H$_2$O in [5]$^{2+}$ ($k_{-1}$).** 3 mL of a solution of [**5**]$^{2+}$ (5.6 mg of [**5**](PF$_6$)$_2$ in 25 mL H$_2$O, 2.5×10$^{-4}$ M) was placed in a UV-vis cuvette, which was placed at t=0 in the UV-vis spectrometer pre-equilibrated at 70, 75, 80, 85, or 90 °C. UV-vis spectra were measured every 60 seconds. The concentrations in *[RuHmte]* and *[RuOH$_2$]* were determined by deconvolution of the UV-vis spectra knowing the extinction coefficients of both RuHmte and RuOH$_2$ species (see Appendix I, Section *AI.1*). The first-order rate constant $k_{-1}$ at each temperature was determined by plotting ln*([RuOH$_2$]/[Ru]$_{tot}$) vs.* time. The slope and y-intercept of an Eyring plot afforded the activation enthalpy and entropy, respectively (see Figure AIII.8). $k_{-1}$ at 24° C was extracted from extrapolating the Eyring Equation down to room temperature; a value of 1.5(4) × 10$^{-8}$ s$^{-1}$ was found.

**Thermal substitution of Hmte by H$_2$O on [6]$^{2+}$, [7]$^{2+}$, and [8]$^{2+}$ ($k_{-2}$, $k_{-3}$, $k_{-4}$).** At the thermodynamic equilibrium between RuOH$_2$, free Hmte, and RuHmte in water, the rates for the formation and hydrolysis of RuHmte complex are equal:

$$k_{-i} \cdot [RuHmte]_{eq} = k_i \cdot [RuOH_2]_{eq} \cdot [Hmte]_{eq}$$

Thus the first order rate constant $k_{-i}$ for the thermal substitution of Hmte by water is numerically given by Equation 3.6. The activation Gibbs energy $\Delta G^{\ddagger}_{-i}$ for the thermal substitution of Hmte by $H_2O$ were calculated using the Equation $\Delta G^{\ddagger}_{-i} = \Delta G^{\ddagger}_{i} - \Delta G^{\circ}_{i}$ (see Table 3.3).

### 3.5.4. Photochemistry

The photochemical quantum yield for $[\mathbf{5}]^{2+}$ was measured using a Varian Cary 50 UV-visible spectrometer and a LOT 1000 W Xenon arc lamp, fitted with a water filter and a 450FS10-50 Andover interference filter ($\lambda_e$=452 nm, $\Delta\lambda_{1/2}$=8.9 nm). Irradiation was thus performed close to the isosbestic point of the reaction, which was at 449 nm. The photochemistry measurements for $[\mathbf{6}]^{2+}$, $[\mathbf{7}]^{2+}$, and $[\mathbf{8}]^{2+}$ were done using a Perkin-Elmer Lambda 900 spectrometer equipped with a custom-made LED lamp fitted to the top of a 1 cm quartz UV-vis cuvette, using an OSRAM Opto electronics LEDs LB W5KM-EZGY-35 ($\lambda_e$=465 nm or $\lambda_e$=520 nm, $\Delta\lambda_{1/2}$=25 nm). In these cases, UV-vis measurements of a sample during irradiation was superimposable with a spectrum of the sample when the LED lamp was switched off, which means that the light used to irradiate the sample perpendicularly to the optical axis of the spectrophotometer was not detected by the spectrometer. Photon fluxes of the three irradiation setups were measured using the ferrioxalate actinometer;[89] a value $\Phi = 6.4(6)\times10^{-8}$ Einstein·s$^{-1}$ was measured at 452 nm for the filtered LOT lamp; $\Phi = 3.9(4)\times10^{-9}$ Einstein·s$^{-1}$ was found for the LED at 465 nm, and $\Phi = 9.8(8)\times10^{-10}$ Einstein·s$^{-1}$ was found for the LED at 520 nm. In the latter two cases, the irradiation path length was 3 cm, and the volume of the irradiated solution was 3 mL.

**Photosubstitution quantum yield determination for complex $[\mathbf{5}]^{2+}$ ($\varphi_I$).** 0.75 mL of a stock solution of the complex $[\mathbf{5}](PF_6)_2$ (5.0 mg in 10 mL $H_2O$, $5.7\times10^{-4}$ M) was put in a UV-vis cuvette. The volume of the solution was completed to 3 mL with $H_2O$ (Final concentration: $1.5\times 10^{-4}$ M). The sample was irradiated using the same setup as was used for actinometry ($\Phi = 6.4(6)\times10^{-9}$ Einstein·s$^{-1}$). After each irradiation period (1 minute) a UV-vis spectrum was measured until a total irradiation time of 10 minutes. The concentrations in $[\mathbf{5}]^{2+}$ and $[\mathbf{1}]^{2+}$ were determined by deconvolution knowing the extinction coefficients of both species (see Appendix I, section AI.2). The evolution of ln*([RuHmte]/[Ru]$_{tot}$)* was plotted as a function of irradiation time, and from the slope *S* of the plot and using Equation AIII.4 the quantum yield $\varphi_i$ was determined to be 0.022(6) (see Table AIII.4*).

**Irradiation of an equilibrated sample of the biq system** ($[2]Cl_2 \leftrightarrows [6]Cl_2$) **and photosubstitution quantum yield determination for** $[6]^{2+}$ **($\varphi_2$).** A UV-vis cuvette containing 2 mL of a stock solution of $[10]Cl$ (1.5 mg in 10 mL $H_2O$, $2.3 \times 10^{-4}$ M) and 1 mL of a solution of Hmte (31 mg in 10 mL $H_2O$, 0.030 M) was prepared and stirred overnight to reach equilibrium at 24 °C. Then, UV-vis spectra were measured, once in the dark, and then during 45 minutes under irradiation using LED lamp at $\lambda_e = 520$ nm. After 45 minutes the LED lamp was switched off, and UV-vis spectra were measured for 90 minutes in the dark (1 minute interval between each spectrum, either under irradiation or in the dark). The cycle was repeated 3 more times for a total experimental time of 9 hours (see Figure 3.8). For each spectrum *[RuHmte]* and *[RuOH₂]*, i.e., the concentration in $[6]^{2+}$ and $[2]^{2+}$, respectively, were determined by deconvolution, knowing the extinction coefficients of both species. By calculating the ratio *[RuHmte]/[RuOH₂]* at the equilibrium in the dark (Equation 3.8a) and at the photochemical steady state (Equation 3.8b), reporting the second order rate constant $k_2$ and the photon flux $\Phi$, the quantum yield $\varphi_2$ was calculated using Equations 3.9, to be 0.12(5) (see Table AIII.4 for all numerical values).

**Determination of the photosubstitution quantum yield for** $[8]^{2+}$ **($\varphi_4$).** 2.0 mL of a stock solution of $[8]Cl$ (7.0 mg in 50 mL $H_2O$, $2.2 \times 10^{-4}$ M) was put in a UV-vis cuvette and 1 mL of a solution of Hmte (277 mg in 5.00 mL $H_2O$, 0.600 M) was added. After equilibration at 24 °C in the dark, UV-vis spectra of the sample were measured in the dark and then 10 times during 10 minutes irradiation with an LED lamp at $\lambda_e = 465$ nm to calculate $\varphi_4$ in the same procedure as that for $[6]^{2+}$. A value of 0.30(10) was found for $\varphi_4$ (see Table AIII.4).

### 3.5.5. Supporting Information available

Appendix I: general procedures for extinction coefficient determination, calculation concentration of RuHmte and RuOH₂ from by deconvolution of the UV-vis data, and photosubstitution quantum yield measurements for $[1]^{2+}$.

Appendix III: The synthesis of $[10]Cl$, $[12]Cl$, proton attribution schemes, NMR spectra of $[4]^{2+}$ and $[8]^{2+}$ in D2O, procedure for X-ray crystal structure determination, NMR spectra of hydrolyzing of $[10]Cl$ and $[11]Cl$, pKa measurements for $[2]^{2+}$ and $[4]^{2+}$, mathematical modeling of the fast equilibrium between $[4]^{2+}$ and $[8]^{2+}$, numerical values of first-order and second-order rate constant for all four systems, determination of the rate law (order of Hmte) of the thermal coordination reaction for N-N=bpy, biq, and dmbpy, Eyring plot for the thermal hydrolysis of $[5]^{2+}$, photosubstitution quantum yield measurements for $[2]^{2+}$, $[3]^{2+}$, and $[4]^{2+}$.

## 3.6. References

[1]     A. D. Ryabov, L. G. Kuzmina, N. V. Dvortsova, D. J. Stufkens, R. Van Eldik, *Inorg. Chem.* **1993**, *32*, 3166-3174.
[2]     H. Nishihara, *Coord. Chem. Rev.* **2005**, *249*, 1468-1475.
[3]     O. S. Wenger, L. M. Henling, M. W. Day, J. R. Winkler, H. B. Gray, *Polyhedron* **2004**, *23*, 2955-2958.
[4]     M. Han, T. Hirade, M. Hara, *New J. Chem.* **2010**, *34*, 2887-2891.
[5]     P. Pratihar, T. K. Mondal, A. K. Patra, C. Sinha, *Inorg. Chem.* **2009**, *48*, 2760-2769.
[6]     T. Mitsuoka, H. Sato, J. Yoshida, A. Yamagishi, Y. Einaga, *Chem. Mater.* **2006**, *18*, 3442-3447.
[7]     R. A. Kopelman, S. M. Snyder, N. L. Frank, *J. Am. Chem. Soc.* **2003**, *125*, 13684-13685.
[8]     A. Bannwarth, S. O. Schmidt, G. Peters, F. D. Sönnichsen, W. Thimm, R. Herges, F. Tuczek, *Eur. J. Inorg. Chem.* **2012**, *2012*, 2776-2783.
[9]     K. Takahashi, Y. Hasegawa, R. Sakamoto, M. Nishikawa, S. Kume, E. Nishibori, H. Nishihara, *Inorg. Chem.* **2012**, *51*, 5188-5198.
[10]    M. D. Segarra-Maset, P. W. N. M. van Leeuwen, Z. Freixa, *Eur. J. Inorg. Chem.* **2010**, 2075-2078.
[11]    M. L. Boillot, J. Zarembowitch, A. Sour, *Top. Curr. Chem.* **2004**, *234*, 261-276.
[12]    D. A. Lutterman, A. A. Rachford, J. J. Rack, C. Turro, *J. Phys. Chem. Lett.* **2010**, *1*, 3371-3375.
[13]    A. A. Rachford, J. L. Petersen, J. J. Rack, *Inorg. Chem.* **2006**, *45*, 5953-5960.
[14]    J. J. Rack, J. R. Winkler, H. B. Gray, *J. Am. Chem. Soc.* **2001**, *123*, 2432-2433.
[15]    J. P. Sauvage, *Chem. Commun.* **2005**, 1507-1510.
[16]    V. Balzani, M. Clemente-Leon, A. Credi, B. Ferrer, M. Venturi, A. H. Flood, J. F. Stoddart, *Proc. Natl. Acad. Sci. U. S. A.* **2006**, *103*, 1178-1183.
[17]    U. C. Agrawal, H. L. Nigam, *J. Indian Chem. Soc.* **2008**, *85*, 677-690.
[18]    S. Campagna, F. Puntoriero, F. Nastasi, G. Bergamini, V. Balzani, *Photochemistry and Photophysics of Coordination Compounds I* **2007**, *280*, 117-214.
[19]    V. Balzani, A. Credi, M. Venturi, *Chem. Soc. Rev.* **2009**, *38*, 1542-1550.
[20]    S. Bonnet, J. P. Collin, M. Koizumi, P. Mobian, J. P. Sauvage, *Adv. Mater.* **2006**, *18*, 1239-1250.
[21]    S. Bonnet, J.-P. Collin, *Chem. Soc. Rev.* **2008**, *37*, 1207-1217.
[22]    J. P. Collin, V. Heitz, S. Bonnet, J. P. Sauvage, *Inorg. Chem. Commun.* **2005**, *8*, 1063-1074.
[23]    P. Mobian, J. M. Kern, J. P. Sauvage, *Angew. Chem. Int. Ed.* **2004**, *43*, 2392-2395.
[24]    A. C. Laemmel, J. P. Collin, J. P. Sauvage, *Eur. J. Inorg. Chem.* **1999**, 383-386.
[25]    P. J. Bednarski, F. S. Mackay, P. J. Sadler, *Anti-Cancer Agents Med. Chem.* **2007**, *7*, 75-93.
[26]    N. J. Farrer, L. Salassa, P. J. Sadler, *Dalton Trans.* **2009**, 10690-10701.
[27]    B. S. Howerton, D. K. Heidary, E. C. Glazer, *J. Am. Chem. Soc.* **2012**, *134*, 8324-8327.
[28]    E. Wachter, D. K. Heidary, B. S. Howerton, S. Parkin, E. C. Glazer, *Chem. Commun.* **2012**, *48*, 9649.
[29]    M. Indelli, C. Chiorboli, *Top. Curr. Chem.* **2007**, *280*, 215-255.
[30]    R. E. Mahnken, M. A. Billadeau, E. P. Nikonowicz, H. Morrison, *J. Am. Chem. Soc.* **1992**, *114*, 9253-9265.

[31]  U. Schatzschneider, J. Niesel, I. Ott, R. Gust, H. Alborzinia, S. Woelfl, *ChemMedChem* **2008**, *3*, 1104-1109.
[32]  R. E. Goldbach, I. Rodriguez-Garcia, J. H. van Lenthe, M. A. Siegler, S. Bonnet, *Chem. Eur. J.* **2011**, *17*, 9924-9929.
[33]  C. Moucheron, A. KirschDeMesmaeker, J. Kelly, *J. Photochem.* **1997**, *40*, 91-106.
[34]  S. L. H. Higgins, K. J. Brewer, *Angew. Chem., Int. Ed. Engl.* **2012**, *51*, 2-5.
[35]  R. N. Garner, J. C. Gallucci, K. R. Dunbar, C. Turro, *Inorg. Chem.* **2011**, *50*, 9213-9215.
[36]  A. G. De Candia, J. P. Marcolongo, R. Etchenique, L. D. Slep, *Inorg. Chem.* **2010**, 100625124914047.
[37]  L. Zayat, C. Calero, P. Albores, L. Baraldo, R. Etchenique, *J. Am. Chem. Soc.* **2003**, *125*, 882-883.
[38]  N. L. Fry, P. K. Mascharak, *Acc. Chem. Res.* **2011**, *44*, 289-298.
[39]  M. J. Rose, P. K. Mascharak, *Coord. Chem. Rev.* **2008**.
[40]  F. Barragán, P. López-Senín, L. Salassa, S. Betanzos-Lara, A. Habtemariam, V. Moreno, P. J. Sadler, V. Marchán, *J. Am. Chem. Soc.* **2011**.
[41]  L. Salassa, C. Garino, G. Salassa, R. Gobetto, C. Nervi, *J. Am. Chem. Soc.* **2008**, *130*, 9590-9597.
[42]  B. S. Howerton, D. K. Heidary, E. C. Glazer, *J. Am. Chem. Soc.* **2012**, *134*, 8324-8327.
[43]  T. Respondek, R. N. Garner, M. K. Herroon, I. Podgorski, C. Turro, J. J. Kodanko, *J. Am. Chem. Soc.* **2011**, *133*, 17164-17167.
[44]  D. A. Lutterman, P. K. L. Fu, C. Turro, *J. Am. Chem. Soc.* **2006**, *128*, 738-739.
[45]  V. Balzani, G. Bergamini, S. Campagna, F. Puntoriero, *Top. Curr. Chem.* **2007**, *280*, 1-36.
[46]  J. P. Paris, W. W. Brandt, *J. Am. Chem. Soc.* **1959**, *81*, 5001-5002.
[47]  C. P. Anderson, D. J. Salmon, T. J. Meyer, R. C. Young, *J. Am. Chem. Soc.* **1977**, *99*, 1980-1982.
[48]  J. Van Houten, R. J. Watts, *J. Am. Chem. Soc.* **1976**, *98*, 4853-4858.
[49]  B. Durham, J. V. Caspar, J. K. Nagle, T. J. Meyer, *J. Am. Chem. Soc.* **1982**, *104*, 4803-4810.
[50]  C. R. Hecker, P. E. Fanwick, D. R. McMillin, *Inorg. Chem.* **1991**, *30*, 659-666.
[51]  E. Baranoff, J. P. Collin, Y. Furusho, A. C. Laemmel, J. P. Sauvage, *Chem. Commun.* **2000**, 1935-1936.
[52]  B. Durham, J. L. Walsh, C. L. Carter, T. J. Meyer, *Inorg. Chem.* **1980**, *19*, 860-865.
[53]  S. Bonnet, J. P. Collin, N. Gruber, J. P. Sauvage, E. R. Schofield, *Dalton Trans.* **2003**, 4654-4662.
[54]  P. R. Ashton, R. Ballardini, V. Balzani, A. Credi, K. R. Dress, E. Ishow, C. J. Kleverlaan, O. Kocian, J. A. Preece, N. Spencer, J. F. Stoddart, M. Venturi, S. Wenger, *Chem. Eur. J.* **2000**, *6*, 3558-3574.
[55]  P. R. Ashton, R. Ballardini, V. Balzani, E. C. Constable, A. Credi, O. Kocian, S. J. Langford, J. A. Preece, L. Prodi, E. R. Schofield, N. Spencer, J. F. Stoddart, S. Wenger, *Chem. Eur. J.* **1998**, *4*, 2413-2422.
[56]  E. Baranoff, J. P. Collin, J. Furusho, Y. Furusho, A. C. Laemmel, J. P. Sauvage, *Inorg. Chem.* **2002**, *41*, 1215-1222.
[57]  P. Mobian, J. M. Kern, J. P. Sauvage, *J. Am. Chem. Soc.* **2003**, *125*, 2016-2017.
[58]  T. D. Nguyen, K. C. F. Leung, M. Liong, Y. Liu, J. F. Stoddart, J. I. Zink, *Adv. Funct. Mater.* **2007**, *17*, 2101-2110.
[59]  J. P. Collin, D. Jouvenot, M. Koizumi, J. P. Sauvage, *Inorg. Chem.* **2005**, *44*, 4693-4698.
[60]  S. Bonnet, J. P. Collin, P. Sauvage, *Inorg. Chem.* **2006**, *45*, 4024-4034.

[61]	T. Gianferrara, A. Bergamo, I. Bratsos, B. Milani, C. Spagnul, G. Sava, E. Alessio, *J. Med. Chem.* **2010**, *53*, 4678-4690.
[62]	S. Bonnet, J. P. Collin, J. P. Sauvage, E. Schofield, *Inorg. Chem.* **2004**, *43*, 8346-8354.
[63]	C. A. Bessel, J. A. Margarucci, J. H. Acquaye, R. S. Rubino, J. Crandall, A. J. Jircitano, K. J. Takeuchi, *Inorg. Chem.* **1993**, *32*, 5779-5784.
[64]	R. A. Leising, J. S. Ohman, K. J. Takeuchi, *Inorg. Chem.* **1988**, *27*, 3804-3809.
[65]	D. J. Wasylenko, C. Ganesamoorthy, B. D. Koivisto, M. A. Henderson, C. P. Berlinguette, *Inorg. Chem.* **2010**, *49*, 2202-2209.
[66]	C. M. Che, C. Ho, T. C. Lau, *J.Chem.Soc.,Dalton Trans.* **1991**, 1901-1907.
[67]	K. J. Takeuchi, M. S. Thompson, D. W. Pipes, T. J. Meyer, *Inorg. Chem.* **1984**, *23*, 1845-1851.
[68]	T. W. Swaddle, *Coord. Chem. Rev.* **1974**, *14*, 217-268.
[69]	B. Mahanti, G. S. De, *Transition Met. Chem.* **1994**, *19*, 201-204.
[70]	N. Aebischer, G. Laurenczy, A. Ludi, A. E. Merbach, *Inorg. Chem.* **1993**, *32*, 2810-2814.
[71]	N. Aebischer, R. Churlaud, L. Dolci, U. Frey, A. E. Merbach, *Inorg. Chem.* **1998**, *37*, 5915-5924.
[72]	F. P. Rotzinger, *J. Phys. Chem. A* **2000**, *104*, 8787-8795.
[73]	K. A. Bunten, D. H. Farrar, A. J. Poe, A. J. Lough, *Organometallics* **2000**, *19*, 3674-3682.
[74]	A. Czap, F. W. Heinemann, R. van Eldik, *Inorg. Chem.* **2004**, *43*, 7832-7843.
[75]	M. P. Gamasa, J. Gimeno, C. GonzalezBernardo, B. M. MartinVaca, D. Monti, M. Bassetti, *Organometallics* **1996**, *15*, 302-308.
[76]	T. Kojima, T. Morimoto, T. Sakamoto, S. Miyazaki, S. Fukuzumi, *Chem. Eur. J.* **2008**, *14*, 8904-8915.
[77]	A. Rilak, B. Petrovic, S. Grguric-Sipka, Z. Tesic, Z. D. Bugarcic, *Polyhedron* **2011**, *30*, 2339-2344.
[78]	A. M. Goswami, K. De, *Transition Met. Chem.* **2007**, *32*, 419-424.
[79]	M. M. Shoukry, M. R. Shehata, M. S. A. Hamza, R. van Eldik, *Dalton Trans.* **2005**, 3921-3926.
[80]	R. M. Naik, R. Singh, A. Asthana, *Int. J. Chem. Kinet.* **2011**, *43*, 21-30.
[81]	V. Thiel, M. Hendann, K.-J. Wannowius, H. Plenio, *J. Am. Chem. Soc.* **2012**, *134*, 1104-1114.
[82]	R. G. Wilkins, in *Kinetics and Mechanism of Reactions of Transition Metal Complexes*, 2nd ed., Wiley-VCH, Weinheim, **1991**, pp. 199-256.
[83]	C. H. Langford, W. R. Muir, *J. Am. Chem. Soc.* **1967**, *89*, 3141-3144.
[84]	A. Mukherjee, K. De, *Transition Met. Chem.* **2005**, *30*, 677-683.
[85]	R. Krishnan, R. H. Schultz, *Organometallics* **2001**, *20*, 3314-3322.
[86]	F. Wang, H. M. Chen, S. Parsons, L. D. H. Oswald, J. E. Davidson, P. J. Sadler, *Chem. Eur. J.* **2003**, *9*, 5810-5820.
[87]	R. A. Leising, S. A. Kubow, M. R. Churchill, L. A. Buttrey, J. W. Ziller, K. J. Takeuchi, *Inorg. Chem.* **1990**, *29*, 1306-1312.
[88]	E. C. Constable, K. R. Seddon, *Tetrahedron* **1983**, *39*, 291-295.
[89]	J. G. P. Calvert, J. N., *Chemical actinometer for the determination of ultraviolet light intensities. In Photochemistry*, Wiley and Sons, New York, **1967**; 780.

# 4

# Binding of a ruthenium complex to a thioether ligand embedded in a negatively charged lipid bilayer:

## a two-step mechanism
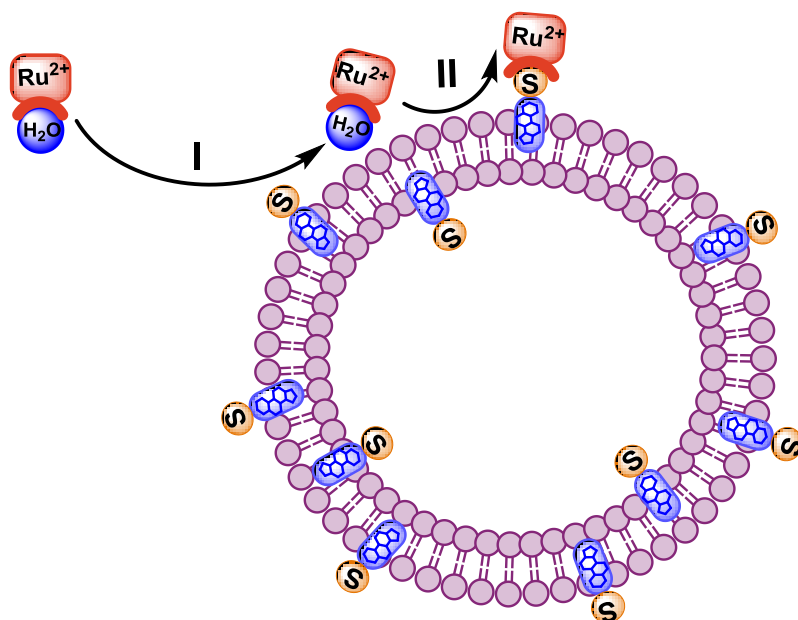
**Abstract**

The interactions between the ruthenium polypyridyl complex $[Ru(terpy)(dcbpy)(H_2O)]^{2+}$ (terpy=2,2';6',2"-terpyridine, dcbpy=6,6'-dichloro-2,2'-bipyridine) and phospholipid membranes containing either neutral thioether ligands or cholesterol were investigated using UV-visible spectroscopy, Langmuir-Blodgett monolayer surface pressure measurements, and Isothermal Titration Calorimety (ITC). The first technique shows that when embedded in a membrane a thioether ligand coordinates to the ruthenium complex only with negatively charged phospholipids, *i.e.,* in presence of attractive electrostatic interaction between the dicationic ruthenium center and the negatively charged phospholipid head groups. Lipid monolayer surface pressure and ITC measurements revealed that initial adsorption of the ruthenium aqua complex to the surface of negatively charged DMPG monolayers and bilayers is faster than coordination of the sulfur ligand to the metal. Unexpectedly this adsorption phenomenon is endothermic, thus entropy driven, and must result from dehydration of the ruthenium cations and phospholipid head groups. In the presence of thioether ligands, initial adsorption to the membrane is followed by two-dimensional diffusion ultimately leading to the formation of the Ru-S coordination bond. This two-step reaction is faster than the coordination of neutral thioether ligands to the same complex in homogeneous aqueous solutions. When an uncharged lipid bilayer is used, adsorption of the complex to the membrane is negligible and the coordination reaction does not occur.

## 4.1.    Introduction

Transition metal complexes, and in particular those involving second- and third-row metals like platinum, ruthenium, or gold, have been extensively studied as anticancer agents.[1] To explain their cytotoxicity, direct coordination of the metal complexes to the binding sites of biomolecules such as DNA[2-3] or proteins[4] has been proposed. Next to coordination, non-covalent interactions such as electrostatic force or/and intercalation may also play a role.[5] However, interpreting the mode of action of metallodrugs is often considered to be a challenge,[6] as cellular environments contain a striking diversity of ligands that may bind to metal complexes, such as proteins, enzymes, saccharides, or plasma membrane lipids. On the one hand, interactions of metallodrugs with non-targeted ligands may be the cause of drug resistance or non-selective toxicity. Phospholipids, in particular, have been reported as possible targets for platinum-based drugs,[7] whereas membrane proteins, which are formally ligands embedded in lipid bilayers, often govern influxes and effluxes of metal-based anticancer compounds. [4, 8-9] On the other hand, the metal-lipid affinity may be used as a tool to carry metallodrugs to its target using liposomes.[10-12] In this context, investigating the interactions of metal complexes with phospholipids or ligands embedded in lipid bilayers is crucial for understanding and controlling the therapeutic action of inorganic compounds.

The electrostatic interaction between phospholipids and metal cations, in particular alkali or alkaline earth metals like $Na^+$ and $Ca^{2+}$, have been extensively investigated.[13-25] However, to date very few studies report on the interaction of transition metal complexes with phospholipid membranes.[7, 26-32] Despite the growing number of ruthenium-based anticancer compounds their interaction with phospholipid membranes remains essentially unexplored, with the exception of a study on the adsorption of the highly charged  ruthenium red cations on phospholipid bilayers.[33] In all published studies, the role of electrostatic interaction between metal cations and negative phospholipids is only investigated from a thermodynamic point of view, and kinetics has been mostly ignored.

On our way to building artificial molecular machines based on polypyridyl ruthenium complexes[34] the reversible binding and light-induced unbinding of the ruthenium aqua complex $[Ru(terpy)(dcbpy)(H_2O)]^{2+}$ (terpy:2,2';6',2"-terpyridine, dcbpy: 6,6'-dichloro-2,2'-bipyridine) to thioether ligands embedded in negatively charged phospholipid

bilayers was demonstrated in Chapter 2 (Figure 4.1). In these studies, it was observed that whereas coordination of neutral thioether ligands to ruthenium aqua complexes occurred in homogenous aqueous solution, incorporating the thioether ligand in a lipid bilayer had strong influence on the coordination reaction, which becomes highly dependent on the charge of the membrane. Centrifugation experiments showed that positively charged ruthenium aqua complexes interact significantly with negatively charged lipid bilayers, irrespective whether or not the thioether-cholesterol ligand was present.[34]

In the present Chapter UV-vis spectroscopy, Langmuir-Blodgett monolayer surface pressure measurements, and calorimetric methods were used to investigate the time scale and thermodynamics of the adsorption of the ruthenium complex to the lipid membranes, and to see whether adsorption and coordination of the membrane-embedded ligands to the metal occur simultaneously or sequentially. A two-step mechanism for the binding of ruthenium complexes to membrane-embedded thioether ligands is proposed.
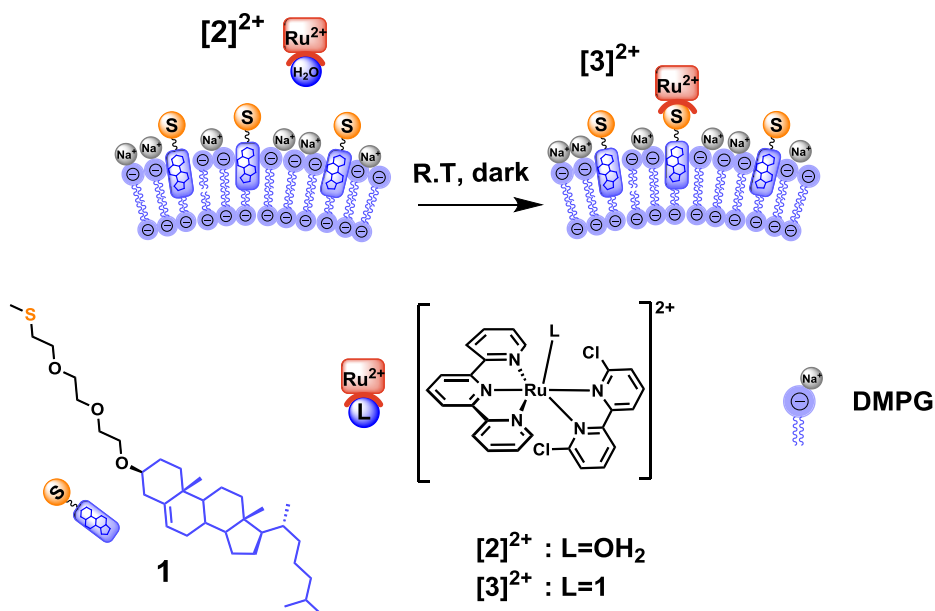


**Figure 4.1.** Cartoon representing the thermal binding of the ruthenium aqua complex $[2]^{2+}$ to a DMPG (1,2-dimyristoyl-*sn*-glycero-3-phospho-(1'-rac-glycerol) (sodium salt)) lipid bilayer containing ligand **1**, to give the thioether complex $[3]^{2+}$. Not all sodium cations are shown for clarity.

## 4.2. Results

### 4.2.1. UV-vis experiments

UV-vis experiments were performed in order to check the influence of the electrostatic interaction between liposomes and ruthenium complexes on the rate of the coordination reaction at the membrane surface. The kinetics of the coordination of thioether-cholesterol ligand **1** inserted in negatively charged DMPG (DMPG=1,2-dimyristoyl-*sn*-glycero-3-phospho-(1'-rac-glycerol) sodium salt) liposomes to the ruthenium complex [Ru(terpy)(dcbpy)(H$_2$O)]$^{2+}$ (compound [**2**]$^{2+}$) was investigated in buffer solutions with different ionic strengths at 298 K and in the dark (Figure 4.1). Liposomes decorated with 25 mol% ligand **1** with diameter of 140 nm were prepared as characterized by dynamic light scattering (DLS). After addition of 5 mol% of the aqua ruthenium complex [**2**]$^{2+}$ the UV-vis spectrum of the liposome solution gradually evolved and an equilibrium was obtained after several hours. The liposomes were stable during the reaction and did not show any sign of aggregation or fusion at the end of the reaction as confirmed by DLS. The absorbance at 500 nm decreased exponentially over time (see Figure 4.2b-I, for *I*=50 mM), which allowed for determining the half reaction time ($t_{1/2}$) for the coordination reaction. The plot of $t_{1/2}$ *vs.* the ionic strength I of the buffer solution is shown in Figure 4.2a. As expected, the half-reaction time increased almost linearly with *I*, *i e.*, the ligand substitution became slower when the electrostatic interaction between the ruthenium dications and the negative liposomes was shielded by the other ions present in solution. Interestingly, the coordination reaction at the surface of negatively charged membranes is significantly faster than that in homogenous aqueous solution using thioether ligands not bound to liposomes. The kinetics for the coordination of the water-soluble thioether ligand 2-(methylthio)ethanol (Hmte) to [**2**]$^{2+}$ was already reported in Chapter 2 and follows a second-order rate law with a second-order rate constant $2.3 \times 10^{-2}$ M$^{-1}$·s$^{-1}$ at 297 K. However, with the low concentration used (*i.e.*, 0.3 mM for Hmte and 0.067 mM for [**2**]$^{2+}$) the coordination rate in a *I*=50 mM buffer solution is very low as $t_{1/2}$ is over 68 h (Figure 4.2a-IV) while the coordination at DMPG membranes showed to have $t_{1/2}$~2.6 h (see Figure 4.2a-I).

To prove that the charge of the liposome is the major factor controlling the kinetics of the coordination, two control experiments were performed. In the first experiment, the coordination reaction was performed using another negatively charged lipid 1,2-

dioleoyl-*sn*-glycero-3-phospho-(1'-rac-glycerol) sodium salt (hereafter DOPG)). DOPG liposomes containing 25 mol% ligand **1** were mixed with 5 mol% [**2**]$^{2+}$ in the dark. As shown in Figure 4.2b-II, the kinetics of the reaction with DOPG is almost the same as that with DMPG liposomes, in a buffer with *I*=50 mM ($t_{1/2}$ =154 min and 160 min, respectively). Thus, the kinetics of the reaction are almost the same for two different negatively charged liposomes. A second control experiment was performed with non-charged liposomes to check the influence of hydrophobic interactions. Neutral liposomes made of DOPC (DOPC=1,2-dioleoyl-*sn*-glycero-3-phosphocholine) and functionalized with the same amount of ligand **1** (25 mol%) were prepared. After addition of [**2**]$^{2+}$ the UV-vis spectrum of the solution remained unchanged at least for 20 hours in the dark, which is longer than the longest experiment (*I*~1000 mM) realized with DMPG liposomes (Figure 4.2b-III). Overall, These experiments confirm that the electrostatic interaction between the ruthenium complex and the surface of the lipid bilayer is crucial for the binding of the Ru(II) cations to the sulfur atom of ligand **1** embedded in a lipid bilayer.
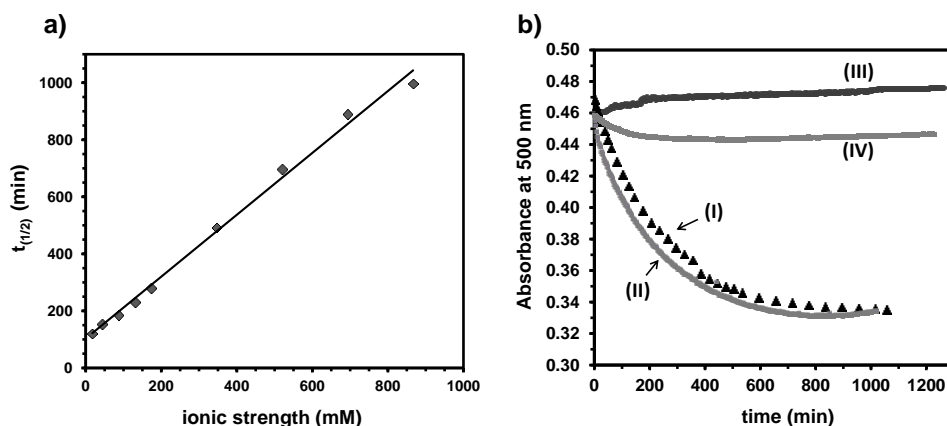


**Figure 4.2.** a) Plot of the half reaction time $t_{1/2}$ *vs.* the total ionic strength *I* of the buffer for the thermal binding of aqua complex [**2**](PF$_6$)$_2$ to ligand **1** incorporated in DMPG liposomes.  b) Time evolution of the absorbance at 500 nm for a solution containing (I) DMPG, (II) DOPG, (III) DOPC liposomes containing 25 mol% of ligand **1**, or (IV) Hmte (no liposome), after addition of [**2**](PF$_6$)$_2$ at *t*=0, using a 10 mM phosphate buffer at pH=7 with a total ionic strength of 50 mM.  Conditions for a) and b): in the dark, *T* = 298 K, total concentration of [**2**]$^{2+}$=0.067 mM, bulk concentration of ligand **1** or Hmte=0.3 mM in all samples, lipid concentration= 1.3 mM (as liposomes in plot b-IV lipid concentration is 0 mM).

In all these experiments however, UV-vis spectroscopy could only probe changes occurring in the coordination sphere of the metal center. It does not allow for studying changes in the environment of the complex that would not involve ligand exchange, such as for example the adsorption of the ruthenium aqua complex at the water-bilayer interface. Two other experimental techniques, *i.e,* surface pressure measurements on lipid monolayers, and Isothermal Titration Calorimetry (ITC) were used to gain insight into the adsorption step.

## 4.2.2. Langmiur-Blodgett monolayer experiments

Langmuir monolayers are composed of amphiphilic molecules self-assembled at the air/water interface. The interaction of these monolayers with molecules dissolved in the aqueous subphase can be probed by measuring changes of the surface pressure ($\Delta\Pi$) of the monolayer by means of a platinum Wilhelmy plate. Langmuir monolayers are recognized as a good model for one leaflet of a lipid bilayer,[35] surface pressure measurements were performed to study the interaction of the ruthenium complex $[2]^{2+}$ with negatively charged and zwitterionic lipid monolayers at the buffer/lipid interphase. First, four types of lipid monolayers were prepared at the air/buffer interface using DMPG, DMPG containing 25 mol% of ligand **1**, DMPC, and DMPC containing 25 mol% of ligand **1** lipid mixtures. Stock solutions of the lipids were spread onto the phosphate buffer subphase ($I$=50 mM, pH=7, $T$=298 K) and the monolayer was compressed at a constant rate. Upon compression, the surface pressure ($\Pi$) was measured as a function of the area of water surface available to each lipid molecule ($A$). The surface pressure-area ($\Pi$-$A$) isotherms that were obtained for each sample (see Appendix IV, Figure AIV.1); were in good agreement with previously reported data for DMPG and DMPC monolayers.[36-38] Addition of the thioether-cholesterol ligand **1** to the lipid compositions shifted the $\Pi$-$A$ isotherms to lower molecular areas compared to pure DMPG or DMPC, which indicates to a slightly better packing of the monolayer at the air-buffer subphase in presence of **1**.

In a second series of experiments, lipid monolayers of DMPG containing 25 mol% of ligand **1** were prepared on the phosphate subphase at a constant surface pressure, at 298 K and in the dark. After equilibration a buffered solution of $[2]^{2+}$ was injected into the subphase underneath the lipid film, and the resulting change in surface pressure was recorded as a function of time in the dark. As shown in Figure 4.3a-II after injection of

$[\mathbf{2}]^{2+}$ an increase in the surface pressure takes place within 6-7 min, to reach an equilibrium at a slightly higher pressure. The observed evolution time scale is too short for ligand coordination to the ruthenium complex to be completed (see Figure 4.2b-I). Furthermore, a control experiment was performed using cholesterol as additive instead of ligand **1**. For such sulfur-deprived DMPG monolayers the surface pressure also increased within a couple of minutes after injection of $[\mathbf{2}]^{2+}$, and $\Delta\Pi$ was roughly identical to that observed for the DMPG sample containing ligand **1** (Figure 4.3a-I). Thus, the observed increase of $\Pi$ cannot be caused by sulfur coordination to the metal.
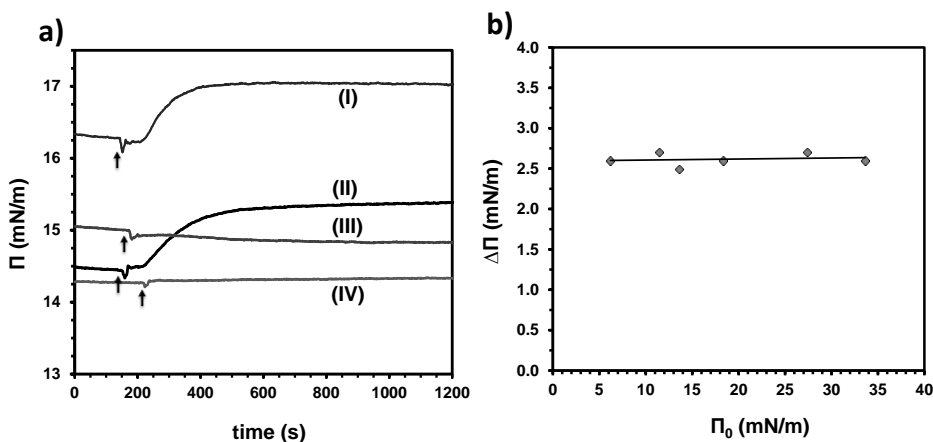


**Figure 4.3.** a)Plots of surface pressure *vs.* time for phospholipid monolayers after injection of $[\mathbf{2}]^{2+}$ (final concentration= 0.5 μM) into a buffer subphase. (I) DMPG and 25 mol % cholesterol (*I*=50 mM), (II) DMPG and 25 mol% ligand **1** (*I*=50 mM), (III) DMPG and 25 mol% ligand **1** (*I*=400 mM), (IV) DMPC and 25 mol% ligand **1** (*I*=50 mM). Each arrow represents an injection of 50 μL of $[\mathbf{2}]^{2+}$, Conditions: concentration of $[\mathbf{2}]^{2+}$ in the stock solution = 0.65 mM, *T*=298 K, pH=7.0, volume of the trough: 65 mL. b) Plot of the surface pressure variation $\Delta\Pi$ as a function of the initial surface pressure $\Pi_0$ for data obtained for DMPG monolayers containing 25 mol% ligand **1** after injection of $[\mathbf{2}]^{2+}$ (final concentration=3.5 μM) in a buffer subphase at different initial surface pressure $\Pi_0$. Condition: 10 mM phosphate buffer, total ionic strength=50 mM, concentration of $[\mathbf{2}]^{2+}$ in the stock solution=2.3 mM, *T*=298 K.

Consecutive injection of $[\mathbf{2}]^{2+}$ to the buffer subphase of DMPG monolayers containing either cholesterol or ligand **1** ($\Pi_0$=14 mN/m ) showed a total surface pressure variation ($\Delta\Pi$) of about 6 mN/m at saturation condition (see Figure AIV.2). Such a surface pressure variation $\Delta\Pi$ was small compared to those reported for penetrating peptides, enzymes, or other lipophilic macromolecules interacting with lipid monolayers, where $\Delta\Pi$ is usually higher than 10 mN/m.[39-45] This qualitative comparison suggested that

insertion of the metal complex into the membrane was limited. Such a conclusion was confirmed by another experiment showing that the surface pressure variation $\Delta\Pi$ was independent of the initial surface pressure of the monolayer, $\Pi_0$. When DMPG monolayers containing 25 mol% of ligand **1** at various initial surface pressures were prepared, in all cases injection of $[\mathbf{2}]^{2+}$ (final concentration:3.5 μM) to the subphase led to equal surface pressure increase ($\Delta\Pi$=2.6 mN/m, see Figure AIV.4). As shown in Figure 4.3b, the slope of the plot of $\Delta\Pi$ *vs.* $\Pi_0$ is almost zero, which is differs from the behavior of hydrophobic macromolecules that penetrate the hydrophobic core of the monolayer. In such cases, $\Delta\Pi$ typically decreases when the initial surface pressure $\Pi_0$ becomes higher,[39-40, 46-48] In fact, the affinity of $[\mathbf{2}]^{2+}$ for the DMPG monolayer is not high. It can be assumed that the ruthenium complex does not penetrate into the lipid monolayer, but rather migrates at the monolayer-water interface and adsorbs to the polar head groups of the phospholipids.[24, 48-49]

In order to investigate whether the incidence of the adsorption process is due to electrostatic or hydrophobic interactions, two control experiments were performed. In the first experiment, a DMPG monolayer containing ligand **1** was formed onto a buffer subphase with a high ionic strength ($I$=400 mM instead of 50 mM). As shown in Figure 4.3a-III, injections of $[\mathbf{2}]^{2+}$ in the subphase did not affect the surface pressure of the monolayer. Thus, adsorption of the positively charged ruthenium complex at the surface of the DMPG monolayer does not occur when the ionic strength of the subphase is high, which is in good agreement with the UV-vis data and highlights the role played by electrostatic interaction in the adsorption process. The second control consisted in replacing the DMPG lipid by the zwitterionic analogue DMPC. In presence of 25 mol% of ligand **1** in a DMPC monolayer no measurable variation of the surface pressure was observed after injection of complex $[\mathbf{2}]^{2+}$ (Figure 4.3a-IV), which proves the low affinity of the ruthenium complex for the zwitterionic monolayer surface. In addition, it confirms the low hydrophobicity of the ruthenium complex $[\mathbf{2}]^{2+}$ that does not penetrate into the membrane. Overall, our data support the hypothesis that electrostatic forces are crucial for the adsorption of the ruthenium complex at negatively charged membranes and that hydrophobic force does not play a significant role.

### 4.2.3.   ITC experiments

Surface pressure experiments allow for studying the initial adsorption of ruthenium complexes to negatively charged monolayers before the coordination occurs. Considering the fast kinetics of the adsorption process on monolayers ITC measurements were used to determine the thermodynamic parameters characterizing the adsorption of complex $[\mathbf{2}]^{2+}$ at the surface of the lipid bilayers. Titrations of DMPG liposomes supplemented with 25 mol% cholesterol or ligand **1** by a 0.62 mM solution of complex $[\mathbf{2}]^{2+}$ were performed at 298 K, pH=7, and $I$=50 mM. After each ruthenium addition, the return to equilibrium took less than 100s, which confirms that the adsorption step is characterized by fast kinetics, in accordance with the results obtained for the monolayer experiments. As mentioned above, such time scales are significantly shorter than that of the coordination of ligand **1** to complex $[\mathbf{2}]^{2+}$ at the DMPG membrane. In addition the adsorption phenomenon observed by titration of DMPG liposomes containing ligand **1** was found to be endothermic (Figure 4.4-II). For DMPG membranes containing cholesterol an exothermic process was observed during the initial injections of $[\mathbf{2}]^{2+}$, but further addition of $[\mathbf{2}]^{2+}$ led only to an endothermic process similar to that observed with ligand **1** (Figure 4.4-I). The initial exothermic evolution may be related to structural changes in the negatively charged lipid bilayer due to the interaction of a small amount of divalent cations with the cholesterol and/or the DMPG lipids, as reported for $Ca^{2+}$.[16, 50]

Two control titrations with $[\mathbf{2}]^{2+}$ were made, on the one hand for DMPG liposomes containing 25 mol% cholesterol in presence of a high ionic strength buffer ($I$=400 mM), and on the other hand of zwitterionic DOPC liposomes containing 25 mol% cholesterol using a buffer with $I$=50 mM. The measured heat exchange was negligible in high ionic strength buffer (see plots III and II in Figure 4.4b), and in the case of the DOPC liposomes the heat exchange was even comparable with the heat exchange observed in absence of liposomes. Overall, the results of the ITC measurements are in good agreement with those obtained with UV-vis and surface pressure monolayer experiments. They confirm that adsorption of the ruthenium complexes to negatively charged membranes is a fast process that does not involve coordination to sulfur.

**Table 4.1.** Thermodynamic data for the adsorption of [**2**]Cl$_2$ to DMPG liposomes. Conditions: buffer with $I$=50 mM, pH=7 and 298 K, Concentrations: *[lipid]*=2.5 mM, [**2**]Cl$_2$ in titrating solution:5 mM.

| Bilayer additive | Apparent $K_a$ (M$^{-1}$) | $\Delta H°$ (kJ·mol$^{-1}$) | $\Delta G°$ (kJ·mol$^{-1}$) | $\Delta S°$ (kJ·mol$^{-1}$·K$^{-1}$) | binding stoichiometry (Ru/lipid ratio) n |
|---|---|---|---|---|---|
| Ligand **1** (25 mol%) | 1.8(3)×10$^{+4}$ | +9.1 ±0.3 | −24 | +112 | 0.28±0.01 |
| cholesterol (25 mol%) | 9.2(10)×10$^{+3}$ | +24±1 | −23 | +160 | 0.19 ±0.01 |

Due to the low solubility of [**2**](PF$_6$)$_2$ in the buffer saturation of the DMPG liposomes with ruthenium cations could not be reached (Figure 4.4-II). As a consequence, the fit of the model to the experimental data did not give reliable binding parameters. Thus, the counter ions of [**2**]$^{2+}$ were changed to chlorides, which allowed to reach much higher ruthenium concentrations (5 mM) and thus for obtaining quantitative information on the thermodynamics of the adsorption process. By dissolving [Ru(tpy)(dcbpy)(Cl)]Cl in an aqueous solution, the coordinated chloride ligand is quickly substituted by an aqua ligand to form [**2**]Cl$_2$ quantitatively (see Chapter 2 and 3). Changing the counter ions from PF$_6^-$ to Cl$^-$ had a negligible influence on monolayer experiments and ITC data at low ruthenium concentrations (0.62 mM, see Appendix AIV, Figure AIV.5 and Table AIV.1). Titrations of DMPG liposomes containing ligand 25 mol% ligand **1** or cholesterol were undertaken with more concentrated (5 mM) solutions of [**2**]$^{2+}$ and more concentrated liposome solutions (lipid concentration: 2.5 mM). Sigmoidal binding curves were obtained, showing that in such conditions saturation of the membrane with ruthenium cations could be reached (Figure 4.4-V and II).
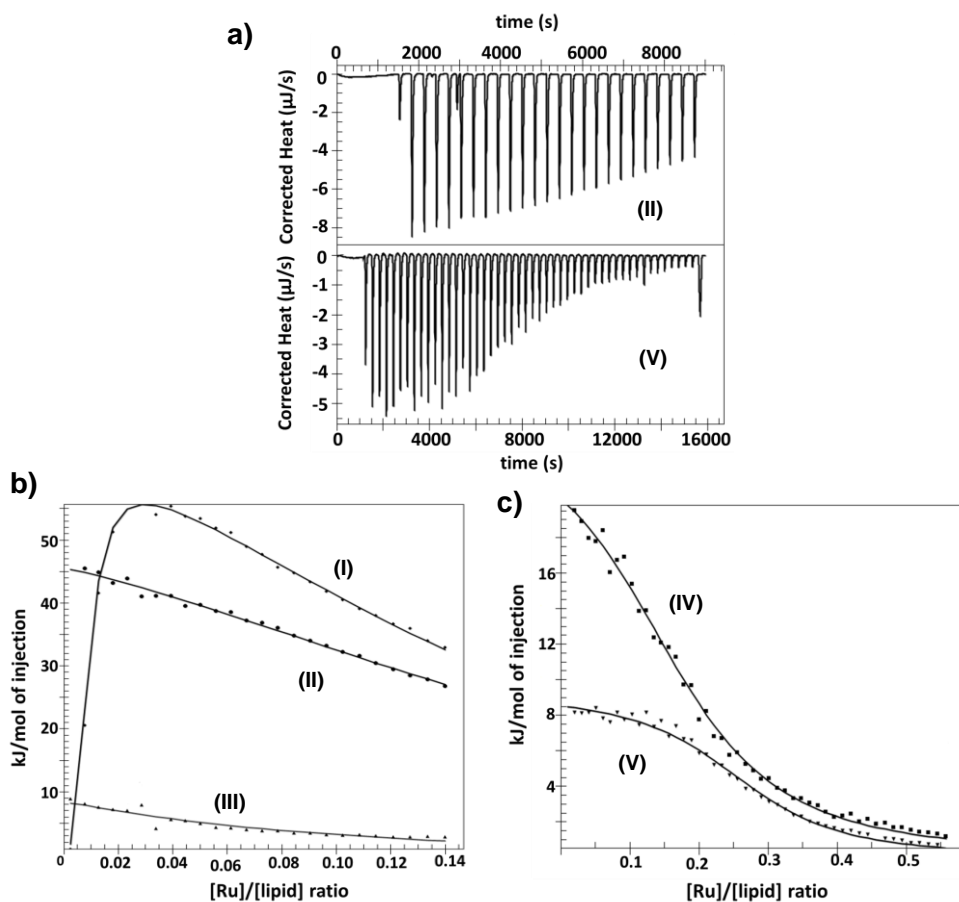
**Figure 4.4.** Representative binding isotherms obtained upon titration of liposomes with [**2**]$^{2+}$ in phosphate buffer at pH=7.0 and 298 K. a) Heat pulses per injection of 10 μL [**2**](PF$_6$)$_2$ (II) or 5 μL of [**2**]Cl$_2$ (V) to a liposome solution containing DMPG and 25 mol% ligand **1**. b) and c) corresponding integrated areas (points) and best fitted isotherms; x axis shows the molar ratio between total added ruthenium concentration *[Ru]* and the total lipid concentration *[lipid]* in the solution. Conditions: (I) DMPG and 25 mol% cholesterol (*[lipid]*=1.3 mM, concentration of [**2**](PF$_6$)$_2$ in titrating solution:0.62 mM, *I*=50 mM), (II) DMPG and 25 mol% ligand **1** (*[lipid]*=1.3 mM, concentration of [**2**](PF$_6$)$_2$ in titrating solution:0.62 mM, *I*=50 mM), (III) DMPG and 25 mol% cholesterol (*[lipid]*=1.3 mM, concentration of [**2**](PF$_6$)$_2$ in titrating solution:0.62 mM, *I*=400 mM), (IV) DMPG and 25 mol% cholesterol (*[lipid]*=2.5 mM, concentration of [**2**]Cl$_2$ in titrating solution:5 mM, *I*=50 mM), and (V) DMPG and 25 mol% ligand **1** (*[lipid]*=2.5 mM, concentration of [**2**]Cl$_2$ in titrating solution:5 mM, *I*=50 mM).

Unlike at lower concentrations the cholesterol-containing DMPG liposomes were found to behave very similarly to DMPG liposomes containing ligand **1**, and only an endothermic adsorption process was observed. Line-fitting of the sigmoidal binding

curves to a single set of $n$ identical binding sites provided the adsorption enthalpy ($\Delta H°$), affinity constant ($K_a$), and binding stoichiometry ($n$), from which the adsorption free energy ($\Delta G°$) and entropy ($\Delta S°$) could be derived (Table 4.1).

For both systems $\Delta H°$ and $\Delta S°$ were found to be positive, while $\Delta G°$ was negative. Thus, the adsorption of the ruthenium complex to the DMPG bilayer is endothermic and driven by entropy. Presumably, the entropy gain upon adsorption is due to the release of water molecules and counter ions ($Na^+$ ions) when the ruthenium dications come into contact with the phospholipid head groups.[51-55] This interpretation is consistent with monolayer surface pressure experiments, as the surface pressure increased upon adsorption of the complex. Such an increase advocates for the disruption of the hydrogen bonding network between the water molecules and the polar heads of the phospholipids, which must significantly contribute to the overall unfavorable adsorption enthalpy measured by ITC. In addition, comparison between the binding stoichiometry values $n$ obtained for the two systems containing cholesterol or ligand **1** revealed that about 5 or 4 lipid molecules, respectively, are bound for each ruthenium complex when saturation of the DMPG liposomes is reached. Since only the outer leaflet of the lipid bilayer is available for adsorption of the ruthenium complex ion, the apparent Ru/lipid ratio at saturation is 2.5 or 2 lipid molecules per ruthenium for cholesterol and ligand **1**, respectively. This stoichiometry almost fits with two monoanionic lipid molecules for one dicationic ruthenium complex, *i.e.,* at saturation of the liposome surface all the initial $Na^+$ counter cations have been replaced by dicationic ruthenium complexes at the membrane surface. Apparent binding constant values (see Table 4.1) are very close for both systems and rather low, which highlights that sulfur coordination to the ruthenium does not play a significant role at the time scale of these experiments, and that it is mostly the electrostatic adsorption onto the membrane that is actually monitored.

## 4.3.  Discussion

According to our results binding of the ruthenium complex [**2**]$^{2+}$ to ligand **1** embedded in a negatively charged liposome occurs *via* a two-step mechanism. As proposed in Scheme 4.1, the outer leaflet of the negatively charged lipid bilayer can be regarded as a "heterogeneous" surface, which first adsorbs ruthenium complexes with fast kinetics (minutes). In a second, slower step (hours), the ruthenium complex [**2**]$^{2+}$ undergoes a thermal ligand substitution reaction at the membrane surface, during which the $H_2O$

ligand is replaced by ligand **1** to form the Ru-S coordination bond ($[\mathbf{3}]^{2+}$). In this model coordination of the sulfur ligand to the metal center occurs *via* two-dimensional diffusion of both the ligand and the metal complex at the membrane surface. Metal binding to ligands embedded in a negatively charged membrane is faster than in homogeneous systems because the fast electrostatic adsorption of the complex to the negative surface of the lipid bilayer increases the local ruthenium concentration near the thioether ligands, *i.e.*, in the electrostatic double layer.[50, 56] Counter-intuitively, the initial adsorption step is not enthalpy driven, because the energy gained by the approach of the dicationic ruthenium center to the negatively charged bilayer must be paid back by removing two monocationic sodium ions. As a result, the adsorption is driven by entropy and occurs *via* dehydration of the phosphate head groups and of the ruthenium dications, and re solvation of the $Na^+$ monocations. With neutral lipids, *i.e.*, in the absence of electrostatic interaction, hydrophobic interactions are very weak and adsorption does not proceed. Thus, the ruthenium concentration in the electrical double layer, where most of the sulfur ligands are concentrated, remains low, which hampers the coordination reaction.
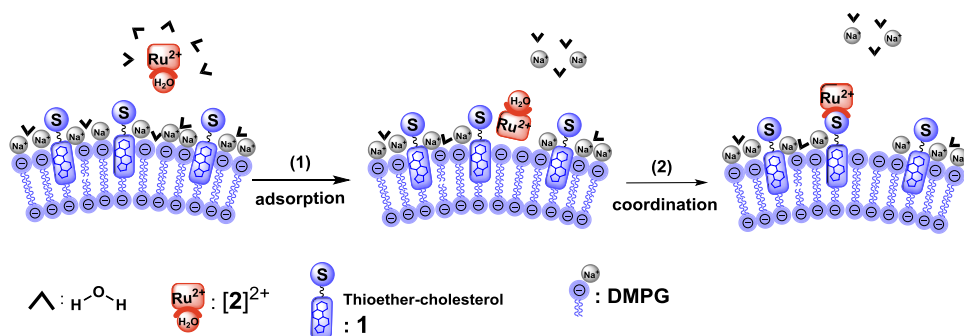


**Scheme 4.1.** A two-steps model for the thermal binding of the metal complex $[\mathbf{2}]^{2+}$ to ligand **1** embedded in a negatively charged membrane. Step (1): adsorption; step (2): ligand substitution at the water-membrane interface.

Although the charge of metal cations is an important parameter for their adsorption to lipid bilayers, other parameters such as the type of metal cation, the ligands that may be coordinated to it, the number of coordination sites available, and also the surrounding environment (ionic force, pH, *etc.*), all can have a strong influence on the adsorption process. The metal-phospholipid interaction differs from case to case, even when similar divalent cations like $Ca^{2+}$ and $Mg^{2+}$ are used with the same phospholipid.[23-24,

[57-60] Furthermore, upon changing the nature of the lipids the adsorption driving force for a given metal cation may change as well. In a study by Blume *et al.* [61] large negative enthalpies were obtained upon addition of $CaCl_2$ to DMPG liposomes, which was interpreted as a phase transition occurring in the membrane upon adsorption of $Ca^{2+}$.[53] This interpretation may be relevant to our observations when very low concentrations in [**2**]$^{2+}$ (~0.03 mM) come into contact with DMPG liposomes containing cholesterol (1.3 mM, Figure 4.4-I). In contrast, Dimova *et al.*[50] reported the endothermic adsorption of $Ca^{2+}$ ions to mixed neutral/negative liposomes, which is similar to the behavior of higher concentrations in [**2**]$^{2+}$ adsorbing on DMPG membranes. Finally, membrane fusion or aggregation does not occur upon addition of [**2**]$^{2+}$ to DOPC, DOPG, DMPG, or DMPC membranes, whereas it is a common phenomenon in presence of $Ca^{2+}$ or other divalent cations.[62-63] In spite of their identical charge $Ca^{2+}$ and the Ru(II) complex [**2**]$^{2+}$ are quite different, as the latter is surrounded with large, hydrophobic polypyridyl ligands, and has only one potentially available coordination site. Overall, the interaction between metal complex ions and phospholipid membranes appears to comprise a delicate balance between electrostatics, hydrophobic forces, and coordination. In the case of [**2**]$^{2+}$ and ligand **1** neither phase changes, nor vesicle aggregation take place, but simply the fast, entropy-driven adsorption of the cation at the water-membrane interface.

## 4.4. Conclusion

Using three different techniques, the present study distinguishes for the first time the time scales for the adsorption of a dicationic coordination compound on a negatively charged membrane, and the coordination of a membrane-embedded sulfur ligand to the metal center. These results have two major consequences. First, a sequential, two-step model is proposed for the binding of the metal complex to the membrane-embedded ligands. The outer leaflet of a negatively charged lipid bilayer is a surface which quickly adsorbs positively charged metal complexes such as [**2**]$^{2+}$. Any slower coordination event will thus take place subsequently, *via* diffusion of both reagents in the two dimensions of the membrane. The relevance of this model for late transition metallodrugs binding to membrane proteins will need to be evaluated.

Secondly, when studying the interaction of metallodrugs with large, negatively charged biomolecules such as DNA, proteins, or lipid membranes, electrostatic interaction may be strong enough to keep the metal complexes in close proximity to the biomolecules

even in absence of coordination to the metal center, which may take place at much longer time scales. In other words, studying the interactions between metal complexes and biomolecules by precipitation or centrifugation experiments, *i e.,* by experimental methods involving short time scales, may conclude to metal-ligand "binding", whereas, formation of the coordination bond between the metal center and the biological ligand did, actually, not occur. This fact should be taken into consideration in future studies looking at the fate of metallodrugs in a biomimetic or biological environment.

## 4.5. Experimental Section

### 4.5.1. General

The thioether-cholesterol ligand **1** and the aqua ruthenium complex [**2**]$(PF_6)_2$ were synthesized as reported in Chapter 2. 2-Dimyristoyl-*sn*-glycero-3-phosphoglycerol Sodium salt (DMPG), 1,2-dimyristoyl-*sn*-glycero-3-phosphocholine (DMPC), 1,2-dioleoyl-*sn*-glycero-3-phosphocholine (DOPC), and 1,2-dioleoyl-*sn*-glycero-3-phospho-(1'-rac-glycerol) sodium salt (DOPG) were obtained from Avanti Polar Lipids or Lipoid and stored at −20 °C. Cholesterol, $K_2HPO_4$, $K_2HPO_4$, and $K_2SO_4$ were obtained from commercial sources and used as received. A Perkin-Elmer Lambda 900 UV-vis spectrometer equipped with stirring and temperature control was used for UV-vis measurements. Liposomes size distributions were determined by dynamic light scattering in a Zetasizer (Malvern Instruments Ltd.,U.K.), operated at a wavelength of 633 nm. A KSV Instrument equipped with a 230 mL or 60 mL trough was used for Langmuir monolayer measurements. A NanoITC-2G instrument (TA Instruments, Delaware, USA) with a 1 mL titration cell was used to perform ITC experiments.

### 4.5.2. Phosphate buffer preparation

Phosphate buffers at pH=7.0 with ionic strengths of 20, 50, 100, 150, 200, 400, 600, 800, and 1000 mM were prepared by dissolving phosphate salts of $KH_2PO_4$ and $K_2HPO_4$ (total phosphate salt: 0.90 mmol) and 0.0, 0.97, 2.6, 4.6, 5.9, 12.5, 19.2, 26.0, or 32.5 mmol of $K_2SO_4$ , respectively, in 100 mL Milli-Q water at 298 K.

### 4.5.3. Liposome preparation

The lipid (5.0 μmol) and ligand **1** or cholesterol (1.25 μmol) were mixed from chloroform (DOPC, DOPG) or chloroform/methanol 4:1 (DMPG) stock solutions, and dried under reduced pressure using rotary evaporation. The lipid films were subsequently placed under vacuum for at least 1 h to remove traces of organic solvents, and then hydrated in a

phosphate buffer with a desired ionic strength at pH 7.0. The final concentration of the lipids was 2.5 mM. The lipid suspensions were freeze-thawed 10 times above the transition temperature of the corresponding lipid (from liquid $N_2$ temperature to 323 K), and then extruded 11 times above the transition temperature of the lipid by using an Avanti mini-extruder and polycarbonate membranes with 200 nm pore diameter. The size distribution of the liposomes was measured by DLS to give a value centered between 130 and 150 nm. The samples were kept at 277 K and used within 10 days.

### 4.5.4. UV-vis measurements

A liposome sample (1.6 mL) containing DMPG, DOPG, or DOPC (2.5 mM) and ligand **1** (25 mol%, 0.62 mM) in a buffer solution (ionic strength: 20, 50, 100, 150, 200, 400, 600, 800, or 1000 mM, pH=7.0), or a solution of Hmte in a buffer with $I$=50 mM (Hmte concentration: 0.62 mM) was placed into a UV-vis cell. 1 mL of the corresponding buffer solution was added to the cuvette and at $t$=0 the volume of the cell was completed by adding [**2**]$^{2+}$ in MilliQ (0.4 mL, 0.5 mM stock solution; ratio [**2**]$^{2+}$/ligand **1**= 0.5). The final concentrations of the lipid, sulfur ligand, and [**2**]$^{2+}$ in the cell were 1.3 mM and 0.3 mM, and 0.067 mM, respectively. The initial absorbance of the sample at 496 nm after base-line correction (subtraction of the absorbance of a liposome sample containing 25 mol% ligand **1** and without ruthenium) was typically 0.46. The sample was stirred in the dark overnight while UV-vis spectra were measured every 3 min, until the thermal equilibrium was reached. The final absorption maximum at 473 nm indicates the formation of complex [**3**]$^{2+}$. The plot of $ln((A_0-A_{inf})/(A_t-A_{inf}))$ *vs.* time was obtained ($A_0$=Absorbance at $t$=0, $A_t$=Absorbance at time t, and $A_{inf}$= absorbance at equilibrium time "$t_{inf}$", all absorbance values measured at λ=500 nm), and the slope of the plot corresponded to the rate constant ($k$). The half reaction time for each reaction was obtained using the equation $t_{1/2}=ln(2)/k$.

### 4.5.5. Langmuir monolayer

All the measurements were performed at pH=7.0 and 298 K. The Teflon troughs and platinum Wilhelmy plate were cleaned properly using cleaning instructions prior to use. Hamilton syringes (25 μL, 50 μL, or 100 μL) were used for monolayer spreading and ruthenium injections.

### 4.5.6. Surface Pressure-Mean Molecular Area Compression Isotherms

Compression isotherms were carried out on a KSV (U.K.) Langmuir teflon trough (area 24300 mm$^2$, volume 230 mL). The pure lipid or lipid-ligand spreading solutions were prepared by mixing appropriate volumes of chloroform or chloroform/methanol (4:1) stock

solutions of phospholipids (1 mg/mL) and of ligand **1** or cholesterol (1 mg/mL). Monolayers were formed by depositing small drops of the spreading solutions on the phosphate buffer subphase (pH=7.0, *T*=298 K) with a 25 µL Hamilton microsyringe. For a maximum molecular area of 180 Å$^2$/molecule, around 15 µL of each lipid solution was spread onto the buffer subphase. The monolayers of the desired composition were compressed with 2.4 mm/min and the surface pressure was recorded using a platinum Wilhelmy plate.

## 4.5.7. Injection of [2]$^{2+}$ and surface pressure *vs.* time isotherms

The experiments were performed on a KSV (U.K.) Langmuir teflon round trough (area 1963 mm$^2$, volume 65 mL). The pure lipid or lipid-ligand spreading solutions were prepared by mixing appropriate volumes of chloroform or chloroform/methanol (4:1) stock solutions of phospholipids (0.3 mg/mL) and of ligand **1** or cholesterol (0.30 mg/mL). The desired surface pressure for the monolayer corresponded to a specific molecular area (Å$^2$/molecule) as shown in Figure AIV.1. Thus, the amount of lipid spreading solution was estimated for a desired molecular area (Å$^2$/molecule). The monolayers were spread onto the proper subphase (around 8-18 µL of the lipid solution, 3.6 to 8.0 nmol) while recording the surface pressure until a desired surface pressure was obtained. After 20-30 min equilibration, a stock solution of the ruthenium complex [**2**](PF$_6$)$_2$ (0.65 mM) (Figure 4.3a) or [**2**]Cl$_2$ (3.5 mM) (Figures 4.3b and AIV.4) in the appropriate buffer was injected into the subphase and gently mixed (≤100 rpm) at a slow speed taking care not to disturb the monolayer. The surface pressure changes were then recorded until the equilibrium was obtained. Control experiments were performed by injection of [**2**]Cl$_2$ or [**2**](PF$_6$)$_2$ to the subphase without any monolayer or buffer injection under monolayer which did not show any changes on the surface pressure of the subphase.

## 4.5.8. Isothermal Titration Calorimetry

The experiments were performed on a TA instruments nano-ITC 2G at 298 K and all the solutions were degassed prior to use. The reaction cell (V=1 mL) was filled with the liposome solution containing cholesterol or ligand **1** in the appropriate buffer, and the reference cell with the corresponding liposome-free buffer solution. The liposome solution was titrated by consecutive injections of 5 µL (49 injections) or 10 µL (24 injections preceded by one 5 µl injection) injections of the ruthenium complex [**2**]$^{2+}$ solution under constant stirring at 300 rpm. The time interval between successive injections was 300 s. The dilution heat of the ruthenium complexes were determined by injection of [**2**]$^{2+}$ into the corresponding buffer and subtracted from the corresponding titrations. Titrations were

duplicated to check reproducibility. The data were analyzed using the NanoAnalyze software TA Instruments, Delaware, USA) using a 1:n independent binding sites model.

### 4.5.9. Supporting Information available

Surface pressure-mean molecular area compression isotherms (Figure AIV.1); a plot of surface pressure variation upon titration of DMPG monolayers containing 25 mol% ligand **1** with [**2**]$^{2+}$ (Figure AIV.2); the surface pressure variation upon injection of [**2**]$^{2+}$ to zwitterionic monolayers of DOPC and DMPC (Figure AIV.3); the surface pressure variation upon injection of [**2**]$^{2+}$ to DMPG at different $\Pi_0$ (Figure AIV.4);ITC and surface pressure data for [**2**](PF$_6$)$_2$ and [**2**]Cl$_2$ (Figure AIV.5 and Table AIV.1), are shown as Supplementary Information.

## 4.6.    References

[1]     A.-L. Laine, C. Passirani, *Curr. Opin. Pharmacol.* **2012**, *12*, 420-426.
[2]     P. J. Stone, A. D. Kelman, F. M. Sinex, *Nature* **1974**, *251*, 736-737.
[3]     O. Novakova, J. Kasparkova, O. Vrana, P. M. Vanvliet, J. Reedijk, V. Brabec, *Biochemistry* **1995**, *34*, 12369-12378.
[4]     A. P. Martins, A. Marrone, A. Ciancetta, A. Galan Cobo, M. Echevarria, T. F. Moura, N. Re, A. Casini, G. Soveral, *PLoS One* **2012**, *7*, e37435.
[5]     C. Metcalfe, J. A. Thomas, *Chem. Soc. Rev.* **2003**, *32*, 215-224.
[6]     M. T. Dimanche-Boitrel, O. Meurette, A. Rebillard, S. Lacour, *Drug Resist. Updat.* **2005**, *8*, 5-14.
[7]     M. Jensen, M. Bjerring, N. C. Nielsen, W. Nerdal, *J. Biol. Inorg. Chem.* **2010**, *15*, 213-223.
[8]     X. Liang, D. J. Campopiano, P. J. Sadler, *Chem. Soc. Rev.* **2007**, *36*, 968-992.
[9]     A. Casini, J. Reedijk, *Chem. Sci.* **2012**, *3*, 3135-3144.
[10]    G. Mangiapia, G. D'Errico, L. Simeone, C. Irace, A. Radulescu, A. Di Pascale, A. Colonna, D. Montesarchio, L. Paduano, *Biomaterials* **2012**, *33*, 3770-3782.
[11]    L. Paasonen, T. Sipila, A. Subrizi, P. Laurinmaki, S. J. Butcher, M. Rappolt, A. Yaghmur, A. Urtti, M. Yliperttula, *J. Control. Release* **2010**, *147*, 136-143.
[12]    H. Chen, R. C. MacDonald, S. Li, N. L. Krett, S. T. Rosen, T. V. O'Halloran, *J. Am. Chem. Soc.* **2006**, *128*, 13348-13349.
[13]    A. Lau, A. McLaughlin, S. McLaughlin, *Biochim. Biophys. Acta* **1981**, *645*, 279-292.
[14]    M. Fragata, F. Bellemare, E. K. Nenonene, *J. Phys. Chem. B* **1997**, *101*, 1916-1921.
[15]    W. Hubner, A. Blume, *Chem. Phys. Lipids* **1998**, *96*, 99-123.
[16]    M. Suwalsky, B. Ungerer, L. Quevedo, F. Aguilar, C. P. Sotomayor, *J. Inorg. Biochem.* **1998**, *70*, 233-238.
[17]    M. J. Scott, M. N. Jones, *Colloids Surf., A* **2001**, *182*, 247-256.
[18]    H. Binder, O. Zschornig, *Chem. Phys. Lipids* **2002**, *115*, 39-61.
[19]    M. S. Villaverde, S. V. Verstraeten, *Arch. Biochem. Biophys.* **2003**, *417*, 235-243.
[20]    S. D. Shoemaker, T. K. Vanderlick, *J. Colloid Interface Sci.* **2003**, *266*, 314-321.

[21]  V. Cael, A. Van der Heyden, D. Champmartin, W. Barzyk, P. Rubini, E. Rogalska, *Langmuir* **2003**, *19*, 8697-8708.

[22]  P. T. Vernier, M. J. Ziegler, R. Dimova, *Langmuir* **2009**, *25*, 1020-1027.

[23]  S. Kewalramani, H. Hlaing, B. M. Ocko, I. Kuzmenko, M. Fukuto, *J. Phys. Chem. Lett.* **2010**, *1*, 489-495.

[24]  Y.-H. Wang, A. Collins, L. Guo, K. B. Smith-Dupont, F. Gai, T. Svitkina, P. A. Janmey, *J. Am. Chem. Soc.* **2012**, *134*, 3387-3395.

[25]  G. Laroche, E. J. Dufourc, J. Dufourcq, M. Pezolet, *Biochemistry* **1991**, *30*, 3105-3114.

[26]  A. P. Ramos, C. Pavani, Y. Iamamoto, M. E. D. Zaniquelli, *J. Colloid Interface Sci.* **2010**, *350*, 148-154.

[27]  C. Gasbarri, G. Angelini, A. Fontana, P. De Maria, G. Siani, I. Giannicchi, A. D. Cort, *Biochim. Biophys. Acta, Biomembr.* **2012**, *1818*, 747-752.

[28]  G. Speelmans, W. Sips, R. J. H. Grisel, R. Staffhorst, A. M. J. FichtingerSchepman, J. Reedijk, B. deKruijff, *Biochim. Biophys. Acta, Biomembr.* **1996**, *1283*, 60-66.

[29]  G. Speelmans, R. Staffhorst, K. Versluis, J. Reedijk, B. deKruijff, *Biochemistry* **1997**, *36*, 10545-10550.

[30]  H. Binder, K. Arnold, A. S. Ulrich, O. Zschornig, *Biophys. Chem.* **2001**, *90*, 57-74.

[31]  M. Delnomdedieu, A. Boudou, D. Georgescauld, E. J. Dufourc, *Chem-Biol. Interact.* **1992**, *81*, 243-269.

[32]  N. S. Raja, K. Sankaranarayanan, A. Dhathathreyan, B. U. Nair, *Biochim. Biophys. Acta, Biomembr.* **2011**, *1808*, 332-340.

[33]  D. Voelker, P. Smejtek, *Biophys. J.* **1996**, *70*, 818-830.

[34]  S. Bonnet, B. Limburg, J. D. Meeldijk, R. J. M. K. Gebbink, J. A. Killian, *J. Am. Chem. Soc.* **2011**, *133*, 252-261.

[35]  D. Marsh, *Biochim. Biophys. Acta* **1996**, *1286*, 183-223.

[36]  F. Castelli, M. G. Sarpietro, F. Rocco, M. Ceruti, L. Cattel, *J. Colloid Interface Sci.* **2007**, *313*, 363-368.

[37]  O. Maniti, M. Cheniour, O. Marcillat, C. Vial, T. Granjon, *Mol. Membr. Biol.* **2009**, *26*, 171-185.

[38]  S. Nathoo, J. K. Litzenberger, D. C. Bay, R. J. Turner, E. J. Prenner, *Chem. Phys. Lipids* **2013**, *167–168*, 33-42.

[39]  F. Nsimba Zakanda, L. Lins, K. Nott, M. Paquot, G. Mvumbi Lelo, M. Deleu, *Langmuir* **2012**, *28*, 3524-3533.

[40]  E. Polverini, S. Arisi, P. Cavatorta, T. Berzina, L. Cristofolini, A. Fasano, P. Riccio, M. P. Fontana, *Langmuir* **2003**, *19*, 872-877.

[41]  F. N. Zakanda, K. Nott, M. Paquot, G. M. Lelo, M. Deleu, *Colloids Surf., B* **2011**, *86*, 176-180.

[42]  F. Bringezu, M. Majerowicz, E. Maltseva, S. Y. Wen, G. Brezesinski, A. J. Waring, *ChemBioChem* **2007**, *8*, 1038-1047.

[43]  N. Vernoux, O. Maniti, F. Besson, T. Granjon, O. Marcillat, C. Vial, *J. Colloid Interface Sci.* **2007**, *310*, 436-445.

[44]  A. Rosengarth, A. Wintergalen, H. J. Galla, H. J. Hinz, V. Gerke, *FEBS Lett.* **1998**, *438*, 279-284.

[45]  M. Jesus Sanchez-Martin, I. Haro, M. Asuncion Alsina, M. Antonia Busquets, M. Pujol, *J. Phys. Chem. B* **2010**, *114*, 448-456.

[46]  A. Junghans, C. Champagne, P. Cayot, C. Loupiac, I. Koeper, *Langmuir* **2010**, *26*, 12049-12053.

[47]  V. Shapovalov, A. Tronin, *Langmuir* **1997**, *13*, 4870-4876.

[48]  F. Gambinossi, B. Mecheri, M. Nocentini, M. Puggelli, G. Caminati, *Biophys. Chem.* **2004**, *110*, 101-117.

[49]    B. Gzyl-Malcher, M. Filek, G. Brezesinski, *Langmuir* **2011**, *27*, 10886-10893.
[50]    C. G. Sinn, M. Antonietti, R. Dimova, *Colloids Surf., A* **2006**, *282*, 410-419.
[51]    B. Klasczyk, V. Knecht, R. Lipowsky, R. Dimova, *Langmuir* **2010**, *26*, 18951-18958.
[52]    G. J. Gabriel, J. G. Pool, A. Som, J. M. Dabkowski, E. B. Coughlin, M. Muthukurnar, G. N. Tew, *Langmuir* **2008**, *24*, 12489-12495.
[53]    R. Lehrmann, J. Seelig, *Biochim. Biophys. Acta, Biomembr.* **1994**, *1189*, 89-95.
[54]    M. S. Lin, H. M. Chiu, F. J. Fan, H. T. Tsai, S. S. S. Wang, Y. Chang, W. Y. Chen, *Colloids Surf., B* **2007**, *58*, 231-236.
[55]    A. Beck, X. Li-Blatter, A. Seelig, J. Seelig, *J. Phys. Chem. B* **2010**, *114*, 15862-15871.
[56]    C. G. Sinn, R. Dimova, M. Antonietti, *Macromolecules* **2004**, *37*, 3444-3450.
[57]    N. Duzgunes, J. Wilschut, R. Fraley, D. Papahadjopoulos, *Biochim. Biophys. Acta* **1981**, *642*, 182-195.
[58]    A. Martin-Molina, C. Rodriguez-Beas, J. Faraudo, *Biophys. J.* **2012**, *102*, 2095-2103.
[59]    J. M. Ruso, L. Besada, P. Martinez-Landeira, L. Seoane, G. Prieto, M. Sarmiento, *J. Liposome Res.* **2003**, *13*, 131-145.
[60]    P. Garidel, A. Blume, W. Hubner, *Biochim. Biophys. Acta, Biomembr.* **2000**, *1466*, 245-259.
[61]    P. Garidel, A. Blume, *Langmuir* **1999**, *15*, 5526-5534.
[62]    D. E. Leckband, C. A. Helm, J. Israelachvili, *Biochemistry* **1993**, *32*, 1127-1140.
[63]    D. K. Hincha, *Biochim. Biophys. Acta, Biomembr.* **2003**, *1611*, 180-186.

# 5

Liposomes functionalized with ruthenium complexes: towards tumor targeted light-controlled anticancer prodrugs
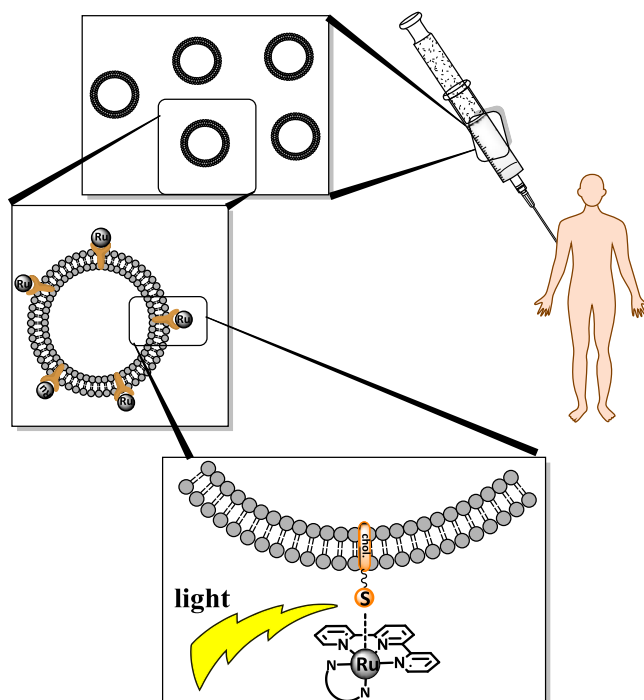
**Abstract**

Ruthenium complexes [**1**](PF$_6$)$_2$ to [**4**](PF$_6$)$_2$ with the general formula [Ru(terpy)(N-N)(SRR')]$^{2+}$ were synthesized, where terpy is 2,2';6',2''-terpyridine, N-N is 2,2'-bipyridine (bpy) or phenylpiridin-2-ylmethylene-imine (pymi), and SRR' is a thioether-cholesterol conjugate with a cholesterol tail. Stable DMPC, DMPG, DOPC or DOPG liposomes functionalized with these complexes were prepared by extrusion. The ruthenium complexes supported on liposomes were photosensitive: substitution of the SRR' ligand by an aqua ligand occurred upon blue light irradiation ($\lambda_e$=452 nm), thus leading to the detachment of the complex from the liposome surface. Kinetic studies using UV-vis spectroscopy on DOPC and DMPG liposomes decorated with the ruthenium complexes [**1**](PF$_6$)$_2$ to [**4**](PF$_6$)$_2$ showed that the photoreactivity of these complexes increased at human body temperature as compared to room temperature, or when the liposome is composed of neutral lipids (DOPC) as compared to negatively charged lipids (DMPG). The Ru-S coordination bond of complex [**2**](PF$_6$)$_2$ supported on a DOPC liposome in a PBS buffer was shown to be stable in the dark at 4 °C for at least 7 days.

Cancer cells were incubated with Ru-functionalized liposomes to study the influence of liposome formulation on cellular uptake. For HepG2 cells confocal microscope images proved that fluorescently labeled liposomes containing [**1**](PF$_6$)$_2$ were better taken up when the lipid composing the membrane was neutral (DMPC) than when it was negatively charged (DMPG). The same effect was observed for the cellular uptake of neutral (DOPC) or negatively charged (DOPG) liposomes functionalized with [**1**](PF$_6$)$_2$ by ovarian cancer cells (A2780 and A2780 R). When PEGylated lipids were added in the liposome formulation, the effect of the lipid charge was shielded and no difference in cellular uptake was observed between DOPC- and DOPG-based formulations functionalized with [**1**](PF$_6$)$_2$, [**2**](PF$_6$)$_2$, [**3**](PF$_6$)$_2$, or [**4**](PF$_6$)$_2$.

The cytotoxicity of PEGylated liposomes functionalized with complexes [**1**](PF$_6$)$_2$ – [**4**](PF$_6$)$_2$ in the dark was tested on A2780 and A2780 R ovarian cancer cells. The results show that none of the ruthenium-functionalized liposomes is significantly toxic in the dark after 6 hours incubation time. Light cytotoxicity tests for non-PEGylated DMPC and DMPG liposomes functionalized with [**1**](PF$_6$)$_2$ showed up to five times  higher cytotoxicity after blue light activation, compared to dark toxicity.

## 5.1    Introduction

Ruthenium-based compounds have attracted much attention as potential anticancer agents.[1-3] A significant number of the ruthenium complexes studied in this field exert their anticancer activity *via* initial substitution of a ligand by a water molecule.[4] The hydrolyzed ruthenium complex is believed to be cytotoxic by interacting with DNA or other biomolecules in the cancer cells.[5-6] The released ligand might also be biologically active and bind to nucleic acids or protein active sites.[7] Ruthenium complexes often absorb light in the visible region ($\lambda_{max}$~450 nm) and their photophysical properties can be tuned. In particular complexes with distorted octahedral geometry may undergo photosubstitution reactions upon visible light irradiation, which can be used in photoactivated chemotherapy (PACT).[8] The great advantage of photoactivation of ruthenium-based prodrugs is to control the time and place of complex activation, which results in a greater selectivity of the cytotoxicity.[9-10] In this case the ground state complex should be thermally stable and not undergo spontaneous ligand exchange or hydrolysis.[11-13]

When developing ruthenium-based cytotoxic compounds efficient drug targeting is also an important issue. Nano-sized drug delivery systems such as nanoparticles, micelles, or liposomes, can be used for specific delivery of the prodrug to cancer cells.[14] Provided that these drug delivery systems stay long enough in the blood circulation, increased accumulation of the prodrug can be obtained at the tumor sites.[15] For example, Sauvage and coworkers[16] recently used mesoporous silica nanoparticles (MSNPs) as drug carriers for photosensitive ruthenium dipyridophenazine (dppz) complexes. The resulting supramolecular assembly showed fast cellular uptake and induced cytotoxic activity upon visible light irradiation.

Liposomal drug carriers have been extensively used in anticancer therapy since 1974.[17-20] In tumor tissues the endothelium (blood vessel wall) is distorted and can be crossed by liposomes. As a result liposomes penetrate well cancer tissues, and less well healthy tissues.[21] It is known that several factors such as liposome size, surface charge, and composition, influence their clearance by cells of the immune system and thus their circulations lifetime in the blood stream.[22-25] For example liposomes with small sizes (<200 nm), with cholesterol in the membrane composition, and a high phase transition temperature, show a longer biological half-life.[26-28] In particular, adding poly(ethylene glycol) (PEG)-functionalized lipids in the composition of the

liposomes was reported to be the most successful method to increase the blood circulation lifetime of liposomes. The hydrophobic PEG groups protect the liposome surface and prevent its clearance by cells of the immune system.[29-30] Although several formulations are now clinically tested with organic drugs, liposomal drug carriers have not often been used for metal-based drugs,[31-33] and the first liposomal system for an anticancer ruthenium(III) complexes was reported only recently by Paduana and co-workers.[34-35] To the best of our knowledge liposomes have not yet been used for the delivery of light-activatable ruthenium complexes.
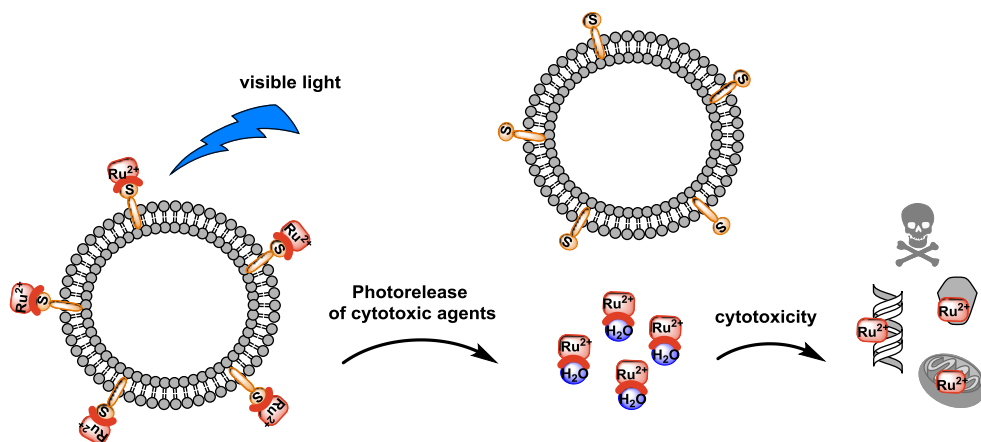


**Scheme 5.1.** Schematic drawing of a liposome functionalized with photosensitive ruthenium complexes. Photosubstitution of membrane-embedded sulfur ligands by aqua ligands releases ruthenium-aqua complexes, which may be cytotoxic by interacting with DNA, mitochondria, or other biomolecules.

In Chapters 2 and 3 polypyridyl ruthenium complexes of the type [Ru(terpy)(N-N)(SRR')]$^{2+}$ were described, where terpy is 2,2′;6′,2″-terpyridine, N-N is a diimine ligand, and SRR' is a sulfur-containing ligand. These complexes undergo selective photosubstitution of the SRR' ligand by an aqua ligand upon visible light irradiation. In addition it was shown in Chapter 3 that for less distorted complexes (*e.g.,* N-N=2,2'-bipyridine) the Ru-S bond is rather stable in the dark below 50 °C. Thus, these complexes are potentially interesting as light-activatable anticancer agents, if the corresponding aqua complex is cytotoxic. Moreover, a strategy to decorate liposomes with these photosensitive ruthenium complexes was recently published in our group;[36] such a supramolecular assembly may deliver the ruthenium complex to cancer cells. Provided the Ru-functionalized liposomes are taken up by cancer cells, light-induced

substitution of a membrane-bound sulfur ligand by an aqua ligand would result in the dissociation of the ruthenium aqua complex from the liposome carrier, followed by the diffusion of the complex into the cell, its interaction with biomolecules, and possibly to cell death (see Scheme 5.1). In this Chapter the preparation, characterization, and biological activity are described of liposomes functionalized with a photoactive ruthenium complex (see Figure 5.1).



[Ru(terpy)(bpy)(**5**)](PF$_6$)$_2$ : [**1**](PF$_6$)$_2$

[Ru(terpy)(bpy)(**6**)](PF$_6$)$_2$ : [**2**](PF$_6$)$_2$

[Ru(terpy)(bpy)(**7**)](PF$_6$)$_2$ : [**3**](PF$_6$)$_2$

[Ru(terpy)(pymi)(**7**)](PF$_6$)$_2$ : [**4**](PF$_6$)$_2$
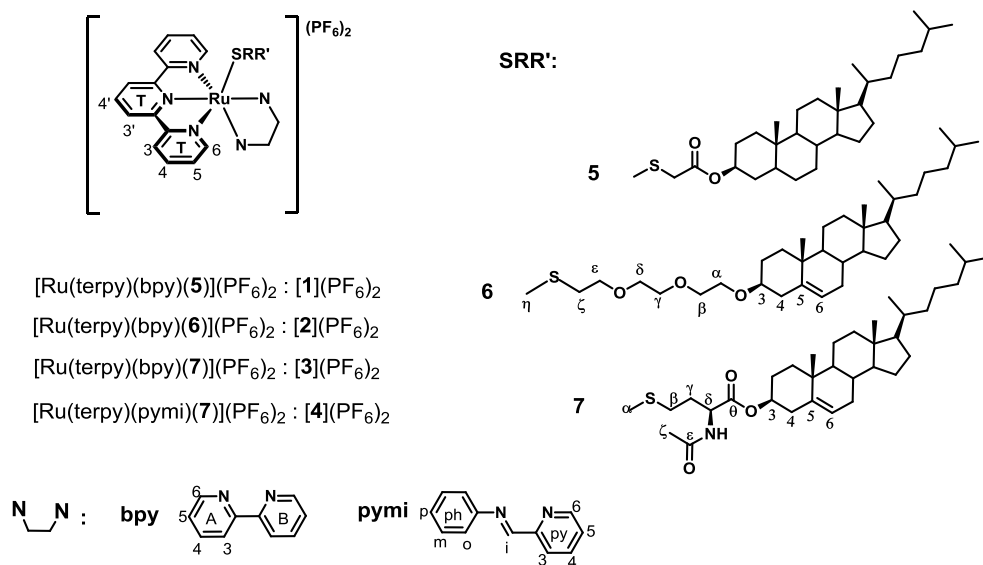
**Figure 5.1.** Chemical structures and numbering scheme of polypyridyl ruthenium complexes [**1**](PF$_6$)$_2$ − [**4**](PF$_6$)$_2$.

## 5.2    Results

### 5.2.1.    Synthesis

The synthesis of ligands **5**[36] and **6** (Chapter 2, Appendix II) is reported elsewhere. Ligand **7** was synthesized following a modified literature procedure,[37] consisting in the esterification of cholesterol with N-acetylated methionine using DCC (dicyclohexylcarboiimide) as coupling reagent and DMAP (N,N-dimethylaminopyridine) as catalyst. The sulfur-sterol conjugates **6** and **7** were

coordinated to ruthenium following the procedure reported for complex [1](PF$_6$)$_2$, by the reaction of [Ru(terpy)(bpy)(Cl)]Cl or [Ru(terpy)(pymi)(Cl)]Cl with 6 or 7 in the presence of two equiv. of AgBF$_4$ in acetone, followed by column chromatography.[36] Complexes [Ru(terpy)(bpy)(6)](PF$_6$)$_2$ ([2](PF$_6$)$_2$), [Ru(terpy)(bpy)(7)](PF$_6$)$_2$ ([3](PF$_6$)$_2$), and [Ru(terpy)(pymi)(7)](PF$_6$)$_2$ ([4](PF$_6$)$_2$) were obtained as orange, water-insoluble powders. They were characterized by ^{1}H NMR, ^{13}C NMR, mass spectrometry, UV-vis spectroscopy, and elemental analysis.

## 5.2.2. Photoreactivity and dark stability of a Ru-S bond at liposomes

### 5.2.2.1. Visible light irradiation of Ru-decorated liposome samples

In order to study the photosubstitution kinetics for complexes [1](PF$_6$)$_2$, [2](PF$_6$)$_2$, [3](PF$_6$)$_2$, or [4](PF$_6$)$_2$ at a lipid bilayer surface, liposomes composed of 1,2-dioleoyl-sn-glycero-3-phosphocholine (hereafter DOPC) or 1,2-dimyristoyl-sn-glycero-3-phospho-(1'-rac-glycerol) sodium salt (hereafter DMPG) functionalized with 5 mol% of one of the ruthenium complexes were prepared a in phosphate buffer ($I$=50 mM, pH=7.0) (Table 5.1). Each liposome sample was characterized by DLS prior to performing other experiments; their average diameter was 130-140 nm. The photosubstitution of the sulfur-sterol conjugate 5, 6, or 7 by an aqua ligand upon irradiation with blue light ($\lambda_e$=452 nm) was investigated by UV-vis spectroscopy either at 25 °C or at 37 °C. For a typical experiment the liposome sample was irradiated from the top of the UV-vis cuvette, while UV-vis spectra were measured perpendicular to the irradiating light beam (see Appendix I, Figure AI.1). The absorption spectrum of the irradiated sample gradually evolved until a photochemical steady state was obtained, characterized by an absorption maximum at a longer wavelength. In each case an isosbestic point was observed, which indicated that a single photochemical reaction was taking place. The UV-vis spectrum at the photochemical steady state corresponded with that of the ruthenium-aqua species [Ru(terpy)(N-N)(OH$_2$)]$^{2+}$ (N-N=bpy or pymi). The concentration of the ruthenium-sulfur complex (RuSRR') was calculated in each experiment as a function of irradiation time (see Appendix I, section AI.2.1). As shown in Equation 5.1, the photosubstitution first-order rate constants $k_\varphi$ was obtained from the slope of a plot of ln$([RuSRR']/[Ru]_{tot})$ vs. irradiation time (Figure 5.2a), where $[RuSRR']$ and $[Ru]_{tot}$ represent the bulk concentration in RuSRR' and the total ruthenium concentration in the sample, respectively. Half-reaction times were also calculated using Equation 5.2.

$$-\frac{d[RuSRR']}{dt} = \frac{d[RuOH_2]}{dt} = k_\varphi \cdot [RuSRR'] \quad \textbf{(Equation 5.1)}$$

$$t_{1/2} = \frac{ln2}{k_\varphi} \qquad \textbf{(Equation 5.2)}$$

The photosubstitution quantum yield $\varphi$ was obtained from the slope of a plot of the number of moles of RuSRR' remaining in solution, $n_{RuSRR'}$, vs. the number of moles of photons Q absorbed by the RuSRR' species since $t$=0 (see Figure 5.2b and Appendix I, section AI.3.2). The photosubstitution reactivity ($\xi=\varphi \cdot \varepsilon^{\lambda e}$) of the ruthenium complex, where $\varepsilon^{\lambda e}$ is the extinction coefficient of RuSRR' at the irradiation wavelength, better represents the photoreactivity of a complex in a given irradiation condition, and was calculated as well (see Chapter 6). All photochemical data are reported in Table 5.1.

**Table 5.1.** Data for the photosubstitution of the thioether-sterol conjugate **5**, **6**, or **7** by water for liposomes functionalized with ruthenium complexes [**1**](PF$_6$)$_2$, [**2**](PF$_6$)$_2$, [**3**](PF$_6$)$_2$, or [**4**](PF$_6$)$_2$. Irradiation conditions: $\lambda_e$ = 452 nm, photon flux $\Phi_{452}$ = 3.0(8)×10$^{-9}$ Einstein·s$^{-1}$, irradiation pathlength = 3 cm. Lipid bulk concentration=1.3 mM (as liposomes), total ruthenium concentration [$Ru$]$_{tot}$ = 0.065 mM, phosphate buffer pH=7.0, $I$=50 mM.

| Ru complex (5 mol%) | Liposome | $T$ (°C) | $\varepsilon^{\lambda e}$ (M$^{-1}$·cm$^{-1}$) | $t_{1/2}$ (min) | $k_\varphi$ (s$^{-1}$) | $\varphi$ | $\xi$ ($\varphi \cdot \varepsilon^{\lambda e}$) | $\lambda_{isosb.}$ (nm) |
|---|---|---|---|---|---|---|---|---|
| [**1**](PF$_6$)$_2$ | DOPC | 37 | 6700 | 21(2) | 5.2(3)×10$^{-4}$ | 0.019(5) | 127(8) | 455 |
| [**2**](PF$_6$)$_2$ | DOPC | 37 | 6800 | 53(3) | 2.2(2)×10$^{-4}$ | 0.013(3) | 88(6) | 455 |
| [**3**](PF$_6$)$_2$ | DOPC | 37 | 6700 | 47(3) | 2.5(2)×10$^{-4}$ | 0.012(4) | 80(5) | 453 |
| [**4**](PF$_6$)$_2$ | DOPC | 37 | 5400 | 95(5) | 1.2(3)×10$^{-4}$ | 0.0080(5) | 43(3) | 479 |
| [**3**](PF$_6$)$_2$ | DOPC | 25 | 6700 | 90(5) | 1.3(2)×10$^{-4}$ | 0.0068(5) | 46(3) | 453 |
| [**3**](PF$_6$)$_2$ | DMPG | 25 | 5900 | 156(8) | 7.4(5)×10$^{-5}$ | 0.0048(4) | 28(2) | 464 |
| [**4**](PF$_6$)$_2$ | DOPC | 25 | 5400 | 135(8) | 8.6(7)×10$^{-5}$ | 0.0049(4) | 26(2) | 479 |
| [**4**](PF$_6$)$_2$ | DMPG | 25 | 4600 | 325(9) | 3.6(3)×10$^{-5}$ | 0.0031(6) | 14(1) | 483 |

The effect of temperature on the photosubstitution reactivity of complexes [**3**](PF$_6$)$_2$ and [**4**](PF$_6$)$_2$ was investigated first. The photochemical data for these complexes (Table 5.1) show that the photosubstitution rate and quantum yield are almost twice higher at 37 °C than at 25 °C. Most probably, it is the dependence of the quantum yield $\varphi$ with temperature that explains the faster reaction at human body temperature. The

transition from the photochemically generated $^3$MLCT state to the $^3$MC state leading to ligand substitution is a thermally activated process, which explains why the elevated temperature of the human body is an advantage on the point of view of photoactivation of polypyridyl ruthenium complexes.
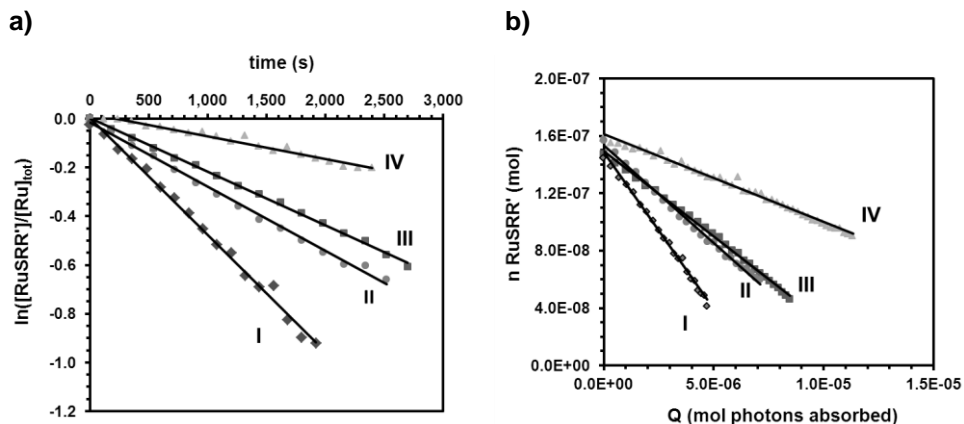


**Figure 5.2.** a) Plots of ln*(RuSRR']/[Ru]$_{tot}$) vs.* irradiation time during the blue light irradiation of liposomes functionalized with ruthenium complexes [**1**](PF$_6$)$_2$, [**2**](PF$_6$)$_2$, [**3**](PF$_6$)$_2$, or [**4**](PF$_6$)$_2$. *[RuSRR']* represents the bulk concentration in *RuSRR'*, and *[Ru]$_{tot}$* the total ruthenium concentration in the solution. The slope of each plot is $-k_\varphi$ (s$^{-1}$). (b) Plots of the number of moles of RuSRR' *vs.* the number of moles of photons absorbed by RuSRR' at time *t*, since *t*=0; the slope is the photosubstitution quantum yield *φ*. RuSRR'=[**1**](PF$_6$)$_2$ (I), [**2**](PF$_6$)$_2$ (II), [**3**](PF$_6$)$_2$ (III), [**4**](PF$_6$)$_2$ (IV). Total ruthenium concentration=0.065 mM, bulk lipid concentration=1.3 mM (as liposomes), phosphate buffer (pH=7, *I*=50 mM). Irradiation condition: blue light ($\lambda_e$=452 nm), photon flux $\Phi_{452}$=3.0(8)×10$^{-9}$ Einstein.s$^{-1}$, *T*=37 °C, irradiation pathlength=3 cm.

Comparing the photosubstitution reactivity of [**1**](PF$_6$)$_2$ − [**4**](PF$_6$)$_2$ on DOPC liposomes at 37 °C shows that the highest quantum yield *φ* and photosubstitution reactivity value *ζ* were obtained for complex [**1**](PF$_6$)$_2$, and the lowest for complex [**4**](PF$_6$)$_2$. The higher quantum yield of [**1**](PF$_6$)$_2$ may be due to the higher steric hindrance of the thioether ligand **5**, as the linker between the sulfur atom and the cholesterol moiety is very short. The sulfur ligand is also close to an electron-withdrawing ester, which might exert reductive effects and modify the ability of the ligand to coordinate to the ruthenium. In [**2**](PF$_6$)$_2$ and [**3**](PF$_6$)$_2$ the thioether ligands are electronically similar, leading to similar quantum yields. For [**4**](PF$_6$)$_2$ the non-conjugated imine ligand of the ligand pymi leads to an absorption maximum at higher

wavelength (475 *vs*. 460 nm), thus to a more stable $^3$MLCT state and (in the absence of steric hindrance) to a lower quantum yield, compared to the bpy-containing complex [**3**](PF$_6$)$_2$. Overall, for a given light intensity the time necessary to activate 50% of the complex slightly depends on the chemical structure of the thioether and bidentate ligands.

Another phenomenon was noticed when comparing the photochemical reactivity of two of the four complexes on neutral (DOPC) or negatively charged (DMPG) liposomes at 25 °C. For complex [**3**](PF$_6$)$_2$ and [**4**](PF$_6$)$_2$ the photosubstitution reactivity $\xi$ and quantum yield $\varphi$ were found to be about 1.7 and 1.5 times higher, respectively, for DOPC liposomes compared with DMPG liposomes. This observation indicates a non-negligible contribution of the electrostatic interaction between the positively charged ruthenium complex and the negative surface charge of DMPG liposomes, to the strength of the Ru-S bond.

Overall, changing the temperature, the electronic or steric properties of the ligands, or the surface charge of the liposome, all contribute to influencing the photosubstitution quantum yield and reaction rate of the ruthenium complexes upon irradiation.

### 5.2.2.2.    Ruthenium-sulfur bond stability in PBS buffer in the dark

For phototherapy applications the Ru-S bond of Ru-functionalized liposomes as described above is expected to remain stable in the dark and *in vitro*, *i.e.*, the sulfur ligand should not be substituted by water or other ligands (in particular Cl$^-$) present in biocompatible buffers. Thus, prior to *in vitro* experiments the thermal stability of the Ru-S bond was investigated for complex [**2**](PF$_6$)$_2$ supported on PEGylated DOPC liposomes in a PBS (Phosphate Buffered Saline) buffer containing high chloride concentrations (~140 mM). A DOPC:DSPE-PEG2K (98:2) liposome sample (DSPE-PEG2K=1,2-distearoyl-*sn*-glycero-3-phosphoethanolamine-N-[amino(polyethylene glycol)-2000] as the ammonium salt)  containing 5 mol% of [**2**](PF$_6$)$_2$ was prepared by extrusion. The sample was stored in the refrigerator (4 °C) during one week, and fractions of the sample were subjected to ultracentrifugation (40,000 rpm; 1 h; $T = 25$ °C) at day 0, 1, 3 and 7. In all cases the lipid pellet obtained after centrifugation was orange and the supernatant was colorless, which qualitatively meant that most of the ruthenium complex was still attached to the lipid bilayer. The ruthenium concentration of the samples before and after centrifugation was quantitatively measured using inductively coupled plasma optical emission spectroscopy (ICP-OES). In all cases ($t$=0,

1, 3 and 7 days) the total Ru concentration in the supernatant was found to be ~5% (~230 ppb) of the ruthenium concentration found before centrifugation (4170(40) ppb, at $t=0$). These results showed that no ruthenium complex dissociated from the liposome surface after 7 days in such conditions, and that the 5% already present at $t=0$, *i.e.*, just after preparation, were probably produced during extrusion of the sample, which occurs at elevated temperatures (50 °C). Thus, the ruthenium-sulfur bond of complex [**2**](PF$_6$)$_2$ supported on DOPC stealth liposomes was found to be stable in the dark in PBS and in the fridge, and the sulfur ligand was not substituted by chloride or water in such conditions.

### 5.2.3. In vitro experiments

### 5.2.3.1. Cellular uptake of fluorescently-labeled, Ru-functionalized liposomes

The role of a drug delivery system is to deliver the prodrug inside the target cell, hence the cellular uptake of Ru-functionalized liposomes was investigated first. Liver hepatocellular carcinoma cells (HepG2), non-cisplatin resistant human ovarian cancer cells (A2780), and cisplatin-resistant human ovarian cancer cells (A2780 R), were chosen for *in vitro* experiments. The liposome formulation comprised a phospholipid (DMPC, DMPG, DOPC, or DOPG), 4 – 5 mol% of the fluorescent lipid 1-acyl-2-{12-[(7-nitro-2-1,3-benzoxadiazol-4-yl)amino]dodecanoyl}-*sn*-glycero-3-phosphocholine (hereafter NBD-PC, $\lambda_{exc}$=460 nm, $\lambda_{em}$=534 nm), 5 mol% of one of the four ruthenium complexes [**1**](PF$_6$)$_2$ – [**4**](PF$_6$)$_2$, and in some cases 4 mol% of DSPE-PEG2K. All liposomes were prepared by extrusion using a 200 nm polycarbonate filter, resulting in size distributions around 130-150 nm. The cancer cells were incubated with the liposomes for 1 hour, after which the cellular uptake was determined based on the fluorescence of the NBD-PC lipid.

The effect of lipid charge on cellular uptake by HepG2 cells was first investigated for complex [**1**](PF$_6$)$_2$ supported on negatively charged (DMPG) or zwitterionic 1,2-dimyristoyl-*sn*-glycero-3-phosphocholine (DMPC) liposomes. Confocal microscopy images were taken after cellular incubation with the liposomes (Figure 5.3). Although Ru-free DMPC liposomes were poorly taken up, Ru-functionalization led to an increased uptake by HepG2 cells. For DMPG liposomes the reverse effect was observed: Ru-free liposomes were well taken up, whereas Ru-functionalized liposomes were less taken up. Thus, the surface charge of the liposome has a critical influence on liposome uptake for HepG2 cells. Overall, for HepG2 cells using neutral lipids in the

liposome formulation seems more beneficial in terms of cellular uptake than using negative lipids.

| DMPG | DMPG+Ru | DMPC | DMPC+Ru |
|------|---------|------|---------|
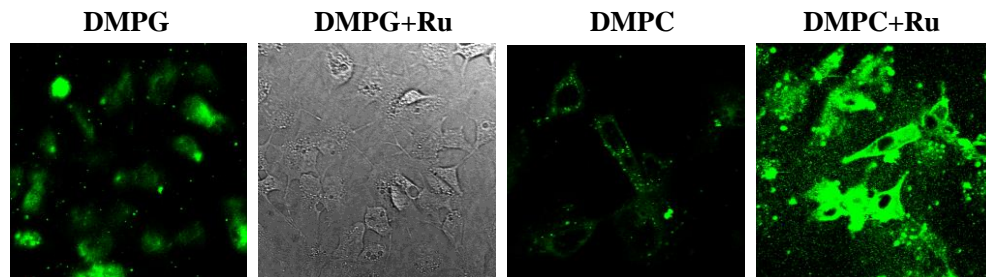


**Figure 5.3.** Confocal microscope images after cellular uptake of liposomes by HepG2 cells. Intense green color represents higher cellular uptake. Liposome compositions: DMPG:NBD-PC (95:5) and 0 or 5 mol% [**1**](PF$_6$)$_2$ or DMPC:NBD-PC (95:5) and 0 or 5 mol% [**1**](PF$_6$)$_2$. *[Ru]$_{tot}$* = 0.025 mM, *[lipid]$_{tot}$*=0.50 mM (as liposomes, diameter~140 nm), detection by fluorescence: $\lambda_{ex}$=460 nm, $\lambda_{em}$=534 nm.

Confocal microscopy images do not provide quantitative information on the cellular uptake of fluorescently-labeled liposomes. As mentioned in section 5.1, liposomes with PEGylated lipids ("stealth" liposomes) are known to have higher blood circulation lifetime than non-PEGylated ones. Thus, cellular uptake experiments were realized using PEGylated Ru-functionalized liposomes and either neutral (DOPC) or negatively charged lipids (1,2-dioleoyl-*sn*-glycero-3-phospho-(1'-rac-glycerol) sodium salt, hereafter DOPG). The lipid formulations consisted in DOPC:DSPE-PEG2K:NBD-PC 92:4:4 or DOPG:DSPE-PEG2K:NBD-PC 92:4:4 mixtures containing no or an additional 5 mol% of one of the four ruthenium complexes [**1**](PF$_6$)$_2$ − [**4**](PF$_6$)$_2$. The liposomes were prepared by extrusion and characterized by DLS (average diameter ~140 nm). Their ability to enter cancer cells was measured on A2780 and A2780 R cancer cell lines. After 1 hour incubation in the dark the fluorescence of the cell plate was measured at 534 nm ($\lambda_{exc}$=460 nm, $\lambda_{em}$=534 nm). The fluorescence values *F* were then corrected for the number of cells by dividing *F* by the protein content $A_{prot}$ of each well (after lysis), as determined by the BCA (bicinchoninic acid) assay. This protein assay is based on the reduction of $Cu^{2+}$ to $Cu^{+}$ by proteins in an alkaline medium (the biuret reaction); the $Cu^{+}$ subsequently reacts with bicinchoninic acid to form a highly colored (purple) reaction product.[38] The absorption $A_{prot}$ of the reaction product was measured at 562 nm and correlates linearly to the protein concentration of the sample.

Finally the corrected fluorescence value $F/A_{prot}$ of each well was compared to that of untreated cells ($(F/A_{prot})_{ctrl}=1$ or 100%). The results of these cellular uptake experiments are shown in Figure 5.4a.

In both cell lines PEGylated DOPG liposomes without ruthenium were taken up slightly better than PEGylated DOPC liposomes without ruthenium. No significant difference was observed between the different cell lines. For liposomes with ruthenium, uptake of PEGylated DOPG liposomes was comparable with that of PEGylated DOPC liposomes. Although several parameters had changed compared to the uptake experiment on HepG2 cells (Figure 5.2), these new data suggest that the charge of liposomes may be shielded by the PEG groups. Finally, there were no significant differences found for the uptake of PEGylated liposomes functionalized with the different ruthenium complexes $[1](PF_6)_2 - [4](PF_6)_2$, which suggests that once supported on liposomes, the exact structure of the complex is of minor importance regarding cellular uptake.

According to these data the uptake of liposomes with ruthenium seemed to be lower than that of liposomes without ruthenium. However, since uptake data were based on the fluorescence intensity of an NBD-PC lipid incorporated in the membrane, the presence of the ruthenium complex at the liposome surface might affect the uptake data, as it might influence (for example by quenching) the fluorescence of the NBD dye. In addition, both the NBD-PC lipid and the ruthenium complex have absorbance maxima around 450-460 nm, and the presence of the Ru complex in the sample might filter the excitation of the NBD dye, leading to artificially lower emission intensities. The effect of the presence of the ruthenium complex at the membrane on NBD-PC emission was checked for different concentrations of complex $[1](PF_6)_2$ in PEGylated DOPC liposomes (DOPC:DSPE-PEG2K:NBD-PC(92:4:4)) (Appendix V, Figure AV.1). In PBS buffer the emission of NBD-PC in the liposome membrane indeed was found to depend on the amount of ruthenium present in the same membrane. With 5 mol% ruthenium the fluorescence intensity was decreased by more than 80%, compared to the emission of a similar liposome without ruthenium. Thus, based on this quenching factor the raw uptake data for DOPC stealth liposomes functionalized with $[1](PF_6)_2$ were corrected (Figure 5.4b). According to this correction, the uptake of liposomes functionalized with complex $[1](PF_6)_2$ was found to be much higher, in both cell lines, than that of Ru-free DOPC liposomes (22.6 *vs.* 3.6 for A2780 cells, and 22.5 *vs.* 3.1 for A2780 R cells). These results are consistent with the conclusions drawn

from confocal microscopy images measured with HepG2 cells, that the presence of Ru complexes at the surface of neutral liposomes enhances liposome uptake.

Because of the fluorescence-quenching problem the uptake results shown in Figure 5.3a do not provide quantitative information about the amount of ruthenium complex taken up by the cells. In an attempt to better quantify ruthenium uptake the cells were lysed using NaOH and the ruthenium concentration in the cell lysis was measured by ICP-OES (see Appendix V). Unfortunately, the concentration of ruthenium in most of the samples was too low to be detected by ICP-OES ($[Ru] \leq 20$ ppb).
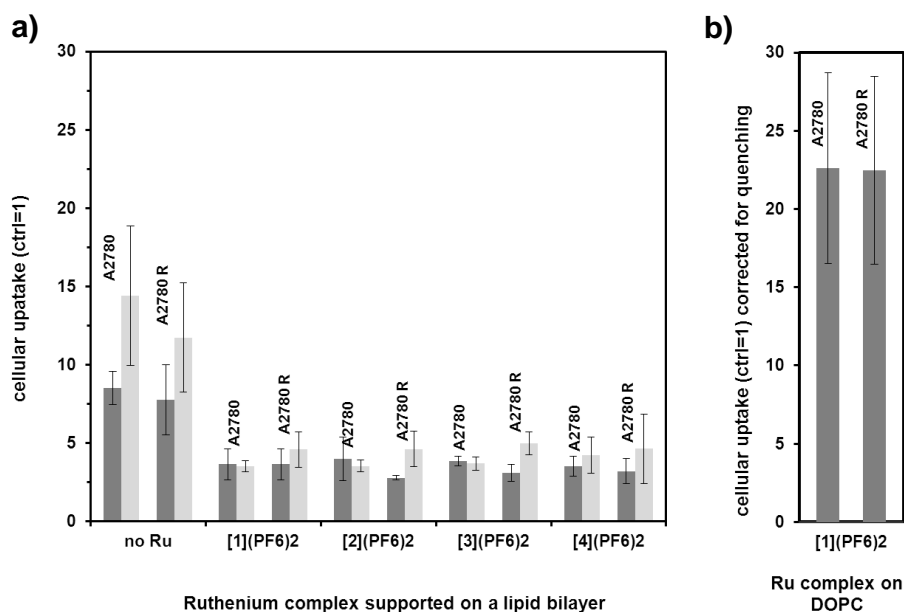


**Figure 5.4.** a) Cellular uptake of DOPC (dark grey) and DOPG (light grey) stealth (4% PEG) liposomes containing 5 mol% RuSRR' by A2780 and A2780 R human ovarian cancer cells. (b) Uptake data corrected for NBD fluorescence quenching by ruthenium for DOPC stealth liposomes containing 5 mol% of complex [**1**]($PF_6$)$_2$. Incubation conditions: bulk lipid concentration $[lipid]_{tot}$ = 1.5 mM (as liposomes) in PBS:DMEM ($-$FCS, +PS, +ph. red) 8:5 medium, total ruthenium concentration $[Ru]_{tot}$ = 0.075 mM, incubation time =1 h, T = 310 K, 7% $CO_2$, in the dark. Control wells contained untreated cells.

In order to investigate how cellular uptake was influenced by PEG groups at the liposome surface and by the lipid charge, uptake experiments were performed on A2780 and A2780R cells for PEGylated and non-PEGylated liposomes containing

[**1**](PF$_6$)$_2$. The fluorescent liposomes were composed of neutral (DOPC) or negatively charged (DOPG) lipids, 0 or 4 mol% DSPE-PEG2K and also an additional 5 mol% [**1**](PF$_6$)$_2$. All liposomes were prepared by extrusion in PBS buffer and characterized by DLS (diameter~140 nm) prior to incubation with the cells.
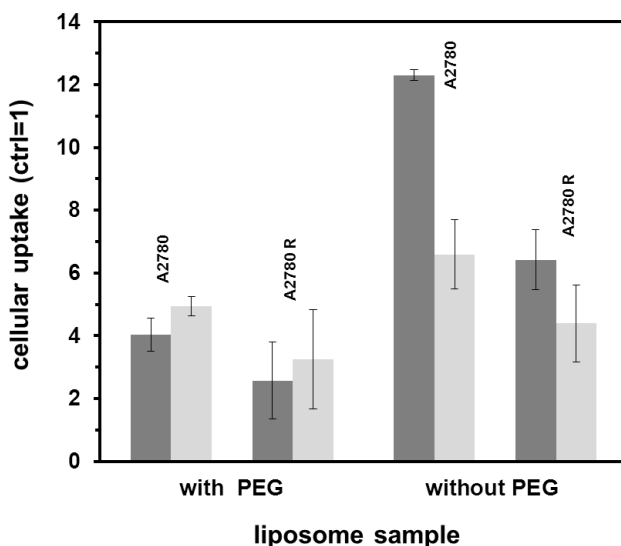


**Figure 5.5.** Effect of PEGylation on cellular uptake by A2780 or A2780 R human ovarian cancer cells of DOPC (dark grey) and DOPG (light grey) liposomes containing 5 mol% [**1**](PF$_6$)$_2$. Liposome formulations: DOPC:DSPE-PEG2K:NBD-PC (92:4:4), DOPG:DSPE-PEG2K:NBD-PC (92:4:4), DOPC: NBD-PC (96:4), or DOPG: NBD-PC (96:4). Incubation conditions: bulk lipid concentration = 1.5 mM (as liposomes) in PBS:DMEM (−FCS, +PS, +ph. red) 8:5, bulk ruthenium concentration $[Ru]_{tot}$ = 0.075 mM, exposure time = 1 h, T = 310 K, 7% CO$_2$, in the dark. Control wells contained untreated cells.

The uptake data (see Figure 5.5) show that for both cell lines the uptake of non-PEGylated DOPC liposomes was more than twice higher than that of PEGylated liposomes. Assuming that the effect of PEGylation on the fluorescence quenching is negligible, PEGylation thus significantly decreases the uptake of neutral liposomes. Moreover, the decrease in cellular uptake of PEGylated liposomes was more distinct for DOPC liposomes in A2780 cells than in A2780R cells. For negatively charged DOPG liposomes, uptake of PEGylated liposomes was only slightly lower than that of non-PEGylated liposomes in both cell lines. For non-PEGylated liposomes DOPC liposomes were taken up in higher amounts than DOPG liposomes in both cell lines.

This observation is in agreement with the results obtained for HepG2 cells; the difference in uptake can be assigned to the higher influence of positive charges of the ruthenium complexes at the surface of neutral DOPC liposomes, compared to that of the same dicationic complexes at the surface of negatively charged DOPG liposomes. Overall, cellular uptake decreases upon PEGylation, and positive ruthenium complexes at the liposome surface increase the cellular uptake of ruthenium functionalized liposomes in absence of PEGylation.

### 5.2.3.2.   Cytotoxicity

In photoactivated chemotherapy the aim is to activate the anticancer complex using light irradiation. Ideally, liposomes functionalized with ruthenium complexes should be non-toxic (or less toxic) in the dark. The dark cytotoxicity of DOPC or DOPG PEGylated liposomes functionalized with ruthenium complexes was determined for A2780 and A2780 R cell lines. Each formulation consisted of DOPC:DSPE-PEG2K (96:4) or DOPG:DSPE-PEG2K (96:4) mixtures containing 0 or 5 mol% of one of the ruthenium complexes $[1](PF_6)_2 - [4](PF_6)_2$. Dark cytotoxicity was determined after 6 h liposome exposure. After incubation the liposomes were removed and cells were incubated in drug-free cell culture medium for 24 h. Then the metabolic activity of the cells was determined using the WST-1 cell proliferation reagent.[39] In this protocol a known quantity of the WST-1 reagent is added to each well, the cells are incubated, and the absorbance $W$ is measured at 450 nm. The formation of a formazan dye is correlated to the metabolic activity of the cells, which can be measured and compared to reference cells. In order to differentiate a large number of poorly active cells from a small number of highly active cells, the metabolic activity obtained by the WST-1 assay was corrected for the amount of cells in each well by dividing the absorbance values $W$ by the protein content $A_{prot}$ of each well as determined in a BCA assay. In order to discuss cell survival, the obtained $W/A_{prot}$ values (corrected metabolic activity) were compared to the corresponding value for untreated cells $(W/A_{prot})_{ctrl} = 1$ or 100%).

The dark cytotoxicity data (Figure 5.6) show that all PEGylated liposomes, with or without ruthenium, exhibited comparably low toxicity against A2780 and A2780 R cells, with cell survival of 70% and 100%, respectively. Thus, no difference was observed between the four different ruthenium complexes and the liposomes were only slightly toxic to A2780 cells and not toxic to A2780 R cells. A low toxicity was observed for A2780 cells treated with liposomes without ruthenium, which suggests

that the toxicity observed in presence of the Ru complex is not due to the metal complexes but to the liposome support. In presence of PEG groups the toxicity of the liposomes was not influenced by the lipid charge (DOPC *vs.* DOPG) in both cell lines.
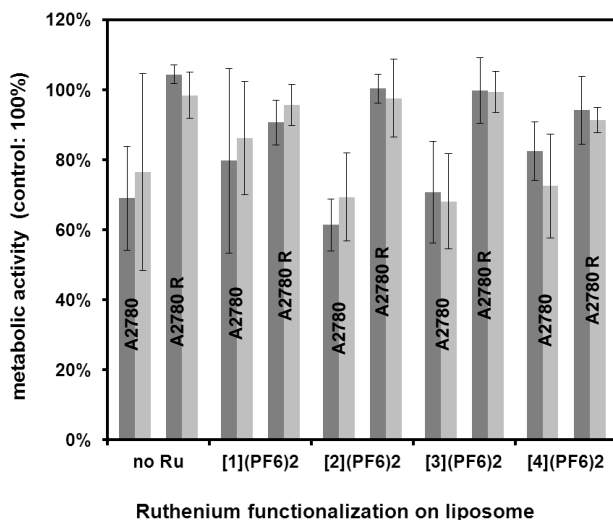


**Figure 5.6.** Metabolic activity ($W/A_{pro}$) of A2780 and A2780 R cells exposed to DOPC (dark grey) and DOPG (light grey) stealth liposomes (4 mol% DSPE-PEG2K) with 5 mol% of ruthenium complexes. Metabolic activity of untreated cells (control) is 100%. Conditions: bulk lipid concentration = 1.5 mM (as liposomes) in PBS:DMEM (−FCS, +PS, −ph. red) (8:5), bulk ruthenium concentration $[Ru]_{tot}$ = 0.075 mM, drug exposure time = 6 h, T = 310 K, 7% $CO_2$ in the dark.

Light cytotoxicity experiments were performed on HepG2 cells exposed to neutral (DMPC) or negatively charged (DMPG) liposomes containing 0 or 5 mol% of complex [**1**]($PF_6$)$_2$. Cells were exposed to the liposomes for 30 min, and after removing the liposome solutions each well was irradiated with blue light ($\lambda_e$=452 nm, power: 69 mW) for 15 min at 37 °C. The metabolic activity of the cells was measured after 24 h incubation in drug-free medium in the dark using the WST-1 assay as explained above. A control cytotoxicity experiment was also performed in the dark to evaluate the effect of light irradiation with HepG2 cells. As shown in Figure 5.7 for all liposome samples, *i.e.*, with or without ruthenium, cell survival was lower after light exposure compared to non-irradiated cells. The best phototoxic activity was obtained for DMPC liposomes functionalized with [**1**]($PF_6$)$_2$, as light cytotoxicity was found to be about 5 times

higher than dark toxicity. For DMPG liposomes with or without ruthenium light cytotoxicity was found to be about 1.6 times higher than dark cytotoxicity.

After irradiation, the metabolic activity of cells treated with DMPC liposomes containing [1]($PF_6$)$_2$ was lower than that of cells treated with DMPC liposomes without ruthenium. This might be related to the photoactivation of the ruthenium complex [1]($PF_6$)$_2$ and releasing the corresponding ruthenium aqua complex inside the cells. In the case of DMPG liposomes the metabolic activity with and without ruthenium was almost the same after light exposure. For DMPG liposomes deprived of ruthenium this may be explained by the absence of light-sensitive element in the liposomes formulation, and the lower metabolic activity might simply be the result of the action of blue light on the cells. For Ru-functionalized DMPG liposomes the uptake was low (Figure 5.3), explaining the limited effect of Ru on phototoxicity.
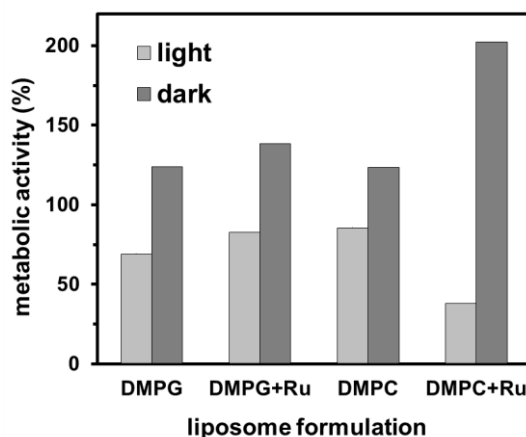


**Figure 5.7.** Metabolic activity $W/A_{prot}$ (see text) of HepG2 cells exposed to non-PEGylated DMPC or DMPG liposomes containing 0 or 5 mol% [1]($PF_6$)$_2$ irradiated with blue light (light grey bars) or kept in the dark (dark gray bars); metabolic activity of untreated cells (control) is 100%. DMPG+Ru or DMPC+Ru represent DMPC or DMPG liposomes containing 5 mol % [1]($PF_6$)$_2$. Conditions: bulk lipid concentration = 2 mM (as liposomes) in phosphate buffer ($I$=50 mM):PBS: (2:3), bulk ruthenium concentration $[Ru]_{tot}$ = 0.1 mM, drug exposure time = 30 min, $T$ = 37 °C, 7% $CO_2$. Irradiation parameters: $\lambda_e$=452 nm (blue light), light power=69 mW, incident spot diameter = 2.3 cm, light intensity: 17 mW.cm$^{-2}$.

## 5.3    Discussion

The uptake data disclosed herein allow for concluding about an optimal liposome formulation. Using PEGylated liposomes decreased liposome uptake by A2780 and A2780 R cells compared to PEG-free formulations, and lowered the effect of positive charge of Ru on cellular uptake. However, PEGylated liposomes are highly beneficial for *in vivo* applications uses as mentioned in the introduction. Actually, finding a compromise between uptake and clearance from the blood stream is not easy; based on the results reported in this chapter 4 mol% PEG in the liposome formulation seems good enough to obtain liposome uptake, in agreement with literature data advocating for ~5 mol% of PEG groups for *in vivo* applications.[40-41]

Cytotoxicity data are not yet complete and suffer from poor statistics. However, initial data disclosed in this work are promising, since liposomes functionalized with ruthenium, either PEGylated or non-PEGylated, showed low dark cytotoxicity against HepG2, A2780 and A2780R cancer cell lines. The poor dark toxicity seems as an advantage for photoactivated chemotherapy (PACT); because in PACT it is the difference in the dark toxicity and the light cytotoxicity that needs to be maximized. In addition high phototoxicity was obtained against HepG2 cells using blue light irradiation (452 nm).  Phototoxicity data on A2780 and A2780R cells are not available yet due to technical problems in the experimental setup used to irradiate cancer cells. Light cytotoxicity was only measured for one ruthenium complex supported on PEG-free liposomes and one type of cancer cells, and these experiments should be performed for the other complexes as well, supported on PEGylated liposomes, and for other cancer cell types. Several critical parameters need to be better controlled or changed in future experiments. For example, the irradiation condition was not optimal, since during irradiation of one well the other wells were not kept in the presence of $CO_2$. Although irradiation time was not too long, the absence of $CO_2$ might also cause cell death. In addition, the drug exposure time for HepG2 cells was very short (30 min) and may not be representative for what happens *in vivo*. Longer drug exposure times should be investigated to see if different cytotoxicities after light irradiation are observed.

As stated by the cellular uptake results, considering the too high detection limit of ICP-OES ruthenium uptake could not be measured using this technique. In absence of the more sensitive ICP-MS apparatus in the laboratory a fluorescent lipid, NBD-PC, was

included in the liposomes to measure the uptake of the Ru-functionalized liposomes by fluorescence spectroscopy. The fluorescence of the NBD-PC lipid, however, was quenched in presence of ruthenium within the same bilayer membrane, as proven for complex [**1**](PF$_6$)$_2$ on DOPC liposomes. The quenching correction for this formulation, however, cannot be generalized for other liposome formulations, as it may be influenced by the detailed structure of the ruthenium complex, by the nature and charge of the lipid, and/or by the presence of PEG groups. Thus, quenching measurements should be performed for each liposome formulation to obtain reliable cell uptake data. In addition, it may be possible that fluorescence quenching in the cellular environment is different from quenching in PBS buffer, as the liposome bilayer might be modified upon entering the cell. Finally, uptake results based on the fluorescence of the NBD-PC lipid would only be correlated to ruthenium uptake if the Ru-S bond is stable and holds the metal complex at the surface of the lipid bilayer in the dark in the cell environment. In this ideal case, cellular uptake of the fluorescently labeled, Ru-functionalized liposomes would indeed mean that the ruthenium prodrug is also taken up by the cells, and that fluorescence data can be interpreted as Ru uptake, after quenching corrections. The thermal stability at 4 °C of the Ru-S bond on DOPC liposomes was good for complex [**3**](PF$_6$)$_2$, but such stability cannot be generalized to other complexes, and it should also be proven at 37 °C and in the buffer:medium solution used to incubate the cells. Overall, uptake data based on the method outlined above are only indicative, and a better measurement of ruthenium uptake would be achieved using a more sensitive and reliable method such as ICP-MS.

## 5.4 Conclusion

Based on the kinetic, uptake, and cytotoxicity data described in this chapter a number of conclusions can be drawn. First, liposomes made of neutral lipids such as DOPC or DMPC are better than negatively charged liposomes based on DOPG or DMPG for supporting the lipophilic Ru polypyridyl complexes [**1**](PF$_6$)$_2$ − [**4**](PF$_6$)$_2$. The photosubstitution quantum yields are higher, and the uptake of the slightly positively-charged liposomes resulting from neutral liposomes and 5 mol% of dicationic ruthenium complexes is better. Even though the cytotoxicity in the dark is not different from that of liposomes built from negatively charged lipids, their phototoxicity after blue light irradiation on HepG2 cells is higher, probably as a result of a higher uptake. The presence of PEG groups at the surface of the liposomes levels out the difference in

uptake between Ru-functionalized liposomes built from neutral lipids and those based on negatively charged lipids (at least for A2780 and A2780R cells), and also resulted in decreased liposome uptake for both DOPC and DOPG liposomes as a result of the steric hindrance of the PEG groups.

The DOPC and DOPG PEGylated liposomes with or without ruthenium were taken up by A2780 and A2780 R cells in 1 h treatment. The uptake seemed poorly affected by the nature of the ruthenium complexes for both cell lines. However, due to the quenching of fluorescence of NBD-PC by the nearby ruthenium complexes, the uptake results based on fluorescence data cannot strictly be interpreted quantitatively. Dark cytotoxicity results showed that DOPC and DOPG PEGylated liposomes functionalized with any of the four ruthenium complexes $[\mathbf{1}](PF_6)_2 - [\mathbf{4}](PF_6)_2$ were poorly toxic against A2780, or A2780 R cells after 6 hour incubation, and that no difference in toxicity was observed between formulations. On the other hand, cell survival after light irradiation of HepG2 cells treated with non-PEGylated DMPC or DMPG liposomes were lower than that of cells kept in the dark, whether ruthenium (as complex $[\mathbf{1}](PF_6)_2$) was present or not.

Overall, liposomes functionalized with polypyridyl ruthenium complexes such as $[\mathbf{1}](PF_6)_2$ are promising light-activatable anticancer prodrugs as they are stable in the dark, taken up by cancer cells, poorly toxic in the dark, and more toxic after visible light irradiation. Light toxicity data suggest that light, ruthenium (as complex $[\mathbf{1}](PF_6)_2$), and lipids, may be combined in a cancer cell to lead to cell death. However, it is not yet proven that such phototoxicity is related to the photosubstitution reaction that can be measured in a UV-vis cell or in an NMR tube. More studies will be needed to conclude on that, in particular, more data are needed with better statistics, the influence of the structure of the ruthenium complex on the phototoxicity should be assessed, as well as the influence of *e.g.* oxygen concentration, irradiation intensity, or irradiation time on phototoxicity must be determined. Finally, in order to conclude on the potential interest of Ru-functionalized liposomes in anticancer therapy, $IC_{50}$ values in the dark and after light irradiation are needed, as well as dark and light toxicity data on healthy cells and in *in vivo* models of cancer.

## 5.5    Experimental

### 5.5.1.   Materials and methods

Pymi,[42] [Ru(terpy)(pymi)Cl]PF$_6$,[42] [Ru(terpy)(bpy)Cl]Cl,[43] ligand **6**,[44] ligand **5**,[36] and ([**1**](PF$_6$)$_2$)[45] were synthesized according to literature procedures. Cholesterol, dicyclohexylcarboiimide (DCC), 4-N,N-dimethylaminopyridine (DMAP), AgBF$_4$, and AgPF$_6$ were bought from Sigma-Aldrich. 1,2-dimyristoyl-*sn*-glycero-3-phosphocholine (DMPC), 1,2-dimyristoyl-*sn*-glycero-3-phospho-(1'-rac-glycerol) sodium salt (DMPG), and 1-acyl-2-{12-[(7-nitro-2-1,3-benzoxadiazol-4-yl)amino]dodecanoyl}-*sn*-glycero-3-phosphocholine (NBD-PC), were purchased from Avanti Polar Lipids. 1,2-dioleoyl-*sn*-glycero-3-phosphocholine (DOPC), 1,2-dioleoyl-*sn*-glycero-3-phospho-(1'-rac-glycerol) sodium salt (DOPG), and 1,2-distearoyl-*sn*-glycero-3-phosphoethanolamine-N-[amino(polyethylene glycol)-2000] ammonium salt (DSPG-2KPEG), were bought from Lipoid. All lipids were stored at −20 °C. Syntheses of the metal complexes were performed in the absence of light and under argon. Pierce™ BCA Protein Assay was purchased as a kit from Thermo Scientific (product #23227). Cell Proliferation Reagent WST-1 was purchased as a kit from Roche Diagnostics (product #05015944001). All media, buffers and sterile plastics used for *in vitro* experiments were purchased from SPL Life Sciences or SARSTEDT AG & Co.

^{1}H and ^{13}C NMR spectra were recorded on a Bruker 300 DPX spectrometer at 25 °C (The notations for proton attribution are shown in Figure 5.1). Chemical shifts are indicated in ppm relative to TMS. Characterization of the liposomes (average size and PDI) was done using a Dynamic Light Scattering (DLS) Zetasizer instrument ($\lambda_{irr}$ = 632 nm) from Malvern. Electrospray mass spectra were recorded on a Finnigan TSQ-quantum instrument by using an electrospray ionization technique (ESI-MS). High resolution mass spectrometry was performed using a Thermo Finnigan LTQ Orbitrap mass spectrometer equipped with an electrospray ion source (ESI) in positive mode (source voltage 3.5 kV, sheath gas flow 10, capillary temperature 275 ºC) with resolution R = 60.000 at *m/z* = 400 (mass range = 150-200) and dioctylphtalate (*m/z* = 391.28428) as "lock mass". Elemental analysis for C, H, N, and S was performed on a Perkin-Elmer 2400 series II analyzer. UV-vis spectra were obtained on a Varian Cary 50 UV-vis spectrometer. The irradiation setup was a LOT 1000 W Xenon arc lamp, fitted with a 400FH90-50 Andover standard cutoff filter and an Andover 450FS10-50 ($\lambda_e$=452 nm, $\Delta\lambda_{1/2}$=8.9 nm) interference filter. Photon fluxes of the irradiation setup was measured using the ferrioxalate actinometer.[46] Tecan M1000 PRO plate reader was used for fluorescence or absorbance measurement of multi-well plates for *in vitro* experiments. The ruthenium concentration after uptake was measured by

inductively coupled plasma atomic emission spectroscopy (ICP-OES) on a Varian VISTA-MPX spectrometer. A Beckman Optima™ L-90K Ultracentrifuge machine was used for ultracentrifugation experiments.

## 5.5.2.    Synthesis

Compound **7**. Cholesterol (200 mg, 0.52 mmol) and N-acetyl-L-methionine (100 mg, 0.52 mmol) were dissolved in anhydrous benzene (10 mL) under argon atmosphere. DCC (140 mg, 0.68 mmol) and DMAP (2 mg, 0.02 mmol, 3%) were added and the mixture was stirred vigorously for 12 hours, after which the solution was filtered to remove insoluble materials. The solvent was evaporated under vacuum by rotary evaporation. The crude product was purified by column chromatography on silica gel (petroleum ether/EtOAc 70:30). The solvents were evaporated by rotary evaporation at 30 ºC, and compound **7** was obtained as a white sticky solid. Yield: 50% (150 mg, 0.26 mmol). $^1$H NMR (300 MHz, CDCl$_3$) δ 6.13 (m, J= 8,18  Hz, 1H, δ), 5.38 (m, J= 4,09  Hz, 1H, 6), 4.70-4.64 (m, 3H, 3, γ), 3.44 (m, 1H, NH), 2.33 (m, 2H, β), 2.10 (s, 3H, α), 2.03 (s, 2H, 4). $^{13}$C NMR (75 MHz, CDCl$_3$) δ 171.70 (Cθ), 169.96 (Cε), 139.30 (C5), 123.18 (C6), 75.65 (C3), 56.79, 56.24, 51.90 (Cγ), 50.11, 39.81, 39.62, 38.07 (Cβ), 36.98, 36.68, 36.29, 33.73, 32.22, 32.01, 31.93 (Cα), 30.05, 28.33, 28.12, 27.82, 27.79, 25.60, 24.93, 23.93, 23.36, 22.93, 21.14 (C4), 19.42, 18.83, 15.67, 11.96. ES MS *m/z* (calc): 560.1 (560.4, [M+H]$^+$), 369.2 (369.4, [M-(acetyl-L-methionine)]$^+$). Elemental analysis (%) for C$_{34}$H$_{57}$NO$_3$S.H$_2$O: (calc); C 70.66, H 10.30, N 2.43, S 5.54; (found); C 70.45, H 9.99, N 2.99, S 5.46.

General procedure for the synthesis of **[2]**(PF$_6$)$_2$, **[3]**(PF$_6$)$_2$, or **[4]**(PF$_6$)$_2$. [Ru(terpy)(N-N)(Cl)](Cl) (0.1 mmol), thioether-cholesterol ligand **6** or **7** (0.15 mmol), and AgBF$_4$ (0.2 mmol) were dissolved in acetone (30 mL). The reaction mixture was refluxed overnight for 24 h in the dark, then it was filtered hot over celite, and the solvent was removed by rotary evaporator under reduced pressure. The product was purified by column chromatography on silica gel (acetone/H$_2$O/sat. aq. KPF$_6$ (100:10:1.5) or (80:20:4)). The acetone was removed from the collected fractions under vacuum, upon which the product precipitated as an orange solid. The product was filtered, washed with water and dried under vacuum for at least 4 h.

**[2]**(PF$_6$)$_2$. Yield: 52%. $^1$H NMR (300 MHz, δ in CDCl$_3$) 9.72 (d, J = 5.3 Hz, 1H, A6), 8.55 (m, J = 8.2 Hz, 3H, A3 + T3'), 8.41 (d, J = 7.9 Hz, 2H, T3), 8.34 (d, J = 8.0 Hz, 1H, B3), 8.27 – 8.14 (m, 2H, A4 + T4'), 8.03 – 7.85 (m, 3H, A5 + T4), 7.74 (t, 1H, B4), 7.68 (d, J = 5.0 Hz, 2H, T6), 7.36 (m, 2H, B5 + B6), 7.16 (m, 2H, T5), 5.30 (d, J = 4.8 Hz, 1H, 6), 3.75 (t, J = 6.6 Hz, 2H, ζ ), 3.64 – 3.37 (m, 10H, α + β + γ + δ + ε), 3.13 (s, 1H, 3), 2.40 – 0.75

(m, 47H), 0.67 (s, 3H). $^{13}$C NMR (75 MHz, δ in CDCl$_3$) 157.67 + 157.01 + 156.31 + 156.29 ( B2+ A2 + T2 + T2'), 153.18 (T6), 151.95 (A6), 149.80 (B6) , 140.86 (5),139.09 (T4), 138.56 +138.37 (B4 + A4), 137.56 (T4'), 128.91 (T5), 128.35 (A5), 127.87 (B5), 125.16 (T3), 124.85 (A3), 124.48 (T3'), 124.03 (B3), 121.86 (6), 79.56 (3), 70.88 + 70.35 + 70.30 + 67.52 + 67.30 (α + β + γ + δ + ε), 56.86, 56.28, 50.26, 42.44, 39.88, 39.64, 39.22, 37.28, 36.97, 36.31, 35.91, 34.47, 32.06, 32.01, 29.82, 28.35, 28.13, 24.42, 23.97, 22.95, 22.69, 21.19, 19.53, 18.85, 15.04, 12.00. UV-vis: $\lambda_{max}$ ($\varepsilon$ in L·mol$^{-1}$·cm$^{-1}$) in CHCl$_3$: 457 nm (6100). ES MS *m/z* exp (calc): 519.7 (519.4, [M−2PF$_6$]$^{2+}$). Elemental analysis for C$_{59}$H$_{79}$F$_{12}$N$_5$O$_3$P$_2$RuS: (calc); C, 53.31; H, 5.99; N, 5.27; S, 2.41. (Found); C, 53.34; H, 6.22; N, 5.15; S 2.41.

**[3]**(PF$_6$)$_2$. Yield: 28%. $^1$H NMR (300 MHz, acetone-d$_6$) δ 9.98 (d, J= 7.5 Hz, 1H, 6A), 8.95 (m, 3H, 3T',3A), 8.78(d, J= 7,5 Hz, 2H, T6), 8.71(d, J= 7,5 Hz, 1H, 6B), 8.56-8.47 (m, 2H, T4',4A), 8.23-8.13 (m, 3H, T5, 5A), 8.04-8.00 (m, 3H, T3, 5B), 7.57-7.54 (m, 3H, 3B, T4), 7.31 (m, 1H, 4B), 7.17 (d, J= 7,5, 1H, δ), 5.35 (m, 1H, 6), 4.45-4.42 (m, 2H, γ, 3). $^{13}$C NMR (75 MHz, acetone-d$_6$) δ 171.21 (θ), 170.47 (ε), 159.01, 158.43, 157.79, 157.67, 154.43, 154.41, 153.35, 151.01, 140.40 (5), 139.99, 139.95, 139.24, 139.19, 138.05, 129.60, 129.56, 128.90, 128.25, 126.06, 125.68, 125.35, 124.84, 123.46 (6), 75.67 (3), 57.57, 57.06, 51.32 (γ), 51.01, 43.11, 40.61, 40.26, 38.68 (β), 37.66, 37.33, 36.96, 36.59, 32.70 (α), 32.59, 31.12, 30.61, 28.69, 28.35, 24.92, 24.53, 23.07, 22.83, 21.74 (4), 19.65, 19.14, 14.04, 12.23. UV-vis: $\lambda_{max}$ in nm ($\varepsilon$ in L·mol$^{-1}$·cm$^{-1}$) in CHCl$_3$: 460 nm (8310). ES MS *m/z* (calc): 1195.9 (1195.4, [M−PF$_6$]$^+$), 525.7 (525.2, [M−2PF$_6$]$^{2+}$). HRMS *m/z* (calc): 525.23715 (525.23685, [M−2PF$_6$]$^{2+}$).

**[4]**(PF$_6$)$_2$. Yield: 34%. $^1$H NMR (300 MHz, acetone-d6) δ 10.04-10.02 (d, J = 7.3 Hz, 1H, 6Py), δ 9.09 (s, 1H, i), δ 8.69 (d, J=6.8 Hz, 3H, T6 +3Py), 8.59 (d, J = 8.1 Hz, 2H, T3'+T5'), 8.53 (t, J = 7.7 Hz, 1H, 4Py), 8.39 – 8.16 (m, 4H, 5T, 5Py, T4'), 8.08 (dd, J = 11.6, 5.4 Hz, 2H, T3), 7.81 – 7.62 (t, J = 8.1 Hz, 2H, T4), 7.14 (t, J = 8.2, 2H, p-Ph + δ), 7.00 (t, J = 7.8 Hz, 2H, o-Ph), 6.00 – 5.87 (d, 7.2 Hz, 2H, m-Ph), 5.34 (s, 1H, 6), 4.43 (d, J = 8.5 Hz, 2H, γ + 3), 3.62 – 3.44 (m, 1H, ε) 2.24 (s, 2H, β), 1.83 (s, 5H), 1.52 (d, J = 12.3 Hz, 5H), 1.00 (s, 4H), 0.94 (d, J = 6.5 Hz, 3H), 0.86 (dd, J = 6.6, 1.0 Hz, 6H), 0.71 (s, 3H). $^{13}$C NMR (75 MHz, acetone-d6) δ 205.31 (θ), 170.34 (ε), 170.07 (i), 158.07 (T2 or T2' or 2Py), 156.77 (T2 or T2' or 2Py), 154.18 (T3), 153.02, 147.13 (T2 or T2' or 2Py), 139.47 (T5), 138.05 (4Py), 136.77 (T4'), 131.44 (3Py), 129.57 (5Py), 129.23 (o-Ph), 129.06 (4T), 129.01, 128.01 (p-Ph, 124.85 (6T), 123.73 (3T'), 122.65 (6), 119.95 (m-Ph), 74.82 (ε), 56.72, 56.21, 50.40 (3), 50.15, 42.26, 39.76, 39.42, 37.84, 36.81, 36.48, 36.12, 35.77, 33.80, 31.85, 31.75, 30.53, 29.79, 29.53, 29.27, 29.02, 28.76, 28.63, 28.50, 28.25, 28.07, 27.87, 27.51, 24.09, 23.69, 22.50, 22.25, 22.00, 20.90, 18.81, 18.31, 14.47, 13.46, 11.39.

ES MS $m/z$ (calc): 1221.5 (1221.45, $[M -PF_6]^+$), 707.0 (707.1, $[M -2PF_6-cholesteryl]^+$), 538.3 (538.2, $[M-2PF_6)]^{2+}$). UV-vis: $\lambda_{max}$ ($\varepsilon$ in L·mol$^{-1}$·cm$^{-1}$) in acetone: 475 nm (10300). Elemental analysis for $C_{61}H_{78}F_{12}N_6O_3P_2RuS$: calc: C 53.62, H 5.75, N 6.15, S 2.35 found: C 54.44, H 5.66, N 5.98, S 1.45.

### 5.5.3. Liposome preparation

Stock solutions of phospholipids ($5.0\times10^{-3}$ M in CHCl$_3$ or CHCl$_3$:CH$_3$OH (4:1)) and of ruthenium complexes [**1**](PF$_6$)$_2$ – [**4**](PF$_6$)$_2$ ($5.0\times10^{-4}$ M in CHCl$_3$) were prepared and stored at $-20$ °C. The stock solutions were mixed in proportions corresponding to the desired liposome formulation. The solvents of the lipid mixture were evaporated to form a lipid film at the bottom of a glass tube. Traces of solvent were removed under high vacuum for at least 1 h. Each sample was then hydrated with the desired buffer (PBS: Phosphate Buffered Saline or chloride-free phosphate buffer: 10 mM of phosphates, $I = 50$ mM, pH = 6.97) at 50 °C. The bulk lipid concentration in each sample was 2.50 mM and the ruthenium concentration for ruthenium-functionalized liposomes was 0.125 mM. Each sample was put through at least 10 freeze/thaw cycles (from liquid nitrogen to 50 °C) until a clear solution was obtained. The liposome solution was then extruded at least 11 times at 50 °C using the Avanti Polar Lipids mini-extruder fitted with a 200 nm pore diameter Whatman polycarbonate filter. After extrusion, the samples were characterized by Dynamic Light Scattering (DLS) at 25 °C to determine the average diameter (130 – 140 nm in general). The samples were stored in the dark at 4 °C if not used right away.

### 5.5.4. Light irradiation of liposome samples and UV-vis experiments

A liposome sample (1.5 mL) containing phospholipids (2.5 mM) and a ruthenium complex [**1**](PF$_6$)$_2$, [**2**](PF$_6$)$_2$, [**3**](PF$_6$)$_2$, or [**4**](PF$_6$)$_2$ (5 mol%, 0.125 mM) in a phosphate buffer solution, ($I$=50 mM, pH=7.0) was placed into a UV-vis cell. 1.5 mL of the phosphate buffer solution was added to the cuvette. The final concentrations of the lipid and of the ruthenium complex in the cuvette were 1.3 mM and 0.065 mM, respectively. The UV-vis spectrum of the sample was first measured in the dark. Then the sample was irradiated at 452 nm using the beam of a LOT 1000 W Xenon arc lamp filtered by an Andover bandpath filter, and directed into an 2.5 mm diameter optical fiber bundle bringing the light inside the spectrophotometer, vertically to the cuvette axis, *i.e,* perpendicular to the horizontal optical axis of the spectrophotometer (see Appendix I, Figure AI.1*)*. The UV-vis spectrum of the sample was measured every 3 minutes during irradiation while stirring at 25 °C or 37 °C. The irradiation time varied between 2 and 6 h (depending to the kinetics of the reaction) to reach the photochemical steady state. The concentrations in *[RuSRR']* ([**1**]$^{2+}$ to [**4**]$^{2+}$) was

determined by deconvolution knowing the extinction coefficients of both RuSRR' and RuOH$_2$ species (see Appendix I and V). The evolution of ln($[RuSRR']/[Ru]_{tot}$) was plotted as a function of irradiation time, and from the slope $S$ of the plot $-k_\varphi$ at $\lambda_e$=452 nm was determined for each sample. Knowing the photon flux and probability of photon absorption $1-10^{-3A_e}$, where $A_e$ is the absorbance of the solution at the excitation wavelength $\lambda_e$, the number of moles of photons $Q$ absorbed at time $t$ by RuSRR' since $t_e$=0 was calculated. Plotting $n_{RuSRR'}$ *vs.* $Q$ gave a straight line in each case. The slope of this plot directly corresponds to the quantum yield of the photosubstitution reaction (see Appendix I, Section AI.3.2*).

### 5.5.5.  Stability of the ruthenium-sulfur bond in PBS in the dark

7 mL of a DOPC:DSPE-PEG2K (98:2) liposome sample containing 5 mol% of complex [**3**](PF$_6$)$_2$ was prepared in PBS (total lipid bulk concentration: 2.5 mM, $[Ru]_{tot}$=0.125 mM). 6.5 mL of this liposome solution was diluted with 6.5 mL of PBS (final lipid concentration: 1.25 mM, $[Ru]_{tot}$=0.065 mM). 4 mL fractions of this solution were subjected to ultracentrifugation (speed = 40,000 rpm, RCF = 100,000 g, T = 20 °C, time = 2 h) at different times (1 day, 3 days, and 7 days) after sample preparation. The ruthenium content of the supernatant and of the liposome sample before ultracentrifugation were measured by ICP-OES (sample was prepared as described in Appendix V).

### 5.5.6.  Cell lines and culture conditions

The human ovarian carcinoma cell line A2780 and its cisplatin resistant analogue A2780R were grown as a monolayer at 37 °C in 7% CO$_2$ atmosphere, and were maintained in a continuous logarithm culture in Dulbecco's Modified Eagle Medium (DMEM) containing phenol red completed with 10% Fetal Calf Serum (FCS), penicillin/ streptomycin (100 units/ml, 0.1 mg/ml, respectively), and Glutamax (2 mM). This medium will be further referred to as 'DMEM (+FCS, +P/S, +ph. red). Human liver hepatocellular carcinoma cells HepG2 were grown in HepaRG medium at 37 °C in 5% CO$_2$ atmosphere.

### 5.5.7.  Cellular uptake assay

For cellular uptake experiments, liposome solutions containing 4% NBD-PC were prepared in PBS as described in section 5.5.3. 24-well plates were seeded with A2780 or A2780 R cells at $5.0 \times 10^4$ cells/well. Typically, a plate seeded with cells was pre-incubated for 3 days (A2780) or 2 days (A2780 R) at 37 °C in 7% CO$_2$ atmosphere until ~100% confluence was reached. At the day of cells treatment with the liposome sample, cell culture medium in the wells was replaced with fresh medium DMEM (−FCS, + P/S, +ph. red) at 37 °C 1.5 h

before treatment. 800 µL of liposome solution in PBS was diluted with 500 µL of DMEM (−FCS, + P/S, +ph. red) (total lipid bulk concentration =1.5 mM, ruthenium concentration = 0.075 mM). Before incubating the cells with liposome solutions, the medium was aspirated from each well. Then the cells were exposed to 300 µL of liposome-DMEM solution for 1 h at 37 °C in 7% $CO_2$ atmosphere in the dark. Control wells were filled with 300 µL of a PBS:DMEM (−FCS, +PS, +ph. red) (8:5) mixture. After 1 h liposome exposure, the liposome solution was removed and the cells were gently washed once with 1 mL PBS. Then 500 µL of PBS was added to each well and the fluorescence of NBD-PC lipids taken up by the cells was read with a fluorescence spectrophotometer ($\lambda_{exc}$ = 460 nm, $\lambda_{em}$ = 534 nm). PBS was then removed, 500 µL of 0.2 M NaOH was added to each well, and the plate was rocked at r.t. for 1 hour to lyse the cells. The cell lysis was either used directly in a BCA protein determination assay or stored at −20 °C for later use in a BCA protein assay (see section 5.5.8). To determine the cellular uptake, the fluorescence measurement $F$ for each well, due to the NBD-PC lipids, were divided by the absorbance values $A_{prot}$ obtained from the BCA assay. Finally, $F/A_{prot}$ for each well was divided by $(F/A_{prot})_{ctrl}$ of the well containing cells that were not treated with liposomes, to obtain the "fold increase of F/A" as compared to the control (normalized values for control = 1 or 100%). The obtained value represents the cellular uptake of each liposome sample. The ruthenium content of the cell lysis was measured by ICP-OES as well (see Appendix AV.2 for the sample preparation protocol).

### 5.5.8. BCA protein determination assay

Protein determination was done using the BCA (bicinchoninic acid) protein determination assay (PierceTM BCA Protein Assay Kit, Thermo Scientific). For this assay, a working reagent was prepared from reagents included in the BCA protein assay kit: Reagent A: Bicinchoninic acid and tartrate in an alkaline carbonate buffer solution. Reagent B: 4% $CuSO_4.5H_2O$ (aqueous solution). The working reagent was prepared by mixing reagent A and B in a volumetric ratio of 50:1. For the BCA assay, a 96-well plate was filled with 200 µL of the working reagent in each well. 25 µL of the cell lysis (in 0.2 M NaOH) after cytotoxicity or uptake experiment (cells were killed in NaOH 0.2 M) was mixed with the working reagent in the corresponding wells of the 96-wells plate. As a control, 25 µL of Milli-Q was added to 200 µL working reagent. After addition, the working reagent and the cell lysis solutions were properly mixed. The plate was then protected from light and incubated at 37 °C and 7% $CO_2$ for 30 minutes, and the absorbance ($A_{prot}$) of each well in the plate was then measured at 562 nm using a Tecan M1000 PRO plate reader.

### 5.5.9. Confocal microscopy measurements

Confocal microscopy culture dishes (cover glass bottom dish, 35×10 mm, gamma irradiated, SPL Life Sciences) were incubated with fibronectin (0.0005%; 1:200 dilution, Sigma-Aldrich, F1141) in 0.9% NaCl for 1-2 h at 37 °C. Typically, 300 μL is used per well in an 8-well plate. This volume should be corrected for well surface if wells of other dimensions are used. HepG2 cells ($3.2 \times 10^5$) were seeded on confocal microscopy culture dishes (on the cover glass only) and grown for 24 h in HepaRG medium (volume = 2.5 mL)at 37 °C in an atmosphere of 5% $CO_2$. Before incubation with liposomes (containing 5% fluorescent NBD-PC lipid) in order to do fluorescence measurements, the growth medium was aspirated and replaced with 1.5 mL of fresh William's E Medium containing penicillin/streptomycin (100 unit/mL and 0.1 mg/mL, respectively) and glutamax (2mM), equilibrated at 37 °C. Next, 500 μL of the liposome suspension (lipid concentration = 0.50 mM in chloride-free phosphate buffer:PBS (1:4), ruthenium 0 or 5 mol%) was added to the culture dish. The cells were incubated for 1 h at 37 °C in an atmosphere of 5% $CO_2$ and 95% air. Before confocal microscopy, cells were washed 3 times with 2 mL PBS equilibrated at 37 °C. 2 mL of PBS was added to the culture dish and the cells were imaged by confocal microscopy (Leica Microsystems, SP2 confocal microscope, 63 times oil immersion objective).

### 5.5.10. Dark cytotoxicity assay

A2780 or A2780 R cells were seeded at $5.0 \times 10^4$ cells/well and grown in 500 μL DMEM (+FCS, +PS, + ph. red) in 24 well-plates. No cells were seeded in well F4. The plates were pre-incubated for either 2 days (A2780 R) or 3 days (A2780) at 37 °C in 7% $CO_2$ atmosphere until ~100% confluence was reached. The medium was refreshed 1.5 h before exposure of the cells with liposome solutions. Liposome samples (without NBD-PC) were prepared in PBS before the start of the experiment as described in section 5.5.3 and diluted with DMEM as described in section 5.5.7. Total lipid concentration and ruthenium concentration were 1.5 mM and 0.075 mM, respectively. The medium was removed from the wells and 300 μL of liposome stock solution at r.t. was added in each well. The cells were then incubated for 6 h at 37 °C and 7% $CO_2$ in the dark. After incubation, the supernatant was removed from the cell wells. The cells were washed once with 1 mL of PBS at r.t and 500 μL of fresh DMEM (+FCS, +PS, −ph. red) was added to each well. The cells were then incubated for 24 h at 37 °C and 7% $CO_2$, before measuring cell metabolic activity using the WST-1 assay (see section 5.5.11).

### 5.5.11. WST-1 assay

WST-1 is a colorimetric assay for the quantification of cellular proliferation and cytotoxicity. As mentioned in section 5.5.10, the cells were incubated in a drug-free medium for 24 h prior to perform WST-1 assay. After 24 h, the medium was replaced with 250 µL of fresh DMEM (+FCS, +PS, −ph. red). Well F4 was filled with 250 µL of DMEM (+FCS, +PS, −ph. red) to be used as a control (no cells in this well). Absorbance of each well was read at 450 nm to check for possible absorption of ruthenium in the absorption range of WST-1 (420 to 480 nm), but the ruthenium absorption was negligible and almost equal to that of wells that contained no ruthenium. The plate was then incubated for 15 minutes at 37 °C and 7% $CO_2$, after which the cell proliferation reagent WST-1 (1/10 of the medium volume: 25 µL) was added to each well. The WST-1 and the medium in the wells were properly mixed and the plate was incubated for 60 minutes at 37 °C and 7% $CO_2$. After incubation, the absorbance of the solution in each well was read again at 450 nm. The supernatant was then removed and cells were washed once with 1 mL of PBS at r.t. Cells were then lysed by adding 500 µL of 0.2 M NaOH to each well and the plate was incubated for 1 h at r.t. while rocking. The protein content of the cell lysis was then determined by a BCA assay (see section 5.5.8). WST-1 cell proliferation results $W'$ were corrected by subtracting the absorbance value found for the control well (F4) $W'_{ctrl}$. The values $W = W' - W'_{ctrl}$ were then divided by the protein absorption data $A_{prot}$ obtained from a BCA assay, to give the metabolic activity of the cells per well $W/A_{prot}$. By dividing the metabolic activity found for each well, by the metabolic activity of the control wells $(W/A_{prot})_{ctrl}$ (no liposomes), the values for metabolic activity (cell survival) were normalized with respect to control (no liposomes), which was set to be 100% cell survival.

### 5.5.12. Light cytotoxicity assay

HepG2 cells were seeded at $2.5 \times 10^4$ cells/well and grown in 500 µL HepaRG (+FCS, +PS, + ph. red) in 24 well-plates. Control wells contained no cells. The plate was pre-incubated for 2 days at 37 °C in 5% $CO_2$ atmosphere. The medium was refreshed 1.5 h before exposure of the cells to the liposomes. Liposome samples (without NBD-PC) in chloride-free phosphate before (800 µL) were diluted with PBS (1200 µL). Total lipid concentration and ruthenium concentration were 2 mM and 0.1 mM, respectively. The medium was removed from the wells and 200 µL of liposome stock solution at r.t. was added to each well in the dark and the cells were incubated for 30 min at 37 °C and 5% $CO_2$ in the dark. After 30 min liposome exposure, the liposome suspension was removed; the cells were washed once with 500 µL of PBS (37 °C) in the dark. Subsequently, 300 µL of HepaRG was added per well and the plate was incubated in the dark at 37 °C in 5% $CO_2$ atmosphere

for 15 min. The plate was placed on a custom-built heated aluminum pad (37 °C, measured with a thermocouple, set temp water bath = 58.5 °C) and irradiated at 452 nm for 15 min per well (light toxicity) in an otherwise dark room (dark toxicity). The filter was cooled with pellets of dry ice (irradiation parameters: incident spot diameter = 2.3 cm; power = 69 mW, light intensity: 17 mW·cm$^{-2}$). After irradiation, 200 μL of HepaRG medium was added to each well of both plates and the cells were incubated for 1 day prior to perform WST-1 assay. The metabolic activity of the cells was determined as described in section 5.5.11 and compared with the metabolic activity of the HepG2 cells which were exposed to the same liposome samples (for 30 min) but kept in the dark during the irradiation time (dark cytotoxicity).

## 5.6    References

[1]     A. Levina, A. Mitra, P. A. Lay, *Metallomics* **2009**, *1*, 458-470.
[2]     A. Bergamo, C. Gaiddon, J. H. M. Schellens, J. H. Beijnen, G. Sava, *J. Inorg. Biochem.* **2012**, *106*, 90-99.
[3]     W. Han Ang, P. J. Dyson, *Eur. J. Inorg. Chem.* **2006**, *2006*, 4003-4018.
[4]     V. Pierroz, T. Joshi, A. Leonidova, C. Mari, J. Schur, I. Ott, L. Spiccia, S. Ferrari, G. Gasser, *J. Am. Chem. Soc.* **2012**, *134*, 20376-20387.
[5]     D. Ossipov, S. Gohil, J. Chattopadhyaya, *J. Am. Chem. Soc.* **2002**, *124*, 13416-13433.
[6]     I. Kostova, *Curr. Med. Chem.* **2006**, *13*, 1085-1107.
[7]     G. Stochel, A. Wanat, E. Kuliś, Z. Stasicka, *Coord. Chem. Rev.* **1998**, *171*, 203-220.
[8]     N. J. Farrer, L. Salassa, P. J. Sadler, *Dalton Trans.* **2009**, 10690-10701.
[9]     M. C. DeRosa, R. J. Crutchley, *Coord. Chem. Rev.* **2002**, *233–234*, 351-371.
[10]    A. Juzeniene, Q. Peng, J. Moan, *Photochem. Photobiol. Sci.* **2007**, *6*, 1234-1245.
[11]    B. S. Howerton, D. K. Heidary, E. C. Glazer, *J. Am. Chem. Soc.* **2012**, *134*, 8324-8327.
[12]    M. J. Clarke, *Coord. Chem. Rev.* **2003**, *236*, 207.
[13]    R. E. Goldbach, I. Rodriguez-Garcia, J. H. van Lenthe, M. A. Siegler, S. Bonnet, *Chem. Eur. J.* **2011**, *17*, 9924-9929.
[14]    D. Peer, J. M. Karp, S. Hong, O. C. FaroKhzad, R. Margalit, R. Langer, *Nat. Nanotechnol.* **2007**, *2*, 751-760.
[15]    T. L. Andresen, S. S. Jensen, K. Jorgensen, *Prog. Lipid Res.* **2005**, *44*, 68-97.
[16]    M. Frasconi, Z. C. Liu, J. Y. Lei, Y. L. Wu, E. Strekalova, D. Malin, M. W. Ambrogio, X. Q. Chen, Y. Y. Botros, V. L. Cryns, J. P. Sauvage, J. F. Stoddart, *J. Am. Chem. Soc.* **2013**, *135*, 11603-11613.
[17]    Gregoria.G, E. J. Wills, C. P. Swain, A. S. Tavill, *Lancet* **1974**, *1*, 1313-1316.
[18]    K. W. Ferrara, M. A. Borden, H. Zhang, *Acc. Chem. Res.* **2009**, *42*, 881-892.
[19]    A. K. Giddam, M. Zaman, M. Skwarczynski, I. Toth, *Nanomed.* **2012**, *7*, 1877-1893.
[20]    G. Sharma, S. Anabousi, C. Ehrhardt, M. Kumar, *J. Drug Target.* **2006**, *14*, 301-310.
[21]    Y. Malam, M. Loizidou, A. M. Seifalian, *Trends Pharmacol. Sci.* **2009**, *30*, 592-599.
[22]    M. L. Immordino, F. Dosio, L. Cattel, *Int. J. Nanomedicine* **2006**, *1*, 297-315.
[23]    M. C. Woodle, M. S. Newman, J. A. Cohen, *J. Drug Target.* **1994**, *2*, 397-403.
[24]    A. S. L. Derycke, P. A. M. de Witte, *Adv. Drug Delivery Rev.* **2004**, *56*, 17-30.

[25]     T. M. Allen, C. Hansen, F. Martin, C. Redemann, A. Yauyoung, *Biochim. Biophys. Acta* **1991**, *1066*, 29-36.

[26]     T. M. Allen, A. Chonn, *FEBS Lett.* **1987**, *223*, 42-46.

[27]     N. Maurer, D. B. Fenske, P. R. Cullis, *Expert Opin. Biol. Ther.* **2001**, *1*, 923-947.

[28]     D. C. Drummond, C. O. Noble, M. E. Hayes, J. W. Park, D. B. Kirpotin, *J. Pharm. Sci.* **2008**, *97*, 4696-4740.

[29]     W. T. Al-Jamal, K. Kostarelos, *Acc. Chem. Res.* **2011**, *44*, 1094-1104.

[30]     K. Djanashvili, T. L. M. ten Hagen, R. Blange, D. Schipper, J. A. Peters, G. A. Koning, *Bioorg. Med. Chem.* **2011**, *19*, 1123-1130.

[31]     G. N. Kaluderovic, A. Dietrich, H. Kommera, J. Kuntsche, K. Maeder, T. Mueller, R. Paschke, *Eur. J. Med. Chem.* **2012**, *54*, 567-572.

[32]     H. Chen, R. C. MacDonald, S. Li, N. L. Krett, S. T. Rosen, T. V. O'Halloran, *J. Am. Chem. Soc.* **2006**, *128*, 13348-13349.

[33]     K. J. Harrington, G. Rowlinson-Busza, K. N. Syrigos, R. G. Vile, P. S. Uster, A. M. Peters, J. S. W. Stewart, *Clin. Cancer Res.* **2000**, *6*, 4939-4949.

[34]     L. Simeone, G. Mangiapia, G. Vitiello, C. Irace, A. Colonna, O. Ortona, D. Montesarchio, L. Paduano, *Bioconjug. Chem.* **2012**, *23*, 758-770.

[35]     G. Mangiapia, G. D'Errico, L. Simeone, C. Irace, A. Radulescu, A. Di Pascale, A. Colonna, D. Montesarchio, L. Paduano, *Biomaterials* **2012**, *33*, 3770-3782.

[36]     S. Bonnet, B. Limburg, J. D. Meeldijk, R. J. M. K. Gebbink, J. A. Killian, *J. Am. Chem. Soc.* **2010**, *133*, 252-261.

[37]     M. Kvasnica, M. Budesinsky, J. Swaczynova, V. Pouzar, L. Kohout, *Bioorg. Med. Chem.* **2008**, *16*, 3704-3713.

[38]     P. K. Smith, R. I. Krohn, G. T. Hermanson, A. K. Mallia, F. H. Gartner, M. D. Provenzano, E. K. Fujimoto, N. M. Goeke, B. J. Olson, D. C. Klenk, *Anal. Biochem.* **1985**, *150*, 76-85.

[39]     M. Ishiyama, M. Shiga, K. Sasamoto, M. Mizoguchi, P. G. He, *Chem. Pharm. Bull.* **1993**, *41*, 1118-1122.

[40]     D. D. Lasic, D. Needham, *Chem. Rev.* **1995**, *95*, 2601-2628.

[41]     S. M. Moghimi, J. Szebeni, *Prog. Lipid Res.* **2003**, *42*, 463-478.

[42]     A. C. G. Hotze, J. A. Faiz, N. Mourtzis, G. I. Pascu, P. R. A. Webber, G. J. Clarkson, K. Yannakopoulou, Z. Pikramenou, M. J. Hannon, *Dalton Trans.* **2006**, 3025-3034.

[43]     K. J. Takeuchi, M. S. Thompson, D. W. Pipes, T. J. Meyer, *Inorg. Chem.* **1984**, *23*, 1845-1851.

[44]     A. Bahreman, B. Limburg, M. A. Siegler, R. Koning, A. J. Koster, S. Bonnet, *Chem. Eur. J.* **2012**, *18*, 10271-10280.

[45]     S. Bonnet, B. Limburg, J. D. Meeldijk, R. J. M. K. Gebbink, J. A. Killian, *J. Am. Chem. Soc.* **2011**, *133*, 252-261.

[46]     J. G. P. Calvert, J. N., *Chemical actinometer for the determination of ultraviolet light intensities. In Photochemistry,*Wiley and Sons, New York, **1967**; 780.

# 6

# Yellow-light sensitization of a ligand photosubstitution reaction in a ruthenium polypyridyl complex covalently bound to a rhodamine dye
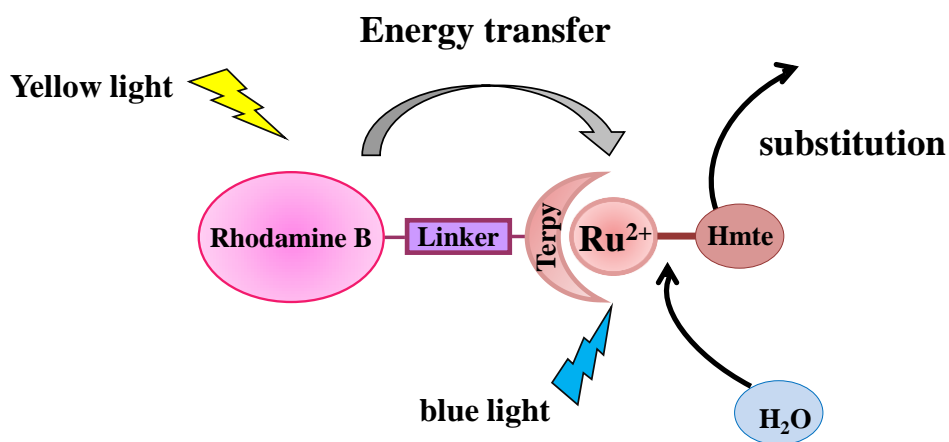
**Abstract**

The ruthenium complex [Ru(terpy)(bpy)(Hmte)]$^{2+}$ ([**1**]$^{2+}$), where terpy is 2,2';6',2"–terpyridine, bpy is 2,2'-bipyridine, and Hmte is 2-methylthioethan-1-ol, poorly absorbs yellow light, and although its quantum yield for the photosubstitution of Hmte by water is comparable at 570 nm and at 452 nm (0.011(4) *vs.* 0.016(4) at 298 K at neutral pH), the photoreaction using yellow photons is very slow. Complex [**1**]$^{2+}$ was thus functionalized with rhodamine B, an organic dye known for its high extinction coefficient for yellow light. Complex [Ru(Rterpy)(bpy)(Hmte)]$^{3+}$ ([**2**]$^{3+}$) was synthesized, where Rterpy is a terpyridine ligand covalently bound to rhodamine B *via* a short saturated linker. [**2**]Cl$_3$ shows a very high extinction coefficient at 570 nm (44000 M$^{-1}\cdot$cm$^{-1}$), but its luminescence upon irradiation at 570 nm is completely quenched in aqueous solution. The quantum yield for the photosubstitution of Hmte by water in [**2**]$^{3+}$ was comparable to that in [**1**]$^{2+}$ at 570 nm (0.0085(6) *vs.* 0.011(4), respectively), which, in combination with the much higher extinction coefficient, resulted in a higher photosubstitution rate constant for [**2**]$^{3+}$ than for [**1**]$^{2+}$. The energy of yellow photons is thus transferred efficiently from the rhodamine antenna to the ruthenium center, leading to efficient photosubstitution of Hmte. These results bring new opportunities for extending the photoactivation of polypyridyl ruthenium complexes towards longer wavelengths.

## 6.1. Introduction

Ruthenium polypyridyl complexes are known for their rich photochemistry, which often requires blue light irradiation.[1-7] In such complexes, photon absorption into a Metal-to-Ligand Charge-Transfer band ($^1$MLCT) typically situated between 400 and 500 nm, leads to the corresponding $^3$MLCT state *via* intersystem crossing. If the distortion of the octahedral coordination geometry is sufficient to decrease the ligand field splitting energy, further thermal population of the Metal-Centered excited states ($^3$MC) may result in ligand photosubstitution reactions.[8-11] Recently, this type of photoactive metal complexes have been proposed as light-activated drugs in phototherapy, as the aqua photoproducts may typically interact with biomolecules and lead to significant cytotoxicity, whereas the initial complex may not.[12-21] As has been shown in the literature dealing with Photodynamic Therapy (PDT)[22-24] light activation allows for controlling the amount of reactive oxygen species produced locally, which may contribute to limiting toxicity and side-effects during chemotherapy. On the other hand, blue light irradiation *in vivo* has a rather limited applicability for PDT since its tissue penetration is low.[25-26] The fact that the MLCT band of most polypyridyl ruthenium complexes is located in the blue region has been restricting, up to now, real phototherapeutic applications of these complexes. Thus, it is of great interest to make the photoactivation of ruthenium polypyridyl complexes possible with photons of longer wavelengths, without sacrificing the complex stability in the dark, which is an important requirement in photochemotherapy.

One strategy, recently reviewed by Brewer *et al.*,[27] is to design complexes having their MLCT band at higher wavelengths. Such strategy sometimes lowers the stability of the complexes in the dark, but a few complexes have been published that are reasonably stable in the dark and photoactive using red light. A second strategy is the coordination of a fluorescent ligand to the ruthenium center in order to sensitize the metal complex with photons of higher wavelength. Mascharak and co-workers [28-30] have used this strategy to bring the sensitization of ruthenium nitrosyl compounds from the UV to the visible region. Typically, direct coordination of the fluorophore to ruthenium promotes merging of the absorption band of both fragments, thus shifting light activation of the metal center towards higher wavelengths.[31] A third, somewhat similar strategy, is to link the fluorophore to the ruthenium complex *via* a non-conjugated linker and to use the "reverse" FRET effect.

Efficient Förster energy transfer (FRET) from a fluorophore to a ruthenium center is typically obtained when the [1]MLCT absorption band of the ruthenium complex overlaps well with the emission band of the fluorophore. The efficiency of FRET is also related to the distance between the energy donor and the energy acceptor.[32-34] When the maximum of the emission spectrum of the dye is at lower wavelength than the absorption maximum of the ruthenium complex, forward FRET is obtained.[35-37] However, for phototherapeutic application, photoactivation of the ruthenium complex *via* forward FRET, *i.e.,* with photons of low wavelength, is not suitable, and "reverse FRET" from a fluorophore with an emission maximum at a higher wavelength than that of the absorption maximum of the ruthenium moiety, is preferable.[34] Etchenique and co-workers recently introduced this strategy by coordinating a green-emitting, rhodamine B-functionalized nitrile ligand to a chlorido- bis(bipyridine)ruthenium(II) compound. The use of a saturated linker avoided orbital overlap between the dye and the complex, and green light irradiation was shown to result in photosubstitution of the nitrile ligand, thus releasing the fluorophore from the ruthenium complex.[38]

We report here a new photoactivatable system relying on reverse FRET, in which coupling of the rhodamine B dye is realized at the 4' position of a spectator terpyridine ligand that is not released upon light irradiation (Figure 6.1). The photosubstitution of the thioether Hmte ligand by an aqua ligand in complex $[Ru(terpy)(bpy)(Hmte)]^{2+}$ (compound $[\mathbf{1}]^{2+}$, where terpy is 2,2';6',2''-terpyridine, bpy is 2,2'-bipyridine, and Hmte is 2-methylthioethan-1-ol) is reported in Chapter 3. The absorption spectrum of $[\mathbf{1}]^{2+}$ extends up to 610 nm and only slightly overlaps with the emission band of rhodamine B ($\lambda_{em}$=570 nm) (Figure 6.1b). The rhodamine B-functionalized analogue complex $[\mathbf{2}]^{3+}$ (Figure 6.1c) may thus allow energy transfer from the fluorophore to the ruthenium center to occur, thus leading to efficient ligand photosubstitution. The high extinction coefficient of the organic dye may allow for more efficient photon collection and thus faster photosubstitution of Hmte when excited near 600 nm, compared to complex $[\mathbf{1}]^{2+}$. In this Chapter, the rate and quantum yield for the photosubstitution of Hmte in the analogous ruthenium complexes $[\mathbf{1}]^{2+}$ and $[\mathbf{2}]^{3+}$ are compared upon both yellow (570 nm) and blue (450 nm) light irradiation, in order to investigate the efficiency of photosensitization on the Ru-based ligand exchange process.
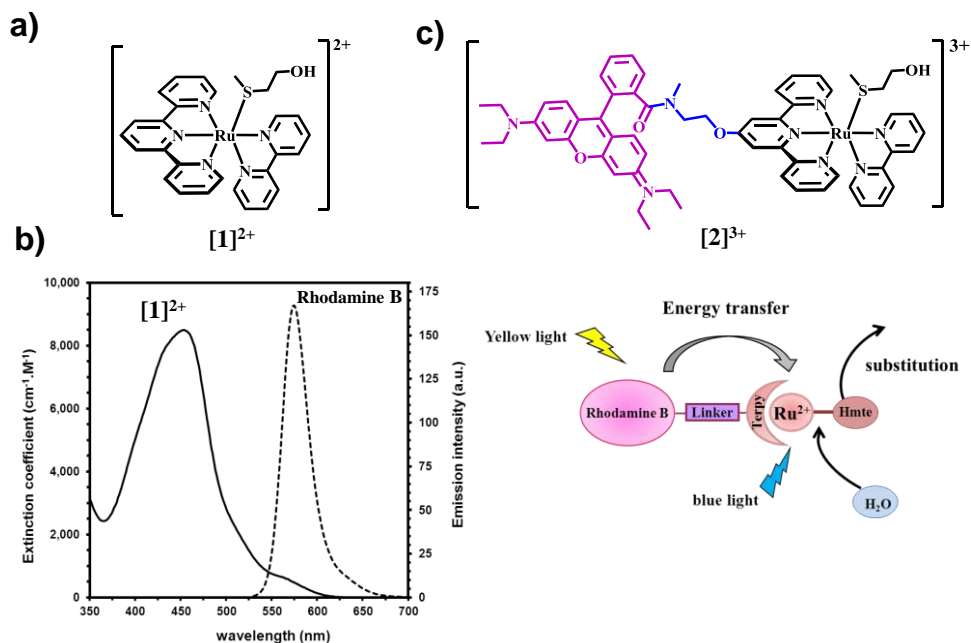
**Figure 6.1.** a) Chemical structure of [Ru(terpy)(bpy)(Hmte)]$^{2+}$ ([**1**]$^{2+}$). b) Absorption spectrum of [**1**]$^{2+}$ (left axis) and emission spectrum of rhodamine B (right axis). c) Chemical structure of the rhodamine B-functionalized ruthenium complex [**2**]$^{3+}$ and photochemical scheme.

## 6.2. Results

### 6.2.1. Synthesis

In order to couple a rhodamine B molecule to the 4' position of the 2,2';6',2"-terpyridine (terpy) ligand an ethanolamine linker may seem at first sight appropriate. However, in basic conditions the secondary amide bond resulting from coupling between the primary amine of ethanolamine and the carboxylic acid of rhodamine B, cyclizes to a spirolactame, which leads to quenching of the fluorescence of the dye.[39-40] Thus, a secondary amine, 2-methylaminoethanol, was used instead, because the resulting tertiary amide cannot be deprotonated and cyclize into the spiro compound. The synthetic route towards ligand [**4**]Cl is shown in Scheme 6.1. In the first step, a literature procedure was modified[41] to substitute the chloride substituent of 4'-chloro-2,2';6',2"-terpyridine by 2-methylaminoethanol using KOH as a base, to form compound **3**. Two structural isomers, compounds **3** (O-bound) and **3'** (N-bound) (Scheme 6.1) can be formed depending on the amount of base, on the temperature, and

on the reaction time. By using a relatively low amount of KOH (2.8 eq) and short reaction times no side product **3'** was detected by $^1$H NMR of the crude product, and compound **3** could be further functionalized.
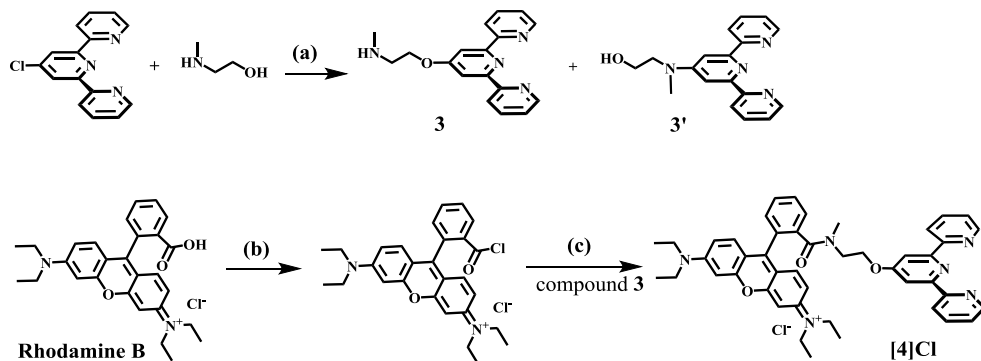


**Scheme 6.1.** Synthetic procedure towards compound **3** and [**4**]Cl. (a) KOH, DMSO (dry), heating at 60 °C for 3 h, overnight at R.T. Yield of **3**: 87% (b) POCl$_3$, C$_2$H$_4$Cl$_2$ (dry), reflux, 5 h. (c) I: Et$_3$N, CH$_3$CN (dry), reflux, 14h, II: KPF$_6$ in water, III: chloride exchange DOWEX resin, acetone:H$_2$O (1:1), 4 h, r.t.  Yield: 31% (from compound **3**).

In the second step, rhodamine B was coupled to **3** following a modified literature procedure [42] involving the acid chloride of rhodamine B and **3** using Et$_3$N as a base in acetonitrile. After precipitation from water using PF$_6^-$ as a counter ion, full water solubility was recovered by anion exchange to Cl$^-$ using an anion exchange resin. Column chromatography on silica gel allowed removing the unreacted rhodamine B to afford compound [**4**]Cl as a purple solid with an overall yield of 31%. The UV-vis spectrum of [**4**]Cl in water (Figure 6.2a and Table 6.1) showed a red shift of the π-π* absorption band of about 14 nm ($\lambda_{abs}$=569 nm), compared to rhodamine B.

Adapting known synthetic procedures[43-45] the ruthenium complex [**2**]Cl$_3$ was synthesized as shown in Scheme 6.2. Refluxing a mixture of ligand [**4**]Cl with RuCl$_3$·3H$_2$O in methanol resulted in the paramagnetic complex [**5**]Cl. Product formation was followed by TLC and the final product was characterized by paramagnetic $^1$H NMR and ESI-MS spectrometry. The unpaired electron of the Ru(III) complex generates short relaxation times, which shields the $^1$H-$^1$H coupling and thus results in broad NMR signals. This effect is significant for hydrogen atoms of the terpyridine moiety in [**5**]Cl that are close to the paramagnetic ruthenium(III) center. Highly upfield-shifted signals were observed in methanol-d4 at −1.43 ppm, −10.26

ppm, −10.71 ppm and −35.94 ppm for T33'', T44'', T55'', or T66''. T3' and T5' are more remote from the paramagnetic center and their signals appear at 10.90 ppm.[46] The peaks in the 6.90-8.10 ppm region most likely correspond to the rhodamine B moiety and traces of the free ligand [4]Cl. In the ESI-MS spectrum a peak at m/z=937.7 for [5]+ was found that confirmed the formation of compound [5]Cl.
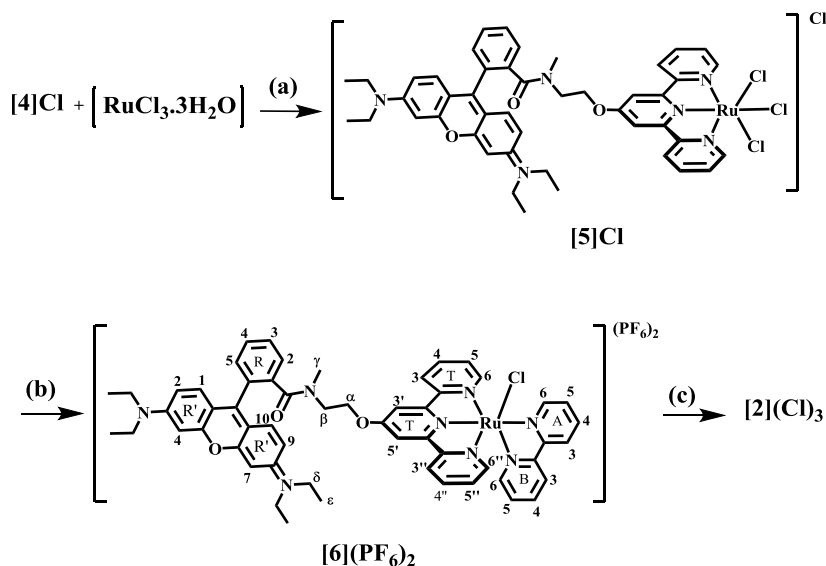




**Scheme 6.2.** Synthetic route towards ruthenium complexes [5]Cl, [6](PF$_6$)$_2$, and [2]Cl$_3$. (a) MeOH, reflux, 7 h, yield: 54%. (b) I: bpy, LiCl, NEt$_3$, EtOH/H$_2$O(3:1), reflux, 6 h. II: KPF$_6$ in water. Yield: 40%. (c) I: Hmte, AgPF$_6$ (2.6 eq), acetone:H$_2$O (5:3), reflux, 9 h. II: chloride exchange DOWEX resin, acetone:H$_2$O (1:1), 4 h, r.t. Yield: 43%.

In a second step, the complex [Ru(**4**)(bpy)(Cl)](PF$_6$)$_2$ ([**6**](PF$_6$)$_2$) was obtained as a purple solid via treatment of [**5**]Cl with 2,2'-bipyridine in presence of EtN$_3$ and LiCl in an ethanol/water mixture, followed by column chromatography and precipitation with aqueous KPF$_6$. Finally, the water soluble, potentially photosensitive ruthenium complex [Ru(**4**)(bpy)(Hmte)]Cl$_3$ ([**2**]Cl$_3$) was synthesized by removal of the chloride ligand in [**6**](PF$_6$)$_2$ using AgPF$_6$ in presence of an excess of Hmte at elevated temperatures. The PF$_6^-$ counter ions were then exchanged using a chloride-loaded exchange resin, to form the purple, water-soluble complex [**2**]Cl$_3$. ^{1}H NMR in methanol-d$_4$ showed that the protons of the coordinated Hmte ligand (3.46, 1.81, and 1.36 ppm) are shielded in [**2**]Cl$_3$ compared to free Hmte (3.75, 2.80, and 2.30 ppm).

159

Moreover, the characteristic aromatic proton for [**2**]Cl$_3$ at 9.80 ppm (6A) appears at different chemical shift compared to that in [**6**](PF$_6$)$_2$ (10.28 ppm). The high resolution mass spectrum showed two peaks for the product at m/z=360.45780 ([**2**]$^{3+}$) and at m/z=540.18289 ([**2**–H]$^{2+}$). Overall the analogous complexes [**2**]Cl$_3$ and [**1**](BF$_4$)$_2$, which was synthesized as reported in Chapter 3, are soluble enough in water for studying their photophysical properties and the photosensitivity of their Ru-S bond.

### 6.2.2. Emission measurements

The As reported by Etchenique et al. for a similar rhodamine-ruthenium system,[38] even though the overlap between the emission spectrum of the rhodamine B dye and the absorption spectrum of the ruthenium complex [**1**]$^{2+}$ is rather small (see Figure 6.1b) the use of a very short linker in [**2**]$^{3+}$ was expected to allow at least some of the energy absorbed by rhodamine B to be donated to the ruthenium center in the covalent dyad. The emission and absorption spectra of [**2**]Cl$_3$ were measured in water and compared to that of [**4**]Cl and rhodamine B (Figure 6.2b). All compounds absorb strongly in the yellow region, with extinction coefficient diminished in [**4**]Cl and [**2**]Cl$_3$, however, compared to rhodamine (Table 6.1). In addition, the emission spectrum of [**2**]Cl$_3$ shows almost complete quenching of the fluorescence of the rhodamine B group upon excitation of [**2**]Cl3 at 570 nm. This effect is not observed in the spectrum of ligand [**4**]Cl, which keeps a significant part of the rhodamine fluorescence (Figure 6.2b and Table 6.1). Thus, the energy absorbed by the rhodamine B substituent at 570 nm is either transferred to the ruthenium center by energy transfer, or wasted via non-radiative decay. If energy transfer to the ruthenium complex is efficient, it may lead to the photosubstitution of Hmte by an aqua ligand. ($\lambda_{max}$~450 nm).

**Table 6.1.** Spectroscopic data in MilliQ water for compounds [**2**]Cl$_3$, [**4**]Cl, and rhodamine B. Emission data were obtained upon excitation at $\lambda$=570 nm.

| Compound | $\varepsilon_{(\lambda Max)}$ (M$^{-1}\cdot$cm$^{-1}$) | $\lambda_{max}$ (abs) (nm) | $\lambda_{max}$ (em) (nm) |
|:---:|:---:|:---:|:---:|
| rhodamine B | 120000 | 555 | 576 |
| [**4**]Cl | 74000 | 569 | 586 |
| [**2**]Cl$_3$ | 44000 | 570 | 585 |
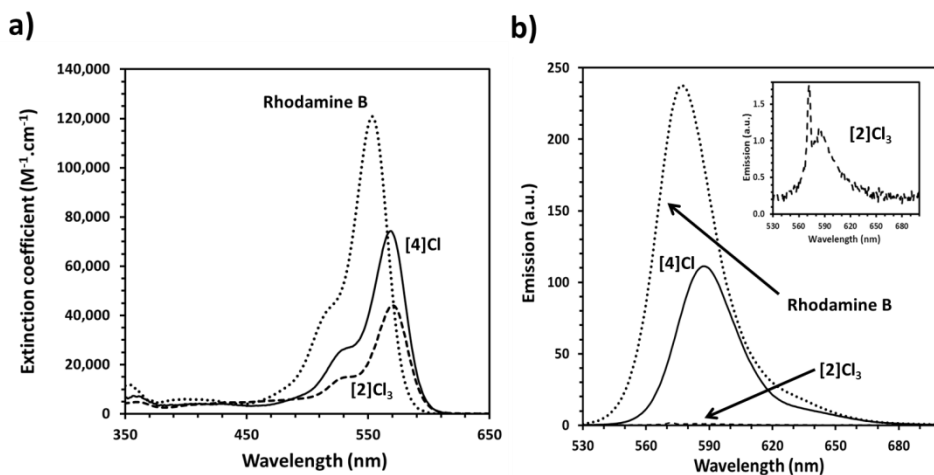
**Figure 6.2.** Absorption (a) and emission (b) spectra of rhodamine B, rhodamine B-terpyridine conjugate [**4**]Cl, and rhodamine B-functionalized ruthenium complex [**2**]Cl$_3$ in MilliQ water at pH=7. Excitation: 570 nm, slit width: 3 nm. The concentrations of the solutions used for emission measurements were chosen so that their absorbance at 570 nm were identical in the three solutions ($A_{570}$=0.23).

### 6.2.3. Photochemistry

The photoreactivity of [**2**]$^{3+}$ (hereafter RuHmte) was investigated by looking at whether the Hmte ligand could be photosubstituted by an aqua ligand, upon either yellow or blue light irradiation in water. The formation of the aqua complex [**7**]$^{3+}$ (see Scheme 6.3) was first monitored by $^1$H NMR spectroscopy in D$_2$O. NMR samples containing [**2**]Cl$_3$ in degassed D$_2$O were prepared, and the samples were irradiated with blue ($\lambda_e$ = 452 nm) or yellow light ($\lambda_e$ = 570 nm) at room temperature. While the $^1$H NMR spectrum of a reference sample in the dark did not change, the spectra of the irradiated samples showed the gradual disappearance of the starting compound [**2**]$^{3+}$ ($\delta$=9.76 ppm for proton 6A (see Scheme 6.2), and $\delta$=3.48 ppm, 1.83 ppm, and 1.37 ppm for coordinated Hmte) and the formation of a single new ruthenium complex ($\delta$=9.61 ppm for proton 6A) and of the free Hmte ligand (at $\delta$=3.74, 2.66, and 2.01 ppm). Figure 6.3 shows the evolution of the $^1$H NMR spectra for proton 6A upon irradiation (the complete spectra before and after irradiation are shown in Figure AVI.1). Mass spectra after irradiation were obtained for both samples, and the peak found at 339.6 is characteristic for the formation of [Ru(**4**)(bpy)(D$_2$O)]$^{3+}$. Integration of the protons 6A for [**2**]$^{3+}$ and [**7**]$^{3+}$ indicated typically 40% photoconversion of [**2**]$^{3+}$ to [**7**]$^{3+}$ after about

500 min irradiation. The present data show that a substantial amount of Hmte is indeed photosubstituted, not only upon blue light irradiation but also upon yellow light irradiation, which is absorbed by the rhodamine dye more than by the ruthenium fragment (see below). However, these NMR experiments could not provide quantitative information on the quantum efficiency of the light-induced substitution reaction, as light intensities in the irradiation setup were difficult to determine.
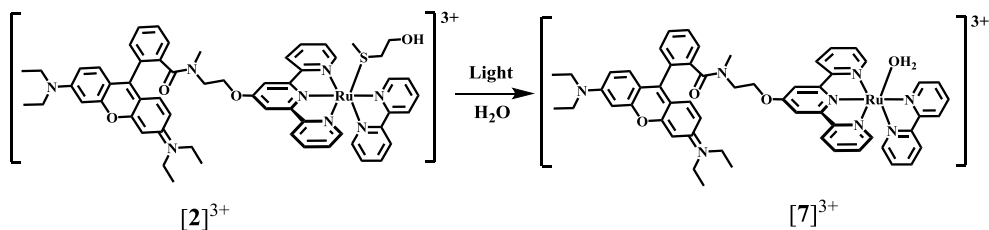


**Scheme 6.3.** Photosubstitution of Hmte in $[\mathbf{2}]^{3+}$ by an aqua ligand upon blue light ($\lambda$=452 nm) or yellow light ($\lambda$=570 nm) irradiation in aqueous solution.
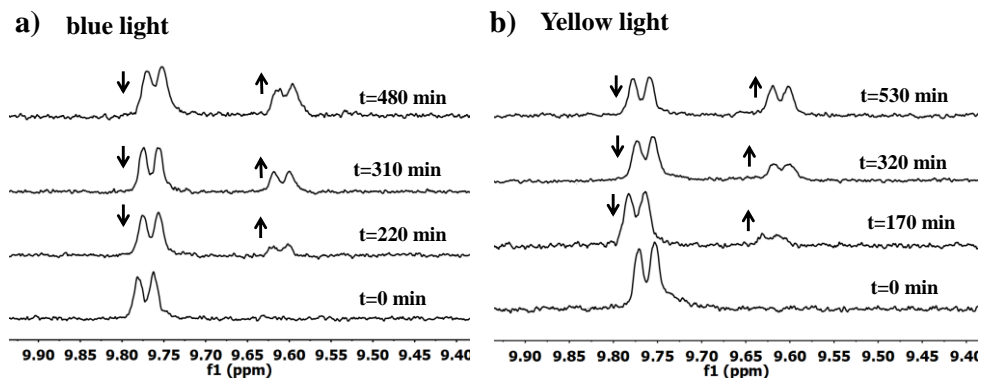


**Figure 6.3.** Evolution of the $^1$H NMR spectra of degassed $D_2O$ solution of $[\mathbf{2}]Cl_3$ upon irradiation with a) blue light ($\lambda_e$=452 nm, $\Delta\lambda_{1/2}$=8.9 nm) or b) yellow light ($\lambda_e$=570 nm, $\Delta\lambda_{1/2}$=8.9 nm). Irradiation times are indicated for each spectrum. Conditions: total ruthenium concentration $[Ru]_{tot}$=5.3×10$^{-3}$ M, room temperature.

In order to get quantitative information about the yellow and blue light-triggered release of Hmte from complex $[\mathbf{2}]^{3+}$, UV-vis experiments were performed in well-controlled irradiation conditions. An aqueous solution of $[\mathbf{2}]Cl_3$ was exposed to yellow light (570 nm) or blue light (452 nm) *via* a fiber optic bundle bringing light to the top of a UV-vis cuvette, *i.e* inside the spectrophotometer and perpendicularly to its optical

axis (see Appendix I, Figure AI.1). The UV-vis spectra were measured during light irradiation (Figure 6.4a). The absorption spectrum of the solution gradually evolved until a steady state was obtained after 150 and 320 mintues of irradiation with yellow and blue light, respectively. Isosbestic points at 380 nm, 460 nm, and 557 nm indicate the occurance of only one photochemical reaction. From the ^{1}H NMR and mass spectrometry studies it is clear that extensive irradiation of $[2]^{3+}$ leads to the full photoconversion into the aqua complex $[7]^{3+}$ (RuOH₂) (see Appendix VI, Figure AVI.2). Thus, in each experiment the concentration of $[2]^{3+}$ and $[7]^{3+}$ could be calculated from the extinction coefficients of both species (see Appendix I, section AI.2.1). Using Equation 6.1, the photochemical substitution first-order rate constants $k_{\varphi570}$ and $k_{\varphi452}$ could be obtained from the slope of a plot of ln*([RuHmte]/[Ru]$_{tot}$) vs.* irradiation time (Figure 6.5a-I and II), where *[RuHmte]* and *[Ru]$_{tot}$* represent the concentration in $[2]^{3+}$ and the total ruthenium concentration in the solution, respectively. Half-reaction times were calculated using Equation 6.2. The data are reported in Table 6.2; they show that the photoconversion rate upon yellow light irradiation, $k_{\varphi570}$, was twice higher compared to that obtained upon blue light irradiation ($k_{\varphi452}$). Since the photon flux values at 570 nm and 452 nm ($\Phi_{570}$ and $\Phi_{452}$) were not equal, the rate constants $k_{\varphi570}$ and $k_{\varphi452}$ cannot be directly compared, but the photosubstitution quantum yields have to be calculated instead. As expressed in Equation 6.3, the photosubstitution rate constant depends on the photon flux $\Phi$, the extinction coefficient of RuHmte at the irradiation wavelength $\varepsilon^{\lambda e}$, the absorbance along the irradiation axis at the irradiation wavelength $3A_e$ (see Appendix I, Figure AI.1), the probability of absorbance of the photon $(1-10^{-3A_e})$, the photosubstitution quantum yield $\varphi$, the absorption pathlength $l$, and the irradiated volume $V$.

$$-\frac{dn_{RuHmte}}{dt} = \frac{dn_{RuOH_2}}{dt} = k_\varphi . n_{RuHmte} \quad \textbf{(Equation 6.1)}$$

$$t_{1/2} = \frac{ln2}{k_\varphi} \quad \textbf{(Equation 6.2)}$$

$$k_\varphi = \Phi \cdot (1 - 10^{-3A_e}) \cdot \left(\frac{\varepsilon^{\lambda_e}.l}{A_e.V}\right) \cdot \varphi \quad \textbf{(Equation 6.3)}$$

The number of moles of RuHmte remaining in solution, $n_{RuHmte}$, was plotted *vs.* the number of moles of photons $Q$ absorbed at time $t$ since $t$=0 by RuHmte (Figure 6.5b

and Appendix I, section AI.3.2). The photosubstitution quantum yields were obtained directly from the slope of these plots; they were found to be $8.5(6)\times10^{-3}$ and $9.2(7)\times10^{-3}$ for yellow and blue light irradiation, respectively (Table 6.2). These values are unexpectedly similar, which demonstrates the non-intuitive results that once absorbed, a yellow photon has almost the same probability to lead to ligand photosubstitution as a blue photon.

However, the quantity of $RuOH_2$ formed in a given irradiation time depends on the amount of light absorbed by the complex at the irradiation wavelength as well. In this regard, the extinction coefficients of compound $[\mathbf{2}]^{3+}$ at 570 nm and 452 nm are very different ($4.4(2)\times10^{4}$ $M^{-1}\cdot cm^{-1}$ and $4.8(2)\times10^{3}$ $M^{-1}\cdot cm^{-1}$, respectively). Thus, in order to compare the photosubstitution rates the extinction coefficients must be considered as well. Multiplying the extinction coefficient by the photosubstitution quantum yield gives a value called the photosubstitution reactivity ($\xi$),[38] which best represents how fast a photoreaction will occur under a given photon flux. Actually, Equation 6.3 simplifies into Equation 6.4 when the absorbance $A_e$ is small compared to 1.

$$k_{\varphi} \approx \left(ln\,10\cdot\frac{l}{V}\right)\cdot\Phi\cdot\varepsilon^{\lambda_e}\cdot\varphi = \left(ln\,10\cdot\frac{l}{V}\right)\cdot\Phi\cdot\xi \quad \textbf{(Equation 6.4)}$$

The calculated values of $\xi$ are reported in Table 6.2. These values show that for complex $[\mathbf{2}]^{3+}$ Hmte substitution is one order of magnitude faster with yellow light than with blue light. In fact, ten times more moles of photoproduct ($[\mathbf{7}]^{2+}$) were produced upon yellow light irradiation compared to blue light irradiation at short reaction times. Quantitatively, the higher molar absorptivity of the complex $[\mathbf{2}]^{3+}$ at 570 nm due to the allowed character of the intraligand $\pi$-$\pi$* transition of the rhodamine B moiety, promotes intensive absorption of yellow photons compared to blue ones.

In order to evaluate the influence of the rhodamine B antenna on the photosubstitution of Hmte, similar irradiation experiments were performed on complex $[\mathbf{1}]^{2+}$, which does not have the fluorophore antenna. Upon yellow light irradiation (570 nm) the absorption band of $[\mathbf{1}]^{2+}$ at 450 nm gradually disappeared to give rise to a new absorption maximum at higher wavelength corresponding to $[Ru(terpy)(bpy)(OH_2)]^{2+}$ ($[\mathbf{8}]^{2+}$, see Figure 6.4b). The first-order photosubstitution rate constant was obtained from the slope of the plots of $ln$*([RuHmte]/[Ru]$_{tot}$) vs.* irradiation time (Figure 6.5a-III), and the photosubstitution quantum yield was obtained as described above (Figure 6.5b-III). The photosubstitution quantum yield of compound $[\mathbf{1}]^{2+}$ upon blue light irradiation

was reported in Chapter 3 different irradiation conditions.[45] For better comparison with $[2]^{3+}$ we repeated the measurement in the same irradiation conditions as for $[2]^{3+}$ (Figure 6.5-IV). All photochemical data, including half-reaction times, are reported in Table 6.2. Like for $[2]^{3+}$ the photosubstitution quantum yields for $[1]^{2+}$ upon blue light and yellow light irradiation were found to be very close to each other, *i.e.*, 0.016(4) *vs.* 0.011(4), respectively. This counter-intuitive result confirms our observations on $[2]^{3+}$, that once absorbed by $[1]^{2+}$ yellow photons are able to lead to ligand photosubstitution as efficiently as blue photons.

In order to compare the photoreactivity of different compounds one should compare their $\xi$ values, which depends on both the extinction coefficient ($\varepsilon_\lambda$) and the photosubstitution quantum yield ($\varphi_\lambda$). Although the photosubstitution quantum yields at 570 nm and 452 nm are comparable for both complexes $[1]^{2+}$ and $[2]^{3+}$, the extinction coefficient at 570 nm ($\varepsilon_{570}$) is two orders of magnitudes higher for $[2]^{3+}$ than for $[1]^{2+}$ due to the presence of the yellow-absorbing dye, while the values of $\varepsilon_{452}$ are of the same order of magnitude for both complexes. As a result, under yellow light irradiation $\xi$ is about two orders of magnitude higher for $[2]^{3+}$ than for $[1]^{2+}$, and it is still four times higher than that of $[1]^{2+}$ under blue light irradiation. Overall, at constant photon flux the different extinction coefficients ($\varepsilon_\lambda$) most strongly influence the photosubstitution rate constants for $[1]^{2+}$ and $[2]^{3+}$ at 450 or 570 nm, whereas the quantum yields poorly depend on irradiation wavelength.

This result is similar to Kasha's rule, which states that the fluorescence quantum yield of a fluorophore is independent on the irradiation wavelength.[47] Indeed, like for fluorophores where emission always occurs from the lowest singlet excited state, for ruthenium complexes such as $[1]^{2+}$ or $[2]^{3+}$ photosubstitution is expected to occur from a ruthenium-based $^3$MLCT state *via* thermal promotion to a nearby dissociative $^3$MC state. Reaching the $^3$MLCT state can be done either by direct excitation of the $^1$MLCT band of the ruthenium complex, or by excitation of the rhodamine dye followed by energy transfer to the ruthenium fragment. In the case of a direct excitation of the metal complex ($[1]^{2+}$) yellow photons need to be absorbed by vibrationally excited ground-state complexes, to be able to lead to the $^3$MLCT excited state. Once there, non-radiative decay will occur with almost the same probability as when the $^3$MLCT state is obtained by absorption of blue photons by a non-vibrationally excited ground state complex. In the case of indirect excitation of $[2]^{3+}$ with yellow photon the $^3$MLCT state is probably reached efficiently *via* absorption by the rhodamine group, followed by

energy transfer. While from Etchenique's work energy transfer was expected to occur in $[2]^{3+}$, it was not expected to be *that* efficient.
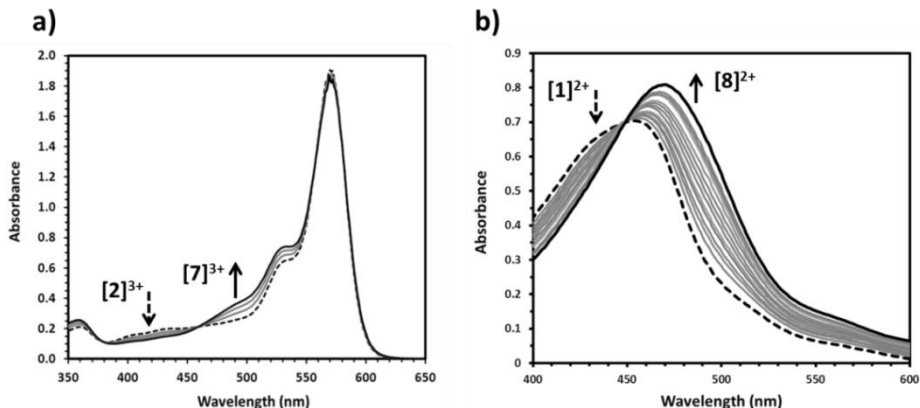


**Figure 6.4.** a) Time evolution of the UV-vis spectrum of an aqueous solution of a) $[2]^{3+}$ and b) $[1]^{2+}$ irradiated with yellow light ($\lambda_e$=570 nm). Condition: photon flux $\Phi$=5.3×10$^{-9}$ Einstein·s$^{-1}$, irradiation pathlength $l'$=3 cm, $T$=298 K. Total ruthenium concentrations: a) $[Ru]_{tot}$ =3.4×10$^{-5}$ M b) $[Ru]_{tot}$ =1.2×10$^{-4}$ M.
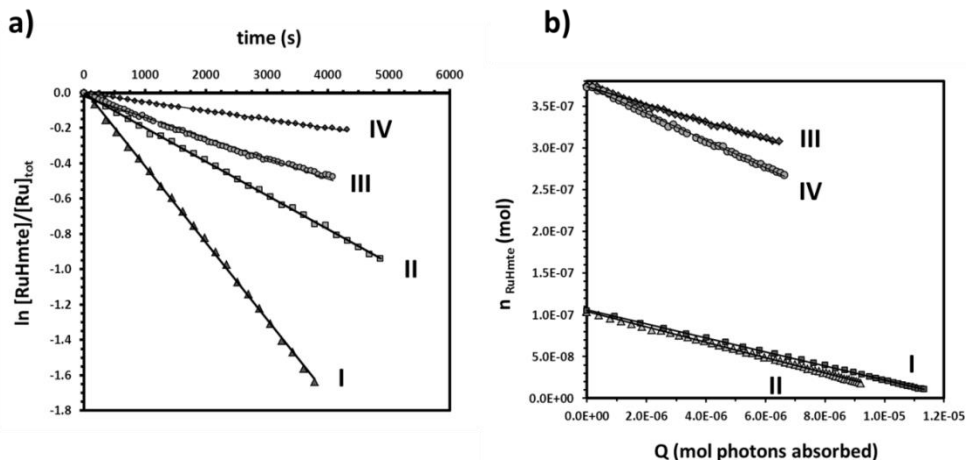


**Figure 6.5.** a) Plots of ln$([RuHmte]/[Ru]_{tot})$ *vs.* irradiation time; $[RuHmte]$ represents the concentration in $[2]^{3+}$ or $[1]^{2+}$, and $[Ru]_{tot}$ the total ruthenium concentration in the solution. The slope of each plot is $k_\varphi$ (s$^{-1}$). b) Plots of the number of moles of RuHmte *vs.* the number of moles of photons $Q$ absorbed by RuHmte at time t, since $t$=0; the slope is the photosubstitution quantum yield $\varphi$. I) RuHmte=$[2]^{3+}$, $[Ru]_{tot}$=3.4×10$^{-5}$ M, yellow light ($\lambda_e$=570 nm). II) RuHmte=$[2]^{3+}$, $[Ru]_{tot}$=3.4×10$^{-5}$ M, blue light ($\lambda_e$=452 nm). III) RuHmte=$[1]^{2+}$, $[Ru]_{tot}$=1.2×10$^{-4}$ M, yellow light ($\lambda_e$=570 nm). IV)

RuHmte=$[\mathbf{1}]^{2+}$, $[Ru]_{tot}$=1.2×10$^{-4}$ M, blue light ($\lambda_e$=452 nm). Photon fluxes: $\Phi_{570}$=5.3(8)×10$^{-9}$ Einstein.s$^{-1}$ and $\Phi_{452}$=3.0(6)×10$^{-9}$ Einstein·s$^{-1}$.

**Table 6.2.** Photochemical data for the photosubstitution of Hmte by $H_2O$ in $[\mathbf{2}]^{3+}$ and $[\mathbf{1}]^{2+}$ in MilliQ water. Condition: $T$=298 K, irradiation pathlength $l'$=3 cm, concentration in $[\mathbf{2}]^{3+}$: 3.4×10$^{-5}$ M, concentration in $[\mathbf{1}]^{2+}$: 1.2×10$^{-4}$ M.

| Ru complex | $\lambda_e$ (nm) | $\varepsilon_{\lambda e}$ (M$^{-1}$·cm$^{-1}$) | $\Phi$ (Einstein·s$^{-1}$) | $k_\varphi$ (s$^{-1}$) | $t_{(1/2)}$ (min) | $\varphi$ | $\xi$ ($\varphi \cdot \varepsilon_{\lambda e}$) |
|---|---|---|---|---|---|---|---|
| $[\mathbf{2}]^{3+}$ | 570 | 44000 | 5.3(8)×10$^{-9}$ | 4.4(3)×10$^{-4}$ | 26(2) | 8.5(6)×10$^{-3}$ | 370(15) |
| $[\mathbf{2}]^{3+}$ | 452 | 4800 | 3.0(6)×10$^{-9}$ | 1.9(3)×10$^{-4}$ | 59(2) | 9.2(7)×10$^{-3}$ | 44(8) |
| $[\mathbf{1}]^{2+}$ | 570 | 450 | 5.3(8)×10$^{-9}$ | 5.2(2)×10$^{-5}$ | 220(5) | 1.1(4)×10$^{-2}$ | 4.8(5) |
| $[\mathbf{1}]^{2+}$ | 452 | 6600 | 3.0(6)×10$^{-9}$ | 1.3(4)×10$^{-4}$ | 89(3) | 1.6(4)×10$^{-2}$ | 100(10) |

## 6.3. Discussion

The covalent binding of a rhodamine B dye to the terpy ligand of the ruthenium complex in $[\mathbf{2}]^{3+}$ leads to rather efficient photosensitization, as photosubstitution upon yellow light irradiation became faster even compared to blue light irradiation of the parent complex $[\mathbf{1}]^{2+}$. Sensitization seems occur via energy transfer from the rhodamine B sensitizer to the $^1$MLCT excited state of the ruthenium complex, which is consistent with the work reported by Etchenique.[38] By using a short saturated linker, the attachment of rhodamine B to the ruthenium complex occurs without mixing the orbitals of the dye and that of the ruthenium complex. Thus, we assume that the spectrum of $[\mathbf{1}]^{2+}$ is a good model for the contribution of the ruthenium moiety to the spectrum of $[\mathbf{2}]^{3+}$, *i.e.*, that the excited states of the rhodamine B part and of the ruthenium part in $[\mathbf{2}]^{3+}$ are not too much affected by each other. By comparing the extinction coefficient of $[\mathbf{2}]^{3+}$ with that of $[\mathbf{1}]^{2+}$ in Table 6.2, it appears that only 1% of the yellow photons are absorbed by the ruthenium-centered $^1$MLCT band in $[\mathbf{2}]^{3+}$, while this fraction goes up to 73% for blue photons. In fact, the presence of rhodamine B is not significantly interfering with the MLCT-based blue photon absorption in $[\mathbf{2}]^{3+}$, whereas, it contributes largely to yellow photon absorption.

Considering on the one hand the emission quenching of the rhodamine B moiety in $[\mathbf{2}]^{3+}$, and on the other hand the very similar photosubstitution quantum yields upon blue and yellow light irradiation, non-radiative decay in $[\mathbf{2}]^{3+}$ seems to mostly occur

from the $^3$MLCT state of the ruthenium moiety, rather than from the $S_1$ excited state of the rhodamine B moiety. According to Etchenique's work the energy transfer in $[\mathbf{2}]^{3+}$ is expected to occur *via* reverse FRET mechanism, *i.e.*, the rather small spectral overlap between the emission of the FRET donor and the absorption of the ruthenium acceptor must be compensated by the very short distance between both components in the dyad. However, other types of energy transfer mechanisms, such as Dexter's,[32] cannot be fully ruled out at that stage. Deeper photophysical and theoretical studies would be needed to assess whether direct orbital overlap between the rhodamine antenna and the ruthenium center in $[\mathbf{2}]^{3+}$ plays a role in the energy transfer process.

From a pure photochemical point of view, such sensitization might find application in photoactivated chemotherapy (PACT), for which the practical efficiency of a given compound will depend on the amount of photoproduct generated in a given irradiation time. Thus, at a given light intensity the photosubstitution quantum yield does not matter too much, but it is the photosubstitution reactivity $\xi$, which also takes the extinction coefficient into account, that should be considered. On the other hand, it cannot be forgotten that functionalization of a light-activatable metallodrug with large, flat aromatic dye is expected to change many biological properties of the complex such as its lipophilicity, uptake mechanism, and/or mechanism of cytotoxicity. In the end, only compounds that combine good uptake, a low toxicity in the dark, a high toxicity after ligand substitution, *and* a high photosubstitution reactivity, might be interesting for medicinal purposes.

## 6.4.    Conclusions

Our data show that yellow photons that do not seem to have enough energy to populate the $^1$MLCT state of $[\mathbf{1}]^{2+}$ or $[\mathbf{2}]^{3+}$ lead, once absorbed, lead to photosubstitution of Hmte with almost the same quantum efficiency as that achieved with blue photons. Thus, for this family of ruthenium compounds Kasha's rule remains valid, *i.e.*, the quantum efficiency of photosubstitution reactions does not depend on the energy of the incoming photons. However, irradiating photosensitive complexes such as $[\mathbf{1}]^{2+}$ far down their absorption band does render photon collection less efficient. Upon covalent attachment of an organic dye with high molar absorptivity (here rhodamine B for yellow photons) the absorption problem was solved, and for complex $[\mathbf{2}]^{3+}$ efficient energy transfer from the dye to the ruthenium center was observed. The resulting

photosubstitution reactivity under yellow light irradiation became even higher than that of compound $[\mathbf{1}]^{2+}$ under blue light irradiation.

To conclude, it may be noted that sensitizing the ruthenium complex with dyes absorbing at still higher wavelengths, *i.e.*, up in the red region, might become increasingly difficult. The efficiency of energy transfer is expected to decrease when the spectrum overlap between the emission of the dye and the MLCT band of the ruthenium complex becomes smaller, as a result of which sensitization might not remain possible with dyes that absorb too far in the red region. In the extreme case of negligible spectral overlap, the photoreactivity of the metal center and the emission of the fluorophore are expected to decouple. In such a case, the absorbed photons are expected to lead either to ligand photosubstitution or to fluorescence, depending on the irradiation wavelength. Such systems might find potential application in molecular imaging, for example to probe the position of a ruthenium complex and follow its fate, either in biological or in artificial systems.[18, 48]

## 6.5.    Experimental section

### 6.5.1.    General

$^1$H and $^{13}$C NMR spectra were recorded using a Bruker DPX-300 spectrometer; chemical shifts are indicated in ppm relative to TMS. Electrospray mass spectra were recorded on a Finnigan TSQ-quantum instrument by using an electrospray ionization technique (ESI-MS). High resolution mass spectrometry was performed using a Thermo Finnigan LTQ Orbitrap mass spectrometer equipped with an electrospray ion source (ESI) in positive mode (source voltage 3.5 kV, sheath gas flow 10, capillary temperature 275 ℃) with resolution R = 60.000 at m/z = 400 (mass range = 150-200) and dioctylphtalate (m/z = 391.28428) as "lock mass". UV-vis spectra were obtained on a Varian Cary 50 UV-vis spectrometer. Emission spectra were obtained using Shimadzu RF-5301 spectrofluorimeter. The irradiation setup was a LOT 1000 W Xenon arc lamp, fitted with a 400FH90-50 Andover standard cutoff filter and a Andover 450FS10-50 ($\lambda_e$=452 nm, $\Delta\lambda_{1/2}$=8.9 nm) or a 570FS10-50 ($\lambda_e$=570 nm, $\Delta\lambda_{1/2}$=8.9 nm) interference filter. DMSO and dichloroethane were dried over $CaSO_4$ and distilled before use. $CH_3CN$ was dried using a solvent dispenser PureSolve 400. 4'-Chloro-2,2';6',2"-terpyridine[49] and [Ru(terpy)(bpy)(Hmte)]$(BF_4)_2$ [**1**]$(BF_4)_2$ (Chapter 3) were synthesized following literature procedures. $AgPF_6$, LiCl, $KPF_6$ and the anionic exchange resin DOWEX 22 were purchased from Sigma-Aldrich. Triethylamine was purchased from Acros; KOH and $POCl_3$ were purchased from Merck;

and rhodamine B was purchased from Lambda Physik. The eluent for column chromatography purification of compound [**6**](PF$_6$)$_2$ was prepared by mixing MeCN, MeOH, and H$_2$O 66:17:17 ratio, followed by addition of solid NaCl until saturation was reached.

## 6.5.2. Synthesis

**Compound 3.** 2-methylaminoethanol (45 mg, 0.60 mmol) was added to a suspension of powdered KOH (94 mg, 1.7 mmol) in dry DMSO (2 mL). The mixture was stirred for 30 min at 333 K. 4'-chloro-2,2':6',2''-terpyridine (160 mg, 0.600 mmol) was added and the mixture was stirred at 333 K for 3 h and then overnight at r.t. Then, the mixture was poured onto water (60 mL). The aqueous phase was extracted with DCM (3×30 mL) and the organic phases were combined and dried over MgSO$_4$. DCM was evaporated under reduced pressure and the product was left 24 h under high vacuum at 40 ºC to remove trace amounts of DMSO. Compound **3** was obtained as pale yellow oil (160 mg, 0.520 mmol, 87% yield). $^1$H NMR (300 MHz, CD$_3$OD, 298 K, *see Scheme 6.2 for proton attribution*) δ (ppm) 8.61 (d, J = 4.8 Hz, 2H, T66''), 8.54 (d, J = 8.0 Hz, 2H, T33''), 7.96 – 7.87 (m, 4H, T44''+ T3' + T5'), 7.41 (ddd, J = 7.5, 4.8, 1.1 Hz, 2H, T44''), 4.29 (t, J = 5.2 Hz, 2H, α), 3.00 (t, J = 5.2 Hz, 2H, β), 2.46 (s, 3H, γ). $^{13}$C NMR (75 MHz, CD$_3$OD, 298 K) δ (ppm) 168.39 (T4'), 158.32 (T1), 157.03 (T1'), 150.09 (T66''), 138.68 (T3',T5'), 125.43 (T44''), 122.91 (T33''), 108.35 (T44''), 68.18 (α), 50.84 (β), 35.85 (γ). High resolution ES-MS m/z (calc): 307.15589 (307.15516, [M+H]$^+$).

**Compound [4]Cl.** Following a literature procedure[42] phosphorus oxychloride (60.0 µL, 0.657 mmol) was added to a solution of rhodamine B (150 mg, 0.313 mmol) in dry 1,2-dichloroethane (5 mL). The mixture was refluxed for 5 h. The solvent was evaporated under reduced pressure and the crude mixture was immediately re-dissolved in dry CH$_3$CN (10 mL). Et$_3$N (131 µL, 0.939 mmol) and compound **3** (96 mg, 0.31 mmol) were added and the mixture was refluxed for 14 h. The solvent was evaporated under reduced pressure at 30 ºC and the crude product was dissolved in water and filtered to remove any solid. The product was precipitated by addition of KPF$_6$, filtered, washed with H$_2$O, and dried in a desiccator at ambient pressure over silica gel blue for 4 h. Exchange of the PF$_6^-$ counter anions with Cl$^-$ was achieved by stirring an acetone/water solution (1:1) of the product with the Cl$^-$ exchange resin DOWEX 22 (2.0 g) for 4 h. The resin was filtered, acetone was evaporated under reduced pressure at 22 ºC, and water was removed using a freeze drier. The product was purified by column chromatography on silica gel (CHCl$_3$/MeOH, 10% to 20% of MeOH). Solvents were evaporated under reduced pressure and compound [**4**]Cl was obtained as a purple solid (75 mg, 0.097 mmol, 31%). $^1$H NMR (300 MHz, CD$_3$OD,

298 K, *see Scheme 6.2  for proton attribution*) δ (ppm) 8.77 − 8.70 (m, 4H, T33'', T66''), 8.06 (td, J = 7.7, 1.8 Hz, 2H, T44''), 7.84 − 7.72 (m, 3H,5R,4R,3R), 7.70 (s, 2H, T3',T5'), 7.54 (ddd, J = 7.5, 4.8, 1.2 Hz, 2H, T44''), 7.47 (dd, J = 6.5, 1.0 Hz, 1H, 5R), 7.34 (d, J = 9.6 Hz, 2H, 10R',1R'), 7.01 (dd, J = 9.6, 2.5 Hz, 2H, 2R',9R'), 6.44 (d, J = 2.4 Hz, 2H, 4R',7R'), 3.84 (t, J = 4.3 Hz, 2H, α), 3.74 (t, J = 4.3 Hz, 2H, β), 3.41 (dd, J = 13.4, 6.6 Hz, 8H, δ), 2.96 (s, 3H, γ), 1.14 (t, J = 7.1 Hz, 12H, ε). $^{13}$C NMR (75 MHz, CD$_3$OD, 298 K) δ (ppm) 171.10 (C=O), 167.99 (3R,8R), 158.80, 158.25, 157.00, 156.87, 156.30, 150.30 (T66''), 138.82 (T55''), 137.59, 133.31 (2R'+9R'), 131.73+131.65 (3R+2R+4R), 131.17, 130.99 (5R), 128.75 (T5'), 125.78 (T44''), 122.89 (T33''), 115.19 (1R'+10R'), 114.43, 108.06 (T'3), 97.19 (4R'+7R'), 68.13 (α+β), 46.80 (δ), 40.53 (γ), 12.78 (ε). High resolution ES-MS m/z (calc): 731.37096 (731.37041 [M]$^+$). UV-vis: $λ_{max}$ (ε in L·mol$^{-1}$·cm$^{-1}$) in pure H$_2$O: 569 nm (74000). Anal. Calcd for C$_{46}$H$_{47}$ClN$_6$O$_3$·CHCl$_3$·H$_2$O: C, 62.39; H, 5.57; N, 9.29. Found: C, 61.77; H, 5.75; N, 9.68.

**Compound [5]Cl**. Compound [**4**]Cl (120 mg, 0.156 mmol) and RuCl$_3$·3H$_2$O (41 mg, 0.16 mmol) were dissolved in MeOH (20 mL) and refluxed for 7 h under argon. The mixture was first cooled down to room temperature, and then cooled in an ice bath for 30 min and overnight in the fridge. The precipitate was filtered off and air dried to yield [**5**]Cl as a dark purple powder (83 mg, 0.075 mmol, 54%). $^1$H NMR (300 MHz, CD3OD, 298 K, *see Scheme 6.2  for proton attribution*) δ (ppm) 10.90 (s, T3',T5'), 8.07 − 7.88 (m, 3H), 7.69 (d, J = 6.9 Hz, 2H), 7.55 (d, J = 9.4 Hz, 2H), 7.01 (d, J = 9.7 Hz, 3H), −1.43 (s, T33''/T44''/T55''), −10.26 (s, T33''/T44''/T55''), −10.71 (s, T33''/T44''/T55''), −35.94 (s, T66''). ES-MS m/z (calc): 938.2 (937.7 [M−Cl]$^+$).

**Compound [6](PF$_6$)$_2$.** [**5**]Cl (78 mg, 0.080 mmol), 2,2'-bipyridine (13 mg, 0.083 mmol), and LiCl (5.0 mg, 0.12 mmol) were mixed in a 3:1 EtOH/H$_2$O mixture (15 mL) and the solution was degassed with argon for 5 min, after which Et$_3$N (15 μL, 0.10 mmol) was added. The reaction mixture was refluxed under argon for 6 h, and then it was filtered hot over celite. The filtrate was evaporated under reduced pressure. Column chromatography purification was performed over silica gel (eluent: MeCN / MeOH / H$_2$O, 66:17:17 saturated in NaCl, R$_f$=0.5). The solvent was evaporated, then the crude product was dissolved in water (50 mL), and precipitated by adding KPF$_6$ (~1 g). After filtration, washing with water and drying in a desiccator at ambient pressure over silica gel blue for 5 h compound [**6**](PF$_6$)$_2$ was obtained in 40% yield as a dark purple powder (41 mg, 0.031 mmol). $^1$H NMR (300 MHz, CD$_3$OD, 298 K, *see Scheme 6.2 for proton notation*) δ (ppm) 10.28 (d, J = 5.6 Hz, 1H, 6A), 8.79 (d, J = 8.2 Hz, 1H, 3A), 8.51 (d, J = 8.1 Hz, 3H, 10R' + 1R'+ 3B), 8.32 (t, J = 8.1 Hz, 1H, 4A), 8.07 − 7.91 (m, 5H, 2R'+ 9R'+ 7R'+ 5R+ 5A), 7.89 − 7.68 (m, 6H, T3'+ T5'+ 3R + 4B + T33''), 7.47 (d, J = 7.6 Hz, 1H, 2R), 7.44 − 7.31 (m,

5H, 4R'+ 4R + 5B+ T44''), 7.13 – 7.01 (m, 3H, 6B + T55''), 6.71 (d, J = 2.4 Hz, 2H, T66''), 4.02 (t, J = 4.5 Hz, 2H, α), 3.88 (d, J = 4.5 Hz, 2H, β), 3.45 (m, 8H, δ), 3.05 (s, 3H, γ), 1.31 (t, J = 12.9 Hz, 12H, ε). $^{13}$C NMR (75 MHz, CD$_3$OD, 298 K) δ (ppm) $^{13}$C NMR (75 MHz, CD$_3$OD, 298 K) δ 171.25 (C=O), 166.26 (3R,8R), 160.55, 160.48, 159.89, 159.07, 159.03, 158.19, 157.10, 153.86 (6A), 153.78, 152.85 (4R'), 138.42 (4R'+ 5R), 137.72 (4A), 137.64, 136.70 (T33''), 133.46 (T44''), 132.43 (2R), 131.99 (T3'), 131.89 (T5'), 130.98 (4B), 129.85 (3R), 128.74 (4R), 128.57 (5B), 127.96 (5A), 127.43 (6B), 125.09 (10R'+1R), 124.85 (3B), 124.58 (3A), 115.40 (T55''), 114.40, 110.89 (2R'+ 9R'), 97.76 (6T +6''T), 69.91(α+ β), 48.15 (δ) , 46.98 (γ), 13.04 (ε). High resolution ESI-MS m/z (calc): 512.15646 (512.15650 [M−2PF$_6$]$^{2+}$). UV-vis: $\lambda_{max}$ ($\varepsilon$ in L·mol$^{-1}$·cm$^{-1}$) in 9:1 acetone/H$_2$O:570 nm (58000).

**Compound [2]Cl$_3$.** [6](PF$_6$)$_2$ (30 mg, 0.023 mmol) and AgPF$_6$ (15 mg, 0.060 mmol) were dissolved in a 3:5 acetone/H$_2$O mixture (8 mL). To this solution was added Hmte (156 μL, 1.80 mmol). The mixture was refluxed under argon for 9 h in the dark, after which it was filtered hot over celite. Acetone was removed under reduced pressure upon which the crude product with PF$_6^-$ counter ions precipitated in water. It was filtered, washed and dried. PF$_6^-$ ions were exchanged by Cl$^-$ by stirring a 1:1 acetone/water solution (20 mL) of the crude product [2](PF$_6$)$_3$ with ion-exchange resin DOWEX 22 (30 mg) for 4 h. After filtration of the resin, acetone was evaporated under reduced pressure, and water was removed using a freeze drier machine to afford [2]Cl$_3$ as a reddish purple powder (12 mg, 0.011 mmol, 43%). $^1$H NMR (300 MHz, CD$_3$OD, 298 K, *see Scheme 6.2  for proton attribution*) δ (ppm) 9.80 (d, J = 6.1 Hz, 1H, 6A), 8.81 (d, J = 8.1 Hz, 1H, 3A), 8.57 (t, J = 8.7 Hz, 2H, 1R' + 3B), 8.39 (m, 2H, 10R' + 4A), 8.0-8.05 (m, 4H, 5R + 9R'+ 7R' + 5A), 7.93 (t, 2H, 4B + 2R'), 7.86 – 7.73 (m, 5H, 3R + T33''+ T3'+ T5'), 7.56 (m, 1H, 2R), 7.48 – 7.32 (m, 4H, 4R'+ 4R + T4 + T4''), 7.27 (d, J = 7.2 Hz, 1H, 5B), 7.20 – 7.07 (m, 3H, 6B + T55''), 6.92 (d, J = 4.1 Hz, 2H, T6 + T6''), 4.46 (d, J = 5.5 Hz, 2H, α), 3.80 (t, 2H, β), 3.69 (q, 8H, δ), 3.46(d, J = 5.7 Hz, 2H, HO-<u>CH$_2$</u>), 3.25 (s, 3H, γ), 1.81 (t, J = 5.8 Hz, 2H, <u>CH$_2$</u>-S), 1.43 – 1.36 (s, 3H, S-<u>CH$_3$</u>), 1.28 (t, J = 6.9 Hz, 12H, ε). $^{13}$C NMR (75 MHz, CD$_3$OD, 298 K) δ (ppm) 173.90 (C=O), 168.19 (3R,8R), 159.51, 159.34, 159.30, 159.12, 158.99, 158.96, 157.22, 154.52 (6A), 153.41, 140.05, 139.95, 139.09, 137.18, 135.81, 135.50, 133.83, 133.34, 133.24, 131.33, 131.16, 129.59, 128.90, 127.22, 126.20, 125.81, 124.98, 115.35, 114.86, 112.95, 97.32, 60.46 (α), 47.05 (β), 46.10 (δ), 46.08 (S-<u>CH$_3$</u>), 39.53 (γ), 38.51 (OH-<u>CH$_2$</u>), 38.08(<u>CH2</u>-S), 12.83 (ε). High resolution ES MS m/z (calc): 360.45788 (360.45780 [M–3Cl]$^{3+}$), 540.18291 (540.18289 [M–3Cl–H]$^{2+}$). UV-vis*:* $\lambda_{max}$ ($\varepsilon$ in L·mol$^{-1}$·cm$^{-1}$) in pure H$_2$O: 570 nm (44000).

### 6.5.3. Emission measurements

Three stock solutions of rhodamine B (solution **A**, 2.4 mg in 50 mL $H_2O$, $1.0\times10^{-4}$ M), of compound [**4**]Cl (solution **B**, 3.8 mg in 50 mL $H_2O$, $1.0\times10^{-4}$ M) and of compound [**2**]Cl$_3$ (solution **C**, 1.2 mg in 10 mL $H_2O$, $1.0\times10^{-4}$ M) were prepared. 150 µL of stock solution **A**, 100 µL of solution **B**, or 120 µL of solution **C** was transferred into a quartz cuvette and was diluted to 3 mL by adding $H_2O$ using a micropipette (final concentrations: of **A'**: $5.0\times10^{-6}$ M, **B'**: $3.3\times10^{-6}$ M, **C'**: $4.0\times10^{-6}$ M). The absorbance of each solution was measured ($A_{570}$=0.23 for all solutions). Emission spectra were recorded with the same excitation parameters ($\lambda_e$=570 nm).

### 6.5.4. Irradiation experiments

**NMR measurements.** [**2**]Cl$_3$ (3.8 mg, 3.2 µmol) was weighed into an NMR tube and degassed $D_2O$ (0.60 mL) was added to the tube in the dark under argon. The $^1$H NMR of the sample was measured as a reference, and irradiation at 452 nm or 570 nm was started at T=298 K using the beam of a LOT 1000 W Xenon arc lamp filtered with an Andover filter at the appropriate wavelength, and arriving on the side of the NMR tube. The temperature of the tube was kept constant by thermostat set at 298 K. After 220 minutes, 310 minutes, and 480 minutes of irradiation at 452 nm, or 170 minutes, 320 minutes, and 530 minutes at 570 nm, $^1$H NMR spectra were measured. A reference sample was also prepared at the same concentration, and kept in the dark for comparison of their $^1$H NMR spectra. Neither of these reference samples showed any observable conversion in the dark.

**UV-vis experiments.** 1 mL of a stock solution **D** of compound [**2**]Cl$_3$ (1.2 mg in 10 mL $H_2O$, $1.0\times10^{-4}$ M) or 0.8 mL of a stock solution **E** of [**1**](BF$_4$)$_2$ (1.7 mg in 5 mL $H_2O$, $4.5\times10^{-4}$ M) was transferred into a UV-vis cuvette. The volume of the solution was completed to 3 mL with $H_2O$ (using a micropipette) in the dark (final concentration: **D'**: $3.4\times10^{-5}$ M, **E'**: $1.2\times10^{-4}$ M). The UV-vis spectrum of each sample was measured and afterwards the sample was irradiated at 452 nm or 570 nm using the beam of a LOT 1000 W Xenon arc lamp filtered by an Andover bandpath filter, and directed into an 2.5 mm diameter optical fiber bundle bringing the light vertically into the cuvette, *i.e*, perpendicular to the horizontal optical axis of the spectrophotometer (*see Appendix I*). After each irradiation period (varying from 1 min to 3 min depending on the samples) a UV-vis spectrum was measured until a total irradiation time of 350 minutes and 82 minutes was reached, for **D'** and **E'**, respectively. The concentrations in *[RuHmte]* ([**2**]$^{3+}$ or [**1**]$^{2+}$) and [RuOH$_2$] ([**7**]$^{3+}$ or [**8**]$^{2+}$) were determined by deconvolution knowing the extinction coefficients of both species (*see Appendix I*). The evolution of ln*([RuHmte]/[Ru]$_{tot}$)* was plotted as a function of irradiation

time, and from the slope $S$ of these plot $k_\varphi$ at $\lambda_e$=452 nm or $\lambda_e$=570 nm were determined to be $1.9(3)\times10^{-4}$ s$^{-1}$ and $4.4(3)\times10^{-4}$ s$^{-1}$, for [**2**]$^{3+}$, respectively, and $1.3(4)\times10^{-4}$ and $5.2(2)\times10^{-5}$ s$^{-1}$ for [**1**]$^{2+}$, respectively. Knowing the photon flux and probability of photon absorption $1-10^{-3A_e}$, where $3A_e$ is the absorbance of the solution at the excitation wavelength $\lambda_e$, the number of moles of photons $Q$ absorbed at time t by RuHmte since $t_{irr}$=0 was calculated. Plotting $n_{RuHmte}$ (the number of moles of RuHmte complex [**1**]$^{2+}$ or [**2**]$^{3+}$) *vs.* $Q$ gave a straight line in each case. The slope of this plot directly corresponds to the quantum yield of the photosubstitution reaction. The values for the photosubstitution quantum yields were $9.2(3)\times10^{-3}$ and $8.5(3)\times10^{-3}$, respectively, for [**2**]$^{3+}$ and $1.6(4)\times10^{-2}$ and $1.1(4)\times10^{-2}$, respectively, for [**1**]$^{2+}$ , at $\lambda_e$=452 nm or $\lambda_e$=570 nm, respectively (see Appendix I, Section AI.3.2*)*.

## 6.6.    References

[1]     C. R. Hecker, P. E. Fanwick, D. R. McMillin, *Inorg. Chem.* **1991**, *30*, 659-666.
[2]     V. Balzani, G. Bergamini, S. Campagna, F. Puntoriero, in *Photochemistry and Photophysics of Coordination Compounds I, Vol. 280* (Ed.: V. C. S. Balzani), **2007**, pp. 1-36.
[3]     B. A. McClure, E. R. Abrams, J. J. Rack, *J. Am. Chem. Soc.* **2010**, *132*, 5428-5436.
[4]     P. S. Wagenknecht, P. C. Ford, *Coord. Chem. Rev.* **2011**, *255*, 591-616.
[5]     E. Baranoff, J. P. Collin, J. Furusho, Y. Furusho, A. C. Laemmel, J. P. Sauvage, *Inorg. Chem.* **2002**, *41*, 1215-1222.
[6]     A. A. Rachford, J. J. Rack, *J. Am. Chem. Soc.* **2006**, *128*, 14318-14324.
[7]     S. Bonnet, J. P. Collin, J. P. Sauvage, E. Schofield, *Inorg. Chem.* **2004**, *43*, 8346-8354.
[8]     P. Mobian, J. M. Kern, J. P. Sauvage, *Angew. Chem. Int. Ed.* **2004**, *43*, 2392-2395.
[9]     J. Van Houten, R. J. Watts, *J. Am. Chem. Soc.* **1976**, *98*, 4853-4858.
[10]    P. C. Ford, *Coord. Chem. Rev.* **1982**, *44*, 61-82.
[11]    S. Bonnet, J.-P. Collin, *Chem. Soc. Rev.* **2008**, *37*, 1207-1217.
[12]    R. B. Sears, L. E. Joyce, M. Ojaimi, J. C. Gallucci, R. P. Thummel, C. Turro, *J. Inorg. Biochem.* **2013**, *121*, 77-87.
[13]    B. S. Howerton, D. K. Heidary, E. C. Glazer, *J. Am. Chem. Soc.* **2012**, *134*, 8324-8327.
[14]    R. N. Garner, J. C. Gallucci, K. R. Dunbar, C. Turro, *Inorg. Chem.* **2011**, *50*, 9213-9215.
[15]    S. Betanzos-Lara, L. Salassa, A. Habtemariam, O. Novakova, A. M. Pizarro, G. J. Clarkson, B. Liskova, V. Brabec, P. J. Sadler, *Organometallics* **2012**, *31*, 3466-3479.
[16]    A. J. Gomes, P. A. Barbougli, E. M. Espreafico, E. Tfouni, *J. Inorg. Biochem.* **2008**, *102*, 757-766.
[17]    F. Barragan, P. Lopez-Senin, L. Salassa, S. Betanzos-Lara, A. Habtemariam, V. Moreno, P. J. Sadler, V. Marchan, *J. Am. Chem. Soc.* **2011**, *133*, 14098-14108.
[18]    R. E. Goldbach, I. Rodriguez-Garcia, J. H. van Lenthe, M. A. Siegler, S. Bonnet, *Chem. Eur. J.* **2011**, *17*, 9924-9929.
[19]    N. J. Farrer, L. Salassa, P. J. Sadler, *Dalton Trans.* **2009**, 10690-10701.

| | |
|---|---|
| [20] | H. M. Chen, J. A. Parkinson, S. Parsons, R. A. Coxall, R. O. Gould, P. J. Sadler, *J. Am. Chem. Soc.* **2002**, *124*, 3064-3082. |
| [21] | D. Crespy, K. Landfester, U. S. Schubert, A. Schiller, *Chem. Commun.* **2010**, *46*, 6651-6662. |
| [22] | A. Juarranz, P. Jaen, F. Sanz-Rodriguez, J. Cuevas, S. Gonzalez, *Clin. Transl. Oncol.* **2008**, *10*, 148-154. |
| [23] | A. P. Castano, P. Mroz, M. R. Hamblin, *Nat. Rev. Cancer* **2006**, *6*, 535-545. |
| [24] | A. M. Bugaj, *Photochem. Photobiol. Sci.* **2011**, *10*, 1097-1109. |
| [25] | P. Zhang, W. Steelant, M. Kumar, M. Scholfield, *J. Am. Chem. Soc.* **2007**, *129*, 4526-4527. |
| [26] | R. Weissleder, V. Ntziachristos, *Nat. Med.* **2003**, *9*, 123-128. |
| [27] | S. L. H. Higgins, K. J. Brewer, *Angew. Chem. Int. Ed.* **2012**, *51*, 11420-11422. |
| [28] | M. J. Rose, M. M. Olmstead, P. K. Mascharak, *J. Am. Chem. Soc.* **2007**, *129*, 5342-+. |
| [29] | M. J. Rose, N. L. Fry, R. Marlow, L. Hinck, P. K. Mascharak, *J. Am. Chem. Soc.* **2008**, *130*, 8834-8846. |
| [30] | N. L. Fry, J. Wei, P. K. Mascharak, *Inorg. Chem.* **2011**, *50*, 9045-9052. |
| [31] | N. L. Fry, P. K. Mascharak, *Acc. Chem. Res.* **2011**, *44*, 289-298. |
| [32] | J. P. Sauvage, J. P. Collin, J. C. Chambron, S. Guillerez, C. Coudret, V. Balzani, F. Barigelletti, L. Decola, L. Flamigni, *Chem. Rev.* **1994**, *94*, 993-1019. |
| [33] | K. Sienicki, W. L. Mattice, *J. Chem. Phys.* **1989**, *90*, 6187-6192. |
| [34] | P. Woolley, K. G. Steinhauser, B. Epe, *Biophys. Chem.* **1987**, *26*, 367-374. |
| [35] | M. H. Lim, S. J. Lippard, *Inorg. Chem.* **2004**, *43*, 6366-6370. |
| [36] | E. K. Kainmuller, E. P. Olle, W. Bannwarth, *Chem. Commun.* **2005**, 5459-5461. |
| [37] | M.-J. Li, K. M.-C. Wong, C. Yi, V.-W. Yam, *Chem. Eur. J.* **2012**, *18*, 8724-8730. |
| [38] | O. Filevich, B. Garcia-Acosta, R. Etchenique, *Photochem. Photobiol. Sci.* **2012**, *11*, 843-847. |
| [39] | H. N. Kim, M. H. Lee, H. J. Kim, J. S. Kim, J. Yoon, *Chem. Soc. Rev.* **2008**, *37*, 1465-1472. |
| [40] | M. Beija, C. A. M. Afonso, J. M. G. Martinho, *Chem. Soc. Rev.* **2009**, *38*, 2410-2433. |
| [41] | S. Burazerovic, J. Gradinaru, J. Pierron, T. R. Ward, *Angew. Chem. Int. Ed.* **2007**, *46*, 5510-5514. |
| [42] | J. del Marmol, O. Filevich, R. Etchenique, *Anal. Chem.* **2010**, *82*, 6259-6264. |
| [43] | R. A. Leising, S. A. Kubow, M. R. Churchill, L. A. Buttrey, J. W. Ziller, K. J. Takeuchi, *Inorg. Chem.* **1990**, *29*, 1306-1312. |
| [44] | C. A. Bessel, J. A. Margarucci, J. H. Acquaye, R. S. Rubino, J. Crandall, A. J. Jircitano, K. J. Takeuchi, *Inorg. Chem.* **1993**, *32*, 5779-5784. |
| [45] | A. Bahreman, B. Limburg, M. A. Siegler, E. Bouwman, S. Bonnet, *Inorg. Chem.* **2013**, *52*, 9456-9469. |
| [46] | M.-P. Santoni, A. K. Pal, G. S. Hanan, A. Proust, B. Hasenknopf, *Inorg. Chem. Commun.* **2011**, *14*, 399-402. |
| [47] | M. Kasha, *Discuss. Faraday Soc.* **1950**, 14-19. |
| [48] | A. Bahreman, B. Limburg, M. A. Siegler, R. Koning, A. J. Koster, S. Bonnet, *Chem. Eur. J.* **2012**, *18*, 10271-10280. |
| [49] | E. C. Constable, M. D. Ward, *Dalton Trans.* **1990**, 1405-1409. |

# 7

## Summary, Conclusions and Outlook

## 7.1. Summary

### 7.1.1. General Introduction (Ch 1)

Polypyridyl ruthenium complexes are classical tools in photochemistry.[1-2] Their photophysical properties can be tuned in order to get the desired behavior under light irradiation. In particular, ruthenium complexes with distorted octahedral geometry are capable of photosubstituting one ligand by a solvent molecule upon visible light irradiation (400-600 nm).[3]

Two potential applications of this kind of complexes are discussed, being the design of light-controlled molecular machines, and light-activatable anticancer prodrugs. In this thesis, a link between these two applications using lipid bilayers was made. Photosubstitution reactions are first studied at the surface of lipid bilayers in order to mimic natural molecular machines. By anchoring monodentate ligands at the membrane, the ruthenium complex can bind thermally to the membrane, and be cleaved by visible light irradiation to realize a model of molecular carrier controlled by light. In the second part the same liposomes functionalized with photosensitive ruthenium complexes are considered for photochemotherapy as the ruthenium aqua complex liberated by light irradiation may be cytotoxic. The ruthenium-functionalized liposomes, which act as pro-drugs, may be delivered to cancer cells. Once taken up they can be activated by light irradiation, resulting in a photosubstitution reaction that releases the active ruthenium aqua complex from the membrane into the cell. Thus, by combining the photochemistry of ruthenium complexes and the biological properties of liposomes we moved from a very fundamental, biomimetic topic dealing with molecular motion, to the second, more applied field of drug delivery.

### 7.1.2. Ruthenium polypyridyl complexes hopping at anionic lipid bilayer surface through a supramolecular bond sensitive to visible light (Ch 2)

In Chapter 2 the new ruthenium complex $[Ru(terpy)(dcbpy)(Hmte)]^{2+}$ (RuHmte) is introduced, where terpy is 2,2';6',2"-terpyridine, dcbpy is 6,6'-dichloro-2,2'-bipyridine, and Hmte is 2-methylthioethan-1-ol. Based on kinetics and thermodynamic data it is shown that steric hindrance of the dcbpy ligand induces destabilization of both the ruthenium thioether complex RuHmte and the aqua analogue $[Ru(terpy)(dcbpy)(H_2O)]^{2+}$ (RuOH$_2$). These two species are in fact in thermal

equilibrium at room temperature and in the dark. However, shining blue light allows for selective substitution of the thioether ligand by an aqua ligand, thus shifting the equilibrium towards the formation of the $RuOH_2$ complex (see Scheme 7.1a). Such light-induced equilibrium shift is shown to be repeatable at least four times in homogenous aqueous solution.

Thermal binding and light-induced unbinding of a thioether ligand to the ruthenium center was also achieved at the surface of negatively charged liposomes (see Figure 7.1b). UV-vis measurements show that the ruthenium aqua complex efficiently coordinates to a membrane-embedded thioether ligand in the dark, and that upon exposure to visible light the Ru-S coordination bond is selectively cleaved to release the ruthenium aqua complex into the solution. This cycle is shown to be repeatable four times by switching on and off the source of visible light. Thus, light-triggered hopping of a ruthenium complex is achieved at a lipid bilayer membrane surface.
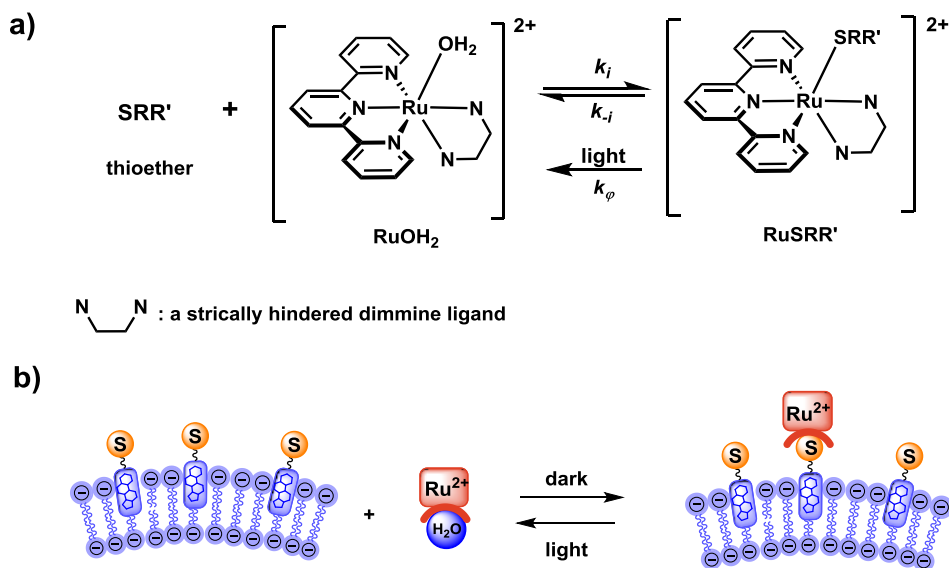


**Scheme 7.1.** a) Thermal equilibrium between $[Ru(terpy)(N-N)(H_2O)]^{2+}$ and $[Ru(terpy)(N-N)(SRR')]^{2+}$ and the photosubstitution of SRR' ligand by $H_2O$. SRR' is a thioether ligand such as 2-methylthioethan-1-ol and N-N is a diimine ligand such as dcbpy. b) Light-induced ruthenium binding and un-binding at a negatively charged bilayer membrane.

The light-controlled hopping of a ruthenium complex at the membrane has two requirements: first, the steric hindrance of the ruthenium complex should be high enough to allow for fast thermal binding and photo-induced unbinding. Secondly, the liposomes should be negatively charged so that the ruthenium aqua complexes actually bind to the membrane-embedded sulfur ligands. These two issues are discussed in Chapters 3 and 4, respectively.

### 7.1.3. Spontaneous formation in the dark, and visible light-induced cleavage, of a Ru-S bond in water: a thermodynamic and kinetic study (Ch 3)

In Chapter 3 the thermal and photochemical reactivity in water of four related ruthenium polypyridyl complexes with the general formula $[Ru(terpy)(N-N)(Hmte)]^{2+}$ is described, where N-N are the four diimine ligands bpy, biq, dcbpy, or dmbpy (see Scheme 3.1a). For each of these complexes photo cleavage of the Ru-S bond occurs, resulting in the formation of the aqua complex $[Ru(terpy)(N-N)(H_2O)]^{2+}$ (RuOH$_2$). In this chapter it is described how the steric hindrance of the N-N ligand influences both the thermodynamic stability and kinetic lability of the RuHmte and RuOH$_2$ complexes in the dark. The kinetics of the photosubstitution reactions are reported as well.

Upon increasing the steric hindrance of the N-N ligand, the rates of thermal binding to and thermal cleavage of the Hmte ligand from the ruthenium center increase. A shift was observed along the series bpy, biq, dcbpy, and dmbpy, from a very slow thermal equilibrium between RuOH$_2$ and RuHmte with N-N=bpy, to a very fast one with N-N=dmbpy. The increased lability of the hindered complexes in water is not due to the change of the enthalpy of activation of the substitution reaction ($\Delta H^{\ddagger}$). Instead, it is due to the variation of the entropy of activation $\Delta S^{\ddagger}$, which from being negative for bpy and biq, becomes positive for dcbpy and dmbpy. Such change in activation entropy indicates a change in the mechanism of the substitution reaction, from an interchange associative mechanism with bpy and biq ($\Delta S^{\ddagger}<0$) to an interchange dissociative mechanism for dcbpy and dmbpy ($\Delta S^{\ddagger}>0$).

On the other hand, the quantum efficiency of the photocleavage of the Ru-S bond upon light irradiation also increases along the series N-N= bpy, biq, dcbpy, and dmbpy. Overall, two requirements were found for shifting with light the equilibrium between the RuHmte and RuOH$_2$ species in water. First, the thermodynamic stability of the RuHmte complex in water and in the dark must be higher than that of the RuOH$_2$

complex ($k_{-i}<k_i$) to lead to the spontaneous formation of the thioether complex. If the establishment of thermal equilibrium is too slow however, such as for the least hindered complex with N-N=bpy, RuHmte formation does not occur at room temperature because there is not enough thermal energy to cross the activation barrier of the coordination reaction. Secondly, the rate of the photosubstitution of the Hmte ligand by water must be higher than that of its thermal dissociation ($k_{-i}<k_\varphi$, see Figure 7.1a). For the most hindered ruthenium complex with N-N=dmbpy this condition is not met, and the thermal lability of RuHmte is so high that light cannot induce a significant shift of the thermal equilibrium between RuHmte and RuOH$_2$. To conclude, only the moderately hindered complexes, *i.e.*, those with N-N=biq and dcbpy, are suitable for shifting with light the equilibrium between RuHmte and RuOH$_2$.

### 7.1.4. Binding of a ruthenium complex to a thioether ligand embedded in a negatively charged lipid bilayer: a two-step mechanism (Ch 4)

As mentioned in section 7.1.2., negatively charged membranes are required for the binding of ruthenium aqua complexes to membrane-embedded thioether ligands. In Chapter 4, the role of the negative charge of the membranes on the coordination reaction occurring at the water-membrane interface is reported. The interaction of the complex [Ru(terpy)(dcbpy)(H$_2$O)]$^{2+}$ with phospholipid membranes containing either neutral thioether ligands or cholesterol was studied using three different techniques: UV-visible spectroscopy, Langmuir-Blodgett monolayer surface pressure measurements, and Isothermal Titration Calorimety (ITC). The first technique proved that ruthenium binding to the thioether ligands becomes slower when the electrostatic interaction between the ruthenium cations and the negative liposomes is shielded by higher ionic strengths. Thus, adsorption of the dicationic ruthenium complex at the surface of the negative membranes plays a prominent role in the formation of the Ru-S coordination bond.

Information about the time scale of such adsorption phenomenon and about its thermodynamics was obtained from lipid monolayer surface pressure and ITC measurements. It was shown that the adsorption of the ruthenium aqua complex to the surface of negatively charged monolayers and bilayers is much faster (minutes) than coordination, *i.e.*, ligand exchange (hours). In addition, the adsorption phenomenon was found to be endothermic, *i.e.*, entropy driven. Based on these results a two-step model is proposed for the binding of the dicationic metal complex to the thioether

ligands embedded in negative liposomes. In the first step, the outer leaflet of a negatively charged lipid bilayer quickly adsorbs the positively charged metal complexes, whereas in the second step the Ru-S bond formation occurs *via* two-dimensional diffusion of both reagents at the membrane (see Scheme 4.2). Such two-step reaction at negative membranes is faster, all other conditions being the same, than the corresponding Ru-S bond formation in homogenous solutions.

## 7.1.5. Liposomes functionalized with ruthenium: towards a tumor-targeted, light-controlled anticancer prodrugs (Ch 5)

In Chapter 5, the potential application of liposomes decorated with photosensitive polypyridyl ruthenium complexes in drug delivery is discussed. Four non-labile ruthenium complexes with the general formula $[Ru(terpy)(N-N)(SRR')]^{2+}$ (N-N = bpy (2,2'-bipyridine) or pymi (phenylpyridin-2-ylmethylene-imine), and SRR' = thioether ligands with a cholesterol tail, were prepared and were supported on neutral and negatively charged liposomes. All ruthenium-functionalized liposomes are photoreactive; shining blue light on them results in the photocleavage of the ruthenium complex from the liposome surface. The photosubstitution reactions are shown to be faster at human body temperature (37 °C) than at room temperature, and slightly faster at neutral bilayer surfaces than at negatively charged ones.

Cellular uptake experiments on human carcinoma cell lines showed that in the absence of PEGylation, ruthenium-functionalized liposomes built from neutral lipids are better taken up by HepG$_2$, A2780, and A2780R cancer cells than their analogues built from negatively charged lipids. When PEGylated lipids are introduced in the liposome formulation, the charge of the resulting ruthenium-functionalized stealth liposomes is shielded, which results in a decreased cellular uptake compared to PEG-free liposomes. Moreover, almost equal cellular uptakes were obtained when neutral and negatively charged lipids are used for PEGylated liposomes containing Ru. Overall, the structure of the ruthenium complexes did not affect significantly these uptake results.

Dark cytotoxicity tests with DOPC and DOPG stealth liposomes functionalized with any of the four ruthenium complexes showed that these liposomes are poorly toxic against A2780 and A2780R cell lines, with no significant variation between the different ruthenium complexes. Light cytotoxicity results were obtained on HepG2 cells for one of the ruthenium complexes supported on non-PEGylated liposomes with different surface charges. The results showed up to five times higher cytotoxicity after light

irradiation than in the dark. Thus, liposomes decorated with ruthenium complexes are promising in drug delivery.

### 7.1.6. Yellow-light sensitization of a ligand photosubstitution reaction in a ruthenium polypyridyl complex covalently bound to a rhodamine dye (Ch 6)

In Chapter 6 the possibility of extending the photoactivation of polypyridyl ruthenium complexes towards longer wavelengths by photosensitization, is discussed. As mentioned in section 7.1.1. some of these metal complexes have been proposed as light-activatable drugs in phototherapy. However, their potential application *in vivo* is limited since they mostly show high molar absorptivities near 450 nm, *i.e.*, for blue light, which is known to poorly penetrate human tissues.[4-5]

The photosubstitution of a thioether ligand by a water molecule was studied with 570 nm photons (*i.e.*, yellow light). A rhodamine B dye, which has a high molar absorptivity for yellow light, was covalently bound *via* a short saturated linker to the terpyridine ligand Rtpy in the complex $[Ru(Rterpy)(bpy)(Hmte)]^{2+}$. The excellent antenna effect of the rhodamine B dye, coupled to efficient energy transfer to the ruthenium center, resulted in faster photosubstitution of the Hmte ligand with yellow photons, than with blue photons.

In this chapter also the rate of photosubstitution reactions is discussed when photons of insufficient energy, compared to that of the [1]MLCT state, are used. Both for the rhodamine B-functionalized ruthenium complex and for its antenna-free analogue $[Ru(terpy)(bpy)(Hmte)]^{2+}$ the quantum yields upon yellow light or blue light irradiation were found to be comparable. In fact, at constant photon flux it is the extinction coefficient that mostly influences the photosubstitution rate for these complexes, whereas the photosubstitution quantum yield hardly depends on the irradiation wavelength.

## 7.2. Conclusions and Outlook

### 7.2.1. General conclusions

In this thesis the thermal- and photo-substitution behavior of polypyridyl ruthenium complexes with the general formula of $[Ru(terpy)(N-N)(SRR')]^{2+}$ is described, either at the surface of lipid bilayers, or in homogeneous solutions. It is shown that the successive thermal binding and light-induced unbinding of the cationic ruthenium complex at the surface of the lipid bilayer requires negatively charged liposomes and ruthenium complexes containing moderately hindered N-N bidentate ligands such as

biq or dcbpy. Our results in homogeneous solution show that changing the steric hindrance of the bidentate ligand influences both the photo- and thermal reactivities of these complexes, by altering the mechanism of the Ru-S bond formation. It is also shown that the Ru-S bond formation at the surface of negative lipid bilayers is faster than the same reaction in homogenous aqueous solutions, and a two-steps mechanism is proposed for the thermal coordination of ruthenium aqua complexes at membrane-embedded ligands.

The application of ruthenium-functionalized liposomes in drug delivery is discussed in Chapter 5. *In vitro* tests on cancer cell lines show that neutral liposomes functionalized with ruthenium compounds are more readily taken up by cancer cells than ruthenium-free liposomes. The liposome samples with ruthenium compounds are shown to be poorly cytotoxic in the dark. After light irradiation, the cytotoxicity increased at least up to five times for ruthenium complexes supported on non-PEGylated liposomes.

Finally, the photoactivation of polypyridyl complexes with low-energy photons was studied using a photosensitization approach. A photosubstitution reaction was made faster upon yellow light irradiation than upon blue light irradiation by covalently linking a rhodamine B dye to the ruthenium complex.

### 7.2.2. Outlook

#### 7.2.2.1. Molecular motion at the surface of a lipid bilayer

In this research it was shown that a ruthenium complex can hop at the surface of a lipid bilayer in a light-controlled manner. The ultimate goal of this research is to achieve unidirectional motion at the lipid bilayer surface, such as reported linear organic molecular machines.[6-7] For this aim the thioether ligands at the membrane should be organized in a way to produce a dissymmetric track. The first issue to solve for extending this research is to modify the ruthenium complex in order to detect its lateral position, and possibly to probe binding and unbinding events by single-molecule techniques. One approach is to use fluorescent imaging techniques, which have shown their potential at the single-molecule level. Since ruthenium complexes of the type $[Ru(terpy)(N-N)(SRR')]^{2+}$ photosubstitute a ligand under light irradiation their luminescence is very poor. Thus, a fluorophore would need to be covalently linked to the ruthenium complex. As discussed in Chapter 6, however, the emission spectrum of the fluorophore overlapped with the $^1$MLCT absorption band of the ruthenium

complex, and the fluorescence of the dye was quenched by Förster energy transfer. To avoid such quenching a fluorophore absorbing in the red region of the spectrum, *i.e.*, at wavelengths higher than 630 nm, should be used. It is expected that in this case the photoreactivity of the metal center and the emission of the fluorophore may be decoupled, which would allow for probing the position of the ruthenium complex *via* excitation of the fluorophore.

### 7.2.2.2.    Liposomes functionalized with ruthenium in photoactivated chemotherapy

Liposomal drug delivery for ruthenium-based anticancer compounds has not been investigated extensively, except for two recent studies in 2012.[8-9] In Chapter 5, it was shown that liposomes functionalized with polypyridyl complexes are potential candidates for drug delivery. However, our results are only preliminary, and more investigations need to be done in this area. The first important point is to modify the uptake detection method. Our uptake results are currently based on the fluorescence of NBD-PC lipids included in the formulation of the liposomes. However, the excitation wavelength of NBD-PC overlaps with the [1]MLCT absorption band of the ruthenium complex, as a result of which the fluorescence of NBD is partially quenched by the ruthenium complex. As explained in Chapter 5, the extent of fluorescence quenching in the cell culture can be estimated based on the data obtained in absence of cells. However, this estimation remains rather qualitative since the cell environment is different from that of an aqueous buffer. Ideally the amount of ruthenium in cells should be quantified by metal trace analysis methods after uptake experiments. Unfortunately valid ruthenium concentrations in cell lysis solutions could not be obtained using ICP-OES. A more sensitive detection method, such as ICP-MS, should be used in the future.

The dark and light cytotoxicity investigations need to be extended in the future in an optimal condition for different drug exposure times using stealth liposomes. Irradiation of the cells after drug exposure should be performed in at least 5% $CO_2$ atmosphere and 37 °C. Light intensity and photon flux also should be measured precisely and correctly. Finally, after finding the optimal conditions, all of the in vitro tests, *i.e.,* uptake, dark toxicity and light cytotoxicity, should be performed on healthy cells as well to determine the toxicity of such liposomes to these healthy cells and conclude on the selectivity of such prodrugs towards cancer cells.

## 7.3.  References

[1]     V. Balzani, A. Juris, *Coord. Chem. Rev.* **2001**, *211*, 97-115.

[2]     K. Kalyanasundaram, *Coord. Chem. Rev.* **1982**, *46*, 159-244.

[3]     S. Bonnet, J.-P. Collin, *Chem. Soc. Rev.* **2008**, *37*, 1207-1217.

[4]     P. Zhang, W. Steelant, M. Kumar, M. Scholfield, *J. Am. Chem. Soc.* **2007**, *129*, 4526-4527.

[5]     R. Weissleder, V. Ntziachristos, *Nat. Med.* **2003**, *9*, 123-128.

[6]     M. von Delius, E. M. Geertsema, D. A. Leigh, *Nature Chem.* **2010**, *2*, 96-101.

[7]     D. A. Leigh, J. K. Y. Wong, F. Dehez, F. Zerbetto, *Nature* **2003**, *424*, 174-179.

[8]     L. Simeone, G. Mangiapia, G. Vitiello, C. Irace, A. Colonna, O. Ortona, D. Montesarchio, L. Paduano, *Bioconjug. Chem.* **2012**, *23*, 758-770.

[9]     G. Mangiapia, G. D'Errico, L. Simeone, C. Irace, A. Radulescu, A. Di Pascale, A. Colonna, D. Montesarchio, L. Paduano, *Biomaterials* **2012**, *33*, 3770-3782.

# Appendix I

## General photochemistry methods

## AI.1. Determination of the extinction coefficients

### AI.1.1. Extinction coefficients of kinetically stable compounds in an aqueous solution

For a non-labile compound RuL (where L is a monodentate ligand, typically L=H$_2$O, or SRR') at room temperature the extinction coefficient was determined as follows:

A stock solution **α** of compound RuL was prepared (typical concentration:$10^{-4}$ M) in water and by successive dilution of solution **α**, five or six solutions with different concentrations (typically between $10^{-4}$ and $10^{-5}$ M) were prepared. The UV-vis spectra of all samples were measured, typically between 350-700 nm. The extinction coefficient at each wavelength was then determined from the slope of the plot of absorbance *vs.* concentration according to Beer-Lambert Equation AI.1. In this equation $l$ is the UV-vis absorbance pathlength, $\varepsilon_{RuL}$ is the extinction coefficient of RuL, and *[RuL]* is the concentration of RuL.

$$A = \varepsilon_{RuL} \cdot l \cdot [RuL] \quad \textbf{(Equation AI.1)}$$

### AI.1.2. Extinction coefficients of kinetically labile compounds involved in a fast thermodynamic equilibrium

When the ruthenium thioether complex RuSRR' is in a thermal equilibrium with the corresponding ruthenium aqua complex RuOH$_2$ (taking into account that none of H$_2$O or thioether ligands absorb light) determination of the extinction coefficient of RuSRR' requires a different method than of kinetically stable compounds. A stock solution **β** of thioether compound SRR' in water and a stock solution **δ** of RuSRR' in solution **β**, were prepared. Four solutions containing 3–x mL of solution **β** and x mL of solution **δ** were prepared, where x = 0.5, 1.0, 1.5 or 2 mL. UV-vis spectra were measured for all samples. In such conditions, the concentration in thioether SRR' compound is the same for all samples, so that the ratio *[RuSRR']/[RuOH$_2$]* remains constant (Equation AI.2). However, due to dilution of the ruthenium complex (solution **δ**) with the SRR' solution (solution **β**), the total concentration in ruthenium *[Ru]$_{tot}$* increases from x=0.5 to x=2. At constant *[RuSRR']/[RuOH$_2$]* ratio, *[RuSRR']* is proportional to *[Ru]$_{tot}$* and can be calculated according to Equation AI.3.

$$K' = \frac{[RuSRR']}{[RuOH_2]} = K \cdot [RuSRR'] \quad \textbf{(Equation AI.2)}$$

$$r = \frac{[RuSRR']}{[Ru]_{tot}} = \frac{K'}{K' + 1} \qquad \textbf{(Equation AI.3)}$$

From the value of r in Equation AI.3 and the extinction coefficient of $RuOH_2$ which was determined using the method in section AI.1.1, the extinction coefficient of RuSRR' was calculated using Equation AI.4. In this equation $\varepsilon_{eq}$ is the extinction coefficient obtained from the slope of the plot of the absorbance versus *[RuSRR']* at the equilibrium.

$$\varepsilon_{RuSRR'} = \frac{\varepsilon_{eq} - \left((1-r) \cdot \varepsilon_{RuOH_2}\right)}{r} \quad \textbf{(Equation AI.4)}$$

## AI.2.  Calculation of the concentration of the compounds from the UV-vis measurements

### AI.2.1. One-wavelength method

There are two distinct methods for calculating the concentrations of two photochemically interconverting compounds in the solution by deconvolution of the UV-vis spectra. The first method needs one wavelength, at which the change in absorbance is large during the experiment. Another requirement for this method is that the reaction goes to completion. If we consider a substitution reaction RuSRR'+$H_2O$→ $RuOH_2$+SRR', after a given amount of time, all of RuSRR' is expected to be converted into $RuOH_2$ (assuming that $H_2O$ and RSS' do not absorb light). The contribution of each compound to the absorbance of the solution (for each absorption measurement at $t_j$ during the reaction) is a function of its concentration, the length of the cell, and the extinction coefficient of the compound, according to Beer-Lambert's law (see Equation AI.5).

$$A_{t_j}^{\lambda} = l \cdot \varepsilon_{RuSRR'}^{\lambda} \cdot [RuSRR'] + l \cdot \varepsilon_{RuOH_2}^{\lambda} \cdot [RuOH_2] \quad \textbf{(Equation AI.5)}$$

If at $t_{\infty}$, RuSRR' is fully converted into $RuOH_2$, thus the equation becomes:

$$A_{t_{\infty}}^{\lambda} = l \cdot \varepsilon_{RuOH_2}^{\lambda} \cdot [Ru]_{tot} \qquad \textbf{(Equation AI.6)}$$

*[Ru]$_{tot}$* is the total Ru concentration. If we replace *[RuOH$_2$]* by *[Ru]$_{tot}$−[RuSRR']*  in Equation AI.5, *[RuSRR']* can be obtained from Equation AI.7.

$$[RuSRR'] = \frac{A_{t_j}^{\lambda} - A_{t_\infty}^{\lambda}}{l \cdot \left(\varepsilon_{RuSRR'}^{\lambda} - \varepsilon_{RuOH_2}^{\lambda}\right)} \quad \textbf{(Equation AI.7)}$$

## AI.2.2. Two-wavelength method

If the reaction does not go to completion, the absorbance at two different wavelengths $\lambda_1$ and $\lambda_2$ can be expressed as:

$$A_{t_j}^{\lambda_1} = l \cdot \varepsilon_{RuSRR'}^{\lambda_1} \cdot [RuSRR'] + l \cdot \varepsilon_{RuOH_2}^{\lambda_1} \cdot [RuOH_2] \quad \textbf{(Equation AI.8.a)}$$

$$A_{t_j}^{\lambda_2} = l \cdot \varepsilon_{RuSRR'}^{\lambda_2} \cdot [RuSRR'] + l \cdot \varepsilon_{RuOH_2}^{\lambda_2} \cdot [RuOH_2] \quad \textbf{(Equation AI.8b)}$$

Thus, *[RuSRR']* can be expressed as:

$$[RuSRR'] = \frac{A_{t_j}^{\lambda_1} - \left(l \cdot \varepsilon_{RuOH_2}^{\lambda_1} \cdot [RuOH_2]\right)}{l \cdot \varepsilon_{RuSRR'}^{\lambda_1}} \quad \textbf{(Equation AI.9)}$$

Equation AI.9 can be substituted in the Equation AI.8b, and *[RuOH_2]* can thus be expressed as a function of $A_{\lambda_1}$ and $A_{\lambda_2}$ to yield Equation AI.10 (with $l$= 1 cm).

$$[RuOH_2] = \frac{A_{t_j}^{\lambda_2} \cdot \varepsilon_{RuSRR'}^{\lambda_1} - A_{t_j}^{\lambda_1} \cdot \varepsilon_{RuSRR'}^{\lambda_2}}{\varepsilon_{RuSRR'}^{\lambda_1} \cdot \varepsilon_{RuOH_2}^{\lambda_2} - \varepsilon_{RuSRR'}^{\lambda_2} \cdot \varepsilon_{RuOH_2}^{\lambda_1}} \quad \textbf{(Equation AI.10)}$$

Calculation of concentrations and kinetic studies using the two-wavelength method depends on the accuracy of four extinction coefficients at two different wavelengths, whereas in the one-wavelength method only two extinction coefficients are needed. However, in the one-wavelength method the rate constant is highly sensitive to the accuracy of the absorbance at $t_\infty$. In fact, if the reaction does not go to completion a wrong value is taken for $A_{t\infty}^{\lambda}$ and the accuracy of the calculated concentrations are slightly lower than the concentrations calculated with two-wavelength method.

## AI.3.   Photosubstitution quantum yield measurements

### A.I.3.1. Irradiation close to an isosbestic point

For a photosubstitution reaction, where SRR' in RuSRR' is substituted by $H_2O$, assuming that the aqua complex $RuOH_2$ is not thermally reactive or photoreactive and that RuSRR' is

thermally stable in water and in the dark at room temperature, the photosubstitution quantum yield can be measured as follows:

The expression of the rate of the photosubstitution reaction is given by Equations AI.11 and AI.12, where $k_{\varphi i}$ is a first-order photosubstitution rate constant, $n_{RuSRR'}$ the number of moles of the RuSRR' complex at time $t$, $\varphi_i$ the photosubstitution quantum yield, and $q_{RuSRR'}$ the number of moles of photons absorbed by the RuSRR' complex per unit time. $q_{RuSRR'}$ can be calculated using Equation AI.13, where $\Phi$ is the photon flux determined by standard ferrioxalate actinometry,[1] $1–10^{-Ae}$ is the probability of photon absorption, $A_e$ is the absorbance of the solution at the irradiation wavelength, and $(A_{RuSRR'}/A_{Ru(tot)})$ the relative contribution of the RuSRR' complex to the total absorbance of the solution at the irradiation wavelength.

$$r_{photo} = \frac{dn_{RuSRR'}}{dt} = -k_{\varphi i} \cdot n_{RuSRR'} \quad \textbf{(Equation AI.11)}$$

$$r_{photo} = -q_{RuSRR'} \cdot \varphi_i \quad \textbf{(Equation AI.12)}$$

$$q_{RuSRR'} = \Phi \cdot (1 - 10^{-A_e}) \cdot \left(\frac{A_{RuSRR'}}{A_e}\right) \quad \textbf{(Equation AI.13)}$$

If the irradiation wavelength $\lambda_e$ is chosen close to the wavelength of the isosbestic point the probability of photon absorption remains constant during irradiation because $A_{RuSRR'}$ and $A_e$ do not vary in time and at $\lambda_e$, $\varepsilon_e = \varepsilon_{RuSRR'} = \varepsilon_{Ru(tot)}$. Equations AI.12 and AI.13 rearrange to Equation AI.14, where $n_{Ru(tot)}$ is the total number of moles of ruthenium complexes in the UV-vis cuvette.

$$r_{photo} = \frac{dn_{RuSRR'}}{dt} = -\Phi \cdot (1 - 10^{-A_e}) \cdot \left(\frac{n_{RuSRR'}}{n_{Ru(tot)}}\right) \cdot \varphi_i \quad \textbf{(Equation AI.14)}$$

By comparison between equation AI.11 and AI.14, quantum yield $\varphi_i$ can be obtained from Equation AI.15.

$$\varphi_i = \frac{k_{\varphi i} \cdot n_{Ru(tot)}}{\Phi \cdot (1 - 10^{-A_e})} \quad \textbf{(Equation AI.15)}$$

**Note 1:** $k_{\varphi i}$ in Equation AI.15 can be obtained from the slope of a plot of ln*([RuSRR']/[Ru]$_{tot}$)* *vs.* irradiation time (see Equation AI.11). For kinetically unstable RuSRR' complex in water, where RuSRR' and RuOH$_2$ are in a thermal equilibrium, another method is used to calculate $k_{\varphi i}$ (see Appendix III, section AIII.9).

## AI.3.2.    Irradiation at the wavelength that is not an isosbestic point

When the irradiation wavelength is not close to an isosbestic point, the absorbance at the irradiation wavelength is not constant throughout the irradiation, which must be taken into account. Thus the procedure below was applied to calculate the photosubstitution quantum yields.[2]

The average absorbance between two consecutive UV-vis measurements at $t_j$ and $t_{j+1}$, at the irradiation wavelength $\lambda_e$, was calculated according to Equation AI.16.

$$(A_e)_{ave} = \frac{(A_e)_j + (A_e)_{j+1}}{2} \quad \textbf{(Equation AI.16)}$$

The number of moles of photons $q_j$ absorbed by the ruthenium complex RuSRR' between two consecutive UV-vis measurements *($\Delta t = t_{j+1} - t_j$)*, was calculated according to Equation AI.17. In this Equation $\Phi$ is the photon flux at irradiation wavelength $\lambda_e$ and $(1 - 10^{(A_e)ave})$ is the probability of photon absorption. If the sample was irradiated from the top of the cuvette (*l'=3 cm*), while the absorbance was measured perpendicular to the light irradiation direction (absorbance pathlength *l*=1 cm), $A_e$ must be multiplied by 3 (see Figure AI.1).

$$q_j = \left(\frac{A_{RuSRR'}}{(A_e)_{ave}}\right)_j \cdot \left(1 - 10^{-(A_e)ave}\right) \cdot \Phi \cdot \Delta t \quad \textbf{(Equation AI.17)}$$

The total number of moles of absorbed photons since $t_0$ ($t_0 \rightarrow t_j$), $Q_j$, can then be calculated at each irradiation time according to Equation AI.18.

$$Q(t) = \sum_j q_j \quad \textbf{(Equation AI.18)}$$

Finally, the quantum yield $\varphi_i$ can be obtained from the slope of a plot of the number of moles of RuSRR'($n_{RuSRR'}$) *vs.* $Q_j$.

**Note 2:** probability of absorbance depends on the irradiation pathlength (*l'*). If the sample is irradiated from the top of the UV-vis cuvette *l'*=3 cm (see Figure AI.1), $A_e$, which is

measured by a spectrometer over a pathlength of l cm, must be multiplied by 3. Thus in Equation AI.15 and AI.17 probability of absorbance is: $(1-10^{-(Ae\times3)})$.
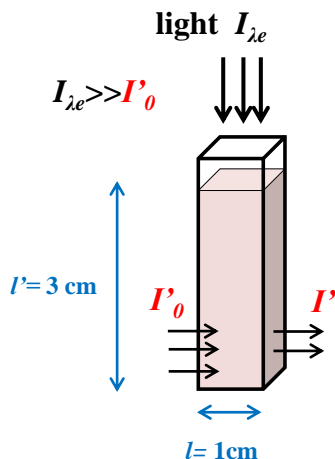


**Figure AI.1**. Irradiation of a solution in a UV-vis cuvette is done *in situ*, perpendicular to the optical axis of the spectrophotometer. Irradiation pathlength=*l'*, UV-vis absorption pathlength=*l*, $I_{\lambda e}$: light power at irradiation wavelength $\lambda_e$. *I'*: UV-vis light beam intensity measured by the spectrophotometer.

## AI.4.   References

[1]     J. G. P. Calvert, J. N., *Chemical actinometer for the determination of ultraviolet light intensities. In Photochemistry.* Wiley and Sons, New York, **1967**, 780**.**
[2]     M. Rougee, T. Ebbesen, F. Ghetti, R. V. Bensasson, *J. Phys. Chem.* **1982**, *86*, 4404.

# Appendix II

## Supporting Information of Chapter 2:

**Ruthenium polypyridyl complexes hopping at anionic lipid bilayers *via* a supramolecular bond sensitive to visible light**

## AII.1. Synthesis

Dcbpy: 6,6-dibromo-2,2'-bipyridine (800 mg, 2.56 mmol) and $PCl_5$ (2.64 g, 12.68 mmol) were dissolved in $POCl_3$ (26 mL). To this solution was added KI (0.26 g, 1.57 mmol). The solution was heated to reflux for 48 hours after which $POCl_3$ was distilled under vacuum. Water was slowly added to the residue after which the suspension was basified using concentrated aqueous ammonia. The suspension was extracted twice with DCM, the organic phase dried with $MgSO_4$, filtered and the filtrate evaporated under reduced pressure. The white solid was recrystallized twice from toluene to yield 6,6-dichloro-2,2'-bipyridine (393 mg, 68%). Characterization was identical to the reference.[1]

**[Ru(terpy)(dcbpy)Cl]Cl ([3]Cl)**: [Ru(tpy)Cl$_3$] (67.1 mg, 0.15 mmol) and dcbpy (58.7 mg, 0.26 mmol) were dissolved in ethylene glycol (1 mL). The mixture was heated to 180 °C for 4 hours, after which EtOH (2 mL) was added. The mixture was filtered to remove insoluble material and the filtrate was put under reduced pressure to remove EtOH. The purple solution was purified over neutral alumina (eluent: 95:5 DCM/MeOH); excess ethylene glygol was removed by coevaporation with toluene. The product was finally reprecipitated from MeOH/Et$_2$O to yield [**3**]Cl as a violet powder (47.5 mg, 50%). *$^1$H NMR (300 MHz, MeOD, see Scheme 2.1 for proton notation) δ* 8.75 (d, *J* = 8.1 Hz, 1H, B3), 8.54 (d, *J* = 8.1 Hz, 2H, T3'5'), 8.51 – 8.41 (m, 3H, T33"+A3), 8.32 (t, *J* = 8.0 Hz, 1H, B4), 8.18 – 8.03 (m, 4H, T66"+T4'+B5), 8.00 (td, *J* = 7.9, 1.4 Hz, 2H, T44"), 7.72 (t, *J* = 8.0 Hz, 1H, A4), 7.45 (dd, *J* = 9.6, 3.6 Hz, 2H, T55"), 7.17 (d, *J* = 7.9 Hz, 1H, A5). *$^{13}$C NMR (75 MHz, CDCl$_3$) δ* 166.17+160.93+160.27+ 160.21+159.75+159.22 (B6+B2+A2+A6+T22"+T2'6'), 153.86 (T66"), 139.76 (B4), 138.39 (A4), 137.82 (T44"), 135.54 (T4'), 128.77 (B5), 127.44 (A5), 127.15 (T55"), 123.47 (T33"), 122.81 (A3), 122.55 (B3), 122.28 (T3'5'). *ES MS m/z (calc):* 595.9 (534.86 [M – Cl$^-$]$^+$), 295.7 (295.7 [M – 2 Cl + MeOH]$^{2+}$). *Anal. Calcd for C$_{25}$H$_{17}$Cl$_4$N$_5$Ru·4H$_2$O*: C, 42.75; H, 3.59; N, 9.97. Found: C, 42.90; H, 3.01; N, 10.05.

**[Ru(terpy)(dcbpy)(H$_2$O)](PF$_6$)$_2$ ([1](PF$_6$)$_2$)**: [**3**]Cl (50 mg, 85 μmol) and AgPF$_6$ (65 mg, 0.26 mmol) were dissolved in 4:1 acetone/H$_2$O (5 mL). The solution was shortly heated to boiling point and allowed to cool down. The solution was filtered over *celite,* concentrated under reduced pressure to 1 mL, after which it was put in the fridge overnight. The suspension was filtered to yield [**1**](PF$_6$)$_2$ as a brown powder (42.7 mg, 58%). $^1$H NMR (300 MHz, D$_2$O, 298 K) δ 8.66 (d, *J* = 8.2 Hz, 1H, B3), 8.51 (d, *J* = 8.1 Hz, 2H, T3'5'), 8.43 (d, *J* = 8.0 Hz, 2H, T33"), 8.38 – 8.27 (m, 2H, B4+A3), 8.21 (t, *J* = 8.1 Hz, 1H, T4'), 8.13 (d, *J* = 5.5 Hz, 2H, T66"), 8.10 – 7.93 (m, 3H, B5+T44"), 7.66 (t, *J* = 8.0 Hz, 1H, A4), 7.45 (ddd, *J* = 7.0, 5.7, 1.1 Hz, 2H, T55"), 7.12 (d, *J* = 8.0 Hz, 1H, A5). *UV-vis:* λ$_{max}$ (ε in L·mol$^{-1}$·cm$^{-1}$) in H$_2$O: 488 nm (7550). *ES MS m/z (calc):* 590.0 (590.45 [M – 2 PF$_6$ – H$_2$O + MeO]$^+$). $^{13}$C NMR was impossible due to the poor solubility of [**1**](PF$_6$)$_2$ in D$_2$O.
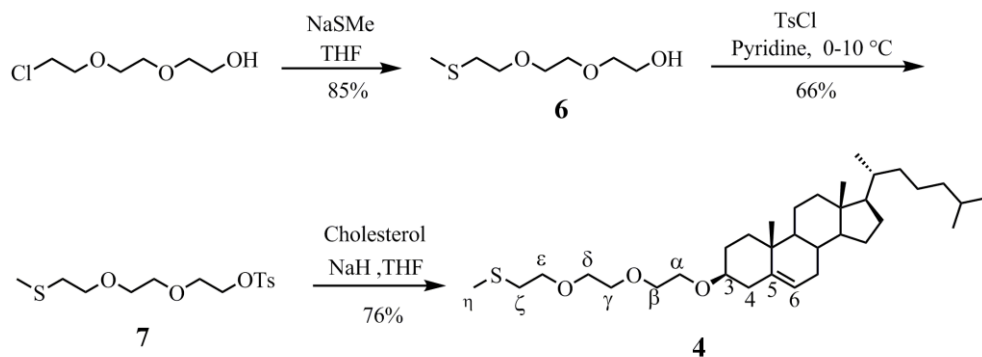
**Scheme AII.1**. Synthesis of ligand **4** and atom numbering scheme for NMR athribution.

**6:** A suspension of NaSMe (6.40 g, 91.3 mmol) in dry tetrahydrofuran (200 mL) was prepared under argon. While stirring 2-[2-(2-chloroethoxy)ethoxy]ethanol (9.62 g, 57.1 mmol) was added to the flask. The reaction mixture was refluxed under argon overnight and the solvent was evaporated under reduced pressure. The crude light yellow oil was dissolved in dichloromethane (130 mL) and washed with water (80 mL) and brine (2 × 80 mL). The organic layer was dried with $MgSO_4$ and concentrated under reduced pressur to give **6** as a colorless oil (8.80 g, 85%). $^1$H NMR (300 MHz, δ in $CDCl_3$): 3.76-3.62 (m, 10H, α + β + γ + δ + ε), 2.71 (t, 2H, ζ), 2.46 (s, 1H, OH), 2.15 (s, 3H, η). $^{13}$C NMR (75 MHz, δ in $CDCl_3$): 72.39 + 70.39 + 70.29 + 70.22 (α + β + γ + δ), 61.67 (ε), 33.35 (ζ), 15.94 (η). ES MS m/z (calc): 180.1 (180.3, $[M +Li]^+$).

**7:** To a solution of **6** (2.20 g, 12.2 mmol) in pyridine (10 ml) at 0 °C was added 4-toluenesulfonyl chloride (2.60 g, 13.6 mmol). The reaction mixture was left to stir at 0 °C for 3 h and at 10 °C for an additional 3.5 h. Toluene (30 ml) and HCl 10% (30 ml) were added. After drying the organic layer with MgSO4, the solvent was evaporated to yield **7** as light yellow oil (2.7 g, 66%). $^1$H NMR (300 MHz, δ in $CDCl_3$): 7.80 (d, $J$ = 8.2 Hz, 1H, CH-tosylate), 7.34 (d, $J$ = 8.0 Hz, 1H, CH-tosylate), 4.16 (t, 2H, α), 3.76 − 3.50 (m, 8H, α + β + γ + δ), 2.67 (t, $J$ = 6.8 Hz, 2H, ζ), 2.44 (s, 1H, η), 2.13 (s, 1H, $CH_3$-tosylate). $^{13}$C NMR (75 MHz, δ in $CDCl_3$): 144.93, 133.17, 129.95, 128.12, 70.91 + 70.74 + 70.38 + 69.35 + 68.89 (α + β + γ + δ + ε), 33.59 (ζ), 21.68, 16.07 (η). ES MS m/z (calc): 357.1 (357.0, $[M +Na]^+$), 373.2 (373.2, $[M+K]^+$).

**4:** A suspension of sodium hydride (0.22 g, 9.2 mmol) in dry tetrahydrofuran (40 mL) was prepared under argon. While stirring, cholesterol (1.20 g, 3.10 mmol) was added to the flask. After 30 min, compound **7** (1.32 g, 3.95 mmol) in dry tetrahydrofuran (5 mL) was added to the mixture. It was then heated to reflux under argon for 48 h. The flask was cooled to room temperature and 60 mL of a (1:1) mixture of water and HCl 1 M was added.

The product was extracted three times with diethylether: petroleum ether 1:15 (v/v) (40 mL). The combined organic layers were washed once with HCl 1 M (30 mL), mixtures dried with $MgSO_4$ and finally evaporated off to give compound **4** as a sticky white solid (1.31 g, 76%). ^{1}H NMR (300 MHz, , δ in $CDCl_3$): 5.34 (d, J = 5.1 Hz, 1H, 6), 3.74 – 3.57 (m, 10H, α + β + γ + δ + ε), 3.17 (m, 1H, 3), 2.69 (t, J = 6.9 Hz, 2H, ζ), 2.42 – 2.19 (m, 2H), 2.14 (s, 3H, η), 2.05 – 0.81 (m, 42H), 0.67 (s, 3H). ^{13}C NMR (75 MHz, δ in $CDCl_3$): 141.17 (C5), 121.70 (C6), 79.67 (C3), 71.58 + 71.13 + 70.81 + 70.51 (α + β + γ + δ), 67.48 (ε), 56.96, 56.34, 50.37, 42.49, 39.97, 39.68, 39.25, 37.42, 37.04, 36.36, 35.94, 33.61, 32.12 (ζ), 32.07, 28.54, 28.39, 28.17, 24.45, 23.99, 22.96, 22.71, 21.24, 19.54, 18.88, 16.20 (η), 12.02. High resolution ES MS m/z exp (calc): 549.43413 (549.43413, [M + H] [+]), 566.46068 (566.45998, [M + $NH_4$][+]), 571.41608 (571.41482, [M + Na] [+]). *Anal. Calcd for* $C_{34}H_{60}O_3S$: calculated: C, 74.39; H, 11.02; N, 0.00; S, 5.84. Found: C, 74.39; H, 11.16; N, 0.0; S, 5.85.

## AII.2. X-ray crystallography for [2]($PF_6$)$_2$

All reflection intensities were measured at 110(2) K using a KM4/Xcalibur (detector: Sapphire3) with enhance graphite-monochromated Mo *K*α radiation (λ = 0.71073 Å) under the program CrysAlisPro (Version 1.171.34.36, Oxford Diffraction Ltd., 2010). The program CrysAlisPro was used to refine the cell dimensions. Data reduction was done using the program CrysAlisPro (Version 1.171.34.36, Oxford Diffraction Ltd., 2010). The structure was solved with the program SHELXS-97[2] and was refined on $F^2$ with SHELXL-97.[2] Analytical numeric absorption corrections based on a multifaceted crystal model were applied using CrysAlisPro. The temperature of the data collection was controlled using the system Cryojet (manufactured by Oxford Instruments). The H atoms were placed at calculated positions using the instructions AFIX 23, AFIX 43, AFIX 137 with isotropic displacement parameters having values 1.2 or 1.5 times *U*eq of the attached C atoms. The H atom located on O1 was found from difference Fourier maps, and its position was restrained so that $d$(O−H) is 0.84(2) Å. The structure of [2]($PF_6$)$_2$ is mostly ordered. One of the two independent $PF_6^-$ counterions is found to be disordered over two orientations, and the occupancy factor of the major component refines to 0.60(3).
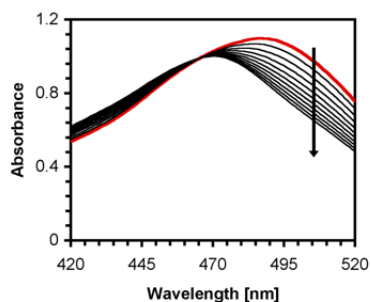
**Figure AII.1**. Time evolution of the UV-vis spectrum of a solution containing $[Ru(terpy)(dcbpy)(H_2O)]^{2+}$ ($[\mathbf{1}]^{2+}$) and Hmte in pseudo-first order conditions.
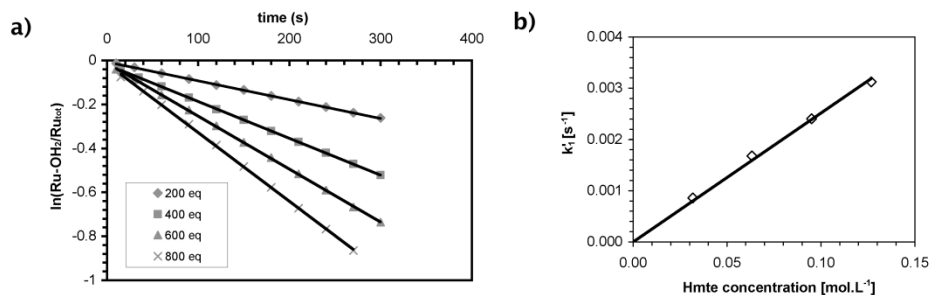


**Figure AII.2**. a) Plot of $ln([RuOH_2]/[Ru]_{tot})$ *vs*. time for 200, 400, 600 and 800 eq. of Hmte (pseudo-first order conditions). b) Plot of $k'_1$ *vs*. [Hmte] in pseudo-first order conditions. Conditions: $T = 297$ K; $[Ru]_{tot} = 1.4 \times 10^{-4}$ M.
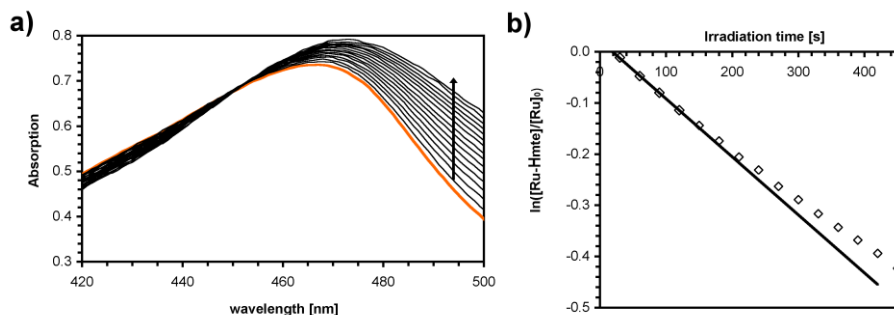


**Figure AII.3**. a) UV-vis spectra of a solution of $[\mathbf{2}](PF_6)_2$ in water irradiated at 465 nm. b) Plot of $ln([RuHmte]/[Ru]_{tot})$ as a function of irradiation time. Conditions: $\lambda_e = 465$ nm, photon flux : $3.9 \times 10^{-9}$ Einstein·s$^{-1}$, sample temperature 297 K, concentration $[Ru]_{tot} = 1.5 \times 10^{-4}$ M, spectra measured at 30 seconds interval.
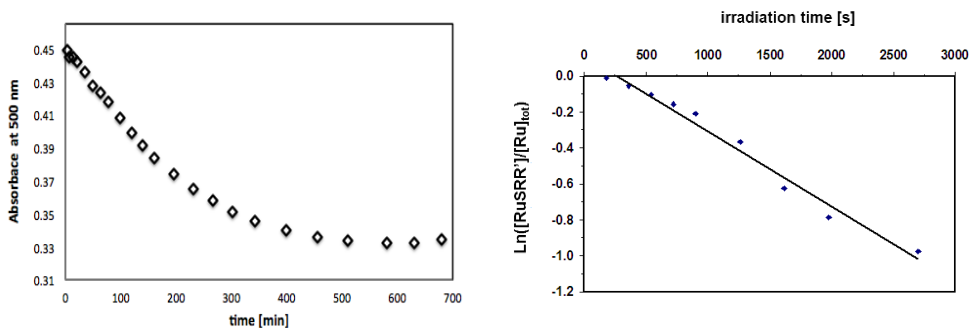
**Figure AII.4**. Left: Time evolution of the absorbance at 500 nm, for a sample containing DMPG vesicles with 25 mol % ligand **4**, and 5 mol % complex [**1**]$^{2+}$ after equilibration at room temperature in the dark, spectra measured every 3 minutes. Right: Plot of ln*([RuSRR']/[Ru]$_{tot}$) vs.* irradiation time for the measurement of the photosubstitution quantum yield at the membrane interface; *[RuSRR']* represents the concentration in [**5**]$^{2+}$ in mol·L$^{-1}$. Conditions: *[lipid]* = 1.3 mM, 25 mol% of ligand **4**, vesicle average diameter 140 nm, 5 mol% of complex [**1**]$^{2+}$ (6.7×10$^{-5}$ M), irradiation wavelength 465 nm, photon flux :3.9×10$^{-9}$ Einstein·s$^{-1}$.

## AII.3. References

[1]      E. C. Constable, K. R. Seddon, *Tetrahedron* **1983**, *39*, 291.
[2]      G. M. Sheldrick, *Acta Crystallogr.* **2008**, *A64*, 112.

# Appendix III

## Supporting Information of Chapter 3:

**Spontaneous formation in the dark, and visible light-induced cleavage, of a Ru-S bond in water: a thermodynamic and kinetic study**

## AIII.1. Synthesis

**[Ru(terpy)(biq)(Cl)]Cl ([10]Cl).**[1] [Ru(tpy)Cl$_3$] (200 mg, 0.453 mmol) and 2,2'-biquinoline (116 mg, 0.452 mmol) were mixed in 3:1 EtOH/H$_2$O mixture (20 mL) and the solution was degassed with argon for 5 min, after which Et$_3$N (0.094 mL, 0.68 mmol) was added. The reaction mixture was refluxed under argon for 7 h in the dark, after which it was filtered hot over celite. The filtrate was evaporated under reduced pressure. Column chromatography purification was then performed over silica gel (eluent: 15:85 MeOH / DCM, Rf=0.4). The solvent was evaporated and the product was finally reprecipitated from ethanol and toluene to yield [10]Cl as a violet powder (95 mg, 32% yield). $^1$H NMR (300 MHz, MeOD, 298 K, see Figure AIII.1 for proton notation) $^1$H δ (ppm) 9.64 (d, $J$ = 8.4 Hz, 1H, B8), 8.95 (dd, $J$ = 20.5, 8.9 Hz, 2H, B3+B4), 8.66 (t, $m$, 3H, A3+T3'), 8.48 (d, $J$ = 8.0 Hz, 2H, 3T), 8.25 (m, 3H, B5+A4+T4'), 8.00 – 7.75 (m, 7H, T4+B6+B7+A5+T6), 7.44 (t, $J$ = 7.5 Hz, 1H, A6), 7.33 (m, 2H, T5), 7.20 (t, $J$ = 8.0, 6.4 Hz, 1H, A7), 6.80 (d, $J$ = 8.8 Hz, 1H, A8). $^{13}$C NMR (75 MHz, CDCl$_3$) δ (ppm) 163.24+160.70+ 160.37+ 159.96 (T2+T2'+A2+B2), 153.87 (T6), 153.18+152.51 (A8a+B8b), 139.77(B4), 138.86 (T4), 137.74+136.84 (A4+B5), 132.05 (A7), 131.84+131.77 (6B+7B), 130.75+129.96 (A4a+B4a), 130.45+130.55 (A5+B8), 129.75 (T4'), 129.65 (A6), 128.37 (T5), 124.92 (T3), 124.86 (A8), 123.95 (T3'), 121.76+121.69 (A3+B3). *ES MS m/z (calc):* 626.0 (625.8 [M - Cl]$^+$). *UV-vis:* λ$_{max}$ (ε in L·mol$^{-1}$·cm$^{-1}$) in MeOH: 571 nm (7400). Anal. Calcd for C$_{33}$H$_{23}$Cl$_2$N$_5$Ru: C, 59.91; H, 3.50; N, 10.59. Found: C, 60.15; H, 3.45; N, 10.54.

**[Ru(terpy)(dmbpy)Cl]Cl ([12]Cl).** [Ru(tpy)Cl$_3$] (500 mg, 1.13 mmol), dmbpy (209 mg, 1.13 mmol) and LiCl (50 mg, 1.2 mmol) were mixed in 3:1 EtOH/H$_2$O mixture (100 mL). The suspension was put under argon. Et$_3$N (0.25 mL, 1.8 mmol) was added and the reaction was refluxed for 20 hours. Then it was filtered hot over celite to remove insoluble byproducts. The filtrate was rotary evaporated, then purified over alumina in the dark (eluent: 1% MeOH / DCM). The product eluted from the column as the initial violet band (Rf=0.3). The solvent was evaporated and the solid was reprecipitated from 1% MeOH / DCM and Et$_2$O to yield [12]Cl as a dark violet powder (337 mg, 51 %). $^1$H NMR (400 MHz, MeOD, 298 K, see Figure AIII.1 for proton assignment) δ (ppm) 8.58 (m, 3H, B5 + T3'), 8.50 (d, $J$ = 8.1 Hz, 2H, T3), 8.29 (d, $J$ = 8.1 Hz, 1H, A3), 8.20 (t, $J$ = 7.9 Hz, 1H, B4), 8.11 – 8.02 (m, 3H, T6 + T4'), 7.97 (t, $J$ = 7.4 Hz, 2H, T4), 7.81 (d, $J$ = 7.8 Hz, 1H, T5), 7.58 (t, $J$ = 7.9 Hz, 1H, A4), 7.48 – 7.40 (m, 2H, T5), 6.89 (d, $J$ = 7.7 Hz, 1H, A5), 3.30 (s, 3H, B7), 1.52 (s, 3H, A7). $^{13}$C NMR (300 MHz, MeOD, 298 K) δ (ppm) 168.91 (B6), 167.09 (A6), 161.57+161.54+161.40 (A2+T2+T2'), 159.36 (B2), 154.47 (T6), 138.72 (B4), 138.63 (T4), 137.66 (A4), 135.85 (T4'), 128.59 (B5), 128.53 (T5), 127.45 (A5), 124.83 (T3), 123.77 (T'3), 122.59 (C5), 122.33 (A3), 28.77 (B7), 23.74 (A7). *ES MS m/z (calc):* 553.81 (554.03 [M - Cl]$^+$), 259.33 (259.28 [M – 2 Cl]$^{2+}$). *UV-vis:* λ$_{max}$ (ε in L·mol$^-$

$^1$.cm$^{-1}$) in MeOH: 504 nm (6400). Anal. Calcd for $C_{27}H_{23}Cl_2N_5Ru·2.5H_2O$: C, 51.11; H, 4.45; N, 11.04. Found: C, 51.98; H, 4.44; N, 11.05.

**[Ru(terpy)(dcbpy)(Cl)]Cl ([11]Cl):** See Chapter 2 and Appendix II.

## AIII.2.    $^1$H NMR and proton attribution



L: H$_2$O , [2]$^{2+}$
L: Hmte, [6]$^{2+}$

L: H$_2$O , [4]$^{2+}$
L: Hmte, [8]$^{2+}$
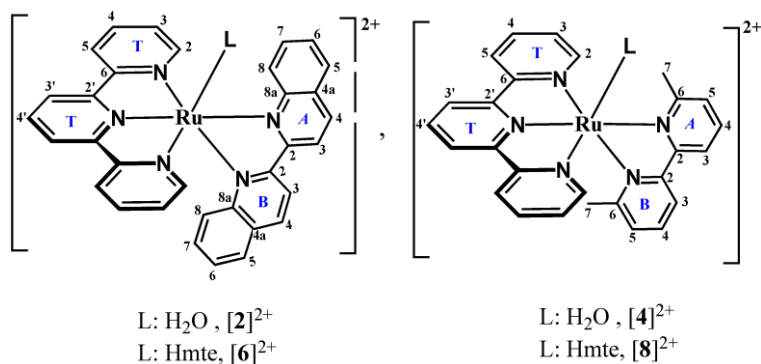
**Figure AIII.1.** Notations for the attribution of the $^1$H and $^{13}$C NMR spectra for compounds [2]$^{2+}$, [6]$^{2+}$, [4]$^{2+}$, and [8]$^{2+}$.
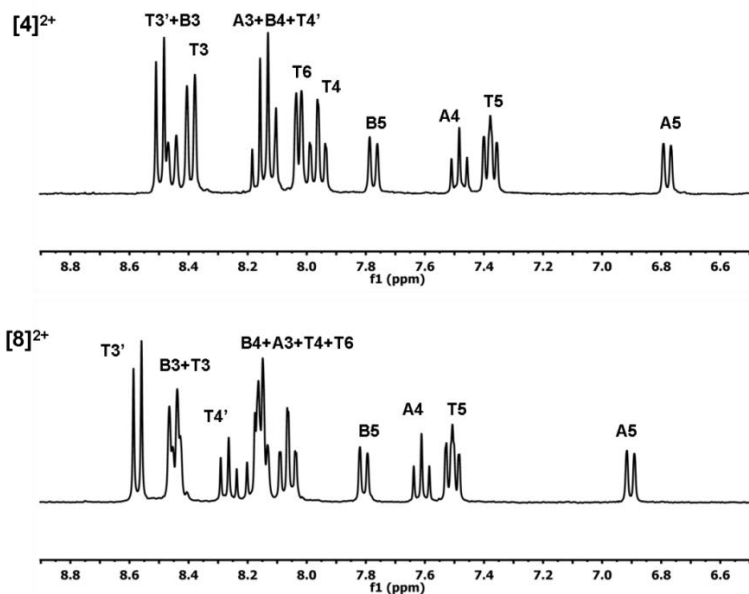


**Figure AIII.2.** $^1$H NMR of [4]Cl$_2$ (top) and [8]Cl$_2$ (down)  in pure D$_2$O (aromatic region, N-N=dmbpy). Conditions:*[Ru]$_{tot}$*=13.6 mM, *[Hmte]*=0 (top) or 0.53 M (bottom), pH ~ 7, 298 K.

## AIII.3.    X-ray crystallography for [5](PF$_6$)$_2$

All reflection intensities were measured at 110(2) K using a KM4/Xcalibur (detector: Sapphire3) with enhance graphite-monochromated Mo $K\alpha$ radiation ($\lambda = 0.71073$ Å) under the program CrysAlisPro (Version 1.171.34.36, Oxford Diffraction Ltd., 2010). The program CrysAlisPro (Version 1.171.34.36, Oxford Diffraction Ltd., 2010) was used to refine the cuvette dimensions. Data reduction was done using the program CrysAlisPro (Version 1.171.34.36, Oxford Diffraction Ltd., 2010). The structure was solved with the program SHELXS-97 (Sheldrick, 2008) and was refined on $F^2$ with SHELXL-97 (Sheldrick, 2008). Analytical numeric absorption corrections based on a multifaceted crystal model were applied using CrysAlisPro (Version 1.171.34.36, Oxford Diffraction Ltd., 2010). The temperature of the data collection was controlled using the system Cryojet (manufactured by Oxford Instruments). The H atoms were placed at calculated positions using the instructions AFIX 23, AFIX 43, AFIX 137 or AFIX 147 with isotropic displacement parameters having values 1.2 or 1.5 times $U$eq of the attached C or O atoms. The structure of [5](PF$_6$)$_2$ is mostly ordered. One of the two independent PF$_6^-$ counter ions is found to be disordered over two orientations, and the occupancy factor of the major component refines to 0.906(4).

## AIII.4. Aquation of hindered chlorido complexes in $CD_3OD/D_2O$ mixtures

### a) biq

$[2]^{2+}$ $[10]^+$

+160 µL $D_2O$

+80 µL $D_2O$

+40 µL $D_2O$

+20 µL $D_2O$

$CD_3OD$

6.98 6.95 6.92 6.89 6.86 6.83 6.80 6.77 6.74 6.71 6.68 6.65
f1 (ppm)

### b) dmbpy

$[4]^{2+}$ $[12]^+$

+160 µL $D_2O$

+80 µL $D_2O$

+40 µL $D_2O$

+20 µL $D_2O$

$CD_3OD$

7.10 7.07 7.04 7.01 6.98 6.95 6.92 6.89 6.86 6.83 6.80 6.77
f1 (ppm)

### C) dcbpy

$[3]^{2+}$ $[11]^+$

+160 µL $D_2O$

+80 µL $D_2O$

+40 µL $D_2O$

+20 µL $D_2O$

$CD_3OD$

7.42 7.40 7.38 7.36 7.34 7.32 7.30 7.28 7.26 7.24 7.22 7.20 7.18 7.1
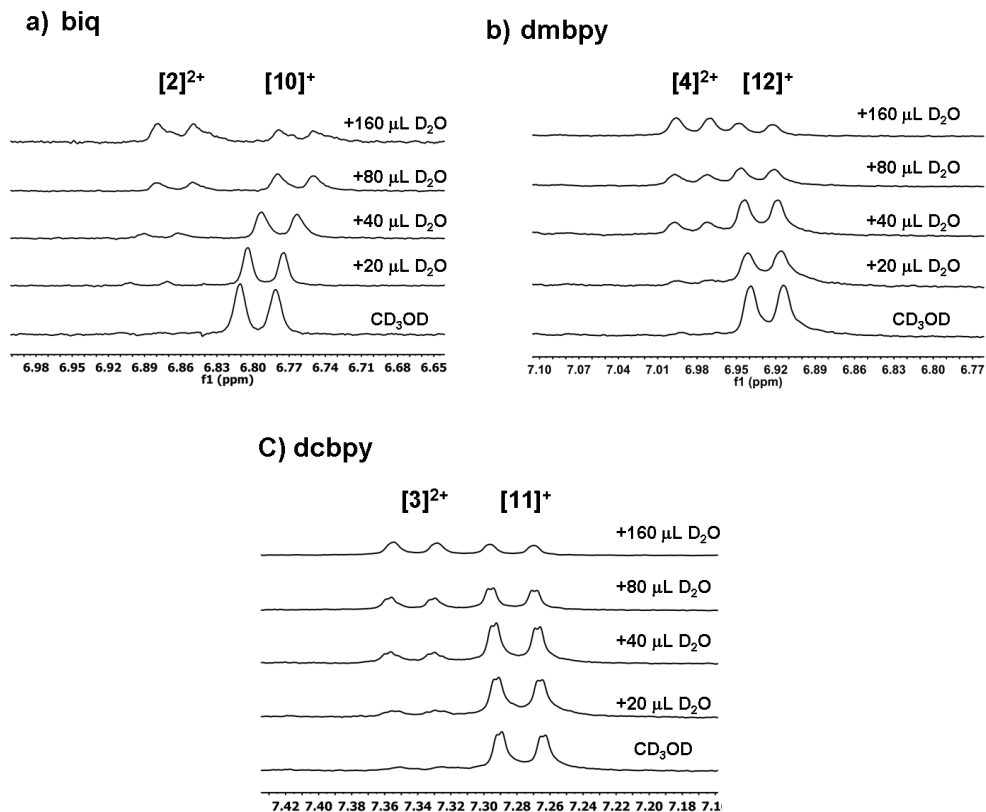
**Figure AIII.3.** ^{1}H NMR spectra showing the hydrolysis of [Ru(terpy)(N-N)(Cl)]Cl ([**10**]Cl, [**11**]Cl, and [**12**]Cl) upon addition of increasing amount of $D_2O$ in MeOD. Conditions: a) initial $[Ru]_{tot}$=6.6×10$^{-3}$ M, b) initial $[Ru]_{tot}$=9.2×10$^{-3}$ M, and c) initial $[Ru]_{tot}$=9.6×10$^{-3}$ M, T= 297K.

## AIII.5. Determination of pKa of $[2]^{2+}$ and $[4]^{2+}$

pH titration: 3 mL of a 67 µM solution of [**10**]Cl or [**12**]Cl in perchloric acid (33 mM) was added to a UV-vis cell. A pH measurement electrode was added to the top and aliquots of aqueous NaOH (0.1 – 1 M) were added to give a range of pH values. After each addition of NaOH, the solution was stirred until a stable pH was observed, then a UV-vis spectrum was obtained. By deconvolution, the relative amounts of $[2]^{2+}$ and $[4]^{2+}$ were plotted *vs.* pH (Figure AIII.4). The data points were fitted to Equation AIII.1, which gave the *pK$_a$* of both

aqua complexes. The pK$_a$ values were determined to be 9.5(1) and 10.5(1) for [**10**]$^{2+}$ and [**12**]$^{2+}$, respectively.

$$[RuOH_2]\% = \frac{a}{1 + 10^{-k(pH - pK_a)}} \quad \textbf{(Equation AIII.1)}$$
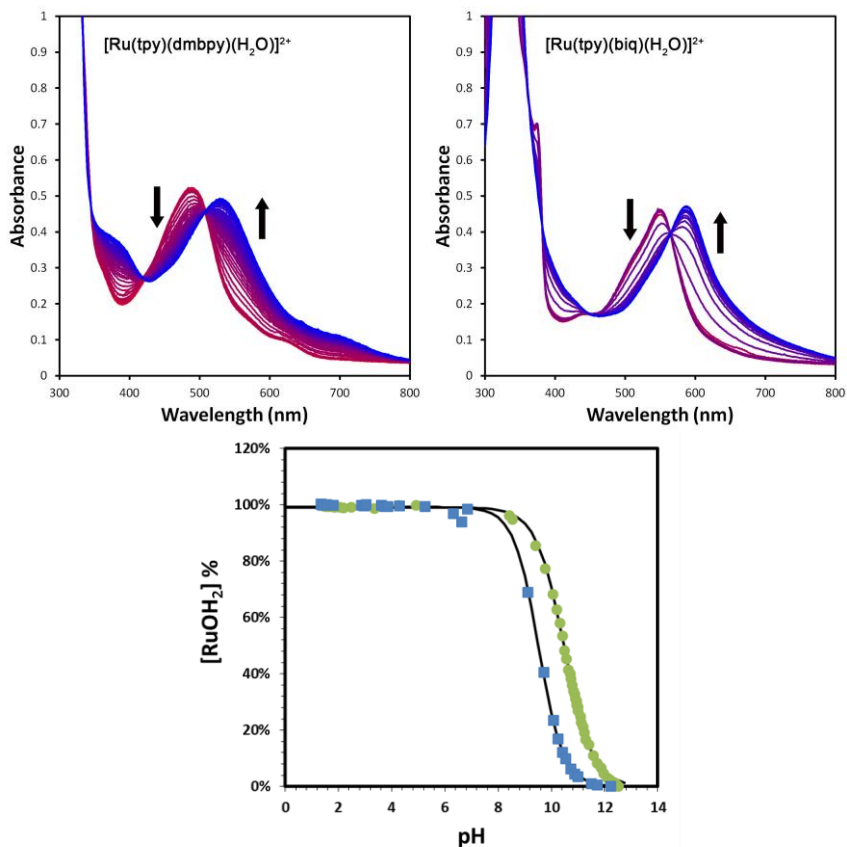


**Figure AIII.4.** tOP: Evolution of the UV-vis spectrum of [**2**]$^{2+}$ and [**4**]$^{2+}$ (67 μM) upon increasing pH using NaOH. Bottom: Composition (expressed in percent of the non-deprotonated species RuOH$_2$) during titration with NaOH. Squares: [**10**]$^{2+}$, circles: [**12**]$^{2+}$. Black lines: fit curves for the data points using Equation AIII.1.

## AIII.6. Calculating the rate constants at different temperatures for the fast equilibrium between $[4]^{2+}$ and $[8]^{2+}$

If we consider the interconversion between $[4]^{2+}$ and $[8]^{2+}$ the rate law of this reaction can be expressed as Equation AIII.2.

$$\frac{d[RuHmte]}{dt} = k_4[RuOH_2] \cdot [Hmte] - k_{-4}[RuHmte] \quad \textbf{(Equation AIII.2)}$$

If pseudo first-order conditions are used (large excess of Hmte), since the concentration of Hmte is constant $k_4 \cdot [Hmte]$ can be replaced by the pseudo first-order rate constants $k'_4$ (see Equation 3.2 in the article).

Since $k_{-4}$ is significant, *[RuOH₂]* is substituted by *[Ru]$_{tot}$ – [RuHmte]* in Equation 3.2 (see Chapter 3), which simplified to Equation 3.3, where $k'_4 + k_{-4} = k_{obs}$ is usually called the "observed" rate constant (unit: $s^{-1}$).

Integration of this differential Equation 3.3 leads to Equation 3.4 (see Chapter 3), where c is a constant derived from integration.

Since there is no linear form of this formula, data had to be fitted with Equation AIII.3, using a non-linear least-squares minimization procedure as described by Lagarias *et al.*[2] (simplex search method). The program MATLAB was used for the optimization.

$$[RuHmte] = \frac{A}{B} - \frac{C}{B} \cdot e^{-B \cdot t} \quad \textbf{(Equation AIII.3)}$$

Figure AIII.5 shows a plot of the experimental data points, compared to the fitted model. The modeled curve closely matches the experimental data and thus $k'_4 = k_4 \cdot [Hmte]$ and $k_{-4}$ could be calculated from the constants $A = k'_4 \cdot [Ru]_{tot}$ and $B = k_{obs} = k'_4 + k_{-4}$ determined numerically (see Table AIII.1).

**Table AIII.1.** The values of A, B, and C used as a model for Equation 3.4 and the kinetic data of the dmbpy system (equilibrium between $[\mathbf{4}]^{2+}$ and $[\mathbf{8}]^{2+}$) at different temperatures. Conditions: $[Ru]_{tot} = 1.5 \times 10^{-4}$ M, $[Hmte] = 3.2 \times 10^{-2}$ M, MilliQ water, pH ~ 7.

| T (K) | A | B | C | $k_{-4}$ (s$^{-1}$) | $k_4$ (M$^{-1}\cdot$s$^{-1}$) |
|-------|-----------------------|-----------------------|-----------------------|-----------------------|-----------------------|
| 283 | $7.6 \times 10^{-8}$ | $1.1 \times 10^{-3}$ | $2.7 \times 10^{-8}$ | $6.3 \times 10^{-4}$ | $1.6 \times 10^{-2}$ |
| 288 | $1.5 \times 10^{-7}$ | $2.3 \times 10^{-3}$ | $1.5 \times 10^{-7}$ | $1.4 \times 10^{-3}$ | $3.0 \times 10^{-2}$ |
| 293 | $2.7 \times 10^{-7}$ | $4.2 \times 10^{-3}$ | $2.6 \times 10^{-7}$ | $2.4 \times 10^{-3}$ | $5.4 \times 10^{-2}$ |
| 297 | $4.3 \times 10^{-7}$ | $6.9 \times 10^{-3}$ | $4.1 \times 10^{-7}$ | $4.1 \times 10^{-3}$ | $8.8 \times 10^{-2}$ |
| 301 | $7.4 \times 10^{-7}$ | $1.2 \times 10^{-2}$ | $6.5 \times 10^{-7}$ | $7.4 \times 10^{-3}$ | $1.5 \times 10^{-2}$ |
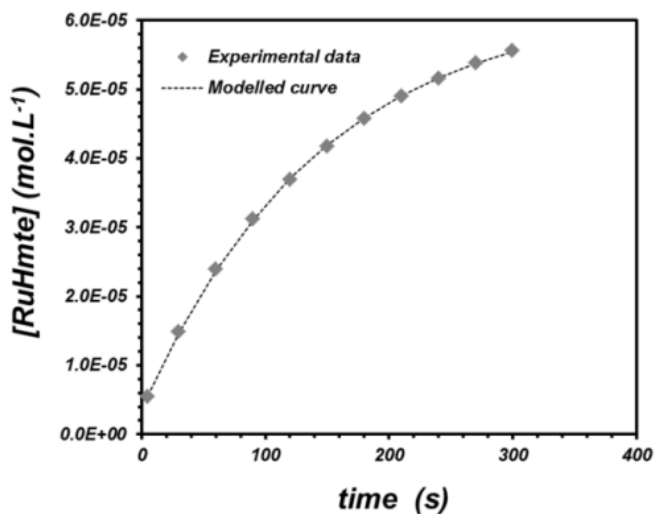


**Figure AIII.5.** Plot of *[RuHmte]* (concentration in $[\mathbf{8}]^{2+}$) *vs.* time during thermal substitution of H$_2$O by Hmte in complex [Ru(terpy)(dmbpy)(H$_2$O)]$^{2+}$ ($[\mathbf{4}]^{2+}$). Conditions: *[Hmte]* = 0.032 M, *[Ru]$_{tot}$* = $1.5 \times 10^{-4}$ M, T = 297 K, in H$_2$O. Experimental data (diamonds) and calculated data (dashed curve).

**Table AIII.2.** Experimental pseudo first-order and second-order rate constants ($k'_i = k_i \cdot [Hmte]$ and $k_i$) at different temperatures for N-N=bpy, biq, and dcbpy. Condition: $[Ru]_{tot} = 6.7 \times 10^{-5}$ M and $[Hmte] = 6.7 \times 10^{-2}$ M for N-N=bpy and biq, $[Ru]_{tot} = 1.4 \times 10^{-4}$ M and $[Hmte] = 1.6 \times 10^{-1}$ M for N-N=dcbpy.

| N-N | T (K) | $k'_i$ (s$^{-1}$) | $k_i$ (M$^{-1} \cdot$s$^{-1}$) |
|-----|-------|--------|--------|
| bpy | 323 | $5.4 \times 10^{-5}$ | $8.2 \times 10^{-4}$ |
| | 333 | $1.4 \times 10^{-4}$ | $2.1 \times 10^{-3}$ |
| | 343 | $3.7 \times 10^{-4}$ | $5.6 \times 10^{-3}$ |
| | 353 | $7.9 \times 10^{-4}$ | $1.2 \times 10^{-2}$ |
| biq | 297 | $4.3 \times 10^{-4}$ | $6.5 \times 10^{-3}$ |
| | 301 | $7.5 \times 10^{-4}$ | $1.1 \times 10^{-2}$ |
| | 308 | $1.7 \times 10^{-3}$ | $2.6 \times 10^{-2}$ |
| | 315 | $3.4 \times 10^{-3}$ | $5.2 \times 10^{-2}$ |
| | 323 | $6.2 \times 10^{-3}$ | $9.3 \times 10^{-2}$ |
| | 327 | $8.8 \times 10^{-3}$ | $1.3 \times 10^{-1}$ |
| dcbpy | 283 | $5.7 \times 10^{-4}$ | $3.6 \times 10^{-3}$ |
| | 288 | $1.1 \times 10^{-3}$ | $7.0 \times 10^{-3}$ |
| | 293 | $2.1 \times 10^{-3}$ | $1.3 \times 10^{-2}$ |
| | 297 | $3.6 \times 10^{-3}$ | $2.3 \times 10^{-2}$ |
| | 301 | $6.4 \times 10^{-3}$ | $4.0 \times 10^{-2}$ |

## AIII.7. Order of Hmte and second-order rate constant determination at 297 K in the thermal coordination reaction for N-N=bpy, biq, and dmbpy

Stock solutions $\theta$ of complex [**1**](PF$_6$)$_2$ (4.0 mg in 25 mL H$_2$O, $2.0 \times 10^{-4}$ M), $\iota$ of [**10**]Cl (2.2 mg in 25 mL H$_2$O, $1.3 \times 10^{-4}$ M), $\kappa$ of [**12**]Cl (3.5 mg in 25 mL H$_2$O, $2.2 \times 10^{-4}$ M), and $\xi$ and $\chi$ of Hmte (600 mg in 25.0 mL H$_2$O, $2.60 \times 10^{-1}$ M ($\xi$), and 1090 mg in 25.0 mL H$_2$O, $4.73 \times 10^{-1}$ M ($\chi$)) were prepared. 2.0 mL of $\theta$, $\iota$, or $\kappa$ was added to a UV-vis cuvette, which was placed in the UV-vis spectrometer. The temperature was set at 50 °C for $\theta$, and at 24°C for $\iota$, or $\kappa$. After obtaining a constant temperature in each cuvette, to each solution was added x mL of H$_2$O, and 1-x mL of $\xi$ or $\chi$, where x is 0.2, 0.6, 0.8 or 1.0 mL of $\xi$ to $\theta$, and 0.2, 0.4, 0.8 or 1.0 mL of $\chi$ to $\iota$, and 0.05, 0.10, 0.15 or 0.20 mL of $\xi$ to $\kappa$. After addition of Hmte, a UV-vis spectrum was taken every 30 seconds. For each spectrum, the concentrations in *[RuHmte]* and *[RuOH$_2$]* were determined by deconvolution of the UV-vis spectra knowing the extinction coefficients of both RuHmte and RuOH$_2$ species. For N-N=bpy and biq ([**1**]$^{2+}$ and [**2**]$^{2+}$) thermal back coordination ($k_{-i}$) is negligible and for each Hmte concentration the pseudo first order rate constants $k_{obs} = k_i \cdot [Hmte]$ were determined from the slope of the (linear) plot of *ln([RuOH$_2$]/[Ru]$_{tot}$) vs.* time (Figure AIII.6). For N-

N=dmbpy ($[\mathbf{4}]^{2+}$), thermal back coordination is *not* negligible and as shown in Figure AIII.6c linear trend lines are not best fits for the data points. In such conditions $k_{obs}$= $k_i \cdot [Hmte] + k_{-i}$, and a plot of *[RuHmte] vs.* time was obtained for each Hmte concentration. All the data were modeled to Equation AIII.3, and $A=k'_4 \cdot [Ru]_{tot}$ and $B=k_{obs}=k'_4+k_{-4}$ were directly obtained from the model (see Equation 3.4). The plot of $k_{obs}$ *vs. [Hmte]* was obtained for each N-N ligand (see Figure AIII.7). Finally, the second-order rate constant $k_i$ were obtained from the slope of these plots for $i$=1 (bpy), 2 (biq), and 4 (dmbpy).

Half reaction times are calculated according to the Equation AIII.4.

$$t_{1/2(i)} = \frac{ln2}{k'_i} \quad \textbf{(Equation AIII.4)}$$
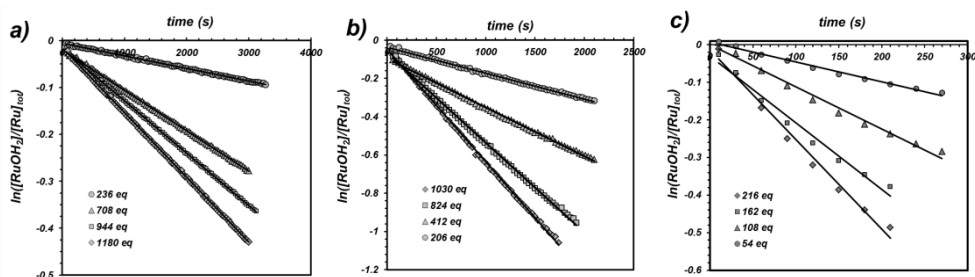


**Figure AIII.6.** Plot of $ln([RuOH_2]/[Ru]_{tot})$ *vs.* time for the coordination of Hmte to a) $[\mathbf{1}]^{2+}$, b) $[\mathbf{2}]^{2+}$, and c) $[\mathbf{4}]^{2+}$ upon adding different equivalents of Hmte to the solution. Conditions: in water, pH~7, a) T=323 K, $[Ru]_{tot}$=1.3×10$^{-4}$ M, b) T=297 K, $[Ru]_{tot}$=8.4×10$^{-5}$ M , c) T=297 K, $[Ru]_{tot}$=1.5×10$^{-4}$ M.
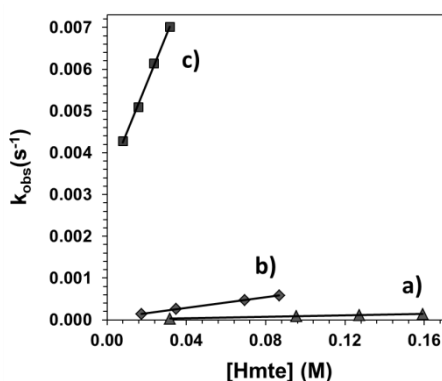


**Figure AIII.7.** Plot of $k'_i$ *vs. [Hmte]* in pseudo-first order conditions. a) N-N=bpy, slope= $k_1$=8.8×10$^{-4}$ M$^{-1}$·s$^{-1}$, T=323 K, pH~7, $[Ru]_{tot}$=1.3×10$^{-4}$ M, b) N-N=biq, slope=$k_2$=6.4×10$^{-3}$ M$^{-1}$·s$^{-1}$, T=297 K, $[Ru]_{tot}$=8.4×10$^{-5}$ M , c) N-N=dmbpy, slope $k_4$=0.12 M$^{-1}$·s$^{-1}$, T=297 K, $[Ru]_{tot}$=1.5×10$^{-4}$ M.

## AIII.8. Kinetics of the thermal hydrolysis of [5]$^{2+}$ (N-N=bpy) in MilliQ water at different temperatures

**Table AIII.3.** Experimental first-order rate constants ($k_{-1}$) at different temperatures for the thermal hydrolysis of [5]$^{2+}$ in MilliQ water. Condition: $[Ru]_{tot}$=2.5×10$^{-4}$ M.

| $T$ (K) | $k_{-1}$ (s$^{-1}$) |
|---------|--------------------|
| 343 | 7.0 ×10$^{-6}$ |
| 348 | 1.2 ×10$^{-5}$ |
| 353 | 2.1 ×10$^{-5}$ |
| 358 | 4.3 ×10$^{-5}$ |
| 363 | 5.8 ×10$^{-5}$ |
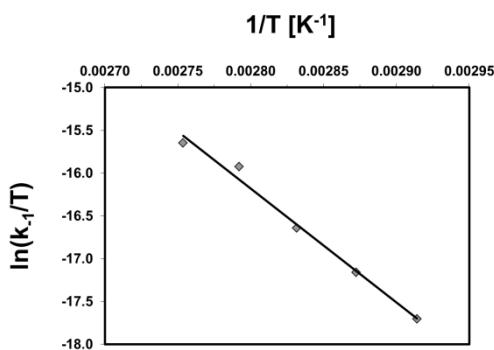


**Figure AIII.8.** Eyring plot for the thermal substitution of Hmte by an aqua ligand in [5]$^{2+}$. The slope and y-intercept in the plot correspond to $-\Delta H^{\ddagger}_{-1}/R$, and $ln(k_b/h)+\Delta S^{\ddagger}_{-1}/R$, respectively. $\Delta H^{\ddagger}_{-1}$, $\Delta S^{\ddagger}_{-1}$, and $\Delta G^{\ddagger}_{-1}$ (at 297K) were found to be 110(6) kJ·mol$^{-1}$, –22(10) J·mol$^{-1}$·K$^{-1}$, and 117(10) kJ·mol$^{-1}$, respectively.

## AIII.9. Quantum yield measurements for [6](PF$_6$)$_2$ and [8](PF$_6$)$_2$

Compound [5]$^{2+}$ is kinetically stable and the photosubstitution quantum yield for this compound was calculated as explained in Appendix I, Section AI.3.1. (see Figure AIII.9).
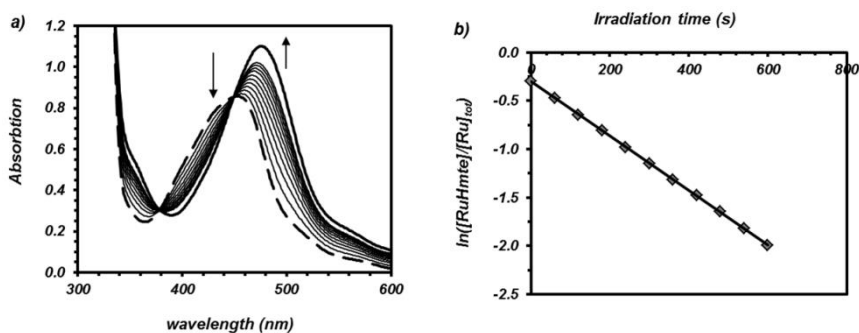
**Figure AIII.9.** a) Evolution of the UV-vis spectra of an aqueous solution of [**5**](PF$_6$)$_2$ irradiated with blue light. Full conversion to [**1**](PF$_6$)$_2$ is achieved within 30 minutes. Spectra were taken at 1, 2, 3, …, 10, and 30 minutes. b) Plot of ln*([RuHmte]/[Ru]$_{tot}$) vs.* irradiation time. Condition: water, *T*=297 K, *[Ru]$_{tot}$*=1.0×10$^{-4}$ M, $\lambda_e$=452 nm, photon flux $\Phi$=6.4×10$^{-9}$ Einstein·s$^{-1}$, slope $k_{\varphi i}$= 2.8×10$^{-3}$ s$^{-1}$, $\varepsilon_e$=6000 L·mol$^{-1}$·cm$^{-1}$, $A_e$=0.88, and irradiation pathlength *l'*= 1 cm.

Compound [**6**]$^{2+}$ or [**8**]$^{2+}$ (RuHmte) are not kinetically stable and the equilibrium between RuHmte and RuOH$_2$ is fast, and the quantum yield cannot be measured for these compounds in a general way as reported in AI.3. In addition, isolation of [**6**](PF$_6$)$_2$ or [**8**](PF$_6$)$_2$ as pure solids was impossible. In order to perform quantum yield measurements a LED lamp was mounted on top of the UV-vis cuvette to irradiate the sample inside the UV-vis spectrometer. In such conditions, temperature stabilization issues during sample transfer are eliminated, and back-coordination of Hmte to RuOH$_2$ is minimized.

To measure $\varphi_i$, an aqueous solution of each complex [**10**]Cl or [**12**]Cl was prepared that contained a large excess of Hmte. After equilibration in the dark, the ratio *[RuHmte]/[RuOH$_2$]* was measured by UV-vis spectroscopy; a value of 1.6 was found for the biq system and of 0.50 for the dmbpy system. The equilibrated samples were then subjected to visible light irradiation at room temperature at $\lambda_e$= 520 nm or $\lambda_e$=465 nm, respectively. In such conditions, three reactions take place simultaneously: 1) the photochemical cleavage of the Ru-S bond, 2) the thermal cleavage of the Ru-S bond, and 3) the thermal binding of Hmte back to the aqua complex (see Scheme 3.1). In such conditions, the variation of *[RuHmte]* is given by Equation AIII.5, which can be rewritten for the thermal equilibrium in the dark (eq) into Equation 3.8a, and for the photochemical steady state (ss) into Equation 3.8b.

$$\frac{d[RuHmte]}{dt} = k_i[RuOH_2] \cdot [Hmte] - k_{-i}[RuHmte] - k_{\varphi i}[RuHmte]$$

**(Equation AIII.5)**

The plot of the ratio *[RuHmte]/[RuOH₂]* as a function of irradiation time was obtained by deconvolution of the UV-vis spectra using the extinction coefficients of RuHmte and RuOH₂. Since [**8**]²⁺ (N-N=dmbpy) is involved in a very fast thermal equilibrium with [**4**]²⁺, visible light irradiation did not change significantly the ratio *[RuHmte]/[RuOH₂]* during irradiation (see Figure AIII.10a), whereas for the biq system the thermal kinetics are lower and light irradiation leads to a photochemical steady state after about 1800 s irradiation. This steady state was characterized by a *[RuHmte]/[RuOH₂]* ratio of 0.10, which is very different from the ratio at the equilibrium in the dark (1.6, see Figure AIII.10b). Since $k_i$ is known, $k_{-i}$ could be calculated using Equation 3.8a. In a second stage, $k_{\varphi i}$ was obtained by using the values of $k_i$ and $k_{-i}$ in Equation 3.8b. The photochemical quantum yields were calculated using Equation 3.9, to give values of 0.12(5) and 0.30(6) for $\varphi_2$ and $\varphi_4$, respectively, at 297 K.

For comparison purposes $\varphi_3$ was also determined by the same method as for biq and dmbpy: an equilibrated solution of [**3**]²⁺ and [**7**]²⁺ was characterized by a *[RuHmte]/[RuOH₂]* ratio of 2.0, and in the steady state at $\lambda_e$= 465 nm a value of 0.13(5) was obtained for $\varphi_3$ (see Figure AIII.10c), which is consistent with the reported value in Chapter 2. All numerical parameters used to perform this calculation are indicated in Table AIII.4.
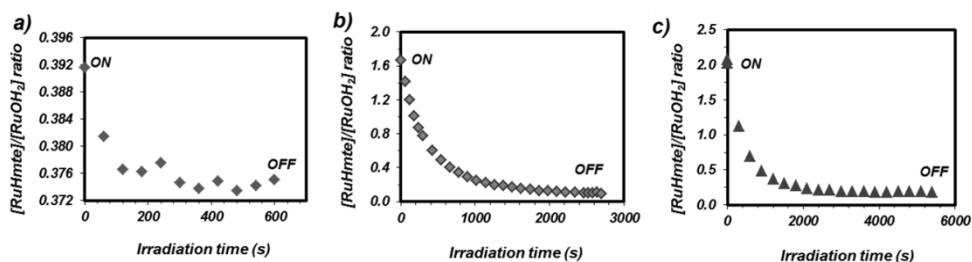


**Figure AIII.10.** Plots of the ratio *[RuHmte]/[RuOH₂]* *vs.* irradiation time for a) N-N=dmbpy  ([**8**]²⁺ ⇆ [**4**]²⁺), Conditions:  *T*= 297 K, blue light ($\lambda_e$=465 nm, photon flux $\Phi$=4.0(4)×10⁻⁹ Einstein·s⁻¹), *[Ru]ₜₒₜ* = 1.9×10⁻⁴ M , *[Hmte]* = 0.20 M. b) N-N=biq ([**6**]²⁺ ⇆ [**2**]²⁺), Conditions: T= 297 K, green light ($\lambda_e$=520nm, photon flux $\Phi$=9.8(5)×10⁻⁹ Einstein·s⁻¹), *[Ru]ₜₒₜ* = 8.6×10⁻⁵ M , *[Hmte]* = 0.011. c) N-N=dcbpy ([**7**]²⁺ ⇆ [**3**]²⁺), Conditions: *T*= 297 K, blue light ($\lambda_e$=465 nm, photon flux $\Phi$=4.0(4)×10⁻⁹ Einstein·s⁻¹), *[Ru]ₜₒₜ* = 1.6×10⁻⁴ M, *[Hmte]* = 0.010 M. Spectra measured every 1 minute in all cases, pH~7.

**Table AIII.4.** Photochemical data for the calculation of the photosubstitution quantum yield for RuHmte complexes $[5]^{2+}$, $[6]^{2+}$ and $[8]^{2+}$. Conditions: $T$=297 K, MilliQ water, pH ~ 7.

| | $[5]^{2+}$ | $[6]^{2+}$ | $[7]^{2+}$ | $[8]^{2+}$ |
|---|---|---|---|---|
| N-N | bpy | biq | dcbpy | dmbpy |
| $[RuHmte]/[RuOH_2]_{dark}$ | | 1.6 | 2.0 | 0.392 |
| $[RuHmte]/[RuOH_2]_{light}$ | | 0.14 | 0.18 | 0.375 |
| $[Hmte]$ (mol·L$^{-1}$) | | 0.011 | 0.010 | 0.20 |
| $k'_i$ (s$^{-1}$) | | $7.3\times10^{-5}$ | $2.2\times10^{-4}$ | $1.8\times10^{-2}$ |
| $k_{-i}$ (s$^{-1}$) | | $4.4\times10^{-5}$ | $1.1\times10^{-4}$ | $4.5\times10^{-2}$ |
| $k_{\varphi i}$ (s$^{-1}$) | $2.8\times10^{-3}$ | $4.2\times10^{-4}$ | $1.1\times10^{-3}$ | $2.0\times10^{-3}$ |
| $A_e$ | 0.88 | 0.57 | 1.0 | 0.66 |
| $[Ru]_{tot}$ (M) | $1.5\times10^{-4}$ | $9.0\times10^{-5}$ | $1.5\times10^{-4}$ | $2.0\times10^{-4}$ |
| $\lambda_e$ (nm) | 450 | 520 | 465 | 465 |
| Photon flux $\Phi$ (Einstein·s$^{-1}$) | $6.4\times10^{-8}$ | $9.8\times10^{-10}$ | $3.9\times10^{-9}$ | $3.9\times10^{-9}$ |
| $\varphi_i$ | 0.022 | 0.12 | 0.13 | 0.30 |

## AIII.10.  References

[1]     C. A. Bessel, J. A. Margarucci, J. H. Acquaye, R. S. Rubino, J. Crandall, A. J. Jircitano, K. J. Takeuchi, *Inorg. Chem.* **1993**, *32*, 5779-5784.
[2]     J. C. Lagarias, J. A. Reeds, M. H. Wright, P. E. Wright, **1998**, *9*, 112-147.

# Appendix IV

## Supporting Information of Chapter 4:

**Binding of a ruthenium complex to a thioether ligand embedded in a negatively charged lipid bilayer:**

**a two-step mechanism**
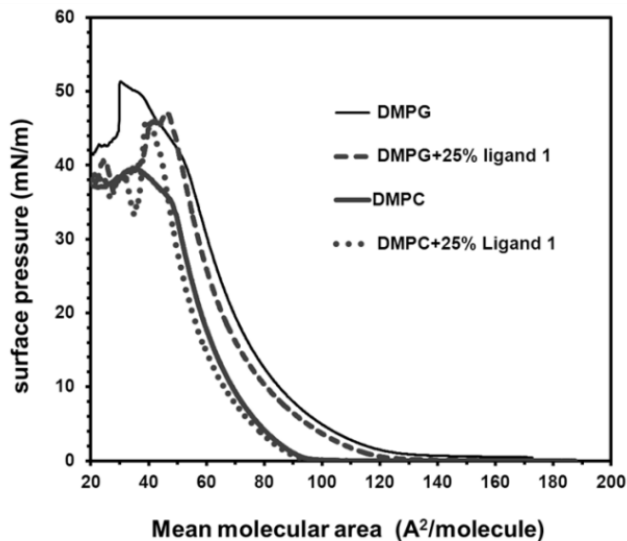
**Figure AIV.1**. Surface pressure *vs.* mean molecular area isotherms for the compression of lipid monolayers made of DMPG, DMPG with 25 mol% ligand **1**, DMPC, and DMPC containing 25 mol % ligand **1**, at the air/buffer interface. Compression rate: 2.4 mm/min, $T$=298 K, 10 mM phosphate buffer with $I$=50 mM, pH=7.0.
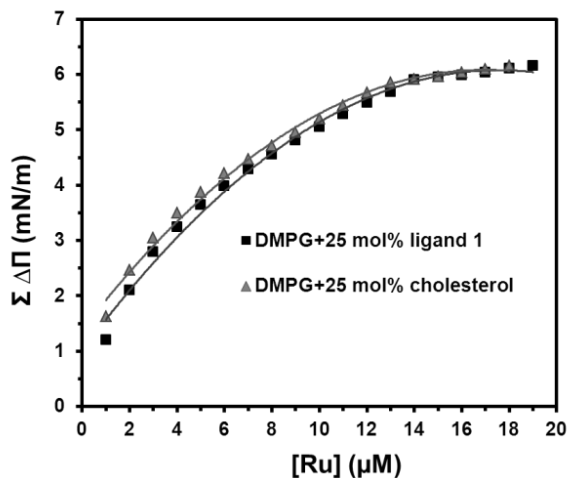


**Figure AIV.2**. Plot of surface pressure variation after each injection of $[2]^{2+}$ *vs.* total concentration of $[2]^{2+}$ in the trough upon titration of DMPG monolayers containing 25 mol% ligand **1**. Conditions: concentration of titrating $[2](PF_6)_2$ solution = 0.65 mM, $T$=298 K, lipid contents: 4.0 to 8.0 nmol.
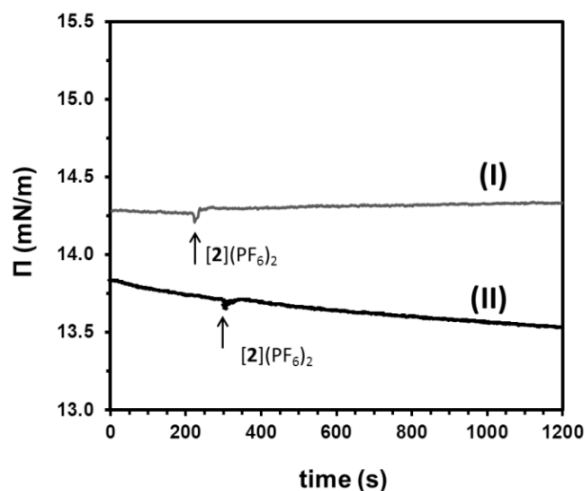
**Figure AIV.3**. Plots of surface pressure *vs.* time for zwitterionic monolayers after injection of $[2]^{2+}$ (0.5 μM) into the buffer subphase: (I) DMPC and 25 mol % cholesterol, and (II) DOPC and 25 mol% ligand **1**. Each arrow represents the injection of 50 μL $[2]^{2+}$. Conditions:  concentration of titrating $[2](PF_6)_2$ solution=0.65 mM, $T$=298 K, phosphate buffer: $I$=50 mM, pH=7.0, volume of the trough: 65 mL.
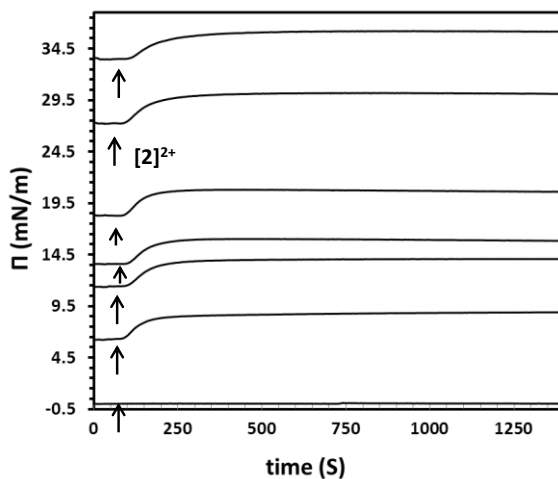


**Figure AIV.4.** Plots of surface pressure *vs.* time for DMPG monolayers containing 25 mol% of ligand 1 after injection of $[2]^{2+}$ (3.5 μM) in a buffer subphase at different initial surface pressure $\Pi_0$. Condition: 10 mM phosphate buffer, total ionic strength=50 mM, concentration of $[2]^{2+}$ in the stock solution=2.3 mM, $T$=298 K. At $\Pi_0$=0, there is no monolayer. Each arrow in the Figure shows an injection of 100 μL of $[2]^{2+}$.
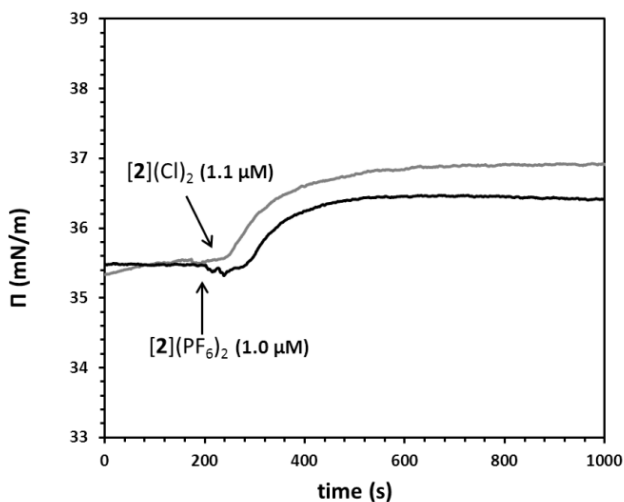
**Figure AIV.5**. Plots of surface pressure *vs.* time for a DMPG monolayer containing 25 mol% ligand 1 after injection of [**2**](PF$_6$)$_2$ (1.0 μM) or [**2**](Cl)$_2$ (1.1 μM) into a buffer subphase at an initial surface pressure $\Pi_0 \sim 35.5$ mN/m. Conditions: $I$=50 mM, concentrations of ruthenium stock solutions: 0.65 mM for [**2**](PF$_6$)$_2$, 3.5 mM for [**2**]Cl$_2$. T=298 K.

**Table AIV.1.** Thermodynamic data for the adsorption of [**2**](PF$_6$)$_2$ or [**2**]Cl$_2$ to DMPG liposomes functionalized with 25 mol% thioether-cholesterol ligand **1**. Conditions: ruthenium concentration = 0.62 mM, lipid concentration = 1.3 mM (as liposomes), phosphate buffer $I$=50 mM, pH=7.0, $T$=298 K.

| Ruthenium complex | Apparent $K_a$ (M$^{-1}$) | $\Delta H°$ (kJ·mol$^{-1}$) | $\Delta G°$ (kJ·mol$^{-1}$) | $\Delta S°$ (kJ·mol$^{-1}$·K$^{-1}$) | (Ru/lipid ratio) $n$ |
|---|---|---|---|---|---|
| [**2**](PF$_6$)$_2$ | $1.5(7)\times10^{+4}$ | 58 ±9 | −23 | +275 | 0.18 ±0.01 |
| [**2**]Cl$_2$ | $2.3(5)\times10^{+4}$ | 50±9 | −25 | +250 | 0.14 ±0.01 |

# Appendix V

## Supporting Information of Chapter 5:

**Liposomes functionalized with ruthenium complexes: towards tumor-targeted light-controlled anticancer prodrugs**

## AV.1. Quantification of the quenching of NBD-PC fluorescence by ruthenium complex [1](PF$_6$)$_2$ supported on a liposome

In order to determine the amount of quenching of NBD-PC by the ruthenium complex [1](PF$_6$)$_2$ incorporated in PEGylated DOPC liposomes (DOPC:DSPE-PEG2K:NBD-PC (92:4:4) in PBS, the following procedure was performed. Liposomes that contained different amounts (0.5 to 5 mol%) of complex [1](PF$_6$)$_2$ were prepared as explained in section 5.5.3. A 24-well plate was prepared with liposome solutions in each well and the plate was read with a fluorescence spectrophotometer set at the excitation wavelength: 460 ± 5 nm and emission wavelength: 534 ± 5 nm. A plot of the fluorescent values *vs.* concentration of the ruthenium in each sample (mol%) was obtained (Figure AIV.1). The emission intensity of NBD-PC was found to be dependent on the amount of ruthenium present in the liposome membrane (expressed in mol% of the complex in the lipid formulation). The ruthenium concentration dependence was modeled as a second order polynomial (for ≤5 mol% Ru) as shown in Equation AV.1.

$$F = 0.038 \cdot [RuSRR']^2 - 0.36 \cdot [RuSRR'] + 1 \ (R^2 = 0.9968) \qquad \text{(Equation AV.1)}$$

In this equation, F is the fluorescence at $\lambda_{em.} = 534$ nm (F$_{(0 \ mol\% \ Ru)} = 100\%$) and *[RuSRR']* is the amount of [1](PF$_6$)$_2$ in mol% in the membrane.
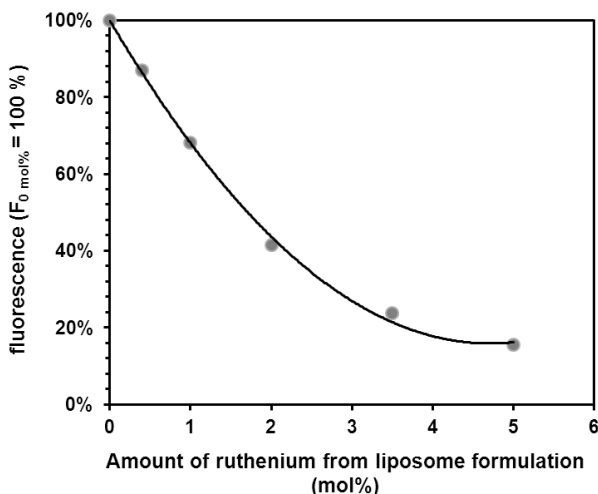


**Figure AIV.1**. Quenching of NBD-PC by different amounts of ruthenium complex [1](PF$_6$)$_2$ in mol% supported on DOPC:DSPE-PEG2K:NBD-PC(92:4:4) liposomes. Bulk total lipid concentration: = 2.5 mM (as liposomes), in PBS, $T = 25$ °C.

## AV.2. Sample preparation protocol for ruthenium concentration measurement by ICP-OES

After cellular uptake of each liposome sample containing Ru, the cell lysis (in NaOH 0.2 M) was collected from each well and mixed together. 2.0 mL of the cell lysis was put in a glass reaction tube and 1000 μL of $HNO_3$ (65%) was added. The tube was closed by a glass marble. It was then put in an oven at 90 °C for 3 h, after which the digested sample was transferred to a volumetric flask and completed to 5.0 mL with Milli-Q. The clear solution was put in a corning tube and the ruthenium concentration was measured by ICP-OES. For all samples, the measured value for ruthenium concentration was lower than the sensitivity of the ICP-OES machine (*[Ru]*<20 ppb), while the concentration of the ruthenium in the liposome stock solution (before exposure to the cells) was measured to be about 3820(40) ppb in 5 mL digested solution (5 mol% Ru complex (*e.g.,* [**1**]($PF_6$)$_2$) functionalized on liposomes, *[Ru]$_{tot}$* = 0.075 mM, *[lipid]$_{tot}$*= 1.5 mM) . The expected concentration for 100% cellular uptake was 3870(40) ppb in 5 mL solution.

**Table AV.1**. Extinction coefficients of the ruthenium complexes at one wavelength. The values were used to calculate concentrations of *[RuSRR']* and *[RuOH$_2$]* via deconvolution of UV-vis spectra.

| Ru complex | [**1**]$^{2+}$ | | [**2**]$^{2+}$ | | [**3**]$^{2+}$ | | [**4**]$^{2+}$ | |
|---|---|---|---|---|---|---|---|---|
| | RuSRR' | RuOH$_2$ | RuSRR' | RuOH$_2$ | RuSRR' | RuOH$_2$ | RuSRR' | RuOH$_2$ |
| $\varepsilon$ (L·mol$^{-1}$·cm$^{-1}$) | 4700 | 1000 | 4600 | 2400 | 5000 | 2100 | 5000 | 3100 |
| $\lambda$ (nm) | 413 | | 421 | | 420 | | 443 | |

# Appendix VI

## Supporting Information of Chapter 6:

**Yellow-light sensitization of a ligand photosubstitution reaction in a ruthenium polypyridyl complex covalently bound to a rhodamine dye**

## AVI.1. $^1$H NMR Spectra of the irradiated compounds
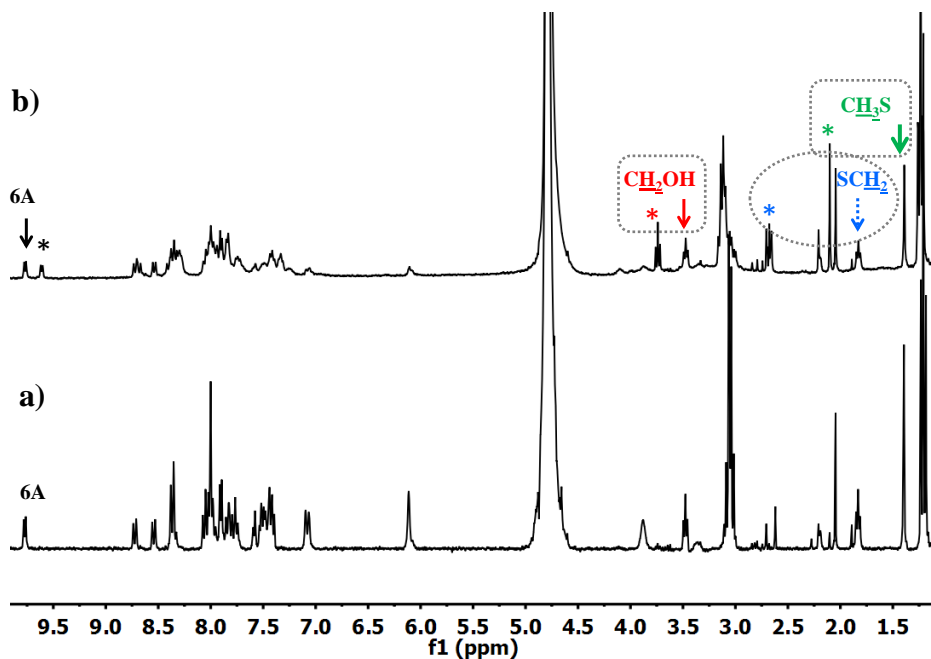


**Figure AVI.1**. $^1$H NMR spectra of [**2**]Cl$_3$ (region 10–1.0 ppm) in D$_2$O before (a) and after (b) irradiation with yellow light for 530 min. The arrows show the peaks of coordinated Hmte and 6A in [**2**]$^{3+}$, and the stars indicate free Hmte (aliphatic part) and 6A in [Ru(**4**)(bpy)(D$_2$O)]$^{3+}$ (aromatic part). Conditions: Yellow light irradiation ($\lambda_e$=570 nm, $\Delta\lambda_{1/2}$=8.9 nm, $t$=530 min, photon flux: 5.3×10$^{-9}$ Einstein·s$^{-1}$), $[Ru]_{tot}$=5.3×10$^{-3}$ M, $T$=298 K.
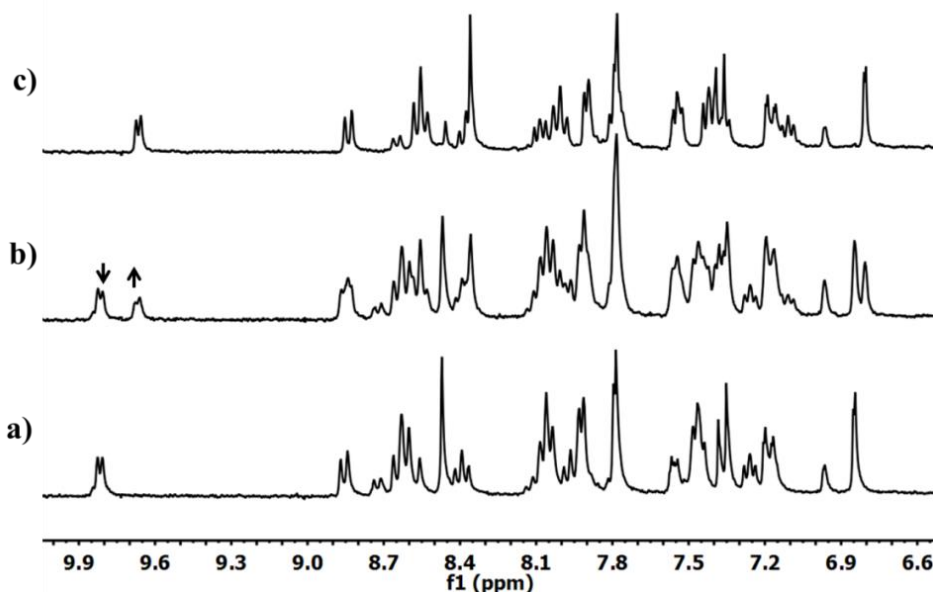
**Figure AVI.2**. $^1$H NMR spectra of [**2**](PF$_6$)$_3$ (region 10–6.6 ppm) in acetone-d6/D$_2$O (90:10) (a) before irradiation and in the dark; (b) after 4 h irradiation with yellow light ($\lambda_e$=570 nm, $\Delta\lambda_{1/2}$=8.9 nm); the solution contains a mixture of [**2**]$^{3+}$ and [Ru(**4**)(bpy)(D$_2$O)]$^{3+}$; and (c) after leaving the sample under sun light for 2 days; full photoconversion to the aqua compound [**7**]$^{3+}$ was reached. Conditions: *[Ru]$_{tot}$*=2.0×10$^{-3}$ M, *T*=298 K.

## AVI.2. Photon flux determination

The photon flux for the irradiation setup at 452 nm was measured using the ferrioxalate actinometer.[1] However, the ferrioxalate actinometer is not suited for 570 nm photons, so that an indirect method was used. The light power (in mW·cm$^{-2}$) at 452 nm ($I_{452}$) and 570 nm ($I_{570}$) was measured using an OPHIR Nova power meter. Knowing the photon flux at 452 nm ($\Phi_{452}$), the photon flux at 570 nm ($\Phi_{570}$) was calculated using Equation AVI.1. In this equation $E_\lambda$ is the photon energy at 452 nm ($E_{452}$=4.4×10$^{-19}$ J) and at 570 nm ($E_{570}$=3.5×10$^{-19}$ J). The photon flux at 570 nm was found to be 5.3×10$^{-9}$ Einstein·s$^{-1}$.

$$\frac{I_{452}}{I_{572}} = \frac{\Phi_{452} \times E_{452}}{\Phi_{570} \times E_{570}} \qquad \textbf{(Equation AVI.1)}$$

# AVI.3. References

[1]    J. G. P. Calvert, J. N., *Chemical actinometer for the determination of ultraviolet light intensities. In Photochemistry.* Wiley and Sons, New York, **1967**, 780.

# Samenvatting (Summary in Dutch)

## Algemene inleiding (H 1)

Polypyridyl-rutheniumcomplexen worden veel gebruikt in fotochemie.[1-2] Hun fotofysische eigenschappen kunnen worden verfijnd om de gewenste reactie te krijgen als ze met licht worden beschenen met licht. Rutheniumcomplexen, in het bijzonder die met een verstoord-octaëdrische geometrie, kunnen een ligand vervangen voor een oplosmiddelmolecuul wanneer ze worden beschenen met zichtbaar licht (400-600 nm).[3]

Twee mogelijke toepassingen van dit soort verbindingen worden besproken: allereerst als lichtgestuurde moleculaire machines en ten tweede als antikankermedicijn dat door licht geactiveerd kan worden. In dit proefschrift wordt er verbinding gelegd tussen deze twee toepassingen door gebruik te maken van een membraan van een dubbele laag van vetten. In het eerste deel van het in dit proefschrift beschreven werk zijn fotosubstitutiereacties van rutheniumverbindingen bestudeerd op het oppervlak van membranen, om natuurlijke moleculaire machines na te bootsen. Door monodentaatliganden in het membraan te binden kan het rutheniumcomplex thermisch aan het membraan binden terwijl het weer worden losgemaakt door bestraling met licht; op deze manier kan een model van een lichtbestuurde moleculaire transporteur worden gerealiseerd. In het tweede deel van het beschreven werk worden dezelfde membranen met daarop verankerde, lichtgevoelige rutheniumcomplexen beschouwd als mogelijke fotochemotherapeutica, omdat het ruthenium-watercomplex dat vrijkomt bij de bestraling met licht mogelijk cytotoxisch is. De membranen met daarop de rutheniumverbinding, die als prodrug fungeren, zouden naar kankercellen gebracht kunnen worden. Eenmaal opgenomen kunnen ze worden geactiveerd met licht, wat resulteert in een fotosubstitutiereactie waarbij het actieve ruthenium-watercomplex vrijkomt in de cel. Door de fotochemie van rutheniumverbindingen en de biologische eigenschappen van liposomen te combineren, zijn we van een fundamenteel biomimetisch onderwerp, moleculaire beweging, naar het tweede onderwerp gekomen, het meer praktisch gerichte medicijntransport.

## Ruthenium-polypyridylcomplexen die springen op het oppervlak van anionische dubbellagen van vetten door middel van een lichtgevoelige supramoleculaire verbinding (H 2)

In hoofdstuk 2 is de nieuwe rutheniumverbinding $[Ru(terpy)(dcbpy)(Hmte)]^{2+}$ (RuHmte) geïntroduceerd (terpy = 2,2';6',2"-terpyridine, dcbpy = 6,6'-dichloro-2,2'-bipyridine, Hmte = 2-methylthioethan-1-ol). Met behulp van kinetiekmetingen en thermodynamische gegevens is aangetoond dat de sterische hindering van de methylgroepen in dcbpy destabilisatie veroorzaakt van zowel het ruthenium-thioethercomplex (afgekort als RuHmte) als ook de waterbevattende verbinding $[Ru(terpy)(dcbpy)(H_2O)]^{2+}$ (afgekort als RuOH$_2$). Bij kamertemperatuur en in het donker zijn deze twee verbindingen in thermisch evenwicht. Echter, bestraling van de oplossing met blauw licht resulteert in selectieve substitutie van het thioetherligand door een waterligand, wat het evenwicht verschuift richting de vorming van RuOH$_2$ (zie schema 7.1a). Het is aangetoond dat deze evenwichtsverschuiving veroorzaakt door licht ten minste vier keer herhaald kan worden in een homogene, waterige oplossing.

Thermisch binden en lichtgeïnduceerde dissociatie van een thioetherligand aan het rutheniumcentrum is ook uitgevoerd op het oppervlak van negatief geladen liposomen (zie schema 7.1b). UV-vis metingen laten zien dat het ruthenium-watercomplex efficiënt coördineert aan een membraangebonden thioetherligand in het donker, en dat tijdens beschijnen met zichtbaar licht de Ru-S-binding selectief wordt verbroken zodat het ruthenium-watercomplex wordt losgelaten. Het is aangetoond dat deze reacties vier keer herhaald kunnen worden door de lichtbron aan en weer uit te schakelen. Hiermee is dus lichtgeïnduceerd 'springen' van een rutheniumcomplex op een membraan van vetten bereikt.

Efficiënt, lichtgestuurde springen van een rutheniumcomplex op het membraan heeft twee vereisten. Allereerst moet de sterische hindering van het rutheniumcomplex hoog genoeg zijn om snelle thermische coördinatie en lichtgeïnduceerde dissociatie mogelijk te maken. Ten tweede moeten de liposomen negatief geladen zijn zodat de rutheniumcomplexen in de buurt van het membraan blijven en weer kunnen binden aan de membraangebonden zwavelliganden. Deze twee zaken worden verder besproken in respectievelijk hoofdstuk 3 en 4.
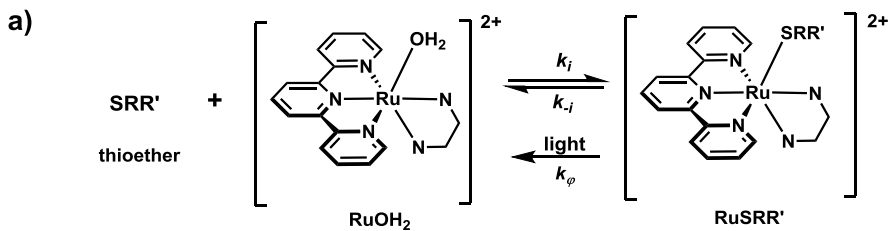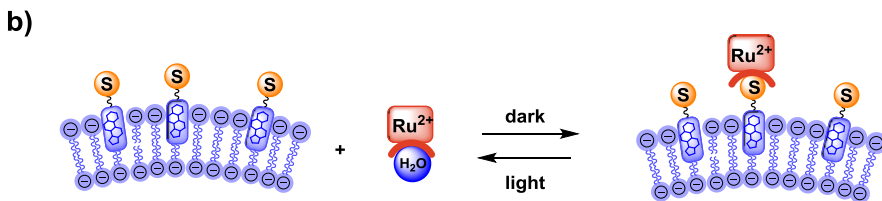
**Schema 7.1.** a) Thermisch evenwicht tussen Ru(terpy)(N-N)(H$_2$O)]$^{2+}$ en [Ru(terpy)(N-N)(SRR')]$^{2+}$ en de fotosubstitutie van SRR´ door H$_2$O. SRR'is een thioetherligand zoals 2-methylthioethan-1-ol en N-N is een diimineligand zoals dcbpy. b) Lichtgeïnduceerde rutheniumbinding en dissociatie op een negatief geladen membraan.

## Spontane vorming in het donker en lichtgeïnduceerde verbreking van een Ru-S-binding in water: een thermodynamische en kinetische studie (H 3)

In hoofdstuk 3 wordt de thermische en fotochemische reactiviteit in water beschreven van vier verwante ruthenium-polypyridylcomplexen met de algemene formule [Ru(terpy)(N-N)(Hmte)]$^{2+}$ (N-N = bpy, biq, dcbpy, of dmbpy, zie schema 3.1a). Bij elk van deze complexen wordt de Ru-S-binding verbroken door bestraling met licht, wat resulteert in de vorming van het ruthenium-watercomplex [Ru(terpy)(N-N)(H$_2$O)]$^{2+}$ (RuOH$_2$). In dit hoofdstuk is beschreven hoe de sterische hindering van het N-N ligand de thermodynamische stabiliteit en kinetische labiliteit van de RuHmte- en RuOH$_2$-complexen in het donker beïnvloedt. De kinetiek van de van fotosubstitutiereacties is ook gerapporteerd.

Met toenemende sterische hindering van het N-N ligand, wordt de snelheid van thermische binding aan en thermische dissociatie van het Hmte-ligand van het rutheniumcentrum vergroot. Een verschuiving is waargenomen langs de serie van bpy, biq, dcbpy, en dmbpy, van een zeer langzaam thermisch evenwicht tussen RuOH$_2$ en RuHmte met N-N=bpy, tot een zeer snel evenwicht met N-N=dmbpy.

De grotere labiliteit van de gehinderde complexen in water wordt niet veroorzaakt door een verandering van de activeringsenthalpie van de substitutiereactie ($\Delta H^{\ddagger}$), maar door een verandering van de activeringsentropie $\Delta S^{\ddagger}$, die negatief is voor bpy en biq en positief is voor dcbpy en dmbpy. Deze verandering in de activeringsentropie geeft aan dat er een verandering is in het mechanisme van de substitutiereactie, van een associatief mechanisme voor de verbindingen met bpy en biq ($\Delta S^{\ddagger}<0$) naar een dissociatief mechanisme voor de complexen met dcbpy en dmbpy ($\Delta S^{\ddagger}>0$).

De kwantumefficiëntie van de fotoverbreking van de Ru-S-binding neemt ook toe langs de serie van N-N = bpy, biq, dcbpy, en dmbpy. In het algemeen zijn er twee voorwaarden gevonden om het evenwicht tussen RuHmte en $RuOH_2$ in water met licht te verschuiven. Allereerst moet de thermodynamische stabiliteit van het RuHmte-complex in het donker in water groter zijn dan dat van $RuOH_2$ ($k_{-i}<k_i$) om te leiden tot de spontane vorming van de ruthenium-thioetherverbinding. Echter, RuHmte wordt niet gevormd als de instelling van het thermische evenwicht te langzaam is, zoals in het geval van het complex met het minst-gehinderde ligand bpy, omdat er niet genoeg thermische energie is om de activeringsbarrière van de coördinatiereactie te overwinnen. Ten tweede moet de snelheid van de fotosubstitutie van het Hmte-ligand voor een waterligand hoger zijn die van de analoge thermische substitutiereactie ($k_{-i}<k_{\varphi}$, zie schema 7.1a). Voor het complex met het meest sterisch-gehinderde ligand dmbpy geldt dit niet; de thermische labiliteit van het RuHmte-complex is zo hoog dat licht geen significante verschuiving kan veroorzaken in het evenwicht tussen RuHmte en $RuOH_2$. De conclusie is dat alleen de complexen die niet al te zeer gehinderd zijn, namelijk die met N-N=biq en dcbpy, geschikt zijn voor de verschuiving van het evenwicht tussen RuHmte en $RuOH_2$ met licht.

## Het binden van een ratheniumcomplex aan een thioetherligand dat gebonden is aan een negatief geladen dubbellaag van vetten: een tweestapsmechanisme (H 4)

Negatief geladen membranen zijn nodig voor de binding van ruthenium-watercomplexen aan membraangebonden thioetherliganden, zoals besproken in hoofdstuk 2. In hoofdstuk 4 wordt de rol gerapporteerd van de negatieve lading van de membranen in de coördinatiereactie die plaatsvindt op het water-membraan grensvlak. De interactie van het complex $[Ru(terpy)(dcbpy)(H_2O)]^{2+}$ met fosfolipidemembranen die neutrale thioetherliganden óf cholesterol bevatten, is bestudeerd door gebruik te maken van drie verschillende technieken: UV-visible spectroscopie, oppervlaktedruk-metingen aan Langmuir-Blodgett monolagen en Isothermische Titratie-Calorimetrie (ITC).

De resultaten van de eerste techniek toonden aan dat de reactie van de rutheniumverbinding met de thioetherliganden langzamer wordt wanneer de elektrostatische interactie tussen de rutheniumkationen en de negatief geladen liposomen wordt afgeschermd door een grotere ionsterkte van de oplossing. Adsorptie van het dikationische rutheniumcomplex op het oppervlak van de negatieve membranen speelt dus een prominente rol in de vorming van de Ru-S coördinatieverbinding.

Informatie over de tijdsschaal van dit adsorptiefenomeen en over de thermodynamica is verkregen uit de metingen van de oppervlaktedruk van een monolaag van vetten en uit ITC metingen. Het is aangetoond dat de adsorptie van het ruthenium-watercomplex aan het oppervlak van de negatief-geladen monolagen en dubbellagen veel sneller is (minuten) dan coördinatie aan de thioetherverbinding (liganduitwisseling) (uren). Bovendien bleek het adsorptiefenomeen endotherm te zijn, oftewel gedreven door entropie. Gebaseerd op deze resultaten is een tweestapsmechanisme voorgesteld voor de binding van het dikationische metaalcomplex aan thioetherliganden die verankerd zijn in negatief-geladen liposomen. In de eerste stap adsorbeert de buitenste laag van een negatief geladen dubbellaag van vetten de positief geladen metaalcomplexen, en in de tweede stap wordt de Ru-S verbinding gevormd via tweedimensionale diffusie van beide reagentia op het membraan (zie Schema 4.2). Deze tweestapsreactie op negatief geladen membranen is sneller dan de corresponderende Ru-S vorming in een homogene oplossing.

## Ruthenium-gefunctionaliseerde liposomen: naar een tumor-gerichte, licht-gecontroleerde antikanker geneesmiddel (H 5)

In hoofdstuk 5 is de potentiële toepassing beschreven van liposomen die gefunctionaliseerd zijn met lichtgevoelige polypyridyl-rutheniumcomplexen. Vier niet-labiele rutheniumcomplexen zijn gemaakt met de algemene formule [Ru(terpy)(N-N)(SRR')]$^{2+}$ (N-N = bpy of pymi (fenylpyridin-2-ylmethylene-imine), en SRR' = thioetherliganden met een cholesterolstaart). Deze verbindingen zijn allemaal geplaatst op neutrale en negatief geladen liposomen. Alle vier de ruthenium-gefunctionaliseerde liposomen zijn fotoreactief; als oplossingen met deze liposomen worden beschenen met blauw licht, wordt de ruthenium-zwavelbinding verbroken. De fotosubstitutiereacties bleken sneller te zijn bij menselijke lichaamstemperatuur (37 °C) dan bij kamertemperatuur (25 °C), en iets sneller op het oppervlak van neutrale liposomen dan op negatief geladen liposomen.

Celopname-experimenten op menselijke kankercellen lieten zien dat, in afwezigheid van PEG, het verhogen van de netto oppervlaktespanning van de liposomen resulteert in hogere celopname voor HepG2, A2780 en A2780R kankercellijnen. Rutheniumgefunctionaliseerde liposomen bestaande uit neutrale vetten worden beter opgenomen dan de analoge liposomen van negatief geladen lipiden. Echter, wanneer gePEGyleerde vetten geïntroduceerd worden in het membraan, wordt de netto oppervlaktespanning van de resulterende rutheniumgefunctionaliseerde "stealthliposomen" afgeschermd, wat resulteert in een verlaagde celopname vergeleken met PEG-vrije liposomen. In het algemeen heeft de exacte structuur van de rutheniumcomplexen geen significant effect op de celopnameresultaten.

De giftigheidtesten van de neutrale en negatief-geladen "stealthliposomen" gefunctionaliseerd met een van de vier rutheniumcomplexen onder uitsluiting van licht, lieten zien dat deze liposomen in lage mate toxisch zijn voor A2780 en A2780R cellijnen, zonder significante verschillen tussen de vier rutheniumcomplexen. De cytotoxiciteit op HepG2 cellen is ook bepaald na bestraling met licht van één van de rutheniumcomplexen gebonden aan niet-gePEGyleerde liposomen. Het resultaat is dat bestraling met licht leidt tot een minimaal 40% hogere cytotoxiciteit ten opzichte van de cytotoxiciteit in het donker. Bij neutrale liposomen is dit effect het sterkst en is de cytotoxiciteit na bestraling met licht zelfs 80% hoger. Op basis van deze resultaten kan geconcludeerd worden dat het gebruik van ruthenium-gefunctionaliseerde liposomen veelbelovend is voor gecontroleerde afgifte van antikankermedicijnen.

## Sensitizatie met geel licht van een ligand-fotosubstitutiereactie in een ruthenium-polypyridylcomplex dat covalent gebonden is aan een rhodaminekleurstof (H 6)

In hoofdstuk 6 wordt de mogelijkheid besproken om de fotoactivering van polypyridyl-rutheniumcomplexen uit te bereiken met langere golflengtes. Zoals vermeld in hoofdstuk 1 zijn verscheidene polypyridyl-rutheniumcomplexen voorgesteld als lichtactiveerbare medicijnen voor fototherapie. Echter, hun potentiële toepassing *in vivo* is gelimiteerd, omdat ze voornamelijk blauw licht (450 nm) absorberen, waarvan bekend is dat het zeer slecht doordringt in menselijk weefsel.

De fotosubstitutie van een thioetherligand op een rutheniumcomplex door een watermolecuul is bestudeerd met geel licht (570 nm). Een rhodamine-B kleurstof met een hoge molaire absorptie voor geel licht is covalent gebonden via een korte verzadigde linker aan het terpyridineligand Rtepy in het complex $[Ru(Rterpy)(bpy)(Hmte)]^{2+}$. Het uitstekende antenne-effect van de rhodamine-B kleurstof, gekoppeld aan efficiënte energieoverdracht naar het rutheniumcentrum via

het omgekeerde Förstermechanisme, resulteerde onverwacht in snellere fotosubstitutie van het thioetherligand door bestraling met geel licht dan met blauw licht.

In hoofdstuk 6 is de snelheid van fotosubstitutiereacties besproken wanneer fotonen met onvoldoende energie, vergeleken met dat van de [1]MLCT toestand, zijn gebruikt. Voor zowel het rhodamine-B-gefunctionaliseerde rutheniumcomplex en voor zijn antenneloze equivalent $[Ru(terpy)(bpy)(Hmte)]^{2+}$ zijn de kwantumopbrengsten vergelijkbaar voor blauw of geel licht. Sterker nog, bij een constante fotonflux is het de extinctiecoëfficiënt die de snelheidsconstante van fotosubstitutie het meest beïnvloedt voor deze complexen, terwijl de kwantumopbrengst van fotosubstitutie nauwelijks afhangt van de gebruikte golflengte.

## References

[1]    V. Balzani, A. Juris, *Coord. Chem. Rev.* **2001**, *211*, 97-115.
[2]    K. Kalyanasundaram, *Coord. Chem. Rev.* **1982**, *46*, 159-244.
[3]    S. Bonnet, J.-P. Collin, *Chem. Soc. Rev.* **2008**, *37*, 1207-1217.
[4]    P. Zhang, W. Steelant, M. Kumar, M. Scholfield, *J. Am. Chem. Soc.* **2007**, *129*, 4526-4527.
[5]    R. Weissleder, V. Ntziachristos, *Nat. Med.* **2003**, *9*, 123-128.
[6]    M. von Delius, E. M. Geertsema, D. A. Leigh, *Nature Chem.* **2010**, *2*, 96-101.
[7]    D. A. Leigh, J. K. Y. Wong, F. Dehez, F. Zerbetto, *Nature* **2003**, *424*, 174-179.
[8]    L. Simeone, G. Mangiapia, G. Vitiello, C. Irace, A. Colonna, O. Ortona, D. Montesarchio, L. Paduano, *Bioconjug. Chem.* **2012**, *23*, 758-770.
[9]    G. Mangiapia, G. D'Errico, L. Simeone, C. Irace, A. Radulescu, A. Di Pascale, A. Colonna, D. Montesarchio, L. Paduano, *Biomaterials* **2012**, *33*, 3770-3782.

# List of Publications

**Efficient Synthesis of Pyrrolo[2,1-a]isoquinoline and Pyrrolo[1,2-a]quinoline Derivatives in Aqueous Media**

Kianmehr, E.; Estiri, H.; **Bahreman**, **A**.; *J. Heterocycl. Chem.* **2009**, *46*, 1203

**Ruthenium polypyridyl complexes hopping at anionic lipid bilayers *via* a supramolecular bond sensitive to visible light**

**Bahreman**, **A**.; Limburg, B.; Siegler, M.A.; Koning, R.; Koster, A.J.; Bonnet, S.; *Chem. Eur. J.* **2012**, *18*, 10271.

**Spontaneous formation in the dark, and visible light-induced cleavage, of a Ru-S bond in water: a thermodynamic and kinetic study**

**Bahreman**, **A**.; Limburg, B.; Siegler, M.A.; Bouwman E.; Bonnet, S.; *Inorg. Chem.* **2013**, *52*, 9456.

**Activation of a photodissociative ruthenium complex by triplet-triplet annihilation upconversion at liposomes**

Askes S.H.C; **Bahreman A.**; Bonnet S.; *Angew. Chem. Int. Ed.* **2013**, in press.

**Yellow-light sensitization of a ligand photosubstitution reaction in a ruthenium polypyridyl complex covalently bound to a rhodamine dye**

**Bahreman**, **A**.; Cuello-Garibo J. A.; Bonnet S.; *submitted for publication*.

**Binding of a ruthenium complex to a thioether ligand embedded in a negatively charged lipid bilayer: a two-step mechanism**

**Bahreman**, **A**.; Rabe M.; Kros A.; Bruylants G.; Bonnet S.; *submitted for publication.*

**Light-induced releasing of a cytotoxic ruthenium complex supported at the surface of a liposome drug carrier**

**Bahreman A.**; Van Geest E.; Heger M.; Balemans C.; Lupica-Spagnolo L.; Bonnet S.; *manuscript in preparation.*

# Curriculum Vitae

Azadeh Bahreman was born in Babol, Iran and grew up in Tehran, Iran. In the last year of high school she became interested in Chemistry while preparing for the national undergraduate entrance examination (Concours). After successfully passing the Concours in 2000, she chose to study pure chemistry in Shahid Beheshti University, Tehran, Iran. After obtaining her bachelor degree she worked in the Tehran International High School as a chemistry laboratory assistant until 2006. She then decided to continue studying chemistry and passed the national graduate entrance exam, to start a MSc's degree in organic chemistry at the University of Tehran. She performed her Master project under the supervision of Dr. E. Kinamehr and worked on the one-pot synthesis of new pyrrolo [1, 2-α] quinoline derivatives and on synthetic methodology for the ipso-substitution of aryl boronic acids. In parallel, she was cooperating as a part-time research assistant with the Chemical Processes Investigation Center of the Chemical Engineering College of the University of Tehran on the production of industrial amines. After obtaining her Master degree in 2008, she was employed in the Barzegar Zonouz research institute, Tehran, Iran as a research expert to work on a hydroformylation project.

In November 2009 she got a position at the Leiden Institute of Chemistry to pursue her PhD under the supervision of Dr. S. Bonnet and Prof. Dr. E. Bouwman on a multi-disciplinary project in the field of bioinorganic photochemistry. During her PhD she collaborated with several research groups such as the Department of Experimental Surgery of the Academic Medical Center in Amsterdam, and the Molecular and Biomolecular Engineering group at the Free University in Brussels. She attended several postgraduate courses and schools organized by the Holland Research School of Molecular Chemistry (HRSMC). In addition, she participated in general training courses such as Effective communication, Time management, and Scientific Integrity organized by the Leiden University graduate school. As a part of the PhD program, she also contributed in assisting several general and organic practical courses and also supervised several MSc students (Lucia Lupica Spagnolo, Jordi-Amat Cuello-Garibo, Rehana Sukhrie, Erik van Geest), and BSc students (Matthew Everhart, Collin Balemans, Michiel Langerman).

She presented her PhD work at several national and international conferences including the HRSMC annual symposia (2010 and 2013 Leiden, 2011 Amsterdam), the Leiden Institute of Chemistry annual Reedijk symposium (2010, Leiden), the NWO-CW Organic Chemistry and Synthesis Study Group Meetings (2010 and 2012 Lunteren), the CHAINS conference (2011, Utrecht), the COST meeting "Supramolecular chemistry in water" (2012, Riccione, Italy), the KNCV Wageningen meeting (2012, Wageningen), and the Gordon Research Photochemistry Conference (Boston, MA, USA). She was awarded two poster prizes in two consecutive HRSMC symposia.

# Nawoord
# (Acknowledgements)